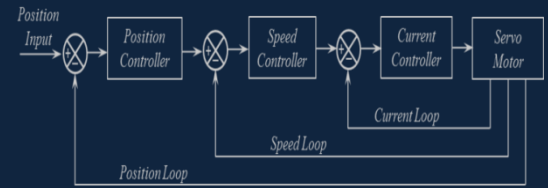




e-ISSN: 2618-575X



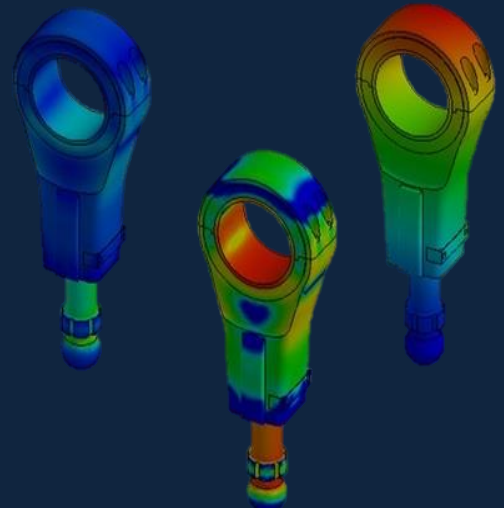
International Advanced Researches and Engineering Journal

Aerospace Engineering,
Aquaculture and Fisheries Engineering,
Architecture,
Bioengineering,
Cell and Tissue Engineering
Chemical Engineering,
Civil Engineering,
Computer Engineering,
Electrical and Electronics,
Energy,
Environmental Engineering,
Food Engineering,
Geomatics Engineering,
Health in Engineering
Industrial Engineering,
Industrial Applications,
Machine Theory and Dynamics,
Marine Science and Technology,
Materials and Nano Science,
Manufacturing,
Mechanical Engineering,
Mechanics,
Mechatronics,
Medical,
Modeling and Simulation,
Physics Engineering,
Robotics,
Sustainable Science Technology,
Textile Engineering
Transport Science and Technology

$$F=ma$$

$$E=mc^2$$

$$\int \frac{dy}{dx} dt$$



Volume: 04 / Issue: 02 / August 2020



e-ISSN: 2618-575X

Available online at www.dergipark.org.tr/en

INTERNATIONAL ADVANCED RESEARCHES
and
ENGINEERING JOURNAL

Journal homepage: www.dergipark.org.tr/en/pub/iarej

International
Open Access



Volume 04
Issue 02
August, 2020

International Advanced Researches and Engineering Journal (IAREJ) is a double-blind peer-reviewed and publicly available online journal that has Editorial Board (<https://dergipark.org.tr/en/pub/iarej/board>). The editor in chief of IAREJ welcomes the submissions that cover theoretical and/or applied researches on **Engineering** and related science with Engineering. The publication language of the Journal is **English**. **Writing Rules** are given in Author Guidelines (<https://dergipark.org.tr/en/pub/iarej/writing-rules>). IAREJ publishes **original papers** that are research papers and technical review papers.

IAREJ publication, which is **open access**, is **free of charge**. There is no article submission and processing charges (APCs).

IAREJ is indexed & abstracted in:

Crossref (Doi beginning: 10.35860/iarej.xxxxxx)
Directory of Open Access Scholarly Researches (ROAD)
Directory of Research Journals Indexing (DRJI)
EBSCO
Google Scholar
Index Copernicus (ICI Journal Master List)
J-Gate
Rootindexing
Scientific Indexing Services (SIS)
TUBITAK ULAKBIM TR Dizin (TR index)
WorldCAT

Authors are responsible from the copyrights of the figures and the contents of the manuscripts, accuracy of the references, quotations and proposed ideas and the Publication Ethics (<https://dergipark.org.tr/en/pub/iarej/page/4240>).

All rights of the issue are reserved by International Advanced Researches and Engineering Journal (IAREJ). IAREJ also allows the author(s) to hold the copyright of own articles.

©

IAREJ

15 August 2020



This is an open access issue under the CC BY-NC license (<http://creativecommons.org/licenses/by-nc/4.0/>).



e-ISSN: 2618-575X

Available online at www.dergipark.org.tr/en

INTERNATIONAL ADVANCED RESEARCHES
and
ENGINEERING JOURNAL

Journal homepage: www.dergipark.org.tr/en/pub/iarej

International
Open Access 

Volume 04
Issue 02
August, 2020

Table of Contents

Research Articles	Pages
Increasing the thermal performance of cooling tower by utilizing swirling jets <i>Mustafa KILIÇ, Mehmet ÖZTATAR, Ali Özhan AKYÜZ, Azim Doğuş TUNCER and Afşin GÜNGÖR</i>	057-063
Numerical and experimental study on thermal characteristics of louvered fin microchannel air preheaters <i>Anıl BAŞARAN and Ali YURDDAŞ</i>	064-075
The effects of the use of acetylene gas as an alternative fuel in a gasoline engine <i>Salih ÖZER, Mehmet AKÇAY, Erdinç VURAL and İlker Turgut YILMAZ</i>	076-086
The investigation of effect of the ceramic coatings with bond-layer coated on piston and valve surface on engine performance of a diesel engine <i>Erdinç VURAL and Serkan ÖZEL</i>	087-093
Layer-by-layer growth of molecular self-assembled monolayers /sputtered gold thin films/graphene oxide on glass substrate <i>Fatma BAYRAKÇEKEN NİŞANCI</i>	094-098
Effect of polymer and surfactant concentrations on PVP nanofibers morphology <i>Hülya KESİCİ GÜLER and Funda CENGİZ ÇALLIOĞLU</i>	099-105
Investigation of plastic zone dimension in front of an external semi-elliptic crack on pipe of molecular bushing <i>İlyas KACAR</i>	106-115
Investigation of nonlinear behavior of high ductility reinforced concrete shear walls <i>Saeid FOROUGHİ and Bahadır YÜKSEL</i>	116-128
A novel design of a compact wideband patch antenna for sub-6 GHz fifth-generation mobile systems <i>Mehmet YERLİKAYA, Seyfettin Sinan GÜLTEKİN and Dilek UZER</i>	129-133
Numerical analysis of the harvester having toroidal structure and examination of the application results <i>Mahmut KABAKULAK and Serdal ARSLAN</i>	134-141
Determination of optimal PID control parameters by response surface methodology <i>Adnan ALDEMİR and Mohammed Sadralddin ANWER</i>	142-153
Removal of Maxilon Red GRL dye in continuous system adsorption column using waste pine sawdust <i>İlknur ŞENTÜRK and Muhammed Reha YILDIZ</i>	154-160



e-ISSN: 2618-575X

INTERNATIONAL ADVANCED RESEARCHES
and
ENGINEERING JOURNAL

Journal homepage: www.dergipark.org.tr/en/pub/iarejInternational
Open Access Volume 04
Issue 02

August, 2020

Research Article**Increasing the thermal performance of cooling tower by utilizing swirling jets**

Mustafa Kılıç^a , Mehmet Öztatar^a , Ali Özhan Akyüz^b , Azim Doğuş Tuncer^{c,d,*} 
and Afşin Güngör^e 

^aAdana Alparslan Türkeş Science and Technology University, Mechanical Engineering, Adana 01250, Turkey^bBurdur Mehmet Akif Ersoy University, Bucak Emin Gulmez Technical Sciences Vocational Higher School, Burdur 15300, Turkey^cBurdur Mehmet Akif Ersoy University, Energy Systems Engineering, Burdur 15030, Turkey^dGazi University, Natural and Applied Science Institute, Ankara 06560, Turkey^eAkdeniz University, Mechanical Engineering, Antalya 07058, Turkey

ARTICLE INFO

Article history:

Received 10 February 2020

Revised 13 April 2020

Accepted 19 April 2020

Keywords:

Direct contact cooling

Effectiveness

Evaporation loss

Swirling jet

ABSTRACT

Cooling towers are generally utilized in heating, ventilation, and air conditioning systems, electric power plants and manufacturing applications. The main problem for cooling towers is evaporation loss. The evaporation loss is decreased with utilizing fans, drift eliminators for more water saving. This work is mainly focused numerical analysis of cooling tower for reducing evaporation loss and increase the efficiency of the tower by utilizing two crosswise swirling jets that reduce the inlet hot water temperature in the outlet of the cylindrical channel to the not harmful to ambient conditions temperature. The model is computed for various parameters; air inlet temperatures (10, 22, 32, 40 °C) and Reynolds number for jets inlet velocities (Re= 3900, 5200, 7800, 8500). This model was studied numerically by utilizing ANSYS Fluent CFD software. In this work, it is achieved that increasing Reynolds number causes an increase on evaporation loss. The higher air inlet temperature causes higher evaporation loss. When the air inlet temperatures are reduced from 40 °C to 10 °C, the evaporation loss is decreased as 62% and 81%, respectively. When Reynolds number is decreased from 8500 to 3900, the evaporation loss decreased as 30%. By utilizing this new design, the outlet water temperature could be reduced of 19 °C. Moreover, the numerical findings were validated by some researches available in the literature.

© 2020, Advanced Researches and Engineering Journal (IAREJ) and the Author(s).

1. Introduction

Cooling towers are widely used for heat rejection into the atmosphere. Cooling towers used in HVAC system, for cooling the process hot water in manufacturing, electric power plant for cooling the condenser and chemical plants. Heat rejection of the tower is accomplished with evaporation air and hot water or steam. In cooling towers, water evaporates due to content of the moisture in air which occurs when the air is fewer than saturated of the water temperature. Hereby, energy transfer occurs among water and air so water cools and

air become hot. Cooling towers are designed and manufactured in various types for specific condition such as ambient wet bulb temperature, intended temperature and flow rates. So, we can classify cooling towers with heat transfer method, build, air draft and air flow pattern. There are two types of cooling tower considering to heat transfer method, dry and wet systems. Wet cooling tower, most commonly using tower which operated with principle of evaporation for cooling the hot water or steam. The hot fluid is cooled with ambient air that comes to the cooling tower. Dry cooling tower has a closed-circuit system which separates the air and hot

* Corresponding author. Tel.: +90-248-213-2773

E-mail addresses: mkilic@atu.edu.tr (M. Kılıç), mehmetoztatar96@gmail.com (M. Öztatar), aliozhanakyuz@gmail.com (A.Ö. Akyüz), azimdtuncer@gmail.com (A.D. Tuncer), afsingungor@hotmail.com (A. Güngör)

ORCID: 0000-0002-8006-149X (M. Kılıç), 0000-0001-5668-3400 (M. Öztatar), 0000-0001-9265-7293 (A.Ö. Akyüz), 0000-0002-8098-6417 (A.D. Tuncer), 0000-0002-4245-7741 (A. Güngör)

DOI: 10.35860/iarej.686816

water or steam. This pipe system protected the cooled water from environment. Evaporation does not occur between the air and hot water. There are three types of cooling towers depends on air draft. The atmospheric type of towers very cost effective and very inefficient. There is no mechanical work for driving to air. Natural draft cooling tower shape is hyperbolic structure and natural air flow is accomplished cooling with using own hyperbolic structure. The air inflow into the tower is a result of the density difference between hot and air inside the cooling tower. Mechanical cooling towers are used forced draft and induced draft fan. Forced draft fan blow the air into the cooling tower and it is located beside of the cooling tower. The fan is in outside of the cooling tower so in cold weather condition freezing may occur in fan. The inlet air velocity is higher than outlet air velocity. Induced draft fan is located on the cooling tower so the fan is absorbed to air vapor mixture to the atmosphere from into the cooling tower. The outlet air velocity is higher than air inlet velocity. There are two types cooling tower based on air flow. Cross-flow tower the direction of air flow is upright to the water flow direction. Thus, the cooling tower has a fill design to allow cross flow at the inlet side of the air. Counter-flow tower the direction of water is vertically downward to bottom and air flow is vertically upward through. It needs more fan power because the fill design causes pressure loss. In large capacity, cooling tower pressure loss can be decrease by increasing surface area.

There are some researches about cooling tower to estimate the evaporation loss and effectiveness. Merkel [1] presented the thermal calculations of cooling towers in 1925. Merkel made three assumptions in calculation. These are: The Lewis factor is equal to 1. The outlet of air is saturated with water vapor and it is designated only enthalpy. The decline of water level by evaporation is unheeded in the energy balance. In Merkel method is very accurate and simplicity when calculating the outlet temperature of air and heat rejection if the outlet air is supersaturated with water vapor. Jaber and Webb [2] developed NTU effectiveness method for cooling tower. E-NTU are completely logical with the fundamental definitions used in heat exchanger design. Using the definitions, can be analyzed easily heat exchanger and also cooling tower in counterflow, crossflow forms. Poppe and Rögener [3] investigated the Poppe model for cooling tower calculation. This model more accurate when calculating Merkel number because Poppe model is considered the assumption which is not considered by Merkel. They obtained if the outlet water temperature is significant, the less accurate Merkel and e-NTU methods can be used. Poppe method can predict lower outlet water temperature under warm dry ambient situations. Kloppers and Kröger [4] investigated the differences between the

Merkel, Poppe, and e-NTU methods. They expanded Poppe method equations give detailed representation of the Merkel number. They obtained pope method is convenient for analyzing in cooling tower as the case of the outlet air is accurately decided. And also [5] investigated the Lewis factor effecting on the performance estimate of the cooling tower fill performance using Lewis factor. The Poppe method is considered in heat and mass transfer analysis. They obtained to increasing Lewis factors, the heat rejection rate increases, the water outlet temperature decreases and the water evaporation rate decreases. Wang et al. [6] easily calculated the analytical solution of outlet water temperature, for calculate performance, the assumption is the enthalpy of the saturated air is a linear function of the water surface temperature on the counter flow wet cooling towers. Yılmaz [7] obtained an analytical method and compared with LMED and corrected LMED method in inlet and outlet temperatures for water between 10-90 °C and for different cooling ranges between 4 and 16 °C. Mansour et al. [8] developed an innovative correlation employing the basic laws of mass and energy balance contact with the heat and mass transfer equations for e-NTU of cooling towers. Those new correlations showed that deviation less than 10%. The advantages of NEM correlations are easily use simple calculation of input parameters and help to optimization of cooling tower when it is working. Deziani et al. [9] developed a system which reduces the evaporation loss in cooling tower by using an air heat exchanger with fan that the minimum dry bulb temperature difference between inlet air and outlet air was reduced to 3 °C so, using this model could be save water about 35% evaporation. Ayoub et al. [10] are worked thermodynamic flow equation for describe the heat and mass transfer for analyzing cost occurs in wet type cooling tower. The purpose of the model is to predict the effects of excessive air conditions on cooling tower efficiency. They showed that considerable efficiency drops could be expected at high ambient temperature and humidity, with a smaller but important effect of the makeup water temperatures. Smrekar et al. [11] showed how the efficiency of a cooling tower can be develop by optimizing the heat transfer along the cooling tower packing using a suitable water distribution from inside the plane area of the cooling tower. They obtained mathematical model which gives optimization of the cooling tower performance regulating a fan power to changing ambient conditions. The mass flow rate of air can be adjusted by remote control robot unit in induced draft due to hot fluid temperature through cooling tower and also the outlet temperature is decrease that is increase the efficiency.

Fisenko et al. [12] developed a model for the differential equation system indicating the boundary-

value problem, describing a change in the velocity, radius and temperature of the droplets, and a change in the temperature and density of the water vapor in the cooling tower. By means of this model, the cooling tower performance can be set of the fan power. Gao et al. [13] found temperature difference and efficiency can be increased by cross wind condition comparison to windless condition in experiment. When the Froud number increase to 0.174 by increasing crosswind condition. In experimental results, it is obtained that temperature difference and efficiency are affected by the cross-wind, and temperature difference and efficiency can reduce by 6% and 5%. Hajidavalloo et al. [14] they are used to conventional mathematical model for see thermal behavior of cooling tower with cross flow at variable wet bulb temperatures. They investigated when the wet bulb temperature increases, the evaporation loss can increase. They obtained the evaporation rate is increased when the dry bulb temperature increases and the increasing rate is almost constant at different wet bulb temperatures. Also, impact separator can be used for decrease the number of suspended solids in the air without evaporation loss in the cooling tower performance. Lu et al. [15] used swirling plume method which increase the overall tower updraft capacity in dry and wet cooling towers. In CFD analysis they found that cooling tower temperature decrease when using swirling plume driven by fan blower. They analyzed 20 m height and 12 m diameter wet cooling tower with swirling plume which improve the air flow rate and the decreased cooling water temperature by at minimum 53.6% and 3.57 °C (39.3%). Rahmati et al. [16] investigated experimentally when changing parameter of cooling tower such as hot water temperature, water flow rate and air flow rate how affect the thermal performance of cooling tower. They showed the efficiency is concerned with air mass flow rate, hot water temperature. They obtained to cooling tower performance can be increased by lower water flow rate and higher values of hot water temperature and air mass flow rate. Klimanek et al. [17] examined the cooling tower with flue gas under wind conditions. They showed the effect of increased air flow on leaving water temperature. They worked with ANSYS CFD model. It has also been shown that, under high wind conditions, the centrally introduced flue gas can flow close to the tower shell due to the inflow of cold air and the bending of the gas flow. Therefore, the risk of wear of the tower shell may increase and a corrosion-resistant layer is required in the cooling tower. Li et al. [18] they are subjected to air flows at the top of the cooling tower and this flow poorly effected to cooling tower performance. In experiment outlet water temperature is can be increase up to 3°C due to incursion of air flow to the cooling tower. So, inlet air temperature can be

carefully select in designing for small cooling tower. Imani-Mofrad et al. [19] experimentally investigated cooling tower performance using four Nano fluids including ZnO-H₂O, SiO₂-H₂O, Al₂O₃-H₂O and graphene-water as process fluid. In experiment they are used Nano fluid separately and find parameters such as effectiveness and evaporation rate. Finally, after experiments they obtained graphene-water Nano fluid parameters provided the best thermal performance. Mahmud et al. [20] studied experimentally about the direct contact cross flow cooling tower for different air and water velocities how effect on cooling capacity, effectiveness and evaporation loss. They worked about six air velocity and three water velocity. As a result, when the increasing air velocity, effectiveness is increase also evaporation loss is increase. In low water velocity effectiveness is high.

The literature suggests that there are many researches about cooling tower performance calculation method such as Merkel, Poppe and effectiveness-NTU methods. According to literature, applying Merkel and effectiveness -NTU methods assumed to assumptions which occurs simple calculation in analysis. Poppe method there is no assumptions so it is very accurate but in calculation is relatively more complex than the Merkel and e-NTU methods. Also, researcher studied to how to decrease evaporation loss in cooling tower by using some configurations in system.

Different from the literature, present study is mainly focused on numerical analysis of a new cooling system which works as a cooling tower for decreasing evaporation loss and increase the efficiency of the tower by using two crosswise swirling jets to decrease the inlet temperature of hot water and also to prevent thermal pollution to the environment. The cooling of the hot water is provided by using direct contact cooling method with two swirling jets which increase the contact surface area between water and air. Swirling jets was chosen to take advantage of both mechanical and thermal effects. The model is calculated for different parameters; Reynolds number for jets inlet velocities ($Re= 3900, 5200, 7800, 8500$) and air inlet temperatures (10°C, 22°C, 32°C, 40°C). This model was studied numerically and by using ANSYS Fluent Computational Fluid Dynamic program. By using this model, the outlet water temperature was reduced by 19°C and the effectiveness is also increased 21% when compared to the experimental studies of Smrekar et al. [11]. Also, the numerical results were validated by some studies in the literature.

2. Numerical Model and Data Reduction

The study is mainly focused on numerical research of cooling tower performance using swirling jet for decrease of outlet air-vapor mixture and condensed water

temperature, and evaporation loss. The model has an 80 mm radius and a 240 mm length. Two swirling jets are placed opposite to each other. The hydraulic diameters of the rotating jets are 0.016 mm. In this numerical analysis, the k- ϵ turbulence model of ANSYS Fluent computational fluid dynamics package program was used. The inlet velocity of air is in turbulence region and the k- ϵ turbulence model was chosen because it gives better results in these ranges for confined jet flows. The geometry of the numerically examined model is shown in Figure 1.

The aim of the experiment is to decrease the evaporation loss with using swirling jet that provide to obtain more cooling, compared to mechanical draft fans in cooling tower and saving the water in the system. There are three method in analyzing cooling tower these are; merkel, poppe, and e-NTU methods. In the present study, calculations were made by using e-NTU method. This model provides simple and precise results in cross flow and counter flow models. This model can be used in cooling tower calculations as well as in heat exchangers.

In analyzing of cooling tower, we applied to dry air, water mass balance and energy balance for find to air mass flow rate [21];

Dry mass balance:

$$m_{inlet\ air} = m_{outlet\ air} \quad (1)$$

Water mass balance:

$$m_{steam} + m_{inlet\ air}\omega_{inlet} = m_{condensed\ water} + m_{outlet\ air}\omega_{outlet} \quad (2)$$

Energy equation:

$$\sum_{in} mh = \sum_{out} mh \quad (3)$$

So, the equations give the mass flow rate of air:

$$m_{air} = \frac{m_w(h_{inlet\ water} - h_{outlet\ water})}{(h_{inlet\ air} - h_{outlet\ water}) - (\omega_{inlet} - \omega_{outlet})h_{outlet\ water}} \quad (4)$$

Where ω is the humidity ratio find from psychrometric chart or correlation formulas. Enthalpy of dry air and water also find correlation formulas show in below [22]:

$$\omega = \frac{1.00416(T - T_{wb})}{[2501.6 - 1.8577(T - 273.15) - 4.184(T_{wb} - 273.15)]} \quad (5)$$

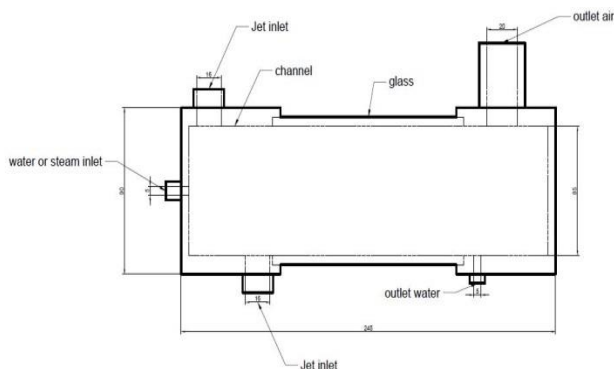


Figure 1. Analysis domain of cooling tower

The enthalpy of air inlet and outlet temperature evaluated by using below formula:

$$h = c_p T_w + \omega(h_{fgw} + c_p T_w) \quad (6)$$

Humidity ratio is also calculated inlet and outlet condition from this formula is;

$$\omega = \frac{0.622P_v}{P - P_v} \quad (7)$$

P is the atmospheric pressure and P_v is the calculated from relative humidity and saturation pressure of air inlet and outlet temperature which shown in below equation:

$$P_v = \phi P \quad (8)$$

$$\phi = \frac{\omega P}{(0.622 + \omega)P_g} \quad (9)$$

The makeup water represents the how much water is evaporated in cooling tower. Also, makeup water is equal to evaporation loss. The makeup water is found with a formula showed below:

$$m_{make\ up} = m_{air}(\omega_1 + \omega_2) \quad (10)$$

Using these equations, we can find how much required air flow rate come through from cooling system to obtain outlet temperature. For finding effectiveness of cooling tower need to evaluate the heat transfer rate Q_{max} and Q_{actual} that is calculated from this equation given below:

$$Q_{actual} = m_w c_p (T_{wi} - T_{wo}) \quad (11)$$

To find the Q_{max} , evaluate the correction factor λ for improving the accuracy of the enthalpy of air regarding to water temperature from using the equation given below:

$$\lambda = \frac{(h_{maswo} + h_{maswi} - 2h_{maswm})}{4} \quad (12)$$

The correction factor used to obtain Q_{max} is defined as:

$$Q_{max} = C_{emin}(h_{maswi} - \lambda - h_{mai}) \quad (13)$$

Following these equations, we can find effectiveness calculated from this equation given below:

$$\varepsilon = \frac{Q_{actual}}{Q_{max}} \quad (14)$$

Finally, we obtain the effectiveness-NTU equation for cooling tower. This equation is given below:

$$\varepsilon = \frac{1 - \exp[-NTU(1 - C_e)]}{1 - C_e \exp[-NTU(1 - C_e)]} \quad (15)$$

So, Evaporation loss is equals to;

$$Evaporation\ loss = \frac{m_{air}(h_{outlet\ air} - h_{inlet\ air})}{hr} \quad (16)$$

Boundary conditions used at this study are shown below;

Table 1. Boundary conditions

	U (m/s)	V (m/s)	W (m/s)	T (K)	K (J/kg)	E (J/kg.s)
Inlet	$U = 0$	$V = -V_i$	$W = 0$	$T = T_i$	$(T_i W_{jet})^2$	$(C_p C_d)^{3/4} k^3 / L$
Wall	$U = 0$	$V = 0$	$W = 0$	$q'' = 0$	$k = 0$	$\partial \epsilon / \partial z = 0$
Outlet	$\partial U / \partial z = 0$	$\partial V / \partial z = 0$	$\partial W / \partial z = 0$	$\partial T / \partial z = 0$	$\partial k / \partial z = 0$	$\partial \epsilon / \partial z = 0$

2.1 Verification of Numerical Results

In this numerical analysis, the k- ϵ turbulence model of ANSYS Fluent computational fluid dynamics program was used. 130973 mesh was used in the modeling study. In the inflation process, smooth transition model was applied. In the modeling, the number of mesh in the jet and water inlets was increased.

3. Results and Discussion

In this study; effect of jet velocities on evaporation loss and efficiency values at different Reynold numbers (Re = 3900, 5200, 7800, 8500) and different air inlet temperatures (10 °C, 22 °C, 32 °C, 40 °C) were investigated numerically. Efficiency-NTU method was used as it was more practical in the calculations.

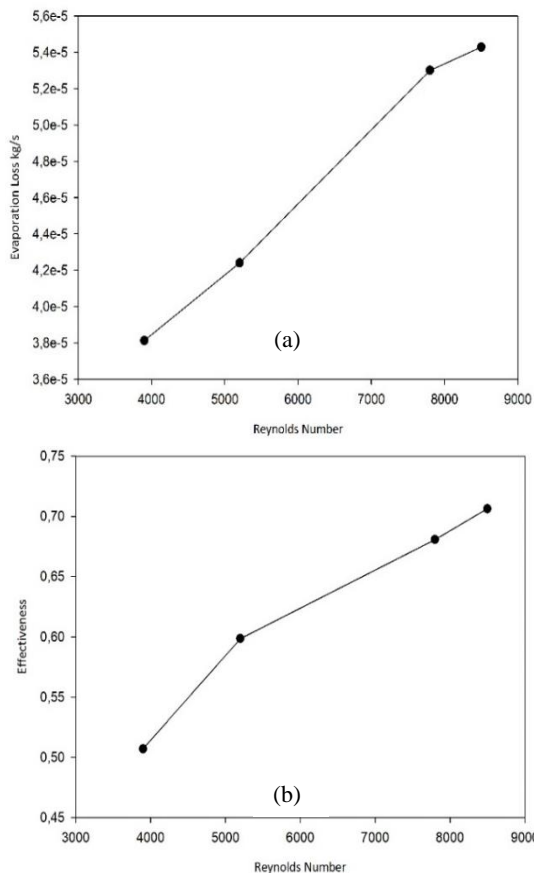


Figure 2. Effects of Reynolds numbers on a) evaporation loss and b) on effectiveness of cooling system

3.1 Effect of Different Reynold Numbers (Re = 3900, 5200, 7800, 8500) On Evaporation Loss and Efficiency

Increase in Reynolds number causes an increase on evaporation loss. Because high jet velocities can take away of more water vapor. For designing a system, air velocity should be selected to decrease evaporation loss. It was found that evaporation loss decreased by 30% when Reynold number decreased from 8500 to 3900 and which decreased by 28.5% of the effectiveness of the cooling system. Figure 2 shows the effect of the Reynolds number on evaporations loss and effectiveness. Temperature contours and streamlines for different Reynolds numbers (Re=3900, 5200, 7800, 8500) are shown in Figure 3.

3.2 Effect of different air inlet temperatures on evaporation loss and efficiency

Increasing the air inlet temperature causes and increase on evaporation loss. The reason is that the water holding capacity of air increases with increasing air temperature. Because of environmental conditions, temperature of air inlet is selected in 10°C, 22°C, 32°C, 40°C. In this model, evaporation loss decreased by 62% when the air temperature was decreased from 40 °C to 10 °C and when increasing the air inlet temperature from 10 °C to 40 °C, the effectiveness decreases of 62.3%. Result are shown in Figure 4.

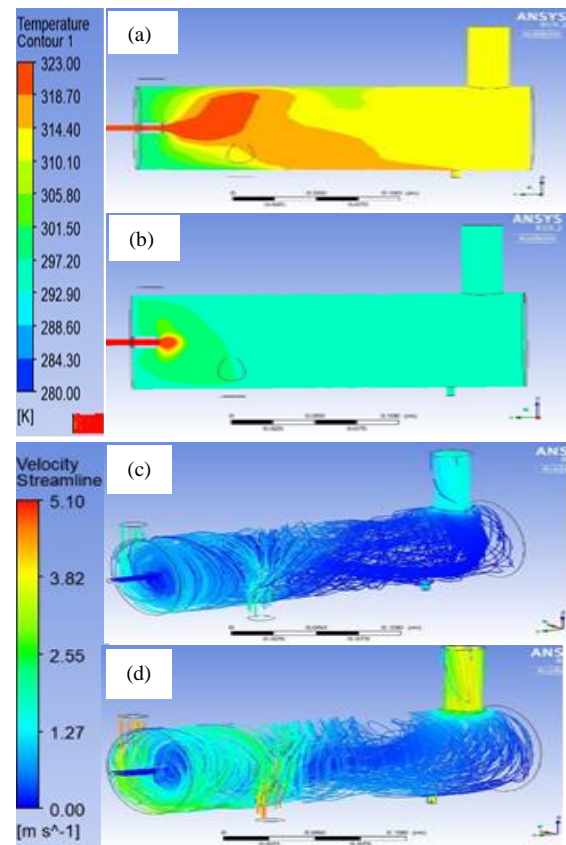


Figure 3. Temperature contours at 22 °C air temperature at different Reynolds numbers a) 3900 b) 8500 and air flow streamlines c) 3900 d) 8500

Temperature contours and streamlines for different inlet temperature ($T_{\text{airinlet}} = 10^\circ\text{C}$ and 40°C) are shown in Figure 5.

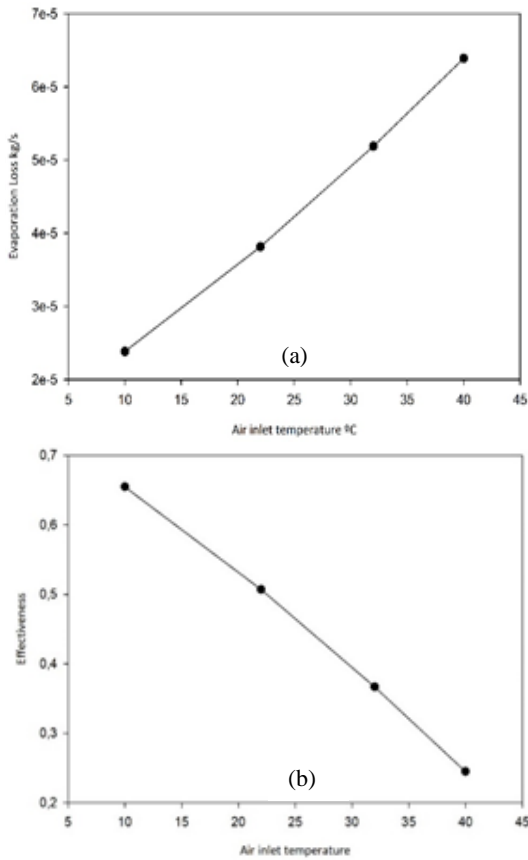


Figure 4. Changing evaporation loss a) and effectiveness b) of cooling system on different air inlet temperature

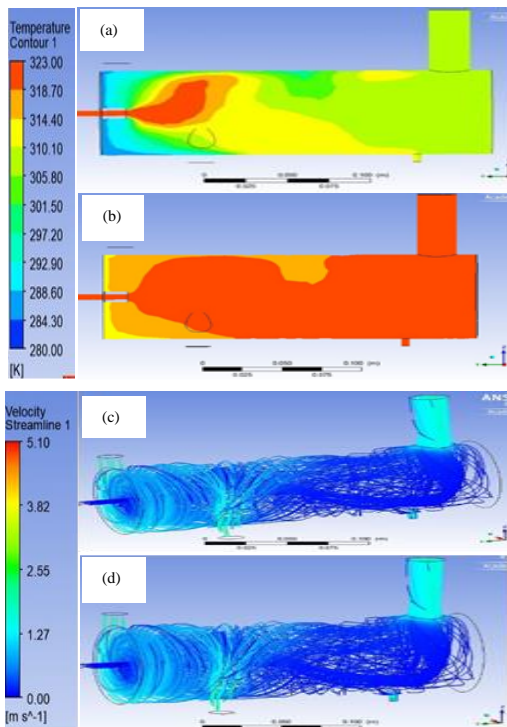


Figure 5. Temperature contour a) 10°C , b) 40°C and streamlines c) 10°C , d) 40°C for $Re = 5200$

4. Conclusions

This study is mainly focused on the numerical investigation of evaporation loss and effectiveness of a new type cooling tower. The e-NTU method is used for calculation of these. The different parameters were used in numerical study. Our model is validated using reference solution. The evaporation loss is depended on the wet bulb temperature and outlet temperature. The mass flow rates are not affected to effectiveness and NTU number. The ANSYS FLUENT analyzed results specify the numerical calculations are the same for outlet temperatures in different parameters. Increasing the air inlet temperature causes an increase on evaporation loss. When decreasing the air inlet temperature from 40°C to 10°C , the evaporation loss is decreased about 62% and when increasing the air inlet temperature from 10°C to 40°C , the effectiveness decreases of 62,3%. The increasing Reynolds number causes an increase on evaporation loss and effectiveness of the system. Because the more air velocity can take away more mass flow rate of water vapor and water. When Reynolds number is decreased from 8500 to 3900, the evaporation loss decreased of 30%. But it also causes a decreased of 28.5% on cooling effectiveness of the system. When the results were compared with the experiment results of Smrekar et al. [11], by using this new cooling system, the effectiveness of the system can be increased of 20%. Results of this study and numerical model, which we used, can be used in many areas such as space requirements, electric power plant, aerospace application and industrial application.

Declaration

The author(s) declared no potential conflicts of interest with respect to the research, authorship, and/or publication of this article. The author(s) also declared that this article is original, was prepared in accordance with international publication and research ethics, and ethical committee permission or any special permission is not required.

Acknowledgment

Old version of this work was presented in 2nd International Conference on Technology and Science (Techno-Science 2019), Burdur / Turkey.

Nomenclature

c_p	: Specific heat at constant pressure (J/kgK)
h	: Heat transfer coefficient ($\text{W}/\text{m}^2\text{K}$)
h_d	: Mass transfer coefficient ($\text{kg}/\text{m}^2\text{s}$)
h	: Enthalpy (J/kg)
h_{fg}	: Latent heat (J/kg)
k	: Thermal conductivity (W/mK)
m	: Mass flow rate (kg/s)
NTU	: Number of transfer units (UA/C_{\min})

P	: Pressure (N/m ²)
Q	: Heat transfer rate (W)
ω	: Humidity ratio (kg water vapor / kg dry air)
Re	: Reynolds number
λ	: Correction factor (j/kg)
Φ	: Relative humidity
ε	: Effectiveness

References

- Kloppers, J.C., Kroger, D.G., *Cooling Tower Performance: A Critical Evaluation of the Merkel assumptions*. R & D Journal, 2004. **20**(1): p.24-29.
- Jaber, H., Webb, R.L., *Design of Cooling Towers by the Effectiveness-NTU Method*. ASME Journal Heat Transfer, 1989. **111**(4): p.837-843.
- Kloppers, J.C., Kroger, D.G., *Cooling tower performance evaluation: merkel pope and e-NTU methods analysis*. Journal of Engineering for Gas Turbines and Power, 2005. **127**(1): p. 1-7.
- Kloppers, J.C., Kröger, D.G., *A critical investigation into the heat and mass transfer analysis of counter flow wet-cooling towers*. International Journal of Heat and Mass Transfer, 2004. **48**(3-4): p. 765-777.
- Kloppers, J.C., Kröger, D.G., *The Lewis factor and its influence on the performance prediction of wet-cooling towers*. Int. J. of Thermal Sciences, 2005. **44**(9): p.879-884.
- Wang, Q., Wang, P., Su, Z., *An Analytical Model on Thermal Performance Evaluation of Counter Flow*. Thermal Science, 2017. **21**(6): p.2491-2501.
- Yılmaz, A., *Analytical Calculation Of Wet Cooling Tower Performance With Large Cooling Ranges*. Journal of Thermal Science and Technology, 2010. **30**(2): p.45-56.
- Mansour, M.K., Hassab, M.A., *Innovative correlation for calculating thermal performance of counterflow wet-cooling tower*. Energy, 2014. **74**: p.855-862.
- Deziani, M., Rahmani, K., Mirrezaei Roudaki, S.J., Kordloo, M., *Feasibility study for reduce water evaporative loss in a power plant cooling tower by using air to Air heat exchanger with auxiliary Fan*. Desalination, 2017. **406**: p.119-124.
- Ayoub, A., Gjorgiev, B., Sansavini, G., *Cooling towers performance in a changing climate: Techno-economic modeling and design optimization*. Energy, 2018. **160**: p.1133-1143.
- Smrekar, J., Oman, J., Širok, B., *Improving the efficiency of natural draft cooling towers*. Energy Conversion and Management, 2006. **47**(9-10): p.1086-1100.
- Fisenko, S.P., Brin, A.A., Petruichik, A.I., *Evaporative cooling of water in a mechanical draft cooling tower*. Int Journal Heat Mass Transfer, 2004. **47**(1): p.165-177.
- Gao, M., Sun, F., Wang, K., Shi, Y., Zhao, Y., *Experimental research of heat transfer performance on natural draft counter flow wet cooling tower under cross-wind conditions*. International Journal of Thermal Sciences, 2008. **47**(7): p.935-941.
- Hajidavalloo, E., Shakeri, R., Mehrabian, M.A., *Thermal performance of cross flow cooling towers in variable wet bulb temperature*. Energy Conversion and Management, 2010. **51**(6): p.1298-1303.
- Lu, Y., Klimenko, A., Russell, H., Dai, Y., Warner, J., Hooman, K., *A conceptual study on air jet-induced swirling plume for performance improvement of natural draft cooling towers*. Applied Energy, 2018. **217**: p.496-508.
- Rahmati, M., Alavi, S.R., Tavakoli, M.R., *Investigation of heat transfer in mechanical draft wet cooling towers using infrared thermal images: An experimental study*. International Journal of Refrigeration, 2018. **88**: p.229-238.
- Klimanek, A., Cedzich, M., Bialecki, R., *3D CFD modeling of natural draft wet-cooling tower with flue gas injection*. Applied Thermal Engineering, 2015. **91**: p.824-833.
- Li, X., Gurgenci, H., Guan, Z., Sun, Y., *Experimental study of cold inflow effect on a small natural draft dry cooling tower*. Applied Thermal Engineering, 2018. Vol. **128**: p.762-771.
- Imani-Mofrad, P., Heris, S.Z., Shanbedi, M., *Experimental investigation of the effect of different nanofluids on the thermal performance of a wet cooling tower using a new method for equalization of ambient conditions*. Energy Conversion and Management, 2018. **158**: p.23-35.
- Mahmud, T., Kamrul, M., Salam, I., Salam, B., *Experimental study of forced draft cross flow wet cooling tower using splash type fill*. International Conference on Mechanical Engineering and Renewable Energy, 2013.
- Çengel, Y.A., Boles, M.A., *Thermodynamics: an engineering approach*. New York, NY: McGraw-Hill Higher Education, 2015.
- Kröger, D.G., *Air-Cooled Heat Exchangers and Cooling Towers*, Tulsa, Oklahoma, 2004.



Research Article

Numerical and experimental study on thermal characteristics of louvered fin microchannel air preheaters

Anıl Başaran^{a,*}  and Ali Yurddaş^a 

^aManisa Celal Bayar University, Engineering Faculty, Department of Mechanical Engineering, Yunusemre, Manisa, 45140, Turkey

ARTICLE INFO

Article history:

Received 12 March 2020

Revised 03 May 2020

Accepted 07 May 2020

Keywords:

Microchannel heat exchanger

Microchannel preheater

Numerical modeling

R600a

Thermal characteristics

ABSTRACT

Microchannel heat exchangers have been gradually getting importance in industrial applications due to offering outstanding benefits. The current study has focused on the development of a numerical model to predict the thermal performance of the microchannel air preheaters (MCPH) for HVAC systems. An experimental study has been performed to validate the numerical model results. A louvered fin multiport microchannel heat exchanger has been employed as an air preheater in the experiments. The proposed model has been developed based on the segment-by-segment approach and calculated the outlet temperature and heat capacity of the MCPH. Different air velocities at the frontal face and varying mass flow rates in passes of the MCPH have been taken into consideration in the model. It has been concluded from experimental data that the model predicts the outlet temperature with an average absolute deviation within $\pm 2\%$ for all investigated test conditions. The proposed model shows high accuracy with respect to temperature calculation. Another conclusion is that the non-uniform air velocity approach improves the precision of the proposed model. The heat capacity predictions with the uniform air velocity approach indicate higher deviations than the non-uniform air velocity approach.

© 2020, Advanced Researches and Engineering Journal (IAREJ) and the Author(s).

1. Introduction

Energy is the one important phenomena for solving the problem requirements in the industry [1]. In this respect, recently, heat transfer requirements from small areas with high heat flux have started to appear with the developing technology. Micro-scale geometries provide some benefits for industrial applications to meet such needs. With the development of micro-manufacturing technologies, various microchannel geometries attracting attention in heat exchangers design for HVAC applications. A compact size-reduced heat exchanger design, improving the total heat transfer coefficient, less air-side pressure drop, and reducing the amount of working fluid are among the outstanding advantages of microchannel heat exchangers [2–4].

Generally, sub-cooling at the outlet of the condenser is desired to guarantee a single phase in the actual application. The main reason for the desiring single-phase

of refrigerants at the outlet of the condensers is the effective operation of the system that is based on the VCRC. Sub-cooling is to cool the refrigerant, at uniform pressure and in a liquid state to a temperature which is less than the saturation temperature corresponding to condenser pressure. Sub-cooling improves system efficiency and reduces flash gas production during expansion. Sub-cooling can be carried out in condensers as a single heat exchanger, as well as in secondary heat exchangers such as preheater. Pre-heaters in HVAC applications can make both duties of pre-heating of intake air and sub-cooling of the refrigerant at the same time.

During the design of the thermal systems, the most common problem in terms of designers is not able to estimate the thermal characteristics of the heat exchangers which is a component of the system. The simulation models reliably predict such parameters may offer a considerable contribution to cost-saving, design and optimization efforts thanks to the reduction of the

* Corresponding author. Tel.: +90-236-201-2382.

E-mail addresses: anil.basaran@cbu.edu.tr (A. Başaran), aliyurddas@gmail.com (A. Yurddaş)

ORCID: 0000-0003-0651-1453 (A. Başaran), 0000-0002-4683-142X (A. Yurddaş)

DOI: 10.35860/iarej.703104

experimental test and cost. Therefore, many researchers have focused on the numerical investigation of heat transfer and fluid flow characteristics inside the microchannels [5–8]. Glazar et al. [9] conducted an experimental and numerical analysis of heat transfer and fluid flow in the compact heat exchanger with different microchannel shapes. They discretized the governing equations using the finite volume method and made a comparison regarding heat transfer effectiveness and pressure drop in single-phase heat transfer. A generalized three dimensional model for microchannel heat exchanger was developed by Ren et al. [10]. Their model uses the port-by-port calculation grid and takes into consideration three-dimensional heat conduction via fins. The governing equations were discretized by using the finite difference method. The model validated by experiments showed the prediction deviations in the heat capacity of the microchannel heat exchangers (evaporator, condenser and gas cooler) within $\pm 5\%$. Yin et al. [11] studied the mathematical model using the finite element method for a CO₂ gas cooler. The mathematical model was developed for single-phase fluid flow conditions and was verified with the experiments. The segment-by-segment model applied the energy equation with the uniform air-flow assumption. The gas cooler capacity and pressure drop on R 744 side prediction of their model were found agreed with experimental results. An analytical model based on the segmented approach was conducted by Fronk and Garimella [12] for the assessment of the compact gas coolers. They presented the validation of the model with experimental data [13]. For validation of the model, a heat pump facility was used for a water-coupled microchannel gas cooler. It is found that the model estimated the heat duty with an average absolute deviation of 7.5% regard with water and refrigerant inlet conditions. A model to analyze air-cooled compact heat exchangers was developed by Garcia-Casceles et al. [14]. In the model, the authors used cell discretization with R134a and R410A refrigerant and conditions that can be found in HVAC heat exchangers. As a result of the validation, the model is suitable for the designing and sizing of the compact heat exchangers with satisfactory results.

To improve the accuracy of the model, the researchers have taken into account the crucial air-side factors like non-uniform air velocity and temperature. Kim and Bullard [15] were one of the researchers who consider the non-uniform air distribution in their model. They developed and verified a model with the aim of assessing the thermal performance of the microchannel evaporator for R744 mobile air conditioning system. The model based on the finite volume method emphasized the air-side heat and mass transfer process. On the other hand, they outlined the significance of selecting appropriate heat transfer and pressure drop correlation for the refrigerant side according

to their simulation results. Yin et al. [16] presented a finite-volume air-cooled microchannel condenser model to evaluate the characteristics of the heat exchanger. They conducted several tests for one-slab and two-slab microchannel heat exchangers on heat transfer and pressure drop. Their model considered maldistribution air velocity and temperature at the front of the microchannel heat exchanger as well as air-side distribution for multi-slabs. Park and Hrnjak [17] carried out an numerical and experimental study on microchannel heat exchanger for an R410A air-conditioning system. The simulation model took into account non-uniform air distribution in front of the microchannel heat exchanger. Simulation and experimental study focused on the air-side hydraulic performance of the louvered fin microchannel automotive heat exchanger was conducted by Liang et al. [18]. In their study, verification with Coil Designer as well experiment was performed with the using of some existing correlations.

Due to environmental impact of Hydrofluorocarbons (HFCs), there are the efforts to find environmental-friendly alternatives of the HCFs. Hydrocarbons (HCs) like isobutane (R600a) are currently under consideration as potential substitutes [19]. Isobutane is one of the widely used refrigerants in the HVAC systems [20]. Although isobutane which is hydrocarbon type refrigerants are flammable and easily ignited, they are widely preferred in air conditioning and refrigeration equipment because of the advantages they offer. The main advantages of isobutane refrigerants may be listed as cheap to produce, non-ozone depletion impact, low contribution to global warming and low toxicity [21,22].

Some experimental and numerical studies have been performed to understand the thermal characteristics of microchannel heat exchangers in the literature. But, reliable and sufficient universal information is lacking especially for isobutane. Most of the studies on air-cooled microchannel heat exchangers have focused on evaporators and condensers in which two-phase refrigerant flow, and relatively few studies have been conducted for microchannel heat exchangers working with single-phase refrigerants such as preheaters. Therefore, the current study aims to provide a contribution to the determination of thermal characteristics of microchannel air preheater for HVAC systems working with isobutane. The finite volume-based model has been numerically applied to predict outlet temperature and heat capacity of the MCPH. The non-uniform air velocity at the frontal face and varying mass flow rates in passes of the MCPH have been taken into consideration in the calculation. The experimental study has been performed using a microchannel pre-heater for the validation of the proposed model.

2. Numerical Modeling

In this study, a louvered microchannel heat exchanger has been modeled as an air preheater. Considered louvered fin microchannel air preheaters (MCPH) is basically composed of inlet and outlet pipes, headers, baffles in headers, flat tubes contain multi-microchannels and louvered fins. A numerical model has been developed with the aim to predict outlet temperature and the heat transfer rate of the MCPH with high accuracy. The considered MCPH can be seen in Figure 1. Test sample MCPH consists of inlet and outlet pipes, right and left-side header, twenty-nine flat tubes and louvered fins between flat tubes. There are baffles in headers to organize the six passes of the test sample MCPH. The first and second passes involve six flat tubes whereas there are five flat tubes in the third and fourth passes. The fifth and sixth passes include four and three tubes, respectively.

The inlet and outlet pipe relate to the right-side header. Refrigerant enters the heat exchanger upper part of the right header and flows out the lower part of the right header after completing the passes. Each flat-tube includes sixteen rectangular and two semi-circular microchannel ports. Detailed schematics of the cross-section of the microchannel flat tubes with geometric parameters of the louvered fin is indicated in Figure 2. The dimensions of the MCPH are given in Table 1.

The proposed model is based on the widely accepted finite volume method and calculation is conducted numerically with an iterative scheme. In the model, there is a need to create finite volumes (in other words grids) for the calculations. The flat tubes have been divided into a certain number of small elements (also called segments) along the refrigerant flow path to achieve low-temperature change in refrigerant in a segment during calculations. Thereby, the refrigerant properties can be assumed to be constant in a segment during calculations. The representation of a calculation segment is given in Figure 3.

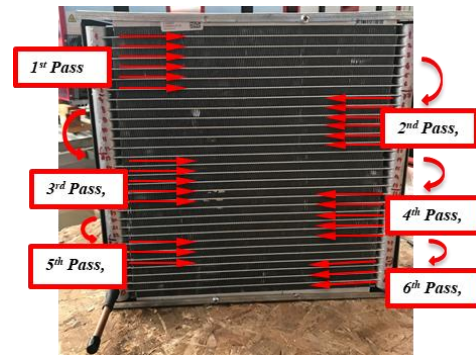


Figure 1. Considered louvered fin microchannel air preheaters (MCPH)

Table 1. Detailed geometrical parameters of the MCPH

Parameters	Dimensions (mm)
Overall structure	
Height, h	300.7
Length, l	330
Depth, d	16.48
Number of the tube, N_t	29
Number of the pass, N_p	6
Pass distribution	6/6/5/5/4/3
Number of port*, N_{mc}	18
Ports (microchannels)	
Height, P_h	0.74
Width, P_w	0.63
Thickness, P_t	0.28
Web thickness, W_t	0.3
Tubes	
Height, T_h	1.3
Width, T_w	16.48
Length, T_l	290
Pitch, T_p	9.4
Fins	
Height, F_h	8.1
Depth, F_d	16
Pitch, F_p	0.55
Thickness, δ_f	0.1
Louvers	
Height, L_l	6.615
Pitch, L_p	1
Angle, θ	18°

* Each tube

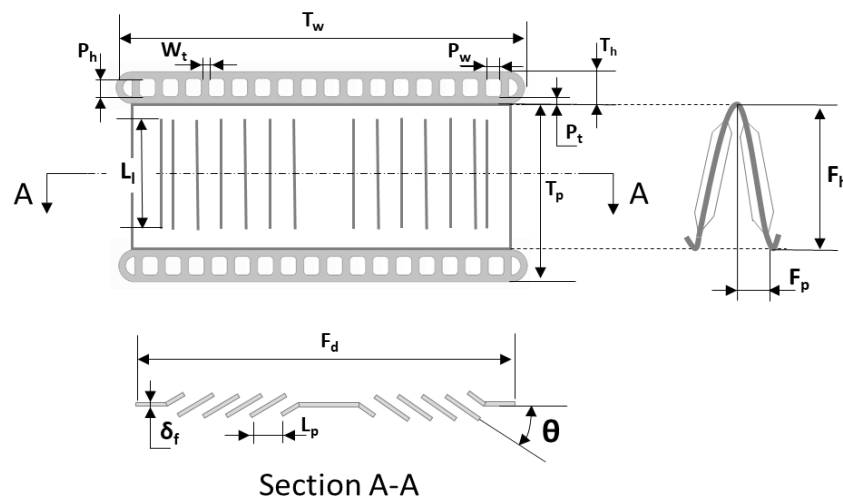


Figure 2. Detailed schematics of the cross-section of the microchannel flat tubes with geometric parameters of the louvered fin

The segments are strictly linked with adjacent segments and thereby a calculation sequence of the segments is created. The outlet conditions of the segments that are calculated with iterative scheme are set inlet conditions of the next segment in the calculation sequence. The calculation sequence of the segments starts at the inlet of the first pass and it is applied in direction of the downstream of the tube.

The solver proceeds to the header which links the following pass of the MCPH. The outlet conditions of the previous header are set as the inlet conditions of the following header (first level of the grid generation). The calculation procedure applied for the segments in next passes in a similar way and it goes on until outlet header. After the solution of all segments, the whole MCPH is simulated to determine thermal characteristics.

The present model suggests that each segment analyzed as an independent cross-flow heat exchanger and the calculation algorithm of the numerical model is applied to each segment for determining thermal characteristics. For all calculation segment, the arithmetic average of the inlet and outlet conditions of the segments are used to evaluate constant refrigerant properties within the segment. The defined refrigerant properties are used to calculate heat duty and pressure drop for that segment. Initially, refrigerant inlet conditions are known, and they are set as the inlet for the first segment. However, firstly, an initial assumption is made due to the fact that the outlet condition cannot be known initially and then an iterative scheme is applied to refine the solution. The iterative scheme is presented in Figure 4.

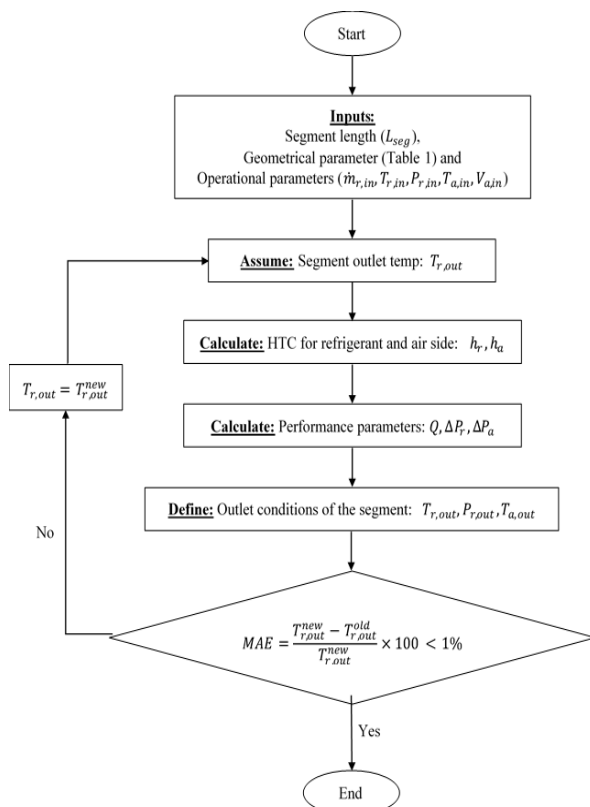


Figure 4. Iterative scheme of the model

The outlet temperature has been considered as a convergence criterion for a segment. In the iteration scheme, convergence criteria between calculated outlet temperatures every iteration have been determined as 1% of Mean Absolute Error (MAE). The MEA for the outlet temperatures of the segment can be calculated by using the following equation:

$$MAE = \frac{T^{new} - T^{old}}{T^{new}} \times 100 \quad (1)$$

The outlet temperature calculated in the previous iteration has been compared with the calculated outlet temperature for that segment. If the MAE percent is lower 1%, iteration is stopped for that segment otherwise iteration proceeds until outlet temperature of the segment converges. After convergence, the iterative calculation is applied next segment in the sequence. It is worth note that initially assumed outlet temperature is used to calculate MAE in the first iteration.

The most of air-cooled heat exchanger applications, the airflow over the heat exchanger is produced by an induced shaft fan. The fan generally is placed in front of the heat exchanger in a canal and it supplies airflow to heat exchangers by means of blowing or pulling off the air. The four walls of this heat exchanger unit give rise to decreasing air velocity near the walls. On the other hand, considering the geometry of the fan blade, the blade connects with a shaft at its middle point and it turns around of this axis. Hence, at this point, the force to blow or pull the air cannot be generated. This configuration of the heat exchanger units causes the non-uniform airflow at the face of the heat exchanger. The proposed model takes into consideration uniform airflow to improve the accuracy of the model. In this content, the model recommends that the face of the MCPH is divided into certain regions to model air-side maldistribution due to fan-driven airflow.

The inputs of the model can be classified into two parts: geometrical inputs and operational inputs. Geometrical inputs cover all principle dimensions of the heat exchanger in both refrigerant and air sides. Geometrical inputs can be listed: height, depth, and length of flat tubes, number of microchannel ports, the dimensions of the microchannels, the fin pitch, length and thickness, the louver angle, pitch, and length. In addition to these parameters, segment length is one of the geometrical inputs of the model. Operational inputs for the model are the mass flow rate of refrigerant, refrigerant inlet temperature and pressure, air velocity distribution and air inlet temperature at the face of each grid region in the second level of grid generation. Refrigerant outlet temperature and heat transfer rate are the output variables of the model.

2.1 Calculation Procedure of the Numerical Model

The suggested numerical model includes the following major assumptions:

- The refrigerant mass flow rate is uniform among the tubes and parallel microchannels in tubes, there is no maldistribution between the microchannels,
- There is one-dimensional refrigerant flow in a segment,
- The air-side velocity in parts created at the second level of discretization are uniform, and air-flow across these parts is independent each other,
- The heat conduction between tubes and are neglected, the center of the fin is considered adiabatic.
- The longitudinal conduction and heat transfer between microchannel are ignored,
- The header is considered as adiabatic and the heat transfer in the header is ignored,
- Refrigerant assumed as well-mixed in headers,
- Both flows in air-side and refrigerant side are considered as steady-state

As stated earlier, each segment is considered as an independent cross-flow heat exchanger and heat transfer between the refrigerant and airflow in a segment is calculated by applying heat exchanger analysis tools. When a segment considered, the Effectiveness-Number of Transfer Units (ε -NTU) method can be applied to calculate heat transfer duty in the segment because of known inlet conditions and unknown outlet conditions initially [23,24]. Meanwhile, the pressure drop of the refrigerant side in the calculation segment is analyzed. As mentioned above, the outlet conditions are calculated by using heat transfer duty and pressure drop and then the iterative scheme is applied. After completed the iterative procedure in each cell, global variables like heat transfer, etc. are calculated by summing all the segment contributions.

In the ε -NTU method, effectiveness is defined for a specified heat exchanger as the ratio of actual heat transfer rate to the maximum possible heat transfer rate [25]:

$$\varepsilon = \frac{\dot{Q}}{\dot{Q}_{max}} \quad (2)$$

Effectiveness is a measure of thermal performance and non-dimensional. The value of the effectiveness ranges from 0 to 1 and it depends on the number of transfer units (NTU), the heat capacity ratio (C_R), and the flow arrangement. In the present study, the mathematical model has been developed for the louvered fin heat exchangers in which both air and refrigerant sides are unmixed. Also, the considered calculation segments have crossflow. Therefore, the effectiveness of a given segment can be calculated by using Eq. (3) for single-phase and Eq. (4) for two-phase refrigerant flow [26].

$$\varepsilon = 1 - \exp\{NTU^{0.22}[\exp(-C_R NTU^{0.78}) - 1]/C_R\} \quad (3)$$

$$\varepsilon = 1 - \exp(-NTU) \quad (4)$$

where the heat capacity ratio, C_R can be written as follows:

$$C_R = \frac{C_{min}}{C_{max}} = \frac{\min(C_r, C_a)}{\max(C_r, C_a)} \quad (5)$$

where $C_r (= \dot{m}_r C_{p,r})$ and $C_a (= \dot{m}_a C_{p,a})$ are stand for the heat capacity rate of refrigerant and air, respectively. The Number of Transfer Units, NTU designates the non-dimensional heat transfer size or thermal size of the heat exchanger and it is defined as the ratio of overall heat transfer coefficient to the minimum heat capacity rate. NTU can be written as [27]:

$$NTU = \frac{UA}{C_{min}} \quad (6)$$

In the Eq. (7), the maximum possible heat transfer, Q_{max} is expressed as:

$$\dot{Q}_{max} = C_{min}(T_{r,in} - T_{a,in}) \quad (7)$$

Based on the earlier stated assumptions, the heat transfer rate between the streams in each segment by employing the ε -NTU method can be written as follows:

$$\dot{Q} = \varepsilon Q_{max} = \varepsilon C_{min}(T_{r,in} - T_{a,in}) \quad (8)$$

The actual heat transfer rate, Q in a segment may be also written as in Eq. (9) and Eq. (10),

$$\dot{Q} = \dot{m}_r(i_{r,in} - i_{r,out}) \quad (9)$$

$$\dot{Q} = \dot{m}_a(i_{a,out} - i_{a,in}) \quad (10)$$

The overall heat transfer coefficient, UA is the definition of the total thermal resistance to heat transfer between the refrigerant and air.

$$UA = \left[\frac{1}{\eta_o h_a A_a} + \frac{P_t}{k_{tube} A_r} + \frac{1}{h_r A_r} \right]^{-1} \quad (11)$$

According to fin and tube model developed by Singh et al. [28], when the heat conduction between tubes is taken into consideration, predicted heat load is agreement within $\pm 3\%$ of the experimental data whereas there is $\pm 5\%$ agreement when the heat conduction ignored between tubes. Asinari et al. [29] reported that adiabatic-fin tip efficiency which neglects the longitudinal heat conduction in fin gives a reasonably accurate prediction of total heat flow exchanged. They also concluded that the longitudinal and the transverse conduction in tubes, as well as the longitudinal conduction in fin, have negligible impacts on the total heat transfers and on the temperature field. In this context, the assumption of heat conduction only in along fin height direction (one-dimensional heat conduction) can be applied to evaluate the fin efficiency.

Overall fin efficiency which is area-weighted fin efficiency is written as follow:

$$\eta_o = 1 - \frac{A_f}{A_a} (1 - \eta_f) \quad (12)$$

where A_a and A_f are air-side overall heat transfer area and fin surface area, respectively. The fin efficiency is given as:

$$\eta_f = \frac{\tanh(ml)}{ml} \quad (13)$$

$$m = \sqrt{\frac{2h_a}{k_{fin}\delta} \left(1 + \frac{\delta}{F_d}\right)} \quad (14)$$

$$l = \frac{F_h}{2} - \delta \quad (15)$$

In the implementation of the ε -NTU methodology, refrigerant and air-side heat transfer coefficient plays a key role. There is thus need the employment of efficient correlations for the heat transfer coefficient calculation in the model.

2.2 Refrigerant Side Heat Transfer and Pressure Drop

In literature, well-known heat transfer correlations for single-phase are Dittus-Boelter [30], Gnielinski [31] and Perukhov [32]. These correlations have been developed for conventional tubes, but some studies have been conducted to examine the usage of these correlations for microchannels. Derby et al. [33] presented a comparison between single-phase Nusselt numbers obtained by experiments for different cross-sectional microchannels and by Gnielinski [31] correlation. They concluded that single-phase experiments for heat transfer coefficients in the microchannel are within good agreement the Gnielinski [31] correlation. The heat transfer coefficient for single-phase flow in the microchannel can be estimated by the Gnielinski correlation [34]. Gnielinski correlation is

$$Nu_{GN} = \frac{\left(\frac{f}{8}\right)(Re_D - 1000)Pr}{1 + 12.7\sqrt{\frac{f}{8}}(Pr^{2/3} - 1)} \quad (16)$$

$$(2300 < Re_D < 10^6) \quad (17)$$

$$Nu_{GN} = 4.36 \quad (Re_D < 2300)$$

where f is the friction factor and defined by Filonenko [35] as:

$$f = [1.82 \log(Re_D) - 1.64]^{-2} \quad (18)$$

where Reynolds number is given in below:

$$Re_D = \frac{G_r D_h}{\mu_r} \quad (19)$$

Adams et al. [36] proposed the correction of the Nusselt number for small diameter based on their experimental data. They present the following equation:

$$Nu = Nu_{GN}(1 + F) \quad (20)$$

$$F = C Re_D \left[1 - \left(\frac{D_h}{D_0}\right)^2\right] \quad (21)$$

The constant C and D_0 have been found by using the least-squares fit to all data sets studied by Adams et al. [36] as $C = 7.6 \cdot 10^{-5}$ and $D_0 = 1.164 \text{ mm}$.

The refrigerant side pressure drop for single-phase flow may be calculated based on the correlation given in below:

$$\Delta P_r = f \rho_r U m_r^2 \frac{L_{seg}}{2D_h} \quad (22)$$

where Um is the mean velocity of the refrigerant.

2.3 Air-side Heat Transfer Coefficient and Pressure Drop

For microchannel heat exchangers, air-side thermal resistance is dominant over refrigerant-side thermal resistance [37], and thus, understanding of louvered fin performance plays a key role in the prediction of the overall performance of the MCPHs. The numerous studies on the air-side performance of louvered fin heat exchangers have been conducted by many researchers. Among them, widely-used correlations are Chang and Wang [38] correlation and Kim and Bullard [39] correlation. In the suggested model, Chang and Wang [38] correlation is considered in order to calculate the air-side heat transfer coefficient. It is possible that the Chang and Wang correlation with respect to the dimensionless heat transfer coefficient: the Colburn-j factor:

$$j = Re_{LP}^{-0.49} \left(\frac{\theta}{90}\right)^{0.27} \left(\frac{F_p}{L_p}\right)^{-0.14} \left(\frac{F_h}{L_p}\right)^{-0.29} \left(\frac{F_d}{L_p}\right)^{-0.23} \left(\frac{L_l}{L_p}\right)^{0.68} \left(\frac{T_p}{L_p}\right)^{-0.28} \left(\frac{\delta}{L_p}\right)^{-0.05} \quad (23)$$

where Re_{LP} is the Reynolds number depend on louver pitch:

$$Re_{LP} = \frac{\rho_a U m_a L_p}{\mu_a} = \frac{G_a L_p}{\mu_a} \quad (24)$$

It is worth note that the above correlation is valid in Reynolds number range from 100 to 3000. When the Colburn-j factor is found, the air-side heat transfer coefficient can be determined as follow:

$$h_a = j \rho_a U m_a C p_a Pr_a^{-2/3} \quad (25)$$

Another well-known correlation Kim and Bullard [39] is used to calculate the air-side pressure drop. Kim and Bullard friction factor correlation is given in below:

$$f_a = Re_{LP}^{-0.781} \left(\frac{\theta}{90}\right)^{0.444} \left(\frac{F_p}{L_p}\right)^{-1.682} \left(\frac{F_h}{L_p}\right)^{-1.22} \left(\frac{F_d}{L_p}\right)^{0.818} \left(\frac{L_l}{L_p}\right)^{1.97} \quad (26)$$

$$\Delta P_a = f_a G_a^2 \frac{F_d}{2\rho_a L_p} \quad (27)$$

3. Experimental Study

A louvered fin microchannel heat exchanger has been tested in order to evaluate the model results. The validation approach of the proposed model against experimental data is employed in this section.

For validation of the model, MCPH tests have been conducted within a vapor compression refrigerant cycle (VCRC). Due to the fact that the VCRC has been used in

many application fields for many years, the equipment with low uncertainties has been developed for the VCRC. Besides, the setup and operation of the VCRC have become easy over the years. All tests have been conducted in a climatic chamber in order to keep constant air properties. The schematics of the test facility and location of the measurement instrumentations can be seen in Figure 5. The MCPH sample has been installed in a small channel with the fan, which supplies air-flow over louvered fins. The test sample heat exchanger has been installed next to the condenser as an air preheater. Thanks to this configuration, a slight increment in temperature of intake air and sub-cooling in after refrigerant can be provided.

The refrigerant flows through the closed-loop the VCRC and a coriolis type flow meter employed in the test facility to measure the refrigerant mass flow rate. The Coriolis flowmeter has an accuracy of less than 0.1% of the rate from -50 to 180 °C temperature until a maximum 410 bar pressure. The temperature at the inlets and outlets of each component of the VCRC were measured to screen the thermodynamic cycle. Temperature measurements were taken from many points on the heat exchanger, which is the focus of this study. The refrigerant temperature was measured at the inlet and outlet of every two flat tubes on the MCPH as well as the MCPH inlet and outlet. The temperature measurements were used to determine the temperature distribution on the MCPH. The temperature measurements were carried out by means of the T-type thermocouples with measurement sensitivity up to 0.02 °C in the range of -200 to 400 °C. Besides temperature measurements, low- and high-pressure measurements on the cycle were conducted. The piezoresistive pressure transmitters with an accuracy $\pm 0.25\%$ FS in the range 2/30 bar were installed for pressure measurements.

Owing to the configuration of the installation of MCPH and supplying the air-flow over the MCPH by an induced-draft-fan, the face of MCPH divided into nine regions in both x and y-direction. As stated earlier, the main purpose of this grid generation, which is characterful of the proposed model, is to take into consideration the effect of the air-side maldistribution. Hence, air-side measurements were conducted at the mid-point of these nine air-side regions. The air-side measurement regions can be seen in Figure 6. The air velocities at air-side regions were measured by using hot-wire anemometer with a resolution 0.01 m/s and an accuracy ± 0.1 m/s in 0 to 30 m/s measuring range. Although the air temperature and relative humidity were kept constant in the climatic chamber, their values were checked with their measurements conducted at nine air-side measurement regions with thermo-hygrometer. The thermo-hygrometer has -20 to 60 °C measuring range, ± 0.5 °C accuracy for temperature measurements and 0 to 100%rH, $\pm 1.8\%$ rH accuracy for relative humidity measurements. Also, the dew point and wet bulb temperature of the air calculated to control the occurrence of wet conditions on the fins.

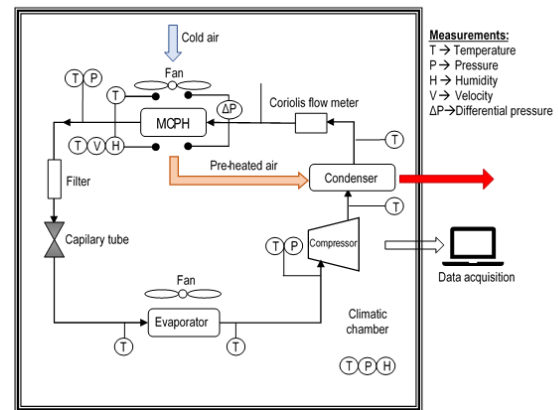


Figure 5. Schematic representation of the test facility

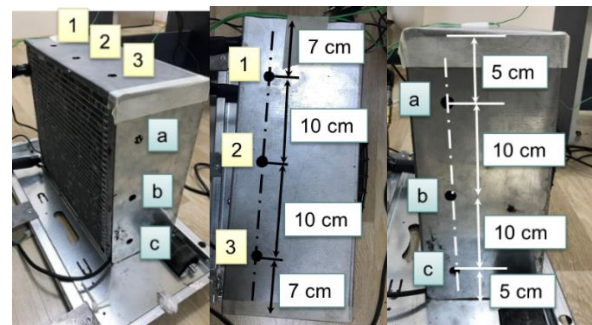


Figure 6. Air-side measurements points

For the verification, experimental measurements were used as the operational inputs of the model in addition to geometrical inputs (Table 1). Iterative scheme and calculation procedure of the model was performed using EES [40]. The outputs variables calculated by using the model have been verified with the output variables obtained from experiments.

The deviations in heat capacity predictions are higher than the ones in the outlet temperature of the MCPH. The main reason for these deviations is more probably to neglected heat transfer in the headers. The model assumes no heat transfer in the header and applies the temperature of the header as the inlet temperature of the next pass. However, in the actual process, there is a slight heat transfer in the header during refrigerant flows from a pass to another. Due to this heat loss, the temperature of the refrigerant decreases a little bit when it changes the passes. Also, it is apparent that the model with non-uniform air velocities overestimates the heat capacity according to experimental results. These overestimated results could have been caused by the heat losses in the header in experiments. Another proof explains this situation can be seen in Table 4. Table 4 exhibits the mean absolute errors between experimental and calculated temperatures at the inlet and outlet of each pass under test conditions. In Table 4, the mean absolute errors at the first pass inlet are equal to zero because experiment measurements at the inlet were applied as inlet conditions in the model. Therefore, in experiments and model calculations, there are the same temperatures in the first part of inlets. It is

obviously seen that the mean absolute errors for temperature in most of the data points have negative value because of the temperature decrease resulted in heat loss in headers. In Table 4, the mean absolute errors at the inlets are higher than the ones at outlets. When the refrigerant flows in the next pass, the model assumes there are no changes in refrigerant temperature between previous and next pass whereas there is a slight temperature decrease in actual operation due to heat losses in the header. Hence, the higher mean absolute errors can be observed at the inlets of the passes. However, these errors have not exceeded 16%. The overall average errors are within the -7 and 2% in terms of the inlet and outlet temperatures of the passes for all tests. Therefore, it can be concluded that the proposed model presents the results with acceptable precisions.

4. Results and Discussion

The present model verification was conducted with a comparison between model and experiment results. Table 2 indicates the refrigerant side test conditions at each data point used to validate model predictions. Air-side test operational conditions for the test are given in Table 3. It is worth note that the air-side parameters were kept constant for test conditions thanks to the climatic chamber. The assessment of the outlet temperature of the MCPH is indicated in Figure 7. It follows from Figure 7 that the proposed model reasonably estimated the outlet temperature of the MCPH. The mean absolute errors for the outlet temperature of the MCPH are in the range $\pm 2\%$. The model has 2.19% maximum and 0.26% minimum deviation in the MAE for the outlet temperature of the MCPH. It is easily seen from Figure 7 that the model mostly under-estimate the outlet temperature of the MCPH. But, the great majority of the data points show a slightly low error percent. The results show that the proposed numerical model in the current study has high accuracy with respect to the outlet temperature of the MCPH.

Figure 8 exhibits the comparisons of heat capacities of the MCPH obtained experiments and models with both non-uniform and uniform air velocity approaches. In the non-uniform approach, different air velocity applied at the mid-point of the nine air-side grid regions which were created at the second level of the grid generation, while the average air velocity was uniformly applied to the face of the MCPH in the uniform air velocity approach. According to Figure 8, the overall deviation in model results with non-uniform air velocity is within nearly 0 to 20% for the heat capacity of the MCPH. The heat capacity prediction with the uniform air velocity approach indicates the deviations higher than the deviations of the non-uniform air velocity approach. It exceeds the -20% mean absolute error compared with experimental data. It can be easily said that the non-uniform air velocity approach improves the precision of the proposed model. It is obvious that the precision of the model can be

increased as the nine air-side regions are augmented.

Under investigated test conditions, the refrigerant enters the MCPH at a temperature in the range 43-49 °C and it is cooled down to nearly 26 °C. Figure 9 demonstrates the refrigerant temperature for investigated test conditions with respect to the length of the refrigerant pass.

Table 2. Test conditions for refrigerant side

Test no	Mass flow rate [g/min]	Inlet temperature [°C]	Inlet Pressure [bar]
1	77	45.02	6.38
2	79	43.16	5.97
3	76	49.61	7.08
4	75	47.43	6.76
5	76	47.70	6.79
6	75	47.77	6.79
7	76	48.00	6.80
8	75	47.4	6.73
9	75	47.71	6.91
10	76	47.46	6.76
11	75	47.08	6.63
12	74	46.67	6.6
13	74	46.83	6.65
14	74	46.35	6.55

Table 3. Test conditions for airside

Location	Inlet Velocity [m/s]
1a	1.6937
2a	1.6383
3a	0.4474
1b	0.4755
2b	0.2011
3b	0.6285
1c	0.6604
2c	1.6765
3c	0.7837

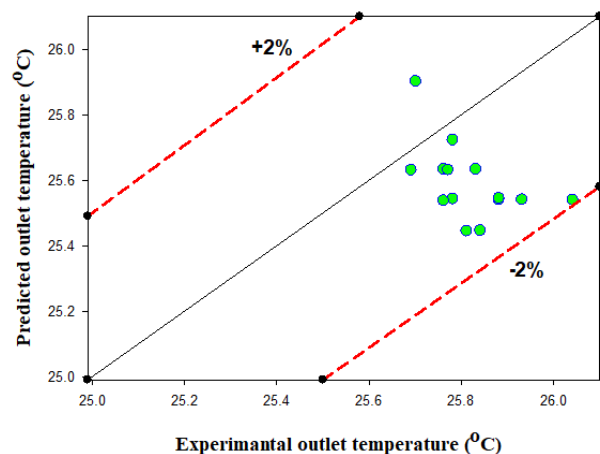


Figure 7. Comparison of the experimental and predicted outlet temperature of the test sample MCPH

Table 4. Mean absolute error between inlet and outlet temperatures of the passes under the test conditions.

		Test 1	Test 2	Test 3	Test 4	Test 5	Test 6	Test 7	Test 8	Test 9	Test 10	Test 11	Test 12	Test 13	Test 14
Pass 1	Inlet	0	0	0	0	0	0	0	0	0	0	0	0	0	0
	Outlet	-0.54	3.41	-14.26	-9.91	-9.29	-9.98	-10.32	-8.61	-11.43	-11.53	-12.26	-10.47	-11.73	-10.63
Pass 2	Inlet	-1.04	8.33	-16.15	-11.12	-11.53	-12.08	-11.97	-10.77	-15.09	-14.27	-13.93	-12.59	-13.44	-12.36
	Outlet	3.84	2.84	-2.07	0.01	-1.10	-1.28	-0.91	-0.81	-1.67	-1.82	-2.15	-1.53	-2.10	-1.68
Pass 3	Inlet	-5.65	-5.28	-9.34	-6.14	-6.75	-6.77	-6.31	-6.08	-6.73	-6.92	-7.08	-6.09	-6.85	-6.56
	Outlet	0.50	1.83	-6.77	-2.10	-3.05	-3.13	-2.49	-2.38	-3.79	-3.72	-3.64	-3.84	-3.93	-3.66
Pass 4	Inlet	-10.21	-10.17	-17.76	-14.44	-14.86	-14.99	-14.71	-14.23	-15.23	-14.92	-14.96	-15.05	-15.18	-14.63
	Outlet	-1.52	-2.03	-4.72	-1.85	-2.68	-2.72	-2.38	-2.15	-2.74	-2.76	-2.76	-2.61	-2.99	-2.89
Pass 5	Inlet	-2.76	-2.87	-4.14	-1.81	-2.82	-2.76	-2.60	-2.34	-2.68	-2.74	-2.78	-2.42	-2.99	-2.84
	Outlet	0.26	0.35	-1.93	0.27	-0.43	-0.54	0.06	0.27	-0.50	-0.44	-0.46	-0.54	-0.62	-0.70
Pass 6	Inlet	-0.76	-0.69	-2.48	-0.31	-0.93	-1.07	-0.44	-0.25	-0.87	-0.80	-0.80	-0.84	-0.95	-0.97
	Outlet	0.26	0.46	-0.47	2.19	1.21	1.25	1.44	1.67	0.97	1.62	1.65	1.56	0.64	0.79
Average	Inlet	-3.40	-1.78	-8.31	-5.64	-6.15	-6.28	-6.01	-5.61	-6.77	-6.61	-6.59	-6.16	-6.57	-6.23
	Outlet	0.47	1.14	-5.04	-1.90	-2.56	-2.73	-2.43	-2.00	-3.19	-3.11	-3.27	-2.91	-3.45	-3.13
	Overall	-1.47	-0.32	-6.67	-3.77	-4.35	-4.51	-4.22	-3.81	-4.98	-4.86	-4.93	-4.54	-5.01	-4.68

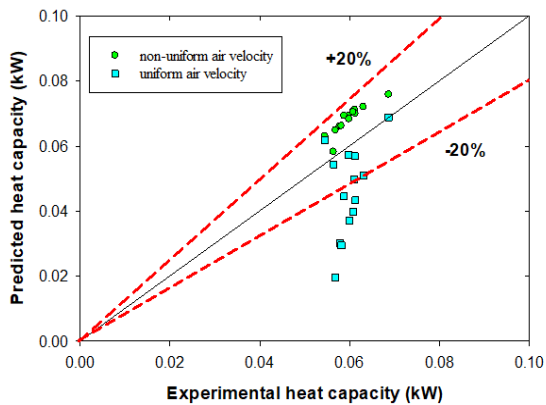


Figure 8. Comparison of the predicted and experimental heat capacities

The temperature of the refrigerant shows a sharp decrease in the first pass (0-0.3 m) in all data points according to Figure 9. In the first pass of the MCPH, decreases in temperature of the refrigerant are 10-12 °C. In the second pass (0-0.7 m), reducing in the temperatures are lower than the decrease in the first pass owing to the decrement of the finite temperature difference between air and refrigerant. Therefore, the amount of the decreasing in refrigerant temperature declines as the refrigerant flows through the passes (lengths after 0.7 m). Under the considered operation condition, the test sample MCPH shows a higher temperature change in the first two passes. In the first and second passes, refrigerant temperatures have been nearly the same as the air temperature in the climate chamber. The high-temperature changes in first and second pass according to the changes in other passes indicate that the MCPH has been completed the great majority of the heat transfer duty in the first two passes

The heat transfer rates in each pass in terms of the length of the passes are depicted in Figure 10 for handled data points. It can be easily observed from the figure that the first pass

shows the highest heat transfer rate among the passes of the MCPH. The heat transfer rate takes place in the second pass have been relatively higher than the heat transfer rate in the next passes under all investigated test conditions. In the next passes of the second pass, the heat transfer rate between air and refrigerant has slowly reduced and it closes to zero in the sixth pass (last pass of the MCPH). As mentioned above, the main reason for this situation is the decrement of the finite temperature difference between air and refrigerant through the length of the passes. It can be concluded that the temperature decrements and higher heat transfer rate in the first and second passes are the indicators of the compactness of the microchannel heat exchangers. The studies conducted by many researchers have always implied as a benefit that the microchannel heat exchangers are the compact design. According to the studies, the MCPHs show higher heat transfer performance in the small volumes. In this respect, the results of the model proposed in the current study indicate agreeable conclusion with the studies available in the literature.

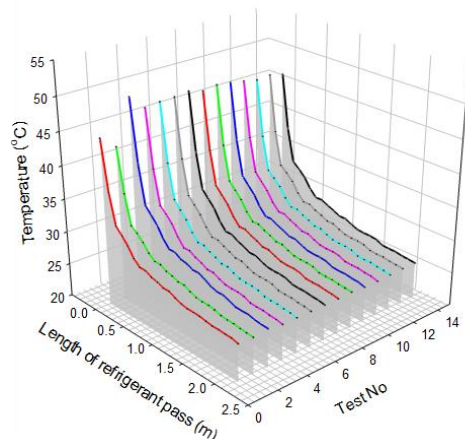


Figure 9. Temperature changes in passes of the MCPH with respect to the length of the refrigerant pass

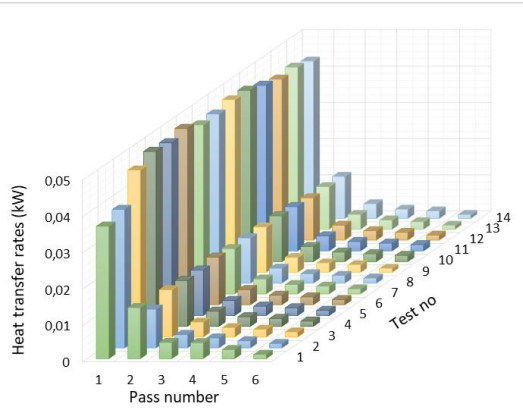


Figure 10. The heat transfer rates between air and refrigerant in passes of the MCPH for investigated test conditions.

4. Conclusion

The development of micro-manufacturing technologies has enabled the reveal of the microchannel heat exchangers for various industrial applications. It is well known that the single-phase conditions of the refrigerant are not widespread, whereas single-phase conditions are common in preheating and precooling, and in superheating and supercooling applications. Within this scope, the current study has presented a study on the prediction of the thermal performance of the louvered fin microchannel heat exchangers as air preheater for HVAC systems. A numerical model that uses the finite-volume approach including effectiveness-NTU procedure was introduced to estimate outlet temperature and heat capacity of the air-cooled microchannel heat exchanger. It is obvious that such simulation models can offer a significant contribution to the cost and time-saving design and optimization efforts of the designers owing to the elimination of the experimental tests. It is important to note here that the proposed model is also capable of simulating the heat transfer from air to the refrigerant even though heat transfer from the refrigerant to the air was considered in the tests conducted to verify the model.

During the simulation, it is observed that the estimations of the model have been in good agreement with experimental data regarding outlet temperature. It is determined that the model has reasonably predicted the outlet temperature of the MCPH with the mean absolute error deviation within 2%. The proposed model shows high accuracy with respect to temperature calculation. On the other hand, the model has indicated a higher deviation in the heat capacity prediction than the temperature estimation. It is concluded that the main reason for the high deviation in heat capacity prediction is the assumption which is neglect of the heat loss in the headers. The model applies the adiabatic header assumption but in the actual process, there is heat transfer from headers to ambient air. Therefore, it is considered that such heat transfer has an impact on heat capacity calculations. It is recommended that it should be taken into account during

further simulation studies.

When comparing the results of heat capacity predictions of non-uniform air-side conditions with uniform ones, it has been apparently seen that applying non-uniform air side velocity with generating independent air-side grid regions improves the accuracy of the model. Considering different air velocities in terms of the actual configuration of the preheaters, especially fan-driven systems, have an important effect on the accuracy of the model.

Declaration

The author(s) declared no potential conflicts of interest with respect to the research, authorship, and/or publication of this article. The author(s) also declared that this article is original, was prepared in accordance with international publication and research ethics, and ethical committee permission or any special permission is not required.

Nomenclature

A_a	air-side overall heat transfer area (m ²)
A_f	fin surface area (m ²)
A_r	refrigerant side effective heat transfer area (m ²)
\dot{Q}	heat transfer rate (kW)
NTU	number of transfer units
C_R	heat capacity ratio (-)
C	heat capacity rate (J K ⁻¹ s ⁻¹)
C_p	specific heat (J kg ⁻¹ K ⁻¹)
D_h	tube hydraulic diameter (m)
f	friction factor (-)
F_d	fin width (m)
F_h	fin height (m)
F_p	fin pitch (m)
G	mass flux (kg m ⁻² s ⁻¹)
h	heat transfer coefficient (W m ⁻² K ⁻¹)
i	specific enthalpy (kJ kg ⁻¹)
j	Colburn-j factor (-)
k_{tube}	thermal conductivity of tube material (W m ⁻¹ K ⁻¹)
k_{fin}	thermal conductivity of fin material (W m ⁻¹ K ⁻¹)
L_l	louver length (m)
L_p	louver pitch (m)
L_{seg}	the segment length (m)
\dot{m}	mass flow rate (kg s ⁻¹)
MAE	mean absolute error (%)
NTU	number of transfer units
Nu	Nusselt number (-)
Nu_{GN}	Gnielinski Nusselt number (-)
P	pressure (bar)
ΔP	pressure drop (bar)
Pr	Prandtl number (-)
P_t	port thickness (m)
\dot{Q}	heat transfer rate (kW)
Re_D	refrigerant side Reynolds number (-)
Re_{LP}	air-side Reynolds number (-)
T	temperature (°C)
ΔT	temperature change (°C)
T_{hi}	inner tube height (m)
T_p	tube pitch (m)

UA	overall heat transfer coefficient (kW K ⁻¹)
Um	mean velocity (m ⁻¹ s ⁻¹)
W_t	web thickness (m)
δ	fin thickness (m)
ρ	density (kg m ⁻³)
ε	effectiveness (-)
η_o	overall fin efficiency (-)
η_f	fin efficiency (-)
η_{web}	web efficiency (-)
μ	dynamic viscosity (Pa.s)
θ	louver angle (°)
max	maximum
min	minimum
r	refrigerant
a	air
in	inlet
out	outlet

References

- Sen, O., Yılmaz, C., *Thermodynamic performance analysis of geothermal and solar energy assisted power generation and residential cooling system*. International Advanced Researches and Engineering Journal, 2020. **04**(01): p.41–7.
- Kandlikar, S.G., *A roadmap for implementing minichannels in refrigeration and air-conditioning systems - Current status and future directions*. Heat Transfer Engineering, 2007. **28**(12): p.973–85.
- Roth, K., Westphalen, D., Dieckmann, J., Hamilton, S., Goetzler, W., *Energy consumption characteristics of commercial building HVAC systems*, Volume III: Energy savings potential, 2002. **3**.
- Kandlikar, S.G., Garimella, S., Li, D., Stephane, C., King, M.R., *Heat transfer and fluid flow in minichannels and microchannels*. 2005, Oxford: UK: Elsevier.
- Gong, L., Lu, H., Li, H., Xu, M., *Parametric numerical study of the flow and heat transfer in a dimpled wavy microchannel*. Heat Transf Research, 2016. **47**(2): p.105–18.
- Kaya, H., Ekiciler, R., Arslan, K., *Entropy generation analysis of forced convection flow in a semicircular microchannel with TiO₂/water nanofluid*. Heat Transf Research, 2019. **50**(4): p.335–48.
- Mohammadpourfard, M., Zonouzi, S.A., Mohseni, F., *Numerical study of the hydrothermal behavior and exergy destruction of magnetic nanofluid in curved rectangular microchannels*. Heat Transf Research, 2015. **46**(9): p.795–818.
- Tiwari, N., Moharana, M.K., *Numerical study of thermal enhancement in modified raccoon microchannels*. Heat Transf Research, 2019. **50**(6): p.519–43.
- Glazar, V., Frankovic, B., Trp, A., *Experimental and numerical study of the compact heat exchanger with different microchannel shapes*. International Journal of Refrigeration, 2015. **51**: p. 144–53.
- Ren, T., Ding, G., Wang, T., Hu, H., *A general three-dimensional simulation approach for micro-channel heat exchanger based on graph theory*. Applied Thermal Engineering, 2013. **59**(1–2): p.660–74.
- Yin, J.M., Bullard, C.W., Hrnjak, P.S., *R-744 gas cooler model development and validation*. Int J Refrig. 2001. **24**: 692–701.
- Fronk, B.M., Garimella, S., *Water-coupled carbon dioxide microchannel gas cooler for heat pump water heaters: Part II - Model development and validation*. International Journal of Refrigeration, 2011. **34**(1): p.17–28.
- Fronk, B.M., Garimella, S., *Water-coupled carbon dioxide microchannel gas cooler for heat pump water heaters: Part I - Experiments*. International Journal of Refrigeration, 2011. **34**(1): p.7–16.
- García-Cascales, J.R., Vera-García, F., González-Maciá, J., Corberán-Salvador, J.M., Johnson, M.W., Kohler, G.T. *Compact heat exchangers modeling: Condensation*. International Journal of Refrigeration, 2010. **33**(1): p.135–47.
- Kim, M.H., Bullard, C.W., *Development of a microchannel evaporator model for a CO₂air-conditioning system*. Energy, 2001. **26**(10): p.931–48.
- Yin, X.W., Wang, W., Patnaik, V., Zhou, J.S., Huang, X.C., *Evaluation of microchannel condenser characteristics by numerical simulation*. International Journal of Refrigeration, 2015. **54**: p. 126–41.
- Park, C.Y., Hrnjak, P., *Experimental and numerical study on microchannel and round-tube condensers in a R410A residential air-conditioning system*. International Journal of Refrigeration, 2008. **31**(5): p. 822–31.
- Liang, Y.Y., Liu, C.C., Li, C.Z., Chen, J.P., *Experimental and simulation study on the air side thermal hydraulic performance of automotive heat exchangers*. Applied Thermal Engineering, 2015. **87**: p.305–15.
- Zhai, R., Yang, Z., Zhang, Y., Lv, Z., Feng, B., *Effect of temperature and humidity on the flammability limits of hydrocarbons*. Fuel, 2020. **270**. Available from: <https://doi.org/10.1016/j.fuel.2020.117442>
- Ahmadpour, M.M., Akhavan-Behabadi, M.A., Sajadi, B., Salehi-Kohistani, A., *Experimental Study of Lubricating Oil Effect on R600a Condensation inside Micro-Fin Tubes*. Heat Transfer Engineering. 2020. p.1–13. Available from: <https://doi.org/10.1080/01457632.2020.1735780>
- American Society of Heating R and AE. *ASHRAE Handbook-Fundamentals*. 2009, Atlanta, GA: ASHRAE Inc.
- Lohbeck, W., *Development and state of conversion to hydrocarbon technology*. Proceedings of the International Conference on Ozone Protection Technologies: Washington, D.C.; 1996. p. 247–51.
- Bergman, T.L., Lavine, A.S., Incropera FP, DeWitt DP. *Fundamentals of Heat and Mass Transfer*. 7th ed. 2011, New York: USA: JohnWiley & Sons.
- Cengel, Y.A., *Heat and Mass Transfer: A Practical Approach*. 3rd ed. 2007, McGraw-Hill.
- Kuppan, T., *Heat Exchanger Desing Handbook*. 2000, NY: USA: Marcel Dekker, Inc.
- Shah, R.K., Sekulic, D.P., *Fundamentals of Heat Exchanger Design*. 2003, New York: USA: John Wiley and Sons, Inc.
- Kakaç, S., Liu, H., *Heat Exchangers: Selection, Rating and Thermal Design*. 2nd ed. 2002, Boca Raton, USA: CRC Press LLC.
- Singh, V., Aute, V., Radermacher, R., *Numerical approach for modeling air-to-refrigerant fin-and-tube heat exchanger with tube-to-tube heat transfer*. Int J Refrig [Internet]. 2008. **31**(8):1414–25.
- Asinari, P., Cecchinato, L., Fornasieri, E., *Effects of thermal conduction in microchannel gas coolers for carbon dioxide*. International Journal of Refrigeration, 2004. **27**(6): p. 577–86.

30. Dittus, F.W., Boelter, L.M., *Heat transfer in automobile radiators of the tubular type*. Publication in Engineering University California, Berkeley. 1930. **2**: p.443.
31. Gnielinski, V., *New equations for heat and mass transfer in turbulent pipe and channel flow*. International Chemical Engineering, 1976. **16**: p.359–68.
32. Petukhov, B.S., *Heat transfer and friction in turbulent pipe flow with variable physical properties*. Advanced Heat Transfer, 1970. **6**: p.503–64.
33. Derby, M., Lee, H.J., Peles, Y., Jensen, M.K., *Condensation heat transfer in square, triangular, and semi-circular microchannels*. International Journal of Heat and Mass Transfer, 2012. **55**(1–3): p.187–97.
34. Saha, S.K., *Microchannel Phase Change Transport Phenomena*. 2016, Oxford: UK: Butterworth-Heinemann.
35. Filonenko, G.K., *Hydraulic resistance in pipes", Heat Exchanger Design Handbook*. Teploenergetica, 1954. **1**(4): p.40–44.
36. Adams, T.M., Jeter, S.M., Qureshis, Z.H., *An experimental investigation of single-phase forced convection in microchannels*. International Journal of Heat and Mass Transfer, 1997. **41**(6–7): p.851–7.
37. Aute, V., Radermacher, R., *Chapter Five - A Validated Framework for Innovation and Design Optimization of Air-to-Refrigerant Heat Exchangers*. In: Sparrow EM, Abraham JP, Gorman JMBT-A in HT, Elsevier, 2018. p. 301–32.
38. Chang, Y.J, Wang, C.C., *A generalized heat transfer correlation for louver fin geometry*. International Journal of Heat and Mass Transfer, 1997. **40**(3): p.533–44.
39. Kim, M., Bullard, C.W., *Air-side thermal hydraulic performance of multi-louvered fin aluminum heat exchangers*. International Journal of Refrigeration, 2002. **25**: p.390–400.
40. Klein, S.A., *Engineering Equation Solver, F-Chart Software*. 2006.

**Research Article****The effects of the use of acetylene gas as an alternative fuel in a gasoline engine****Salih Özer^a , Mehmet Akçay^{a,*} , Erdiñç Vural^b  and İlker Turgut Yılmaz^c **^aMuş Alparslan University Faculty Of Engineering-Architecture Mechanical Engineering, Muş, 0490100, Turkey^bAydın Adnan Menderes University Germencik Yamantürk Vocational School, Aydın, 090100, Turkey^cMarmara University Faculty Of Technology Automotive Engineering, İstanbul, 0340100, Turkey

ARTICLE INFO

Article history:

Received 27 January 2020

Revised 31 March 2020

Accepted 08 May 2020

Keywords:

Acetylene gas

Air supply coefficient

Exhaust emissions

Gas fuel

Spark-ignition engine

ABSTRACT

In internal combustion engines, the use of gas fuels is becoming widespread due to its advantages such as low cost and being more environmentally friendly. Acetylene is one of the gas fuels seen as an alternative to petroleum-based fuels in internal combustion engines. In this experimental study, the availability of acetylene gas, a gas fuel, at 1600 rpm, 2400 rpm and 3200 rpm engine speeds in a spark plug-fired engine was investigated. Acetylene gas was added to gasoline by 5% and 10% of the mass and its effect on exhaust emissions was studied. The results showed that adding acetylene gas to gasoline by mass increased CO, CO₂ and NO_x emissions and exhaust gas temperature. HC, oxygen emissions and air supply coefficient decreased.

© 2020, Advanced Researches and Engineering Journal (IAREJ) and the Author(s).

1. Introduction

In recent years, increasing environmental problems and the rapid reduction of energy resources have exposed the world to an energy crisis. Approximately eighty percent of the world's energy need is met by fossil fuels [1, 2]. Considering the ratio of existing reserves to production, it is said that there is an oil reserve of approximately 40 years [3]. The fact that the emission values of fossil fuels are not suitable and such fuels will be exhausted after a while makes it compulsory to take new measures and look for new options. According to recent studies, if there is no change in the use of energy resources, the prices will rise rapidly and global energy deficit and pollution will increase up to 50% by 2030 [1]. This has led to a quest for alternative energy resources that are renewable and environmentally safe.

Fossil fuels, which are widely used in industrial applications, heating buildings, motor vehicles, etc., cause significant damage to human health and nature with harmful emissions (hydrocarbon (HC), carbon monoxide (CO), carbon dioxide (CO₂), sulfur dioxides (SO₂), nitrogen oxides (NO_x), etc.). Particularly in big cities, the share of

air pollution caused by motor vehicles in the whole air pollution is said to be around 50% [4-6]. For this reason, significant importance has been attached to efforts towards reducing emissions from internal combustion engines.

Among more than 100 polluting emissions generated by internal combustion engines, the most important emissions that negatively affect the environment and human health are CO, HC, NO_x, sulphur oxides (SO_x), aldehydes (HCHO) and particles [3]. Natural gas, liquefied petrol gas (LPG), hydrogen, acetylene, alcohols and vegetable oils can be used as an alternative fuel in internal combustion engines directly or as additions of certain ratios to the main fuel [7, 8]. In studies on gas fuel applications in compression-ignition (CI) and spark-ignition (SI) engines, the gas fuel is taken into the cylinder by adding it to the intake air, and then the ignition is triggered by either pilot fuel or ignition spark [7-9].

1.1 Acetylene Gas and Its Properties

Acetylene gas that has a chemical formula of C₂H₂ is a gas that is colorless, garlic-smelling and highly flammable [10]. The density of acetylene is around 1.1

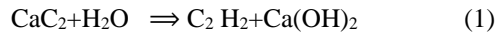
* Corresponding author. Tel.: +90 436 49 49; Fax: +90 436 49 49.

E-mail addresses: s.oz@alparslan.edu.tr (S.Özer), mehmetakcay@yahoo.com (M. Akçay), erdinc009@hotmail.com (E.Vural), ilker.yilmaz@marmara.edu.tr (İ.T. Yılmaz)

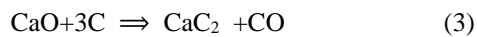
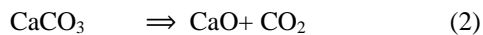
ORCID: 0000-0002-6968-8734 (S.Özer), 0000-0002-5030-1296 (M. Akçay), 0000-0002-8018-2064 (E.Vural), 0000-0002-0398-7635 (İ.T. Yılmaz)

DOI: 10.35860/iarej.680463

kg/m³ and it is approximately 10% lighter than air [8, 9]. It is used in the synthesis process of various organic compounds as well as in the cutting and welding of metals. Acetylene gas is formed during the decomposition of calcium carbide (CaC₂) under the action of water (H₂O) according to the exothermal chemical reaction. The chemical equation is as follows [11,12].



The calcium carbide (CaC₂) mentioned here is produced by the burning of calcium carbonate (limestone-CaCO₃). The initial temperature of CaC₂ formation is between 1700-1800°C. CaCO₃ is formed by burning calcium oxide (lime-CaO), then coal (C) is reacted with CaC₂ and CO₂ is obtained. These chemical equations as follows ; [12, 13]



Because of acetylene gas has low ignition energy, high flame velocity, wide flammability limits, and short quenching distance, these properties lead to engine knocking, a major problem in engines powered with acetylene [7]. Although acetylene gas has a potential of being an alternative fuel in internal combustion engines in terms of its high combustion temperature and rate, rapid ignition and being economical, it has not been widely used so far due to difficulties in its storage and use.

Gas fuels have importance as an alternative fuel with their abundant nature and clean combustion. In the literature, there are many studies on the use of hydrogen gas, a gas fuel, in internal combustion engines [14-19]. When hydrogen and acetylene are compared, the acetylene gas have mostly similar combustion properties in terms of combustion velocity, ignition energy, adiabatic flame temperature and flammability limit. In addition, the self-ignition temperature and production and storage costs in acetylene are lower than in hydrogen [10]. Due to this and other positive properties, it is of significance to investigate the use of acetylene gas as an alternative fuel in internal combustion engines. The physical and chemical properties of acetylene, hydrogen and gasoline (iso-octane) are generally presented in Table 1 [8, 20-25].

As can be seen in Table 1 presenting the general properties of acetylene, hydrogen and gasoline comparatively, acetylene shows properties similar to hydrogen with its low density, high self-ignition temperature and very low ignition energy. Acetylene gas, which has a faster energy yield as well as a high combustion velocity, is more suitable for the

thermodynamically ideal engine cycle efficiency in engines that operate with a stoichiometric mixture. Low ignition energy, high combustion velocity, wide ignition ranges and short quenching distance lead to early ignition and a phenomenon of undesired combustion that is called knocking. This is one of the major problems encountered in engines using acetylene gas. One way to prevent the backfire is the time-adjusted injection of fuel before the fuel is sent and after the intake time when the intake air is taken in. This makes a pre-cooling effect, thus neutralizing the early ignition source [26].

The use of acetylene as an alternative fuel in internal combustion engines is said to compete with hydrogen in the future [8]. When recent studies on gas fuels are examined, it is possible to find many studies on the use of acetylene gas as fuel in internal combustion engines. Some of the related studies are as follows;

İlhak et al., [27], investigated the effects of the use of gasoline and acetylene gas mixtures on the engine performance and emissions of a SI engine. In experiments, acetylene flow rates were fixed at 500 g/h and 1000 g/h. Thermal efficiency decreased with the use of acetylene at almost all loads. Hydrocarbon emissions decreased in all engine loads while NO emissions increased in low loads compared to gasoline.

Lakshmanan and Nagarajan [8], examined the effect of the addition of different rates of acetylene gas on engine performance and exhaust emissions in a single cylinder four-stroke direct injection diesel engine. Diesel fuel was injected as the primary fuel and various proportions of acetylene was sent to the cylinder as secondary fuel. Thermal efficiency decreased with the use of acetylene. Compared to the use of pure diesel fuel, the addition of acetylene led to a reduction in HC and CO emissions. There was a significant increase in NOx emissions due to the high combustion rate with the use of acetylene.

Lakshmanan and Nagarajan [20], investigated the effect of the addition of acetylene gas to diesel fuel as a secondary fuel in a single-cylinder diesel engine on engine performance and exhaust emissions. The brake thermal efficiency was found to be lower with dual fuel application than with diesel fuel when the engine was in full load condition. With the dual fuel application of acetylene, the exhaust gas temperature was observed to decrease when compared to diesel fuel, and the CO, CO₂ and HC emissions were reduced in certain amounts. However, NOx showed a significant increase.

Lakshmanan and Nagarajan [21], examined the effects of the addition of 110 g/h, 180 g/h and 240 g/h of acetylene gas to diesel fuel and the different ratios of EGR application on exhaust emissions and engine performance. Acetylene gas added to diesel fuel led to a decrease in NOx, CO and HC emissions and a considerable increase in smoke emissions.

Table 1. Physical and chemical properties of acetylene, hydrogen and gasoline.

Properties	Acetylene	Hydrogen	Gasoline
Chemical Formula	C ₂ H ₂	H ₂	C ₈ H ₁₈
Density, (1 atm, 20°C) kg/m ³	1.092	0.08	730
Molecular Weight (kg/kmol)	24.06	2.02	114.18
Stoichiometric air fuel ratio (kg/kg)	13.2	34.3	14.7
Flammability Limits (volume %)	2.5-81	4-74.5	1.3-7.6
Adiabatic flame temperature (K)	2500	2400	2226
Lower Calorific Value (kJ/kg)	48225	120000	43400
Lower Calorific Value (kJ/m ³)	50636	9600	-
Auto Ignition Temperature (K)	578	845	530
Ignition energy (Mj)	0.019	0.02	0.24
Flame Speed (m/s)	6.097	2.37	0.415

Nathan et al., [22], conducted a study with different pressure rates of acetylene gas in a homogeneous charge compression ignition (HCCI) engine. In the study, they stated that acetylene could be used in an HCCI engine individually without any fuel additives. Optimum exhaust gas recirculation (EGR) and brake thermal efficiency was found to increase slightly compared to diesel fuel application. Hot EGR at the high brake mean effective pressure (BMEP) caused the engine to knock. While nitrogen oxide and smoke levels went down, HC emissions went up.

In a study by Laksmanan et al., [28], investigated the effect of water injection on acetylene and diesel dual fuel diesel engine performance and exhaust emissions. Acetylene gas was delivered to the intake manifold of a single cylinder diesel engine with a flow rate of 390 g/h. The thermal efficiency and exhaust gas temperature decreased according to the diesel fuel and dual injection of diesel-acetylene by water injection. Water injection to the inlet port caused a significant decrease in NO_x levels. Compared to the acetylene diesel dual fuel operation, there has been an increase in HC and smoke emissions.

Lakshmanan and Nagarajan [26], used a timed manifold injection (TMI) technique to deliver acetylene gas to a direct injection diesel engine. In the study, a four-stroke diesel engine with 4.4 kW power was used. A small modification was made in the intake manifold to mount the gas injector controlled by an electronic control unit (ECU). The study was carried out at gas flow rates of 110 g/h, 180 g/h and 240 g/h. The engine performance achieved by the addition of acetylene gas at full load was reported to be very close to the performance with pure diesel fuel. NO_x, CO, CO₂ and HC emissions decreased although there was a slight increase in smoke emissions.

Choudhary et al., [29], added acetylene to diesel fuel at

constant flow rate in a compression engine, and examined the results. They replicated the experiment by setting the diesel engine at the values of 18:1, 18,5:1, 19:1 and 19,5:1. As a result of the experiment, they examined combustion and motor performance parameters. They stated that the temperature of the exhaust gas increased as the in-cylinder pressure values and brake thermal efficiency increased. They also reported that the highest increase in efficiency was 21.18% maximum in the combustion rate of 19.5:1.

In the literature, there have been very few studies on the effects of acetylene gas on performance and emissions in SI engines [27], but the applications in diesel engines were widely studied [26,28]. Therefore, in the present study, it was preferred to test the acetylene gas in a gasoline engine. Additionally, in this study, the effects of acetylene gas added to the gasoline by mass are investigated in fixed engine speed and fixed throttle opening in terms of emission.

İlhak et al., [30] they studied the effects of the addition of acetylene using ethanol and gasoline as Pilot fuel. For this purpose, they operated a gasoline engine at 1500 RPM under 25% and 50% load. They found that ethanol lowers emissions.

Raman and Kumar [31] they studied the effects of the addition of acetylene gas in a compressed engine. For this purpose, they added 5% and 10% butanol to the fuel used as pilot fuel. They then examined the internal combustion and performance data of the acetylene gas, which they added at different rates by mass. their results showed that they reported that acetylene gas burned more efficiently with pilot fuel use.

İlhak et. al., [32] They studied the effects of the addition of acetylene in a gasoline engine at different air/fuel ratios. They repeated their experiments at 25% and 50% engine loads at 1500 rpm. They showed that the air/fuel ratio is effective in engine parameters.

The aim of this study was to improve exhaust emissions by adding acetylene gas to gasoline by mass. In the study, it was preferred to add 5-10% of acetylene gas into gasoline by mass, at ratios where smooth operation can be ensured without any changes on the engine. The effect of acetylene gas addition into gasoline on exhaust emissions was thus investigated. In the study, experiments were carried out at different engine speeds (1600 rpm, 2400rpm and 3200 rpm) and at different engine loads (20%, 40%, 60%, 80% and 100% (full load)).

2. Material and Method

Engine experiments were conducted at low (1600 rpm), medium (2400 rpm) and high engine (3200 rpm) engine speeds. For this purpose, the engine was primarily operated with 100% gasoline. For engine experiments,

fuel consumption and exhaust emission values were recorded by loading at 20%, 60%, 80% and 100% engine loads at the full throttle position of the engine operated with 100% gasoline at each engine speed. After these preliminary studies, hourly fuel consumption values of the engine were calculated. Based on these calculated values, 5% (5% acetylene+95% gasoline) and 10% (10% acetylene+90% gasoline) were added to the intake manifold by mass. The mixtures used in the experiments are expressed as 5% Act and 10% Act in the graphs. In all these stages, the engine was expected to become stable and the emission values of the pilot fuel-powered engine and fuel consumption values were measured again and the values were recorded. With the addition of acetylene gas, the rising engine speed has been reduced to the desired state with the reduction of gasoline fuel. Acetylene gas was added with kg/h value over flow meter. The hourly rate of the gas, which will be added over the amount of liquid fuel flow calculated at this stage, is adjusted via a sensitive flow sensor and given to the intake manifold. All experiments were repeated three times and the averages of the data were taken.

In the experiment, an electric dynamo-meter that was capable of measuring up to 5000 rpm and absorbing 80 kW of power was used. During the engine experiments, acetylene gas was provided from a RAL 1018-type tube that was compatible with TSE 11169 standards. Acetylene gas initially got out of the manometer on the tube and then passed through a wet type Flash back arrestor. The acetylene gas that passed through a spherical precision valve and then through a safety valve was finally sent to the intake manifold from a hole opening into the intake passage of the carburetor by passing through the check valve. As in other studies on this issue [22-24, 33] the gas was mixed with the intake air of the fuel to be taken into the cylinder.

The MRU Delta 1600L exhaust gas analyzer was used to measure exhaust gas components (CO, CO₂, HC, NO_x and O₂). A schematic view of the experimental setup is given in Figure 1. The sensitivity and properties of the tools used in the experiment are given in Table 2. Properties of the test engine are shown in Table 3.

In the graphs, 5% Act refers to the gas addition of 5% (i.e. 95% gasoline + 5% acetylene gas) and 10% Act refers to the gas addition of 10% (i.e. 90% gasoline + 10% acetylene gas).

3. Results and Discussion

The data yielded by means of the engine experiments are presented in graphs and the results are discussed in this section. Here, the emission values obtained in tests at (a) low, (b) medium and (c) high engine speeds are shown.

Table 2. Measurement sensitivity of the tools used in the experimental setup.

Measurement	Accuracy
Load (N)	±%0.6
Load arm (m)	±%0.1
Velocity (rpm)	±1
Time (s)	±%1
Temperature (°C)	±1
CO (% vol)	±0.01
CO ₂ (% vol)	±0.01
O ₂ (% vol)	±0.1
NO _x (ppm)	±1
HC (ppm)	±1

Table 3. Properties of the test engine

Engine	Honda
Number of cylinders Type	1 4 stroke, air cooled,
Bore x Stroke	70 x 55
Fuel system	Carburetor
Compression ratio	8:1
Maximum Force	1.937 kW (2600 rpm)

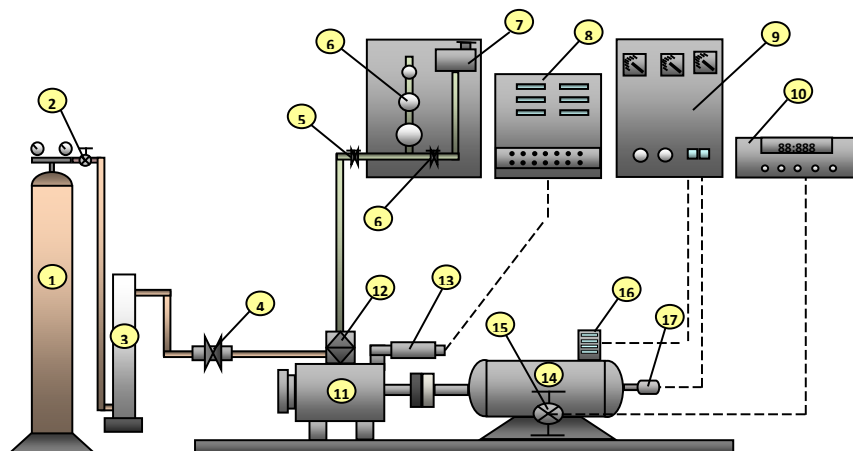


Figure 1. Schematic view of the experimental setup

1. Acetylene gas tube, 2. Acetylene gas valve, 3. Flame trap, 4. Flow meter, 5. Gasoline fuel valve, 6. Fuel measurement apparatus,
7. Gasoline tank, 8. Exhaust gas analyzer, 9. Dynamometer control panel, 10. Force displayer, 11. Gasoline engine, 12. Carburetor,
13. Exhaust pipe, 14. Dynamometer, 15. Load-Cell Sensor, 16. Dynamometer cooler, 17. Encoder

Figure 2 presents the effect of the addition of acetylene gas to gasoline by mass on exhaust gas temperature. Exhaust gas temperature is a function of the combustion inside the cylinder. As the exhaust temperature is an indicator of combustion inside the cylinder, it is also described as an important parameter that indicate combustion in internal combustion engines [29]. In general, the increase in the amount of fuel inside the cylinder would increase the temperature of the exhaust gas, which is reported in many studies [34]. By boosting the throttle opening in gasoline engines, the vacuum inside the cylinder increases and more air/fuel mixture (A/F) is taken into the cylinder. This also varies based on the engine load and revolutions, and the increase of the load and revolutions varies depending on the position of the throttle.

As is seen in Figure 2, the exhaust gas temperature went up with the engine speed and load. Furthermore, the exhaust gas temperature increased depending on the increasing acetylene addition rate to the gasoline. The exhaust gas temperature has reached its maximum value at full engine load for each fuel. Gasoline exhaust gas temperature for different engine speeds of 1600 rpm, 2400 rpm and 3200 rpm it is 287°C, 298°C and 330°C, respectively at full engine load. For 5% acetylene addition 290°C, 310°C and 333°C, for 10% acetylene addition 297°C, 324°C and 337°C, respectively at full engine load. When compared to baseline gasoline operation, the maximum increase in exhaust gas temperature was obtained as 8.7% with 10% acetylene additive at 2400 rpm engine speed and full engine load. This seems to be due to the higher flame temperature of acetylene gas compared to that of gasoline. As is shown in Table 2, the flame temperature of acetylene gas is higher than that of gasoline. The flame temperature can be seen as a value that can partly increase the exhaust gas temperature by changing the combustion temperature. However, there are also studies made with gas fuels that indicate that there is not enough time for the gases to burn after taking them into the cylinder and that some of the combustion continues in the exhaust. Therefore, it is thought that the increase in exhaust gas temperatures may be due to this situation. In accordance with the referee's recommendation, a text such as the following is added to the appropriate place in the article [31]. Similar results have been obtained in previous studies [35].

In internal combustion engines, nitrogen in the air form nitrogen oxides at high temperatures. Nitrogen oxides (NOx) are particularly unwanted groups of gas in internal combustion engines.

Formation of NOx emissions depends on three main factors; combustion temperature, oxygen concentration and high temperature exposure time of nitrogen [36-39]. Maximum NOx emission occurs at 1600-1800°C, but starts to decrease at higher temperatures. In general, the maximum NOx concentration occurs in slightly poorer

mixtures ($\lambda=1.05-1.1$) in terms of stoichiometric conditions [2018, 2020]. The effect of acetylene gas addition to gasoline on NOx emissions is shown in Figure 3.

As seen in Figure 3 the NOx emissions went up with the engine speed and load similar to exhaust gas temperature. Besides, NOx emissions increased with addition of acetylene gas for all engine speeds and loads. NOx emission has reached its maximum value at full engine load for each fuel. NOx emission, at full engine load and engine speeds of 1600 rpm, 2400 rpm and 3200 rpm is 112.2 ppm, 278.7 ppm and 369.5 ppm for gasoline, 131.9 ppm, 298,5 ppm and 379,1 ppm for 5% acetylene addition, 151.1 ppm, 319.6 ppm and 401.5 ppm for 10% acetylene addition, respectively.

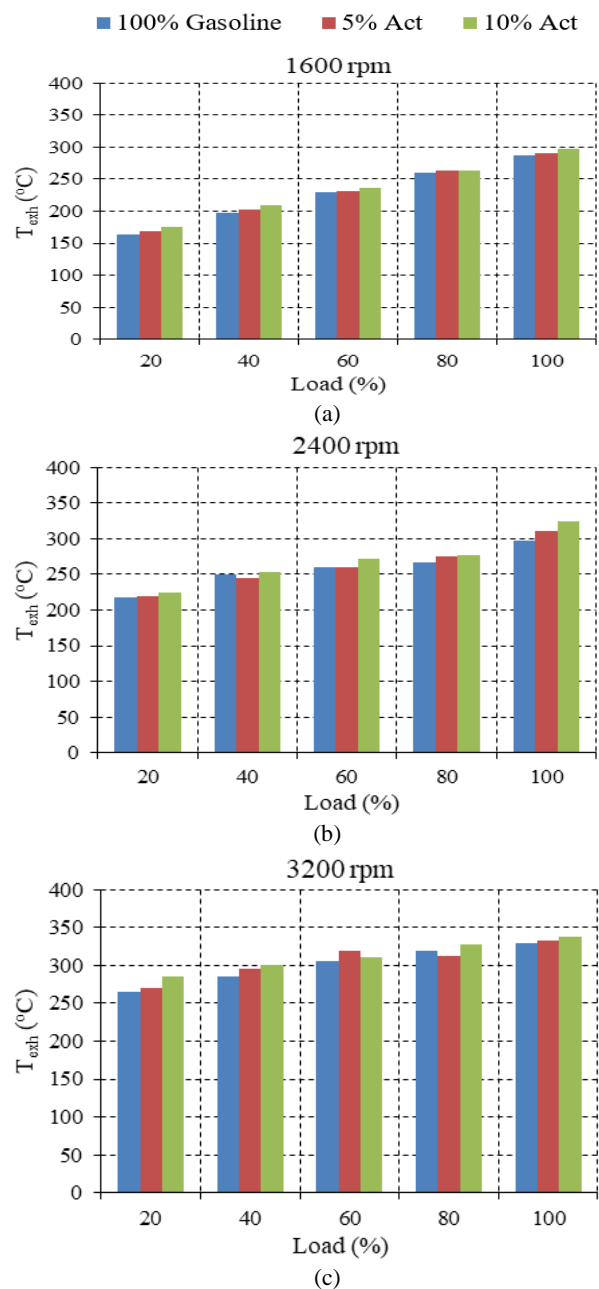


Figure 2. The effect of the mixture of gasoline-acetylene gas on exhaust gas temperature

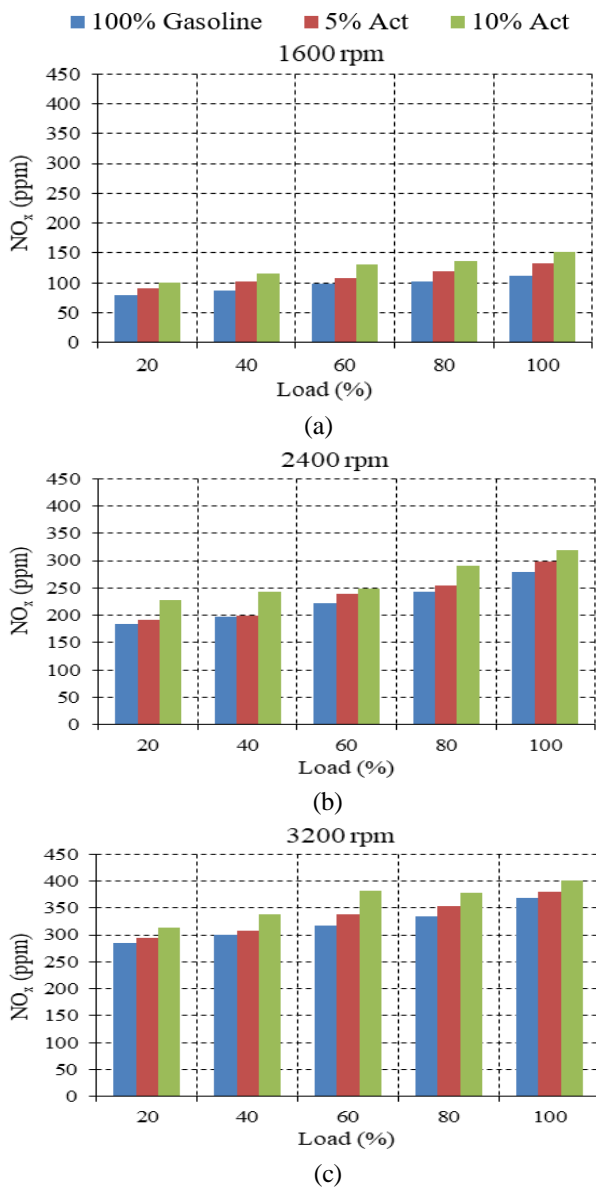


Figure 3. The effect of gasoline-acetylene gas fuel mixture on nitrogen oxide emissions

When compared to baseline gasoline operation, the maximum increase in NO_x emission was obtained as 34.6% with 10% acetylene addition at 1600 rpm engine speed and full load. Considering exhaust gas temperature in the interpretation of NO_x emissions would make the interpretation easier. The increase in exhaust gas temperature indirectly leads to an increase in NO_x emissions. Another factor in the increase of NO_x emissions is that acetylene gas, which is delivered to the intake air, creates a partially poor fuel mixture in the cylinder. Acetylene gas sent into the air creates a poor mixture in the cylinder and may lead to an increase in NO_x emissions. When the exhaust gas temperature is examined, it is observed that it increases with acetylene gas. NO_x emissions increase the upward trend with increased in-cylinder temperature. Therefore, NO_x emissions are thought to be increasing. Furthermore, the high flame temperature of acetylene gas is also considered to be an

important parameter in the increase of NO_x emissions. The increase in NO_x emissions by acetylene addition is similar to the studies in the literature [35].

The ratio of the actual amount of air involved in the combustion to the amount of air theoretically required to combust that fuel is called the air supply coefficient. If the actual amount of air involved in the combustion is equivalent to the amount of air theoretically required, this is called a stoichiometric mixture [40]. Table 2 shows that acetylene gas forms a richer mixture than gasoline. The effect of the addition of acetylene gas to gasoline on air supply coefficient is presented in Figure 4.

As seen in Figure 4, in general, a reduction in the air surplus coefficient with increasing engine speed and load has occurred. The reduction in the air surplus coefficient is due to an increase in the amount of fuel delivered to the cylinder parallel to the increased engine load [41, 42]. In addition to, as the ratio of acetylene gas added to gasoline increased, air supply coefficient decreased for each engine speed and load. Air supply coefficient has reached its minimum value at full engine load for each fuel. When compared to baseline gasoline operation, the maximum reduction in air supply coefficient was obtained as 15.7% with 10% acetylene addition at engine speed of 1600 rpm and full engine load. The stoichiometric ratio of acetylene gas can be regarded as one of the main reasons for this finding. Acetylene gas burns with less air compared to gasoline. Therefore, the mixture is enriched with the addition of acetylene gas in all fuel mixture ratios.

Figure 5 shows the effect of adding acetylene gas to gasoline on oxygen (O₂) emissions. O₂ emissions decreased with increasing engine speed and then showed a tendency to increase again, for each fuel. Besides, a decrease in O₂ emissions was observed with the addition of acetylene gas to gasoline. This decrease was in parallel to the ratio of acetylene gas. As is shown in Table 2, the amount of air required for the combustion of acetylene gas is less than the case for gasoline. Thus, the F/A mixture is enriched by adding acetylene gas to gasoline. In the enriched F/A mixture, O₂ emissions are reduced. As is seen in Figure 4, as the engine load increased, the air supply coefficient value decreased and thus, as is shown in Figure 5, O₂ emissions also decreased. As seen in Figure 5, when compared to baseline gasoline operation, the lowest O₂ emission value was obtained at an engine speed of 2400 rpm with 5% acetylene addition and 60% engine load. Except for 40% and 60% engine loads in engine speed of 2400 rpm, generally, the maximum reduction in O₂ emissions was obtained with 10% acetylene addition for all engine speeds and loads.

Hydrocarbon (HC) emissions in the exhaust gases indicate that some part of the fuel is expelled out without burning. HCs are generally stinky and have an irritating and narcotic effect on the inner skin of the respiratory tract [40].

Two factors come to the forefront, considering the ways in which HC emissions in the engine occur. These are the insufficiency of O₂ atoms present in the cylinder and the inability to provide the sufficient heat to combust the whole fuel [43-45]. The effect of adding acetylene gas to gasoline on HC emissions is shown in Figure 6.

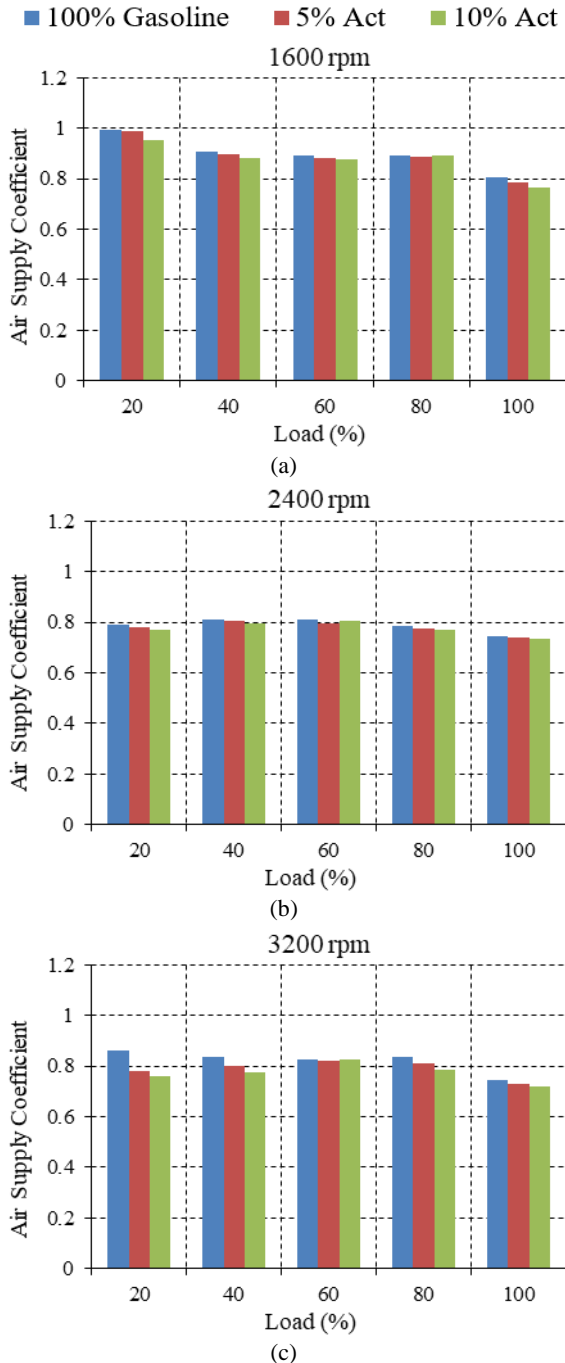


Figure 4. The effect of gasoline-acetylene gas fuel mixture on air supply coefficient

As seen in Figure 6, the HC emission values with the acetylene additive were generally lower than the gasoline at all engine speed and loads. According to working with gasoline, with the addition of acetylene gas, the maximum reduction in HC emissions generally was obtained with a 10% acetylene addition for each engine speed. When compared to baseline gasoline operation, the maximum

reduction in HC emissions, for an engine speed of 1600 rpm was obtained as 15.7% at full engine load. For 2400 rpm and 3200 rpm engine speeds at 80% engine load were obtained as 18.9% and 32.6% respectively. The reason for the decrease in HC emissions by adding acetylene gas to gasoline can be shown as more homogeneous mixture and high burning speed of acetylene [32, 33]. Similar results have been obtained in previous studies [46].

The effect of adding acetylene gas to gasoline on carbon monoxide (CO) emissions is given in Figure 7. CO emissions are due to incomplete combustion of fuel and this is largely due to air fuel ratio [27].

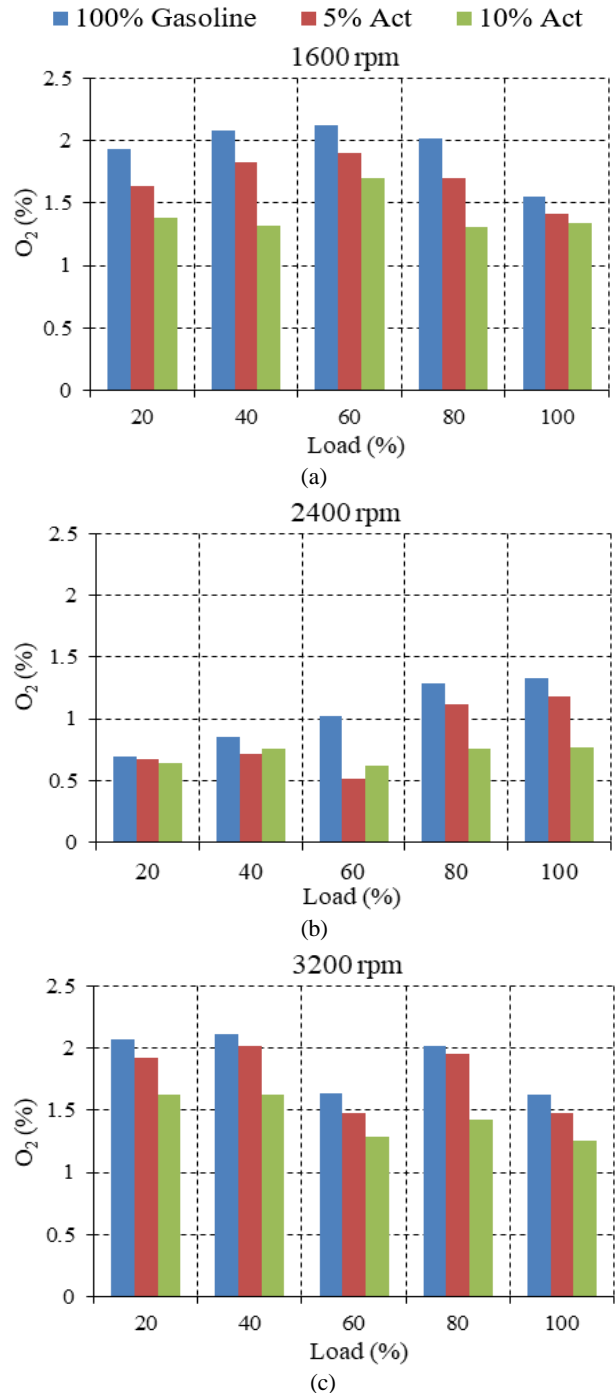


Figure 5. The effect of gasoline-acetylene gas fuel mixture on oxygen emission

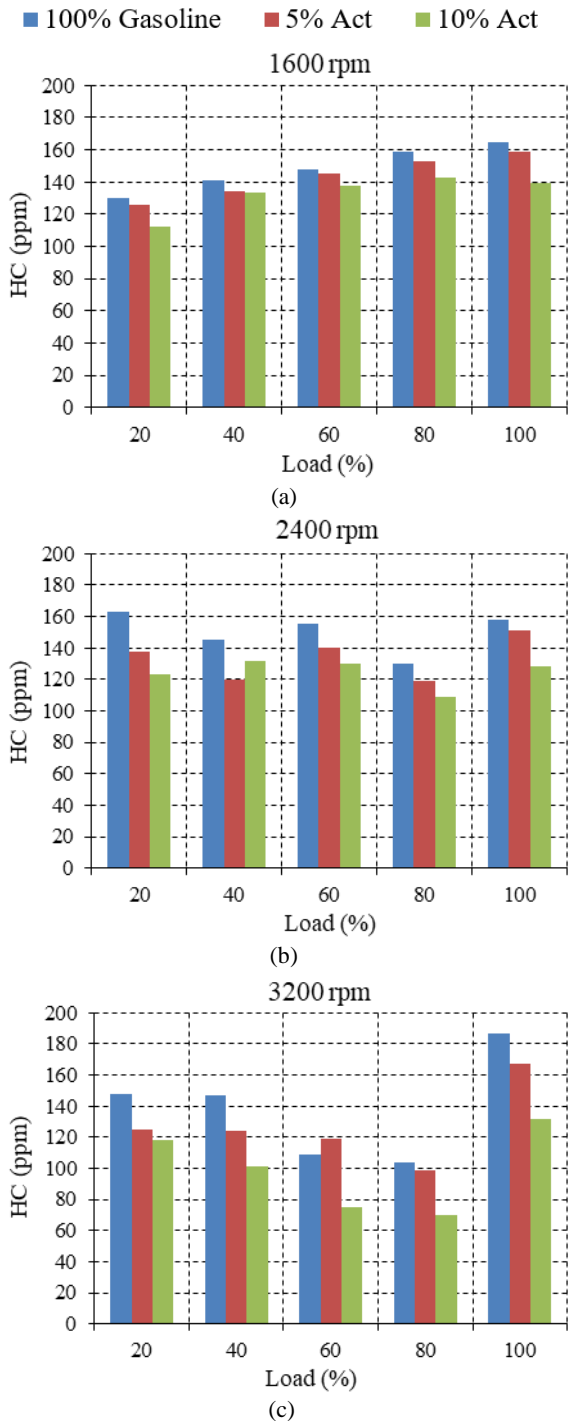


Figure 6. The effect of gasoline-acetylene gas fuel mixture on hydrocarbon emission.

The CO emission is formed by the expulsion of carbon (C) atoms as partially burned by not being able to react fully with O₂ due to O₂ deficiency in the environment [40]. A rich mixture is created with the addition of acetylene gas to the gasoline, which leads to the presence of more fuel than the air in the cylinder can combust, and thus the formation of a non-combusted fuel front. In this way, CO emissions increase in parallel with the increase in the rate of acetylene gas at different engine speeds and engine loads. As see in Figure 7, the highest increase in CO emissions for

each engine speed and load was obtained with 10% acetylene addition. When compared to baseline gasoline operation, the maximum increase in CO for an engine speed of 1600 rpm was obtained as 16.8% at 20% engine load, for 2400 rpm and 3200 rpm engine speeds were obtained as 9.9% and 14.5% respectively at 40% engine load. The reduction in O₂ by the addition of acetylene gas can be clearly seen in Figure 5. Furthermore, the high combustion rate of the acetylene gas is thought to cause the A/F mixture to burn rapidly without forming a complete mixture, which increases CO emissions.

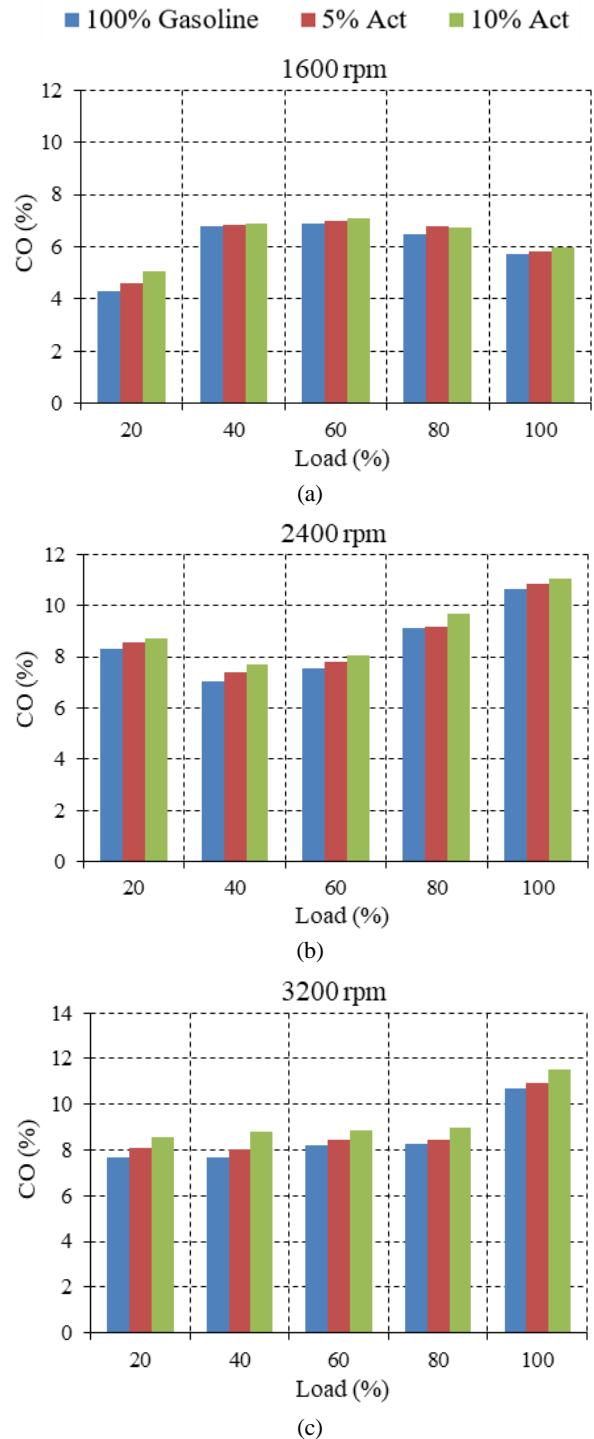


Figure 7. The effect of gasoline-acetylene gas fuel mixture on carbon monoxide emission

Figure 8 shows the effect of the addition of acetylene gas on carbon dioxide (CO₂) emissions. CO₂ emissions are a product of complete combustion. They are formed by the oxidation of C atoms in gasoline and acetylene gas by combining with sufficient O₂ [47]. In addition, the amount of CO₂ emissions in hydrocarbon fuels varies depending on the C/H ratio. As the C/H ratio of acetylene gas is higher than that of gasoline, the CO₂ emission amount is higher than that of gasoline [32]. As is shown in Figure 8, CO₂ emissions increased with the addition of acetylene gas to gasoline and the maximum increase was obtained with a 10% acetylene addition for each engine speed and load.

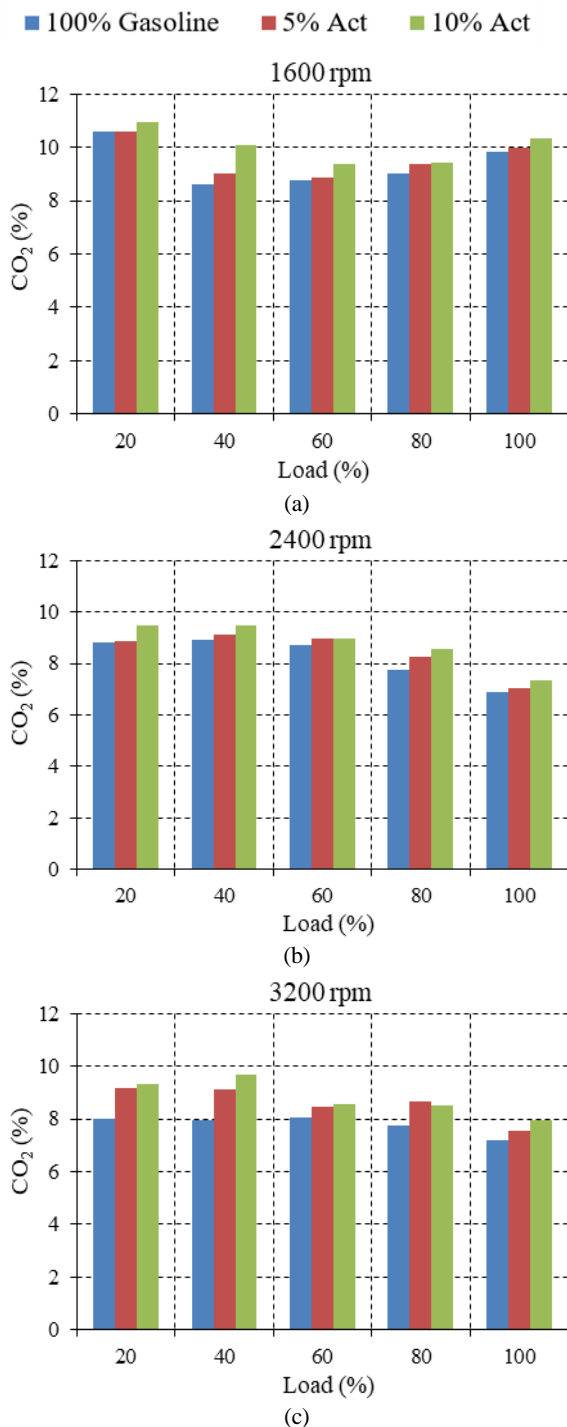


Figure 8. The effect of gasoline-acetylene gas fuel mixture on carbon dioxide emission.

Especially at low engine speeds, there was better combustion compared to high speeds, and accordingly CO₂ emissions were high. When compared to baseline gasoline operation, the maximum increase in CO₂ emissions for an engine speed of 1600 rpm was obtained as 17% at 40% engine load. For an engine speed of 2400 rpm was obtained as 10.8% at 80% engine load and for 3200 rpm engine speed was obtained as 21.3% at 40% engine load. Similar results have been obtained by literature [32].

4. Conclusions

Acetylene gas is an energy resource that can be used as an alternative fuel with its low cost, high thermal value and availability. In present conditions, it cannot be used as fuel in internal combustion engines due to safety problems arising from the storage and transport of acetylene gas. It can be used in welding and cutting processes in heavy industry with its high thermal value. In this study, the effect of the addition of acetylene gas to gasoline in different mass ratios on exhaust emissions was investigated in a single-cylinder gasoline engine. The results can be summarized as in the following;

- Exhaust gas temperature increased with the addition of acetylene gas to gasoline by mass. The maximum increase in exhaust gas temperature was obtained in the addition of 10% acetylene gas at an engine speed of 2400 rpm and full load, compared to the use of baseline gasoline.
- NO_x emissions increased with increasing engine speed and load. Compared to baseline gasoline, the maximum increase in NO_x emissions was achieved as 34.6% at an engine speed of 1600 rpm and at full engine load with the addition of 10% acetylene gas.
- HC emissions decrease with the addition of acetylene gas. The maximum decrease in HC emissions was obtained at an engine speed of 3200 rpm and with 10% acetylene, compared to baseline gasoline fuel operation.
- CO and CO₂ emissions also increased with the addition of acetylene gas. The maximum increase in CO emissions was obtained by adding 10% acetylene at each engine speed (1600, 2400 and 3200 rpm). Compared to baseline gasoline use, the maximum increase in CO emissions was obtained as 16.8% at an engine speed of 1600 rpm and at 20% engine load with the use of 10% acetylene. The maximum increase in CO₂ emissions was obtained by adding 10% acetylene at each engine speed (1600, 2400 and 3200 rpm). Compared to baseline gasoline use, the maximum increase in CO₂ emissions was achieved as 21.33% at an engine speed of 3200 rpm and at 40% engine load with the use of 10% acetylene.
- The addition of acetylene gas to gasoline by mass was found to reduce air supply coefficient. The maximum reduction in air supply coefficient was achieved as 11.6% with 10% acetylene usage at 3200 rpm engine speed and 20% engine load.

• Similarly, O₂ emissions are among those that were reduced by the addition of acetylene gas. The maximum reduction in O₂ emissions, except for 40% and 60% engine loads in engine speed of 2400 rpm, was obtained with 10% acetylene addition for all engine speeds and loads in generally.

According to the results of this study, acetylene gas can be used by mixing in certain proportions to the gasoline without major structural changes in the gasoline engine. It has been observed that acetylene gas can be considered as an alternative fuel that reduces the harm to human and environment health of fossil fuels.

Declaration

The author(s) declared no potential conflicts of interest with respect to the research, authorship, and/or publication of this article. The author(s) also declared that this article is original, was prepared in accordance with international publication and research ethics, and ethical committee permission or any special permission is not required.

References

- Alptekin E. and M. Çanakçı, *Biodiesel and the situation in Turkey*, Engineer and Machinery, 2006. **47**(561): p. 57-64.
- Özel S., Vural, E., M, Binici, *Taguchi method for investigation of the effect of TBC coatings on NiCr bonded diesel engine on exhaust gas emissions*, International Advanced Researches and Engineering, 2020. **04**(01): p. 014-020.
- Batmaz, İ. *Experimental analysis of the effect of hydrogen addition to the fuel on performance and exhaust emissions in spark ignition engines*, J. Fac. Eng. Arch. Gazi Univ., 2007. **22**(1): p.137-147.
- Sayın, C., Çanakçı, M., Kılıçaslan, İ N. Özsezen, *An experimental analysis of influence of using dual fuel (gasoline+LPG) on engine performance and emissions*, J. Fac. Eng. Arch. Gazi Univ., 2005. **20**(4): p. 483-490.
- Sayın, C., Çanakçı, M. İ. Kılıçaslan, *Influence of using gasoline+LPG on the performance and emissions of a gasoline engine*, Erciyes University Journal of Institute of Science and Technology, 2005. **21**(1-2):p.117-127.
- Çalışır, A. and M. Gümüş, *The effect of gasoline-methanol blends on the engine performance and exhaust emission in a spark ignition engine*, 5th International Advanced Technologies Symposium (IATS'09), 13-15 May, Karabük, Turkey, (2009).
- Lakshmanan, T. and G. Nagarajan, *Experimental investigation on dual operation of acetylene in a DI diesel engine*, 2010 Fuel Processing Technology, 2010. **91**(2010): p. 496-503.
- Lakshmanan, T. and G., Nagarajan, *Performance and emission of acetylene-aspirated diesel engine*, *JJMIE*, 2009. **3**(2): p. 125-130.
- Jaikumar, S. and S.K., Bhatti, Srinivas, *Experimental Explorations of Dual Fuel CI Engine Operating with Guizotia abyssinica Methyl Ester-Diesel Blend (B20) and Hydrogen at Different Compression Ratios*, Arabian Journal For Science and Engineering, 2020. **44**(12): p. 10195-10205.
- Meda, V.S. *Optimization of Induction Length and Flow Rates of Acetylene in Diesel Engine*, Ms Thesis, National Enstitute of Technology, Orissa, India, 2011.
- Paizullakhanov, M.S. and S.A Faiziev, *Calcium carbide synthesis using a solar furnace*, Technical Physics Letters, 2006. **32**(3): p. 211-212.
- Poděbradská, J., Maděra, J. and V. Tydlitát, *Determination of moisture content in hydrating cement paste using the calcium carbide method*, *Ceramics-Silikáty*, 2000. **44**(1): pp.35-38.
- Krammart, P. and S. Tangtermsirikul, *Properties of cement made by partially replacing cement raw materials with municipal solid waste ashes and calcium carbide waste*, *Construction and Building Materials*, 2004. **18**: p. 579-583.
- Liu, Z., *National carbon emissions from the industry process: Production of glass, soda ash, ammonia, calcium carbide and alumina*, *Applied Energy*, 2019. **166**(2019): p. 239-244.
- Wang, S. and C.B. Ji, Zhang, *Effect of hydrogen addition on combustion and emissions performance of a spark-ignited ethanol engine at idle and stoichiometric conditions*, *International Journal of Hydrogen Energy*, 2010. **35**(17): p. 9205-9213.
- Miyamoto, T., Hasegawa, H., M., Mikami, *Effect of hydrogen addition to intake gas on combustion and exhaust emission characteristics of a diesel engine*, *International Journal of Hydrogen Energy*, 2011. **36**(20): p.13138-13149.
- Tsujimura, T. and Y., Suzuki, *Development of a large-sized direct injection hydrogen engine for a stationary power generator*, *International Journal of Hydrogen Energy*, 2018. **52**(2018): p.1-15.
- Koten, H., *Hydrogen effects on the diesel engine performance and emissions*, *International Journal of Hydrogen Energy*, 2018. **43**(2018): p.10511-10519.
- Ghazal, O.H., *Combustion analysis of hydrogen-diesel dual fuel engine with water injection technique*, *Case Studies in Thermal Engineering*, 2019. **13**(100380):p.1-10.
- Lakshmanan, T. and G., Nagarajan, *Experimental investigation of port injection of acetylene in DI diesel engine in dual fuel mode*, *Fuel*, 2011. **90**(2011): p.2571-2577.
- Lakshmanan, T. and G., Nagarajan, *Study on using acetylene in dual fuel mode with exhaust gas recirculation*, 2011. *Energy*, **36**(2011):p. 3547-3553.
- Nathan, S., Mallikarjuna, J.M., A., Ramesh, *Effect of charge temperature and exhaust gas re-circulation on combustion and emission characteristics of an acetylene fuelled HCCI engine*, *Fuel*, 2010. **89**(2010): p. 515-521.
- Koşar, M., *Effects of using hydrogen in gasoline engines on performance and emissions*, Ms Thesis, Graduate School of Natural and Applied Sciences, Karabük, Turkey (2007).
- Çelik, M.B. and A., Çolak, *The use of pure ethanol as alternative fuel in a spark ignition engine*, *J. Fac. Eng. Arch. Gazi Univ.*, 2008. **23**(3): p. 619-626.
- Andrea, T., Henshaw, P.F., D.S.K., Ting, *The addition of hydrogen to a gasoline-fuelled SI engine*, *International Journal of Hydrogen Energy*, 2004. **29**(2004): p.1541-1552.
- Lakshmanan, T. and G., Nagarajan, *Experimental investigation of timed manifold injection of acetylene in direct injection diesel engine in dual fuel mode*, *Energy*, 2010. **35**(2010): p.3172-3178.
- İlhan, M.İ., Akansu, S.O., N., Kahraman, *Experimental study on an SI engine fuelled by gasoline/acetylene mixtures*, *Energy*, 2018. **151**(2019): p.707-714.
- Lakshmanan, T., Ahmed, A.K., G., Nagarajan, *Effect of Water Injection in Acetylene-Diesel Dual Fuel DI Diesel Engine*, *Proceedings of the ASME 2012 Internal Combustion*

- Engine Division Fall Technical Conference (ICEF2012)*, September 23-26, Vancouver, Canada.
29. Choudhary, K.D., Nayyar, A., M.S., Dasgupta, *Effect of compression ratio on combustion and emission characteristics of C.I. Engine operated with acetylene in conjunction with diesel fuel*, Fuel, 2018. **214**(2018):p. 489–496.
 30. İlhan, İ.İ., M., Doğan, R., Akansu, S.O., N., Kahraman, *Experimental study on an SI engine fueled by gasoline, ethanol and acetylene at partial loads*, Fuel, 2020. **261**(2020): p.116148.
 31. Roshan, R. and N., Kumara, *The utilization of n-butanol/diesel blends in Acetylene Dual Fuel Engine*, Energy Reports, 2019. **5**(2019):p.1030-1040.
 32. İlhan, İ.İ., M., Doğan, R., Akansu, S.O., N., Kahraman, *An experimental investigation of the use of gasoline-acetylene mixtures at different excess air ratios in an SI engine*, Energy, 2019. **175**(2019):p. 434-444.
 33. Sudheesh, K., and J.M., Mallikarjuna, *Effect of cooling water flow direction on performance of an acetylene fuelled HCCI engine*, *Indian Journal of Engineering & Materials Sciences*, 2010. **17**: p.79-85.
 34. İlkılıç, C., Behçet, R., Aydın, S., H., Aydın, *NOx formation in diesel engines and control methods*, 5th International Advanced Technologies Symposium (IATS'09), 13-15 May, Karabük, Turkey.2009.
 35. Behera, P., Murugan, S., G., Nagarajan, *Dual fuel operation of used transformer oil with acetylene in a DI diesel Engine*, Energy Conversion and Management, 2014. **87**(2014): p.840–847.
 36. Hosseini, S.M., R., Ahmadi, *Performance and emissions characteristics in the combustion of co-fuel diesel-hydrogen in a heavy duty engine*, Applied Energy, 2017. **205**(2017): p. 911-925.
 37. Yılmaz, İ.T., M.,Gümüş, *Investigation of combustion characteristics and exhaust emissions in a dual fuel (hydrogen-diesel) engine*, 8th Transist International Transportation Technology Symposium and Fair, December 17 to 19, 538-547, Istanbul, Turkey. 2017.
 38. Barrios, C.C., Saez, A.D., D., Hormigo, *Influence of hydrogen addition on combustion characteristics and particle number and size distribution emissions of a TDI diesel engine*, Fuel, 2017. **199**(2017): p.162-168.
 39. Kacem, S.H., Jemni, M.A., Z., Driss, *The effect of H₂ enrichment on in-cylinder flow behavior, engine performances and exhaust emissions: Case of LPG-hydrogen engine*, Applied Energy, 2016. **179**(2016): p.961-971.
 40. Ergeneman, M., Mutlu, M., O.A., Kutlar, *Exhaust Pollutants through Vehicles*, Birsen Publishing, Istanbul, p.13-15, (in Turkish). 1998.
 41. Morais, A.M., Justino, M.A.M., O.S., Valente, *Hydrogen impacts on performance and CO₂ emissions from a diesel power generator*, International Journal of Hydrogen Energy, 2013. **38**(2013): p.6857-6864.
 42. Kılıçarslan, A. and M., Qatu, *Exhaust gas analysis of an eight cylinder gasoline engine based on engine speed*, Energy Procedia, 2017. **110**(2017):p.459-464.
 43. Lin, C.Y and R.J., Li, *Engine performance and emission characteristics of marine fish-oil biodiesel produced from the discarded parts of marine fish*, Fuel Processing Technology, 2009. **90**(2009):p.883–888.
 44. Küçükşahin, F., *Diesel Engine*, Birsen Publishing, p.788-790, (in Turkish). 2008.
 45. Heywood, J.B. *Internal Combustion Engine Fundamentals*, McGraw-Hill Publishing Company, p.586-592, New York. 1988.
 46. Brusca, S., Lanzafame, R., A.M.C., Garrano, *On the possibility to run an internal combustion engine on acetylene and alcohol*, Energy Procedia, 2014. **45**(2014): p.889–898.
 47. Özer, S. and E., Vural, *Effects of CNG addition in a diesel engine using diesel/n-heptane, diesel/toluene as pilot fuel*, Gazi Mühendislik Bilimleri Dergisi, 2020. **6**(1): p.1-15.



e-ISSN: 2618-575X

INTERNATIONAL ADVANCED RESEARCHES
and
ENGINEERING JOURNAL

Journal homepage: www.dergipark.org.tr/en/pub/iarejInternational
Open Access Volume 04
Issue 02

August, 2020

Research Article

The investigation of effect of the ceramic coatings with bond-layer coated on piston and valve surface on engine performance of a diesel engine

Erdinç Vural ^{a,*} , **Serkan Özel** ^b 

^aAydin Adnan Menderes University, Aydin, 09000, Turkey

^bBitlis Eren University, Bitlis, 13000, Turkey

ARTICLE INFO*Article history:*

Received 02 March 2020

Revised 08 May 2020

Accepted 04 June 2020

Keywords:

Ceramic coating

Diesel engine

Engine performance

NiCr bond coat

ABSTRACT

The piston and valve surfaces of diesel engine have been coated with Cr_2O_3 , $\text{Cr}_2\text{O}_3+50\%\text{Al}_2\text{O}_3$ and $\text{Cr}_2\text{O}_3 + 75\% \text{Al}_2\text{O}_3$ ceramic powders with bond coat (NiCr) by atmospheric plasma spray (APS) method. The engine performance of the coated engine were compared with the standard engine values by using that the engines tests were applied repeat for each specimen in an electrical dynamometer in full power 1400 rpm, 1700 rpm, 2000 rpm, 2300 rpm, 2600 rpm, 2900 rpm and 3200 rpm engine speeds. In the results; it has been seen that engine power increased from 7% to 29%, engine torque from 7% to 23%, and exhaust gas temperatures from 6% to 17%, thermal brake efficiency from 2.8% to 12.7% while specific fuel consumption decreased of 2.8% to 11.5%.

© 2020, Advanced Researches and Engineering Journal (IAREJ) and the Author(s).

1. Introduction

In the automotive industry, diesel engines are used in the field of agricultural, transportation, shipping and many other fields like these which has made diesel engines become a basic necessity. Basically, businesses set up for profit-making like to benefit from the economic advantages of these diesel engines for being strong and their less usage of fuel to provide customers with a low operating cost. Despite their advantages, diesel engines can have faults most especially with energy transfer. As seen clearly in literature, diesel engines only transfer 40% of the total energy into useful work [1-3]. The internal combustion (IC) engine's energy is exhausted in 3 sections; energy used by the cooling liquid, energy used in attaining useful work and energy loss via the exhaust. Because of this, we can increase the output and general performance of an IC engine by the energy lost and gaining more energy from useful work [4]. In order to reduce thermal losses in the IC engines researchers coat combustion chamber elements with ceramic materials, thereby increasing fuel efficiency and improving engine performance by increasing the useful

work achieved. In his study, Bahattin İşcan measured engine performance and emission values by covering the piston and valve surfaces with ZrO_2 ceramic powder to reduce the thermal losses of an internal combustion single cylinder air cooled diesel engine and by adding waste cotton oil into diesel fuel at different rates. As a result of his experiments, he declared that this reduces brake specific fuel consumption and significantly increases engine power and torque [5]. In another study carried out by Selman Aydın and Cenk Sayin, a thermal barrier was created by covering a combustion chamber with an internal combustion single cylinder air cooled diesel engine with 88% ZrO_2 , 4% MgO and 8% Al_2O_3 materials, and in this engine, they studied engine performance and exhaust emissions using 20 bio-diesel - 80% diesel fuel (B20) and 50% bio-diesel - 50% diesel fuel (B50) mixtures. At the end of the study, it was observed that the engine power in biodiesel fuels did not change with the standard engine, and that the specific fuel consumption decreased, the thermal efficiency increased whereas the exhaust emissions decreased [6]. Kemal Masera and Abul Hossain [7] compiled the study results of the authors who investigated the effects of engine

* Corresponding author. Tel.: +90 256 563 27 20 / 1005; Fax: +90 256 563 27 24
E-mail addresses: erdinc009@hotmail.com (E. Vural), sozel@beu.edu.tr (S. Özel)
ORCID:0000-0002-3398-5593 (E. Vural), 0000-0003-0700-1295 (S. Özel)
DOI: 10.35860/iarej.697009

performance and exhaust emissions using biodiesel in engines with thermal barrier coating in their work. In their study, they reported significant reductions in torque, 4.6% in power output, 7.8% in power output, 15.4% in brake specific energy consumption, 10.7% in brake thermal efficiency and exhaust emission values. Another study carried out by Shailesh Dhomne and Ashish M. Mahalle the properties of various thermal barrier coating (TBC) materials used in IC engines and their effects on engine performance, combustion and emission properties were investigated. At the end of their research, they declared that ZrO_2 , $Al_2O_3+TiO_2$, CeO_2 , TiO_2 etc. materials have a favorable effect on the engine performance and exhaust emission of IC engines, and new materials and specific coating powders that can be formed at different rates can achieve better results [8]. In conclusion of these studies, it is generally seen that ceramic coated materials are an important way to increase the performance of internal combustion engines. However, enough studies have not been carried out on improving engine performances with coatings made with ceramic powders mixed in different proportions.

Per this study, the surface of the combustion chamber elements (piston and valve) of the internal combustion diesel engine was coated with Cr_2O_3 , $Cr_2O_3+50\%Al_2O_3$ and $Cr_2O_3+75\%Al_2O_3$ ceramic powders with NiCr bond coat using the atmospheric plasma spray (APS) coating method. The effects of coated engines on engine performance parameters were investigated by comparing them with the standard engine.

2. Material and Method

2.1 Coating Materials

The coating powders in this experiment are Cr_2O_3 and Al_2O_3 ceramic powders in 20 - 40 μm grain sizes belonging to the standards of Sulzer Metco. These powders are added to Cr_2O_3 with 50% and 75% by weight of Al_2O_3 and mixed homogeneously with a mechanical mixer for 30 minutes at 45 rpm. Using a spraying method, piston and valve surface of an internal combustion diesel engine are coated by the Cr_2O_3 , $Cr_2O_3+50\%Al_2O_3$ and $Cr_2O_3+75\%Al_2O_3$ powders on simple surfacecoated with bond-coat (NiCr). The total coating thickness varies within the range of 0.0025 to 10 mm based on the stress limits of the sprayed material [9, 10]. Schematic image of the APS method is given in Figure 1 and coated pistons and valves are given in Figure 2.

Technical characteristics of single-cylinder diesel engine used in this study are given in Table 1. Diesel engine pistons and valves are made ready for the coating process. In order to keep the standard engines compression ratio constant with the value in the catalogue, sawdust has been removed from the aluminium piston and valve surfaces as much as the coating thickness. At a 200-300 μm thickness, Cr_2O_3 , $Cr_2O_3+50\%Al_2O_3$ and $CrO_3+Al_2O_3$ ceramic powder

(NiCr bond coat) with 3 pistons and valves (intake, exhaust) surfaces have been prepared by coating. The schematic picture of the coated piston is given in Figure3.

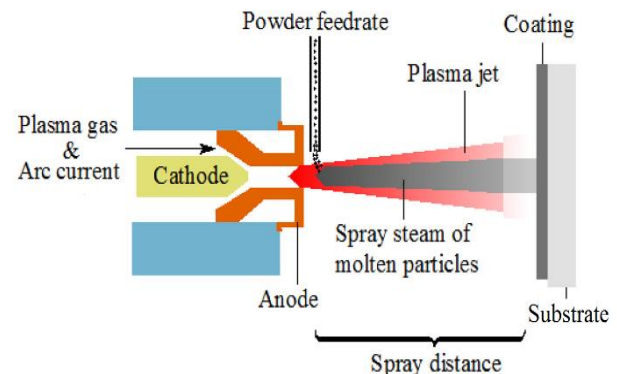


Figure 1. Schematic picture of the atmospheric plasma spray coating method [11]



Figure 2. Pistons and valves coated by APS

Table 1. Technical characteristics of the single cylinder diesel engine used in the experiment [12].

Power	5,5 HP/3600 rpm
Bore*Stroke [mm(in)]	78 x 62 mm
Displacement	296 cc
Operating Method	Starter and Rope
Engine Type	Four Stroke, Single cylinder, Air cooled, Direct injection
Fuel Consumption	285 gr/kWh
Fuel Tank Capacity	3,5 lt
Oil Capacity	1,1 lt
Oil Type	SAE 10W30 - 15W40
Fuel Type	Euro Diesel
Dimension	383×421×450 mm
Weight	38 kg

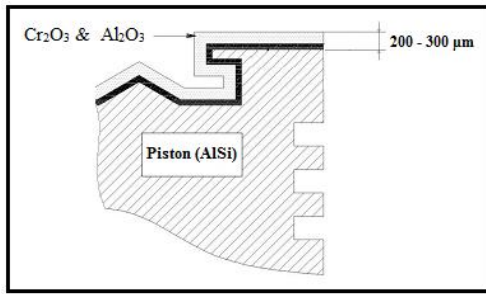


Figure 3. Schematic picture of coated piston

2.2. Engine Performance Tests

In the experiments, Netfren brand, 26 kW Hydrodynamic Dynamometer based on Föttinger Principle was used for performance measurements of the engine. Engine test dynamometer at 26 kW maximum measuring range, braking torque max. 83 Nm., Hydrodynamic Dynamometer based on Föttinger Principle with a weight of 90 kg and working at max. 5000 rpm. The test set can measure the speed, torque, and the power of the internal combustion engines and also the fuel consumption of the engines, and the measured data can be recorded to the computer in real-time. Figure 4 shows a schematic picture of the experiment set.

3. Experimental Results and Discussions

3.1. Microstructure of Coating Layers

Figure 5 demonstrates the SEM picture of the coating surfaces of the coated materials. Piston materials are hardened parts sensitive to temperature. Tribological systems in these parts; It works depending on factors such as contact pressure, contact temperature, lubrication or leanness, wear rate and friction loss. Thermal barrier coatings applied to the engines prevent these surface deformations that may occur, preventing high temperature, pressure and chemical wear (corrosion) taking place during the combustion event by directly touching the main material surface, improve the engine performance by protecting the combustion energy with the high temperatures they create [13]. When the images are examined, it is seen that there is no gap between the coating layers and the backing material and it creates a good coating.

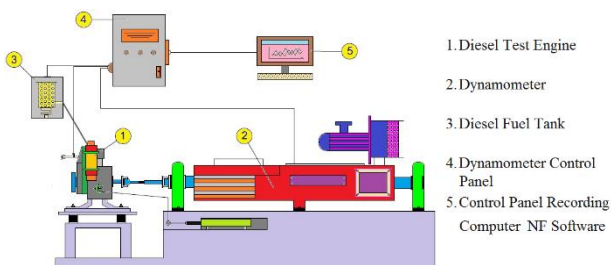
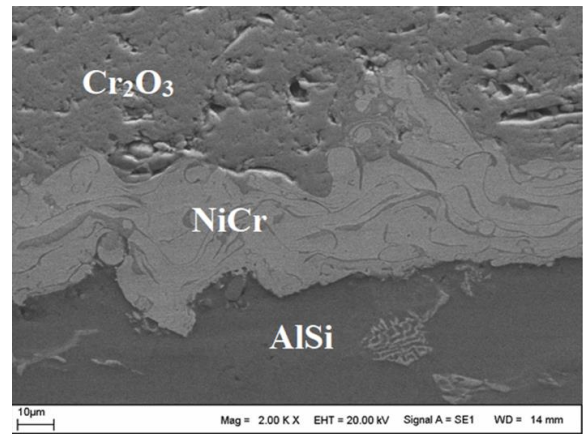
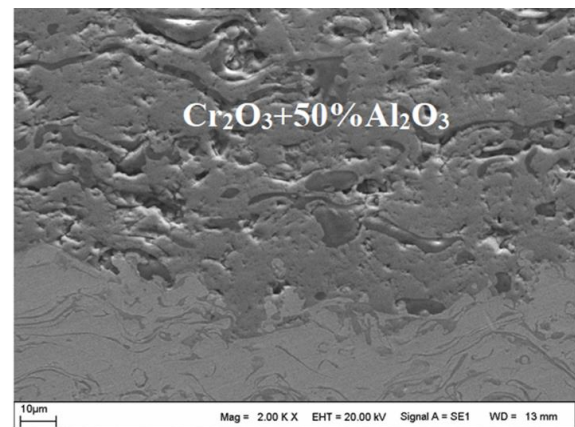


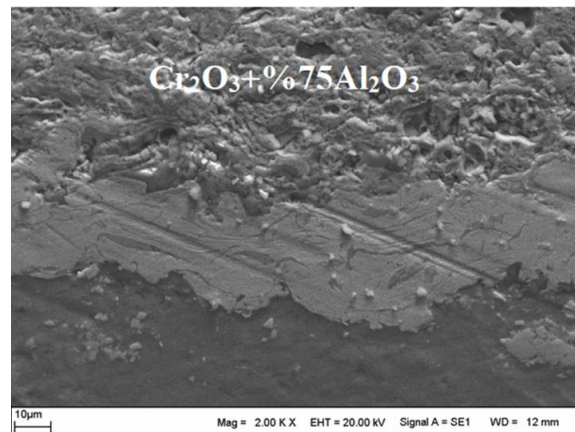
Figure 4. Schematic representation of the engine test equipment



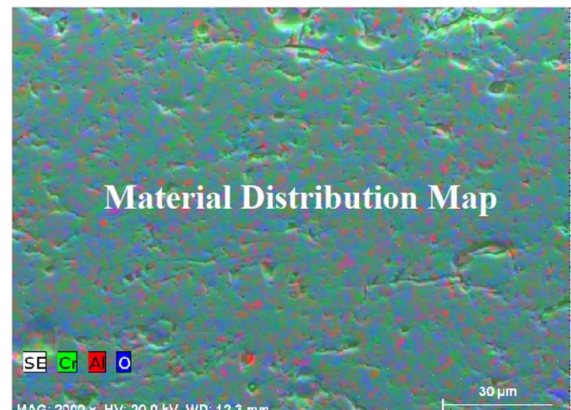
(a)



(b)



(c)



(d)

Figure 5. SEM microstructure of coating layers

3.2. Engine Performance of Coated Engine

The change of engine power according to an engine speed of engines coated with Cr_2O_3 ceramic powders with Al_2O_3 addition is given in Figure 6. The factor that creates the engine power in IC engines is calculated by the useful study obtained as a result of the combustion of the fuel taken into the cylinders, and the useful operation in the cylinders is measured by the average index pressure and the Netfren Brand Dynamometer control software directly calculates this value.

When the graph in Figure 6 is examined, it is seen that the engine power is more in ceramic coatings. As the rate of Al_2O_3 ceramic coating in Cr_2O_3 increases, the increase in engine power is higher than other uncoated engines. Since the fuel that creates the pressure inside the cylinder is caused by the end of combustion temperature and the sudden increase in temperature inside the cylinder, it is thought that the power of Al_2O_3 coated engines increases by creating higher temperatures in the combustion chamber. With the speed increasing, there is a tendency to decrease the power of all engines at 2600 rpm. The reason for this was that with the increase in speed, excessive heat was generated, causing knock and a decrease in engine power. It was stated that the increase in effective power was slowed with the increase in speed, while the increase in speed was effective when the literature sources were examined [14]. When the engines coated with the standard engine are examined during all revolutions, the lowest engine power is seen in the standard engine, while the highest engine power is detected in $\text{Cr}_2\text{O}_3 + 75\% \text{Al}_2\text{O}_3$ coated engine. When compared to the average power at all revolutions with standard engine and coated engines, it was found that there was an increase of 7.18% in Cr_2O_3 coated engine, 21.08% in $\text{Cr}_2\text{O}_3 + 50\% \text{Al}_2\text{O}_3$ coated engine and 29.3% in $\text{Cr}_2\text{O}_3 + 75\% \text{Al}_2\text{O}_3$ coated engine.

The graph giving the change of engine torque according to an engine speed of engines coated with Cr_2O_3 ceramic powders with Al_2O_3 addition is given in Figure 7. Torque is an important measurement criterion for a specific engine's energy, but its size relies on engine dimensions. Much more useful relative engine performance measurement criteria are found by dividing the work by revolutions. The parameter determined in this way is expressed in the unit of force applied to the unit area [15].

Looking at the graph in Figure 7, it is seen that all engines with ceramic coating increase the engine torque compared to the standard engine. As the engine speed in internal combustion rises, a rise in engine torque is seen. This increment passes through the maximum point and causes a decrease again [16]. In Figure 7 also, a decrease is seen after 2600 rpm, friction losses increase with the speed of the beating engine, the engine torque is

decreased after 2600 rpm due to the decrease in the volumetric efficiency as the fuel-air mixture time gets shorter. This is also observed in similar studies [17]. When the engine torque is compared with the standard engine and the thermal barrier coated engines, it has been determined that there is an increase of 7.86% in the Cr_2O_3 coated engine, 13.93% in the $\text{Cr}_2\text{O}_3 + 50\% \text{Al}_2\text{O}_3$ coated engine and 23.13% in the $\text{Cr}_2\text{O}_3 + 75\% \text{Al}_2\text{O}_3$ coated engine.

The graph giving the BSFC change according to the engine speed of the engines coated with Cr_2O_3 ceramic powders with Al_2O_3 addition is given in Figure 8. The amount of fuel that the engine needs to be burned to get one kW of useful work in one hour is called BSFC.

As seen in the graph in Figure 8, the lowest values of BSFC were measured around 2600 rpm. The reason for this situation is that the engines operating temperature is low at low revolutions together with the efficiency of combustion being low. BSFC values decrease with increasing engine combustion efficiency which reaches the ideal operating temperature by approaching medium revolutions.

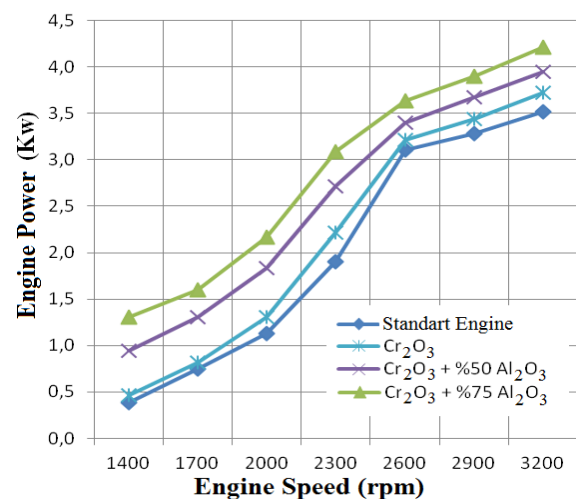


Figure 6. Engine power changes under different speed.

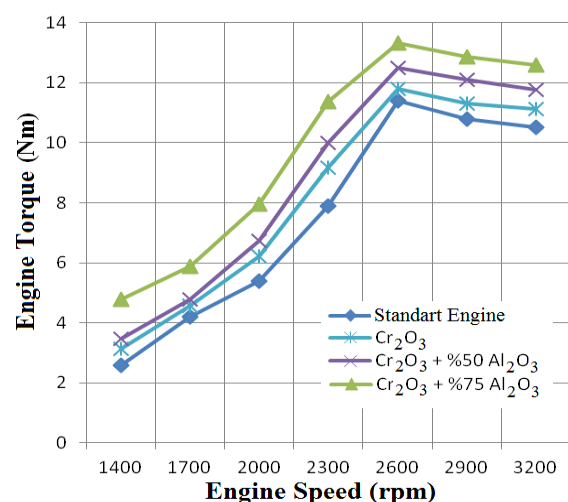


Figure 7. Engine torque changes under different speed

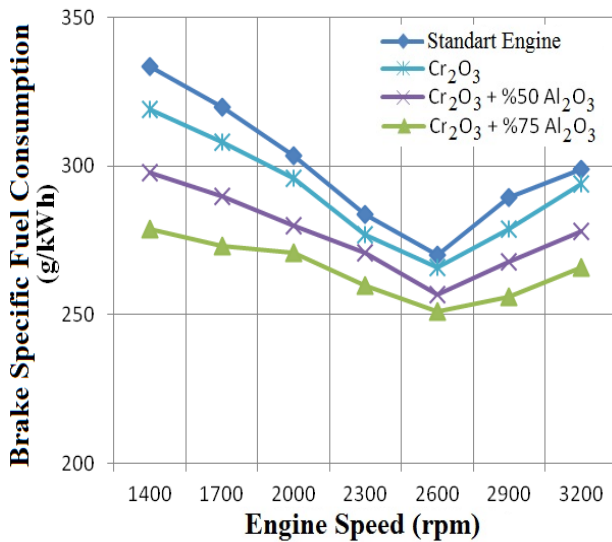


Figure 8. BSFC changes under different speed

Also, the fact that the fuel/air mixture is much closer to the stoichiometric ratio in the engine medium revs is seen as another factor that decreases BSFC values. When high revolutions are attained, the time required for combustion reactions negatively affects combustion and reduces combustion efficiency. Due to the reduced combustion efficiency, the engine needs to transfer more fuel to the combustion chamber to produce the same power and therefore causes an increase in BSFC values. The results of the study are similar to those in the literature [18-20]. When BSFC was compared between standard engine and Thermal barrier coated engines, it was found that there was a decrease of 2.85% in Cr₂O₃ coated engine, 7.47% in Cr₂O₃+50%Al₂O₃ coated engine and 11.57% in Cr₂O₃+75% Al₂O₃ coated engine.

The graph that gives the change of exhaust gas temperature according to the engine speed of the engines coated with Cr₂O₃ ceramic powders with Al₂O₃ addition is given in Figure 9. The exhaust gas temperature can be referred to as the temperatures of the burning fuel in the cylinders, the gases discharged as combustion products at the end of combustion. The exhaust gas temperature is an indicator of the end of the combustion temperature in the cylinder [21].

When the graph in Figure 9 is examined, it is seen that all engines with ceramic coating have higher exhaust gas temperature compared to the standard engine. This is the desired result because it is concluded that there is a thermal barrier coating inside the cylinder with the ceramic coating. Since the thermal conductivity coefficients of Cr₂O₃ and Al₂O₃ materials are lower than the standard combustion chamber of the engine (AlSi), it traps the temperatures in the cylinder, thereby increasing the end of combustion temperatures inside the cylinder [22-26].

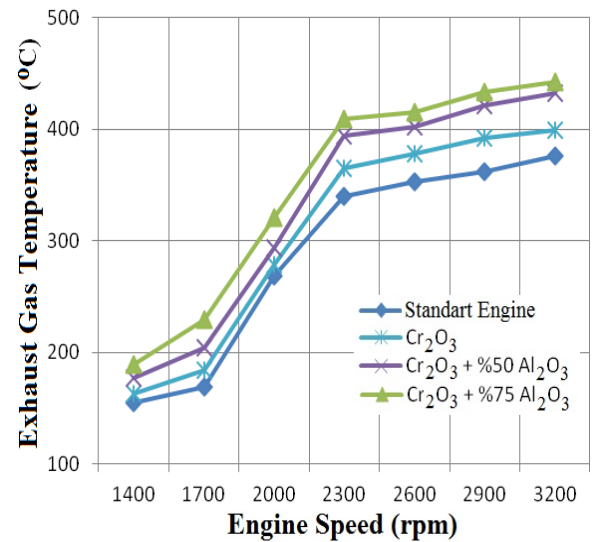


Figure 9. Exhaust gas temperature changes under different speed

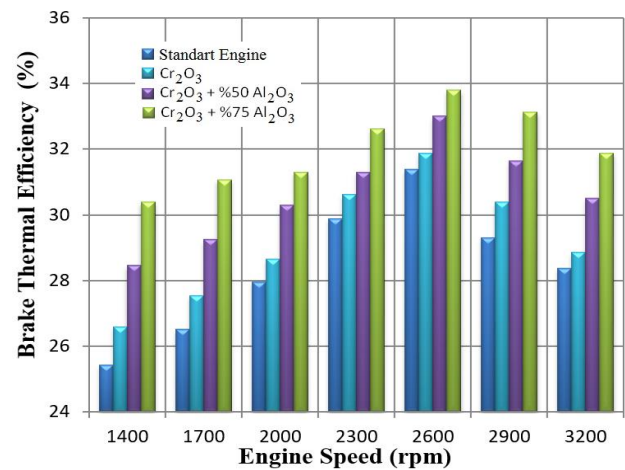


Figure 10. Brake thermal efficiency changes under different speed

When the exhaust gas temperatures were compared between the standard engine and the thermal barrier lined engines, it was found that there was an increase of 6.29% in the Cr₂O₃ coated engine, 12.95% in the Cr₂O₃+50%Al₂O₃ coated engine and 17.02% in the Cr₂O₃+75%Al₂O₃ coated engine.

In Figure 10, the graph shows the change in thermal brake efficiency according to the speed of the engine. Important brake parameters affecting thermal efficiency are ignition delay, a chemical, physical property of fuel and combustion temperature. The TBC coated engines also increase the combustion temperatures due to the temperatures where they lock the combustion chamber [27]. In this case, the thermal brake directly affects efficiency. When the graph is examined, it's been seen that the thermal brake efficiency of the ceramic coated engines rises. Thermal brake efficiency; Compared between the standard engine and thermal barrier coated engines, it was found that there was an increase of 2.84% in Cr₂O₃ coated engine, 7.83% in Cr₂O₃+50%Al₂O₃

coated engine and 12.73% in $\text{Cr}_2\text{O}_3+75\%\text{Al}_2\text{O}_3$ coated engine.

4. Conclusions

In this study, it has been determined that an internal combustion diesel engine piston can be coated with Al_2O_3 added Cr_2O_3 ceramic powders by using an intermediate bond (NiCr) material and these engines can be investigated for performance tests. When the performance results of the coated engines with the standard engine are examined, the following results are obtained.

- The lowest value in engine power was observed in the standard engine during all revolutions and it was found that there was an increase of 1.58% in the Cr_2O_3 coated engine, 9.41% in the $\text{Cr}_2\text{O}_3+50\%\text{Al}_2\text{O}_3$ coated engine and 21.38% in the $\text{Cr}_2\text{O}_3 + 75\% \text{Al}_2\text{O}_3$ coated engine.
- The least value was observed in the standard engine during all revolutions of the engine torque and it was found that there was an increase of 1.51% in the Cr_2O_3 coated engine, 9.40% in the $\text{Cr}_2\text{O}_3+50\%\text{Al}_2\text{O}_3$ coated engine and 21.36% in the $\text{Cr}_2\text{O}_3+75\%\text{Al}_2\text{O}_3$ coated engine.
- The highest value was observed in the standard engine during all cycles in brake specific fuel consumption, it was determined that there was a 4.9% decrease in Cr_2O_3 coated engine, 7.75% in $\text{Cr}_2\text{O}_3+50\%\text{Al}_2\text{O}_3$ coated engine and 9.39% in $\text{Cr}_2\text{O}_3+75\%\text{Al}_2\text{O}_3$ coated engine.
- The lowest value of exhaust gas temperature was observed in the standard engine during all cycles and an increase of 2.17% in Cr_2O_3 coated engine, 6.62% in $\text{Cr}_2\text{O}_3+50\%\text{Al}_2\text{O}_3$ coated engine and 10.018% in $\text{Cr}_2\text{O}_3+75\%\text{Al}_2\text{O}_3$ coated engine was detected.
- The least value in brake thermal efficiency was observed in the standard engine during all revolutions and it was found that there was an increase of 1.58% in the Cr_2O_3 coated engine, 9.41% in the $\text{Cr}_2\text{O}_3+50\%\text{Al}_2\text{O}_3$ coated engine and 21.38% in the $\text{Cr}_2\text{O}_3+75\%\text{Al}_2\text{O}_3$ coated engine.

In general, all engines with Al_2O_3 addition Cr_2O_3 coating give better results in terms of performance compared to the standard engine. To improve this study, performance researches can be conducted on internal combustion engines by using more specific advanced technological ceramic materials.

Declaration

The author(s) declared no potential conflicts of interest with respect to the research, authorship, and/or publication of this article. The author(s) also declared that this article is original, was prepared in accordance with international publication and research ethics, and ethical committee permission or any special permission is not required.

Acknowledgment

I would like to express my gratitude to this noble institution, Bitlis Eren University Scientific Research Project Unit within the scope of No: BEBAP-2014.15 project for its gross support. Moreover, part of this study was presented at the "IATENS2019 Conference", Seydisehir / Konya, Turkey.

References

1. Abbas S.M.,A. Elayaperumal, *Experimental investigation on the effect of ceramic coating on engine performance and emission characteristics for cleaner production*, Journal of Cleaner Production, 2019. **214**: p. 506-513.
2. Oguz H.,H.Ogut, F.Aydin, M.Ciniviz, T.Eryilmaz, *Investigation of engine performance and kit design for the usage of safflower oil as in diesel engine*, Renewable Energy, 2019. **143**: p. 692-702.
3. Aydin, M.,A. Irgin &M. Celik,*The Impact of Diesel/LPG Dual Fuel on Performance and Emissions in a Single Cylinder Diesel Generator*, Applied Sciences, 2018. **8**(5): p. 825.
4. Gehlot R. And B.Tripathi, *Thermal analysis of holes created on ceramic coating for diesel engine piston*, Case Studies in Thermal Engineering, 2016. **8**: p. 291-299.
5. Iscan B.,*Application of ceramic coating for improving the usage of cottonseed oil in a diesel engine*, Journal of the Energy Institute, 2016. **89**(1): p. 150-157.
6. Aydin S. and C. Sayin, *Impact of thermal barrier coating application on the combustion, performance and emissions of a diesel engine fueled with waste cooking oil biodiesel–diesel blends*, Fuel, 2014. **136**: p. 334-340.
7. Masera K. And A.K.Hossain, *Biofuels and thermal barrier: A review on compression ignition engine performance, combustion and exhaust gas emission*, Journal of the Energy Institute, 2019. **92**(3): p. 783-801.
8. Dhomne S. and A.M.Mahalle, *Thermal barrier coating materials for SI engine*, Journal of Materials Research and Technology, 2019. **8**(1): p. 1532-1537.
9. Phillips B.A. and J. K. Knapp, *Thermal spray coatings reduce wear and corrosion on calender rolls*, Tappi Journal, 1995. **78**(10): p. 197-205.
10. Ramaswamy P., S. Seetharamu, K.B.R. Varma, K.J. Rao, *Thermomechanical fatigue characterization of zirconium ($8\%\text{Y}_2\text{O}_3 - \text{ZrO}_2$) and mullite thermal barrier coatings on diesel engine components: effect of coatings on diesel engine performance*, Proceedings of the institution of mechanical Engineers, Part C., 2000. **214**(5): 729-742.
11. Zhang Z.,S.H.Lim, J.Chai, D.M.Y.Lai, A.K.H.Cheong, K.L.Cheong,S.J.Wang, H.Jin, J.S.Pan, *Plasma spray of Ti_2AlC MAX phase powders: Effects of process parameters on coatings' properties*, Surface and Coatings Technology, 2017. **325**: p. 429-436.
12. Access, <http://www.makinaodasi.com/kama-dizel-motor-km178fe>, date: 01.06.2020
13. Vural E.,*The Investigation of Effect on Engine Performance and Exhaust Emissions of Ceramic Coatings*

- Applied to Single Cylinder Diesel Engine, in Manufacturing Engineering* 2014, Karabuk University:Turkey.p. 157.
14. Vural E. And S. Ozel, *The Effect of Al₂O₃ Added Cr₂O₃ Thermal Barrier Coatings on Exhaust Emissions at a Diesel Engine*, Journal of Sciences BEU, 2019.**8**(1): p. 308-318.
 15. Cetinkaya S., *Motor Vehicle Mechanics*. 2011, Turkey: Nobel Publishing.
 16. Gurbuz H.,*An experimental study on the effects of the thermal barrier plating over diesel engine performance and emissions*, in *Mechanical Engineering* 2011, Karabuk University:Turkey. p. 42.
 17. Safgonul B.,H.E. Arslan, M. Ergeneman, C. Sorusbay, *Internal combustion engines*. 1995, Turkey: Birsen Publishing.
 18. Jena P.S., K.S. Acharya, H.C. Das, P.P. Patnaik, S. Bajpai, *Investigation of the effect of FeCl₃ on combustion and emission of diesel engine with thermal barrier coating*, Sustainable Environment Research, 2018. **28**(2): p. 72-78.
 19. Abbas S.M.,A. Elayaperumal, *Experimental investigation on the effect of ceramic coating on engine performance and emission characteristics for cleaner production*, Journal of Cleaner Production, 2019. **214**: p. 506-513.
 20. Venkadesan G.,J. Muthusamy, *Experimental investigation of Al₂O₃/8YSZ and CeO₂/8YSZ plasma sprayed thermal barrier coating on diesel engine*, Ceramics International, 2019. **45**(3): p. 3166-3176.
 21. Parlak A., H. Yasar, B. Sahin, *Performance and exhaust emission characteristics of a lower compression ratio LHR diesel engine*, Energy Conversion and Management, 2003.**44**(1): p. 163-175.
 22. Vural E., S. Ozer, *Thermal Analysis of a Piston Coated with SiC and MgOZrO₂ Thermal Barrier Materials*, International Journal of Scientific and Technological Research, 2015. **1**(7): p. 43-51.
 23. Özel S., *The investigation of coating of oxide and carbide compound on the surface of aluminium alloy and bronze by using plasma spray process* in *Metallurgy Education* 2009, Firat University:Turkey.
 24. Memstnet. [cited 2020 28 February]; Available from: <https://www.memstnet.org/material/chromiumoxidecr2o3b> ulk/.
 25. Vural E., Ozdalyan B. and Ozel S., *Experimental Investigation on Effect of the Zirconium + Magnesium Coating of the Piston and Valve of the Single-Cylinder Diesel Engine to the Engine Performance and Emission*, World Academy of Science, Engineering and Technology International Journal of Mechanical and Mechatronics Engineering, 2016. 10, 12.
 26. Ozel S., Vural E. and Binici M., *Taguchi method for investigation of the effect of TBC coatings on NiCr bond-coated diesel engine on exhaust gas emissions*, International Advanced Researches and Engineering Journal, 2020.**04**(01): 014-020.
 27. Karthikayan S.,S. Ganesan, P. Vasanthakumar, G. Sankaranarayanan, M. Dinakar, *Innovative research trends in the application of thermal barrier metal coating in internal combustion engines*, Materials today: proceedings, 2017. **4**(8): p. 9004-9012.

**Research Article****Layer-by-layer growth of molecular self-assembled monolayers /sputtered gold thin films/graphene oxide on glass substrate****Fatma Bayrakçeken Nişancı**^{a,b,*} ^aAtaturk University, Eastern Anatolia High Technology Application and Research Center, 25240 Erzurum/Turkey^bAtaturk University, Program of Food Technology Narman Vocational Training High School, 25530 Erzurum/Turkey

ARTICLE INFO

Article history:

Received 05 April 2020

Revised 27 April 2020

Accepted 10 May 2020

*Keywords:*Graphene oxide
Heterostructure
Self-Assembly
Sputter deposition

ABSTRACT

In the present study, 1-dodecanethiol self-assembled monolayers (SAMs) on graphene oxide (GO) –Au (Gold) thin films as molecular templates for the selective deposition of multilayer films was performed. Thus, heterostructured GO/Au/DDT and DDT/Au/GO thin film are fabricated by sputtering Au target onto modified GO structure or self-assembled 1-dodecanethiol (DDT) arrays. It has been shown that a new device concept can be made by completing the glass substrate with the surface heterostructures; i.e. layer GO sheet or DDT with Au nanoparticles (Au NPs). In the light of the performed study, the layer-by-layer assembling of DDT on the GO sheet-Au thin films template has been proved for the distinct conjugation. Also, Optical and morphological characterizations are coherent with the instantaneous nucleation and growth model over the modified DDT-Au NPs-GO or GO-Au NPs-DDT thin films in the aspect of surface roughness, the phonon transport, and other multilayer films properties. As a consequence, the multilayer films of DDT-capped Au thin films and GO sheets have shown a better hybrid nanostructure with higher consistency, hierarchy and surface area. In addition, this work will present a new perspective for template preparation based on nanostructured thin films due to its unique properties resulting from nanoscale properties.

© 2020, Advanced Researches and Engineering Journal (IAREJ) and the Author(s).

1. Introduction

In recent years, researchers have focused on layer improving on various surfaces to form a hybrid nanostructured continuous film. Hybrid nanostructures [1] have been paid attention due to their great potential applications in photocatalysis [2], biosensor production [3], magnetic materials [4-9] and super-hydrophobic materials [10]. These functional devices are continuously being developed by using advanced materials, they can be applied to high-tech applications [11]. With the use of SPM- based lithography [12-15] photolithographic techniques [16], molecular resist which is composed of a combination of sputter deposition and patterned monolayers has been used in a number of nanofabrication processes [17].

There are limited number of studies on the modification of graphene oxide (GO) compounds for

pattern fabrication that use Au (Gold) thin films- self assembled monolayers (SAMs) as a resist. The patterned SAMs properties are used as a template for the sputter deposition of Au thin film layers or modification of GO. The inexpensive and simplicity of the present technique can allow to build a reachable implement of coordination of several multilayer films for electro-optical devices. The affecting of selective layer absorption using SAMs as a governing or directing surfaces introduces a new style of control in the formation of multilayers film systems [18]. GO is easily affected by reduction and doping. Thus, its application field has been continuously being developed [19] and it has been used for chemical and biomolecule sensor-based device production due to its p-type behavior in electron transition [20, 21]. In addition to this, Au nanoparticles (AuNPs) show great electrical conductivity, indicate controllability with their size,

* Corresponding author. Tel.: +90 442 231 7001.

E-mail addresses fbayrakceken@atauni.edu.tr (F. Bayrakçeken Nişancı)

ORCID: 0000-0002-3166-2301 (F. Bayrakçeken Nişancı)

DOI: 10.35860/iarej.714811

shape, and surface-volume ratio and they can contain a great variety of ligands [22]. Thus, for decades, AuNPs have been employed for several high-tech applications involving sensors [23-25], optoelectronic devices [26] and drug delivery systems [27, 28].

In this study, self-assembly and sputtering process for layer-by-layer growth of GO, DDT, Au thin films were showed. In order to determine the composition, morphology and the structure, obtained films were examined by scanning electron microscopy (SEM), UV-vis spectroscopy, X-ray photoelectron spectroscopy (XPS) and Raman techniques.

Moreover, the information about nanostructured thin films which exhibits unique properties and could be used for applications in sensors was provided with this work.

2. Materials and Methods

2.1 Experimental

Argon were used as a sputtering gase while Au (99.99 %) was used as the target. The base pressure was $< 3 \times 10^{-4}$ Pa. In the process of deposition, with a sputtering power of 20 W, the substrate was kept at room temperature. After a deposition time between 25 sec-1000 sec, Au thin films with thickness that ranges from 80 to 200 nm were achieved. The experimental conditions were as follows; sputtering time 25 sec-1000 sec and applied voltage 20 W, respectively. GO (aqueous dispersion, 4 mg/mL) was purchased from Sigma Aldrich. 1-Dodecanethiol (DDT) SAMs were prepared by immersion of Au thin film-GO sheet in solutions containing 1 mM DDT ($C_{12}H_{26}-S$) (Fluka, purity $\geq 97\%$) for 24 h. Surface morphological studies of composites were examined and measured by scanning electron microscopy (SEM, Zeiss Sigma 300). WITech alpha 300R spectrometer was used to record Raman spectra of the composites over $4000\sim 200\text{ cm}^{-1}$. X-ray photoelectron spectroscopy (XPS) study was measured in a Specs-Flex XPS. Ultraviolet-visible (UV-Vis) spectroscopy measurements were obtained from a Shimadzu UV-3600 Plus spectrophotometer.

2.2 Results and Discussion

As can be seen in Figure 1, the general experimental strategy used in the present study included the synthesis of thin films that consist of GO sheets and the partial modification of DDT SAMs for producing etch centers with controlled sizes and implementation of sputter deposition of Au into those etch centers. With the sputter coater, the typical sputtering time was varied in the rages of 25 sec-1000 sec. In all samples, the applied voltage was 20 W.

Figure 2a shows SEM micrographs of the Au films deposited on glass substrates as a function of sputtering time (20 W 100 sec sputter deposition). In these diagrams, the surface roughness and uniformly distributed Au grains were observed for the films.

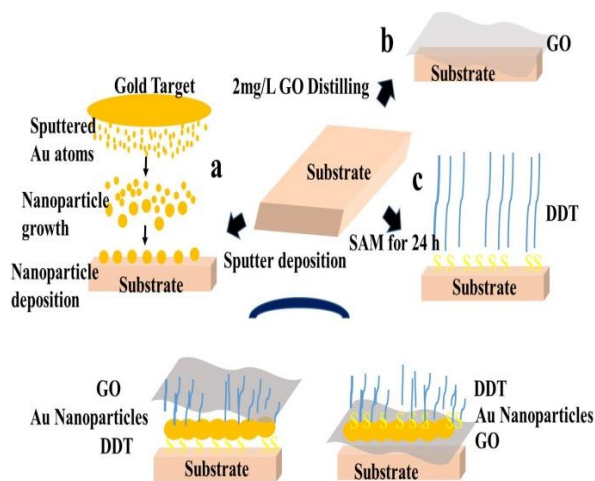


Figure 1. Schematic representation of the experimental strategy for fabricating GO/Au thin film/DDT SAMs heterostructure on substrate

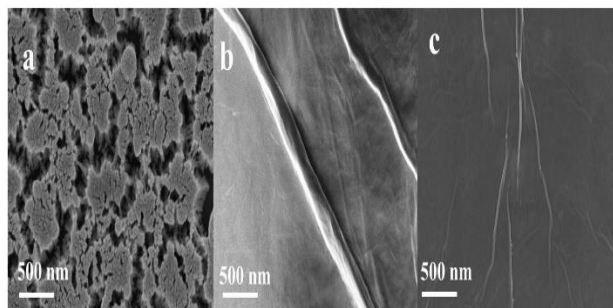


Figure 2. SEM micrographs of (a) 20W 100 sec sputter deposition of Au thin film, (b) 2 mg/mL GO immersion, (c) 20W 100 sec sputter deposition of Au thin film- 2 mg/mL GO immersion on glass substrate.

Also, Figure 2b shows SEM image of the GO absorption layer on a glass substrate and this surface exhibits extended morphology over the larger surface area. The morphologies of 2mg/mL GO modified on 20 W 100 sec sputter deposition of Au thin film structures fabricated by the process in Figure 1 are illustrated in Figure 2c. As shown in Figure 1c, a large surface area is fully covered by GO sheets on Au thin film, showing a good uniformity film. The SEM images of Au deposits obtained after partial defect of DDT SAMs at a constant modified time are shown in Figure 3a. The sputter deposition time was kept as 25 sec. GO which was added for Figure 3b sequential images display that the diameters of disk-shaped Au NP (nanoparticle) deposits with the instantaneous nucleation and growth model. It appears that the Au preferentially grows on etched regions of DDT SAMs. Thus, employing suitable sputtering voltage, it can be possible to control the size and the number Au NP deposits. Figure 3b displays the DDT SAMs-GO- 20 W 25 sec Au NP deposition that could be employed to fabricate compound nanostructures with a combination of the GO patterning and sputter deposition techniques employing using self-assembled monolayer as a resist.

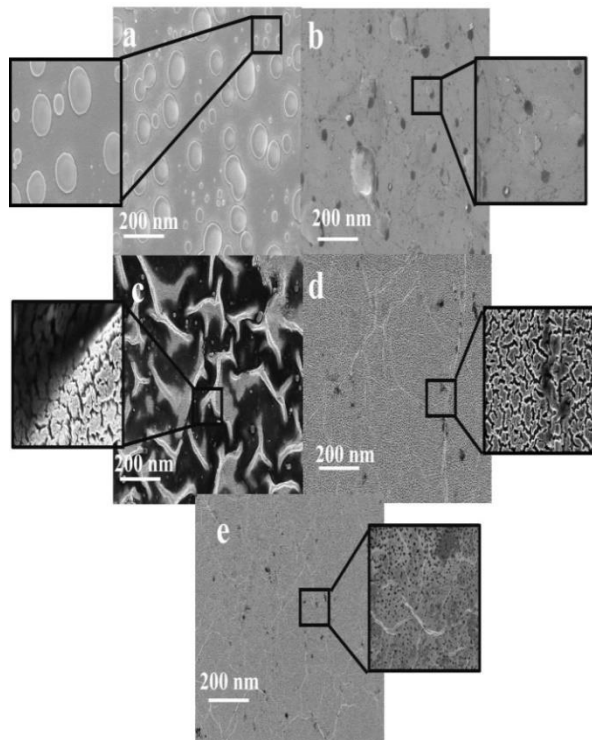


Figure 3. SEM micrographs of (a) DDT SAMs- 20W 25 sec sputter deposition of Au thin film, (b) DDT SAMs - GO-20W 25 sec sputter deposition of Au thin film, (c) 20W 200 sec sputter deposition of Au thin film- DDT SAMs, (d) GO- 20W 200 sec Au-DDT SAMs, (e) GO- 20W 1000 sec sputter deposition of Au thin film - DDT SAMs on substrate.

The effect of sputter deposition time on the structure and the time of Au nanoparticle deposits are shown in Figure 3c without GO. In Figure 3 d-e, SEM images are given as a function of different coating times of gold nanoparticles in GO-AuNP-DDT SAMs layers.

Figure 4 shows representative XPS high-resolution C1s and S2p core-level spectra in DDT SAMs- 20 W 25 sec Au NP and DDT SAMs-GO-Au NP. In especial, looking at the high-resolution XPS spectrum of S2p, it is possible to conclude that the functionalization occurred via S-Au chemical bond because of the presence of the components 157 eV. The 2p peaks were fit using doublet peaks with a 2p_{1/2}/2p_{3/2} ratio of peaks 0.5 and separation of 1,3 eV as described previously. The first component, centered at about 157 eV, is assigned to the bound sulphur; the second one (at about 156 eV) is related to the presence of some unbound sulphur on the surface.

XPS had been applied to confirm the elemental composition and electronic states of DDT SAMs-20 W 25 sec Au thin films and DDT SAMs-GO-20 W 25 sec Au thin films in a wide scan. As displayed in Figure 4a, the DDT SAMs/Au nanostructures showed the elemental composition that appeared at approximately 283.3 eV at C-H, 283.8 eV at C-C and 284.5 eV at C-S which was attributed to the C1s core levels. Further investigations about the high-resolution XPS of the C1s showed three

different components: C=C, C-H was at 283.7 eV, C=C, C-S at 284.5 eV, C-O appeared at 284.9 eV (Figure 4b), respectively.

Figure 5 shows the Raman spectra of DDT SAMs-20 W 25 sec Au NP, DDT SAMs- 20 W 100 sec Au NP-GO, 20 W 1000 sec- DDT SAMs and GO- 20 W 1000 sec- DDT SAMs.

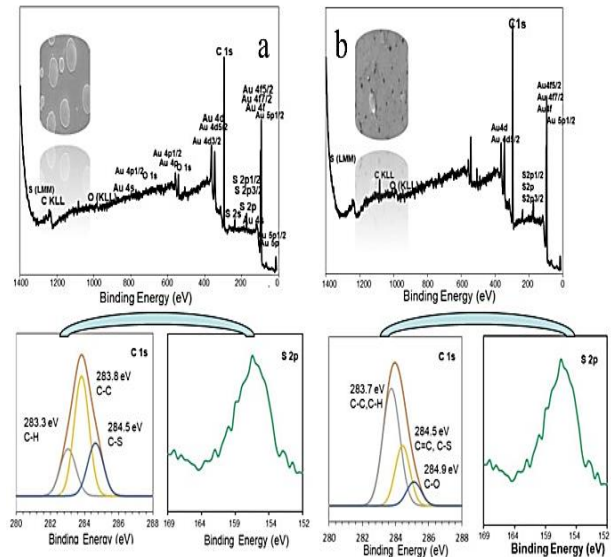


Figure 4. Comparison of the XPS spectra of DDT SAMs-20W 25 sec Au thin films and the DDT SAMs-GO-20W 25 sec Au thin films. The variations of binding energy of C 1s, S 2p, are shown in Figure (a)-(b), respectively. (a) DDT SAMs-20W 25 sec Au thin films; The binding energy for Au 3d (3d_{3/2}, 3d_{5/2}) is (495.3 eV, 486.8 eV), (495.3 eV, 486.9 eV) and (494.9 eV, 486.5 eV) (b) DDT SAMs-GO-20W 25 sec Au thin films; The binding energy for O 1s is 530.7 eV, 530.8 eV and 530.4 eV.

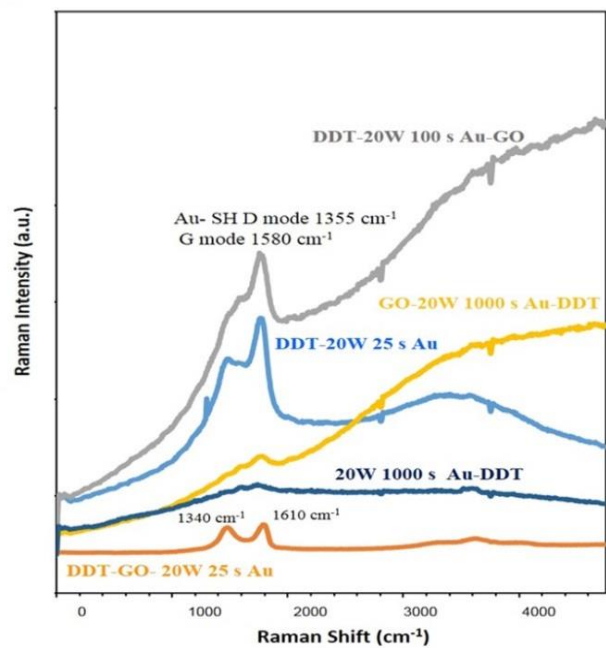


Figure 5. Micro-Raman spectra as measured by planar oriented laser polarization of DDT-GO-20W 25 sec Au, 20W 1000 sec Au-DDT, DDT-20W 25 sec Au, GO-20W 1000 sec Au-DDT, DDT-20W 100 sec Au- GO at room temperature on an glass.

Raman spectrum for the DDT SAMs- 20 W 25 sec Au NP in Figure 5 a shows weak G band at 1597 cm^{-1} and a pronounced D band at 1382 cm^{-1} . The Raman spectra exhibit DDT SAMs-20 W 100 sec Au NP- GO at 1355 cm^{-1} and 1602 cm^{-1} respectively. In the peak S-band with shoulders at 1355 cm^{-1} and 1602 cm^{-1} corresponds to the G band of GO. There is no GO layer on the 20 W 1000 sec Au NP-DDT SAMs surface and therefore, the D and G belonging to the GO are not observed. G band intensity increased at 1605 cm^{-1} due to the addition of GO when 20 W 1000 sec-DDT SAMs surfaces were modified to GO.

UV-visible absorption spectra of DDT SAMs-20W 25 sec Au, DDT SAMs-GO- 20W 25 sec Au, 20W 1000 sec Au—DDT SAMs and GO-20W 1000 sec Au- DDT SAMs multilayer films on glass substrates are shown in Figure 6. An examination of the absorption spectrum at 300 nm spectral windows, which is quite similar to spectra were reported for multilayer films. When GO is added to DDT SAMs – 20W 25 sec Au NP multilayer films, an increase in the absorption spectrum at 300 nm is observed. This is due to the increase in surface areas on the in DDT SAMs-GO-20W 25 sec Au NP multilayer surface formed by the addition of GO. Furthermore, multilayer films produced by increasing Au NP deposition time cause an increase in the absorption spectrum of 300 nm when compared to other samples. When DDT SAMs- 20W 1000 sec Au NP multilayers films are modified on GO films, an increase in the absorption spectrum is observed. At a deposition time of 1000 sec, there was a 27 nm shift in its absorption edge as compared to the desorption time of 25 sec. It also caused differences in UV spectra in changing layers.

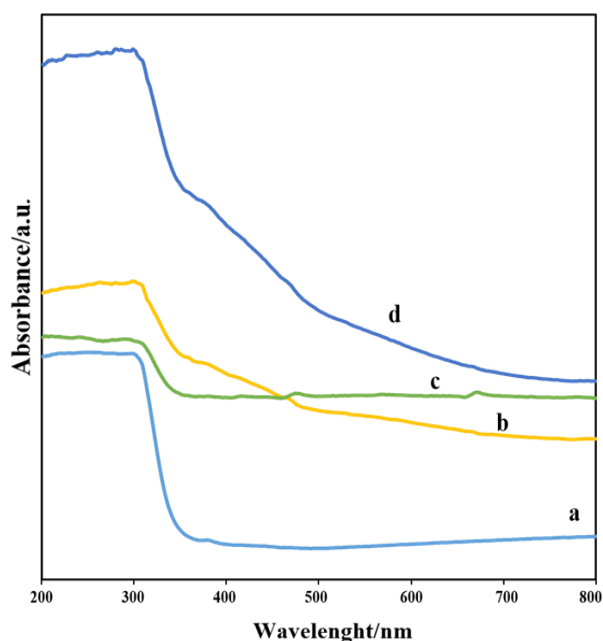


Figure 6. The absorption spectrum of the DDT-20W 25 sec Au (a) DDT-GO-20W 25 sec Au (b) 20W 1000 sec Au- DDT (c) and GO- DDT- 20W 1000 sec Au (d) films on glass

3. Conclusions

Finally, a new method has been figure out to fabricate the nanostructure array by combining the absorption layer of GO sheets and sputter deposition process using DDT SAMs as a resist. In the scope of the resist film, changing array of GO/Au thin film/DDT or DDT/Au thin film/GO, really important and promised nanostructure arrays with different morphological structures were achieved at the end of performed study. Also, the multilayer structures showed different extended morphology over a large surface area. The obtained results show that it is possible for us to propose that nanoporous templates have been used for the fabrication of nanostructured materials with potential applications for devices such as electronic, optical, magnetic and energy storage.

Declaration

The author(s) declared no potential conflicts of interest with respect to the research, authorship, and/or publication of this article. The author(s) also declared that this article is original, was prepared in accordance with international publication and research ethics, and ethical committee permission or any special permission is not required.

References

- Zhang, M., Q. Deng, L. Shi, A. Cao, H. Pang, S. Hu, *Nanobowl array fabrication based on nanoimprint lithography*. *Optik*, 2016. **127**(1): p. 145-147.
- Wanke, M. C., O. Lehmann, K. Muller, Q. Wen, M. Stuke, *Laser Rapid Prototyping of Photonic Band-Gap Microstructures*. *Science*, 1997. **275**(5304): p. 1284-1286.
- Haes, A. J. and R. P. Van Duyne, *A Nanoscale Optical Biosensor: Sensitivity and Selectivity of an Approach Based on the Localized Surface Plasmon Resonance Spectroscopy of Triangular Silver Nanoparticles*. *J. Am. Chem. Soc.*, 2002. **124**(3): p. 10596-10604.
- Kim, Y. N., S. J. Kim, E. K. Lee, E. O. Chi, N. H. Hur, C. S. Hong, *Large magnetoresistance in three dimensionally ordered macroporous perovskite manganites prepared by a colloidal templating method*. *J. Mater. Chem.*, 2004. **14**(11): p. 1774-1777.
- Xu, L., L. D. Tung, L. Spinu, A. A. Zakhidov, R. H. Baughman, *Synthesis and Magnetic Behavior of Periodic Nickel Sphere Arrays*. *J.B, Wiley, Adv. Mater*, 2003. **15**(18): p. 1562-1564.
- Chi, E. O., Y. N. Kim, J. C. Kim, N. H. Hur, *A macroporous perovskite manganite from colloidal templates with a Curie temperature of 320 K*. *Chem. Mater.*, 2003. **15**(10): p. 1929-1931.
- Xu, L., W. L. Zhou, C. Frommen, R. H. Baughman, A. A. Zakhidov, L. Malkinski, J. Q. Wang, J. B. Wiley, *Electrodeposited nickel and gold nanoscale meshes with potentially interesting photonic properties*. *Chem. Commun.*, 2000. **12**(17): p. 997-998.
- Kim, J. C., Y. N. Kim, N. H. Hur, W. S. Kim, Y. G. Kang, *Highly ordered macroporous magnetic materials prepared by electrodeposition through colloidal template*. *Phys.*

- Status Solidi, 2004. **241**(7): p. 1585-1588.
9. Xu, W. G., J. H. Li, S. X. Lu, Y. Q. Duan, C. X. Ma, X. F. Shi, Y. L. Yang, Y. B. Chen, 2012. *Preparation of superhydrophobic ZnO films on zinc substrate by chemical solution method*. Chem. Res. Chin. Univ., 2012. **28**(3): p. 529-533.
 10. Ly, Park S., *Highly sensitive gas sensor using hierarchically self-assembled thin films of graphene oxide and gold nanoparticles*. Journal of Industrial and Engineering Chemistry, 2018. **67**: p. 417-428.
 11. Nisançi, F. B., U. Demir, *Size-controlled electrochemical growth of PbS nanostructures into electrochemically patterned self-assembled monolayers*. Langmuir, 2012. **281**(22): p. 8571-8578.
 12. Booh, B. L., *Polymers for Integrated Optical Waveguides*, ed. B. L. Booh. Academic Press, Boston, 1993. p. 549.
 13. Schoer, J. K., F. P. Zamborini and R. M. Crooks, *Scanning probe lithography. 3. Nanometer-scale electrochemical patterning of Au and organic resists in the absence of intentionally added solvents or electrolytes*. J. Phys. Chem, 1996. **100** (26): p. 11086-11091.
 14. Schoer, J. K. and R. M. Crooks, *Scanning Probe Lithography. 4. Characterization of Scanning Tunneling Microscope-Induced Patterns in n-Alkanethiol Self-Assembled Monolayers*. Langmuir, 1997. **13**(8): p. 2323-2332.
 15. Kramer, S., R. R. Fuieler, C. B. Gorman, *Scanning probe lithography using self-assembled monolayers*. Chem. Rev. 2003. **103**(11): p. 4367-4418.
 16. Li, Y., B. W. Maynor and J. Liu, *Electrochemical AFM "Dip-Pen" Nanolithography*. J. Am. Chem. Soc., 2011. **123**(32): p. 2105-2106.
 17. Demir, U., K. K. Balasubramanian, V. Cammarata, C. Shannon, *Scanning probe lithography of novel Langmuir-Schaefer films: Electrochemical applications*. J. Vac. Sci. Technol. B, 1995. **13**(3): p. 1294-1299.
 18. Clark, S., M. Montague and T. P. Hammond, *Selective deposition in multilayer assembly: SAMs as molecular templates*. Supramolecular science, 1997. **4**(1) : p. 141-146.
 19. Wang, Y., Z. Li, J. Wang, J. Li, Y. Lin, *Graphene and graphene oxide: biofunctionalization and applications in biotechnology*. Trends Biotechnol., 2011. **29**(5): p. 205-212.
 20. Robinson, J. T., F. K. Perkins, E. S. Snow, Z. Wei, P. E. Sheehan, *Reduced Graphene Oxide Molecular Sensors*. Nano Lett., 2008. **8**(10): p. 3137-3140.
 21. He, S., B. Song, D. Li, C. Zhu, W. Qi, Y. Wen, L. Wang, S. Song, H. Fang, C. Fan, *A graphene nanoprobe for rapid, sensitive, and multicolor fluorescent DNA analysis*. Adv. Funct. Mater., 2010. **20**(3) : p. 453-459.
 22. Jung, I., D. A. Dikin, R. D. Piner, R. S. Ruoff, *Tunable electrical conductivity of individual graphene oxide sheets reduced at "low" temperatures*. Nano Lett., 2008. **8**(12): p. 4283-4287.
 23. Segev-Bar, M. and H. Haick, *Flexible sensors based on nanoparticles*. ACS Nano, 2013. **7**(10): p. 8366-8378.
 24. Ly, T. N., S. J. Par and S. J. Park, 2016. *Detection of HIV-1 antigen by quartz crystal microbalance using gold nanoparticles*. Sens. Actuators B, 2016. **237**: p. 452-458.
 25. Kahn, N., O. Lavie, M. Paz, Y. Segev, H. Haick, *Dynamic Nanoparticle-Based Flexible Sensors: Diagnosis of Ovarian Carcinoma from Exhaled Breath*. Nano Lett., 2015. **15**(10): p. 7023-7028.
 26. Olichwer, N., E. W. Leib, A. H. Halfar, A. Petrov, T. Vossmeier, *Cross-linked gold nanoparticles on polyethylene: resistive responses to tensile strain and vapors*. ACS Appl. Mater. Interfaces, 2012, **4** (11): p. 6151-6161.
 27. Ghosh, S. K. and T. Pal, *Interparticle coupling effect on the surface plasmon resonance of gold nanoparticles: from theory to applications*. Chem. Rev., 2007. **107**(11): p. 4797-4862.
 28. Dykman, L. A. and N. G. Khlebtsov, *Gold Nanoparticles in Biology and Medicine: Recent Advances and Prospects* Acta Nature, 2011. **3** (2): p. 34-55.



Research Article

Effect of polymer and surfactant concentrations on PVP nanofibers morphology

Hülya Kesici Güler^a  and Funda Cengiz Çallıoğlu^{a,*} 

^aSüleyman Demirel University, Engineering Faculty, Textile Engineering Department, Isparta, Turkey

ARTICLE INFO

Article history:

Received 05 April 2020

Revised 27 April 2020

Accepted 10 May 2020

Keywords:

Electrospinning

Nanofiber

Polyvinylpyrrolidone

Surfactant

ABSTRACT

In this study, biocompatible polyvinylpyrrolidone (PVP) based nanofiber production was carried out with various polymer and surfactant concentrations. Firstly; various concentrations of PVP (6, 8, 10, 12, 14, 16 wt %) polymer solutions were prepared, solution properties (conductivity, viscosity, surface tension, pH and density) were determined and nanofiber production was achieved under the optimum process parameters. 12 wt % PVP concentration was chosen as an optimum in terms of nanofiber morphology and fiber fineness. Then, polymer concentration was kept constant at 12 wt % and various concentrations of surfactant (1, 2, 3, 4, 5, 6 wt %) added into the polymer solutions. According to the solution properties and Scanning Electron Microscope (SEM) images; conductivity, viscosity and average fiber diameter increased with polymer and surfactant concentrations increase and ultra-fine, bead free and uniform nanofibers were obtained. On the other hand, surface tension and pH values were affected by polymer concentration changing, however, surface tension decreased significantly and pH decreased slightly with the addition of surfactant to the PVP polymer solution. Moreover, the density of polymer solutions increased with both polymer solution and surfactant concentration increase.

© 2020, Advanced Researches and Engineering Journal (IAREJ) and the Author(s).

1. Introduction

Electrospinning is a dry spinning process that technic to produce nanoscale fibers. It is widely using to produce polymeric nanofibers. Advantages of this technic, most polymers can be used for nanofiber production and easy to set up this apparatus [1-2]. Nanofibers have unique properties than compared conventional fibers such as; small fiber diameter (nm), high porosity and large specific surface area (m²/g) [3].

PVP is a polymer that is biocompatible, hydrophilic, synthetic, non-toxic, dissolve in water and many other solvents. Because of these properties, it can be used for medical and cosmetic application areas such as; drug delivery and release, tissue engineering, wound dressing [4-5]. Polymer concentration and surface tension are important factors for spinnability and smooth (bead free) fiber production. Therefore, in literature, there are many studies about this subject [6-11]. Surfactants usually used to reduce the surface tension of polymer solutions for the overcome of electrostatic forces in the electric field [12].

Surfactants can be defined as a stick that has two different parts one of them is a hydrophilic head and another one is a hydrophobic end. Generally, surfactants work that hydrophobic part sticks to the organic phase and hydrophilic head part hold on to the water [13]. In this study, Cremophor RH 40 was used as a nonionic surfactant. Cremophor RH 40 which is a non-toxic commercial surfactant can be used in medical and cosmetic application areas [14]. Surfactants such as Triton X-100, Hexadecyltrimethylammonium Bromide (HTAB), Tween80, sodium dodecyl sulfonate (SDS), cationic cetyltrimethyl ammonium bromide (CTAB), Efska3030 have been used to make a positive impact on the morphology of nanofibers and reduce surface tension of polymer solutions [15-17]

On the other hand, in literature there are some studies effect of polymer concentration on nanofiber morphology such as poly(ethyleneoxide) (PEO) [6], polyvinyl butyral (PVB) [7], poly(vinylidene fluoride) (PBDF) [8], cellulose acetate and poly(vinyl chloride) [9], poly(ethylene terephthalate) (PET) [11].

* Corresponding author. Tel.: +90-246-211-1180.

E-mail addresses: kesicihulya@gmail.com (H. Kesici Güler), fundacengiz@sdu.edu.tr (F. Cengiz Çallıoğlu)

ORCID: 0000-0002-5793-7772 (H. Kesici Güler), 0000-0002-6614-3616 (F. Cengiz Çallıoğlu)

DOI: 10.35860/iarej.692080

The aim of this study is the investigation of the effect of polymer and surfactant concentrations on PVP nanofiber morphology. In addition, this study contributes to the PVP nanofibers morphology with details.

2. Experimental Study

2.1 Material

In this study, PVP K30 (Mw 360.000 g/mol) was used as a polymer, distilled water was used as a solvent and Cremophor RH 40 was used as a surfactant. PVP was purchased from Sigma-Aldrich Corporation (St. Louis, MO, USA) and Cremophor RH 40 was supplied from Ersal Chemistry (İzmir, Turkey).

First part of this study; PVP/distilled water polymer solutions with various polymer concentrations optimization was carried out to obtain fine and bead-free nanofibers. For this purpose, polymer solutions were prepared at six different PVP concentrations. The solution contents and sample codes are given in Table 1.

PVP polymer solution concentration was kept constant at 12 wt % for the second part of the study and various concentrations of surfactant was added into the polymer solutions. The solution contents with various surfactant concentrations and sample codes are given in Table 2.

All solutions were prepared under the same conditions such as; stirring time, stirring speed and temperature.

2.2 Methods

Polymer solutions were characterized after all solutions were prepared. Conductivity was measured with Selecta CD 2005 conductometer, viscosity values were obtained from Lamy Rheology, B-One Touch Screen under a shear rate of 5 s^{-1} , surface tension and density were determined with Biolin Scientific Sigma 702 by Wilhelmy plate method and pH was evaluated using Adwa AD110.

Nanofiber production was achieved via the electrospinning method under the optimum process parameters (voltage, distance between electrodes, solution feed rate). These process parameters are given in Table 3.

To characterize fiber morphology of PVP based nanofibrous surfaces, SEM images were taken at 1.000 times and 20.000 times of magnifications.

Table 1. Various concentrations of PVP polymer solutions and sample codes

Sample Codes	Polymer Concentration (%)
PVP6	6
PVP8	8
PVP10	10
PVP12	12
PVP14	14
PVP16	16

Table 2. Sample codes of PVP polymer solutions with various concentrations of surfactant

Sample Codes	Polymer Concentrations (%)	Surfactant Concentrations (%)
PVP12-1	12	1
PVP12-2	12	2
PVP12-3	12	3
PVP12-4	12	4
PVP12-5	12	5
PVP12-6	12	6

100 different measurements were obtained from each nanofiber samples to determine average fiber diameter with ImageJ software. The statistical analysis program was used for drawing histogram curves. Besides, the fiber uniformity coefficient was calculated from the ratio of A_w/A_n and optimum value is close to 1, which represents uniform fibers. Number average and weight average values were calculated using formulas (1) and (2), given below [18].

$$A_n = \frac{\sum n_i d_i}{\sum n_i} \text{ (number average)} \quad (1)$$

$$A_w = \frac{\sum n_i d_i^2}{\sum n_i d_i} \text{ (weight average)} \quad (2)$$

3. Results and Discussion

Various concentrations of PVP solutions properties such as conductivity, viscosity, surface tension, density and pH were determined. Conductivity, viscosity and surface tension graphs for various concentrations of PVP solutions are given in Figure 1.

According to the Figure 1 (a), viscosity and conductivity increases with polymer concentration increase. Solution viscosity increase with polymer concentration is expected result as known from the literature [19]. Because polymer entanglement increases with polymer concentration which causes higher viscosity. Conductivity is related to the number of ions in the polymer solution [20]. According to the conductivity results; it is thought that the number of ions increases with PVP polymer concentrations. Surface tension was not affected by PVP concentration increase (Figure 1 (b)).

Viscosity, conductivity and surface tension graphs for PVP (12 wt %) solutions with various concentrations of surfactants are given in Figure 2.

As it has seen in Figure 2 (a); viscosity and conductivity increase with surfactant concentration increase. This result is compatible with the literature [21]. There is also a strong relationship between the surfactant and surface tension of the solution. It has been seen clearly in Figure 2 (b), the addition of surfactant to the PVP polymer solution (1w% surfactant) decreased surface tension significantly.

All solution properties determined from this study are given in Table 4.

Table 3. Process parameters of electrospinning

Voltage (kV)	Distance between electrodes (cm)	Solution feed rate (mL/h)	Humidity (%)	Temperature (°C)	Spinning Duration (min)
26.4	16.5	0.6	35	21	30

Table 4. Solutions properties for all samples

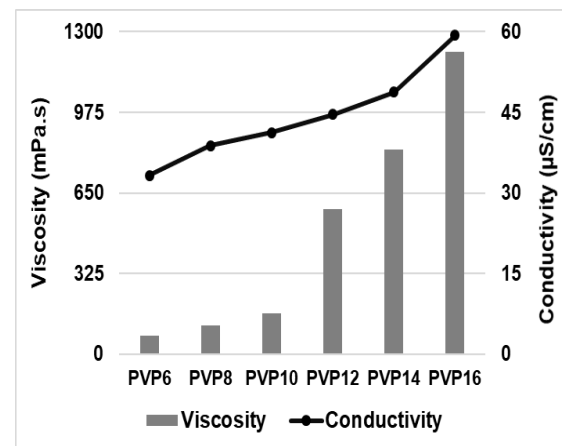
Sample Codes	Conductivity ($\mu\text{S}/\text{cm}$)	Viscosity (mPa.s)	Surface Tension $\pm\text{SD}^*$ (mN/m)	Density (kg/L)	pH
PVP6	33.3	76	59.00 \pm 0.21	1.0046	5.89
PVP8	38.8	115	63.49 \pm 0.44	1.0129	5.54
PVP10	41.2	164	59.61 \pm 0.91	1.0158	5.44
PVP12	44.6	583	63.02 \pm 1.15	1.0218	5.47
PVP14	48.8	826	52.29 \pm 1.97	1.0289	5.38
PVP16	59.3	1218	49.89 \pm 2.14	1.0426	5.38
PVP12-1	56.9	585	42.41 \pm 2.40	1.0224	5.07
PVP12-2	66.3	969	41.29 \pm 2.08	1.0241	4.93
PVP12-3	74.8	1102	40.00 \pm 2.26	1.0333	4.86
PVP12-4	85.3	1267	39.28 \pm 1.55	1.0434	4.80
PVP12-5	89.3	1551	39.27 \pm 2.04	1.0597	4.73
PVP12-6	98.8	1920	38.89 \pm 1.93	1.0730	4.73

*SD: Standard Deviation

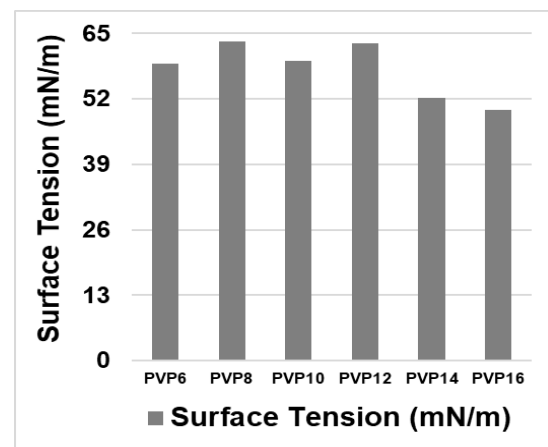
According to Table 4; it is possible to say, there is no relation between polymer concentration and surface tension however, surfactant concentration influences the surface tension of polymer solution noticeably. Besides, density increases slightly with polymer and surfactant concentrations. And, it was determined that the addition of surfactant was decreased pH slightly also.

SEM images and fiber diameter histogram curves for various concentrations of PVP solutions are given in Figure A.1 (in Appendix). And also, relationships between average fiber diameter and fiber diameter uniformity coefficient are given in Figure 3.

As it has been shown clearly in Figure A.1, beads formation can be seen intensively on the nanofibrous structure from PVP polymer solutions with 6 and 8 wt % concentrations. For this reason, fiber diameter could not be measured and histograms could not be drawn. It is determined that beads formation decreases with polymer concentration increasement and all beads were disappeared at 16 wt % PVP polymer concentration. When histograms were analyzed, the average fiber diameter increases with polymer concentration increasement. In Figure 3, it is seen that uniformity increases with PVP concentration in other words fiber diameter uniformity coefficient approaches to value of 1. It is possible to deduce from these results; there is a relationship between solution viscosity and nanofiber morphology. Viscosity is related to polymer molecule chains entanglement in the solution. Lower viscosity causes lower molecule chain entanglement therefore, electrospinning and beads may occur. On the other hand, smooth and bead-free nanofibers can be produced at higher viscosity [13].

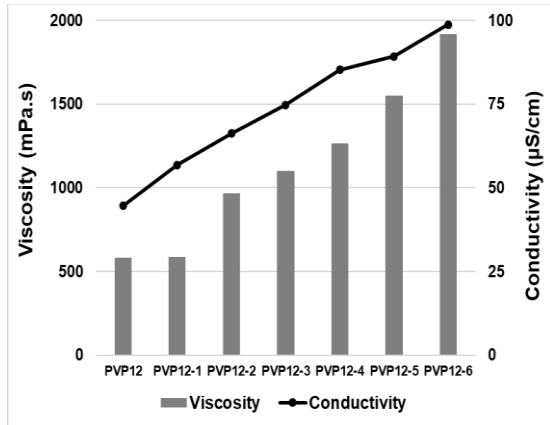


(a)

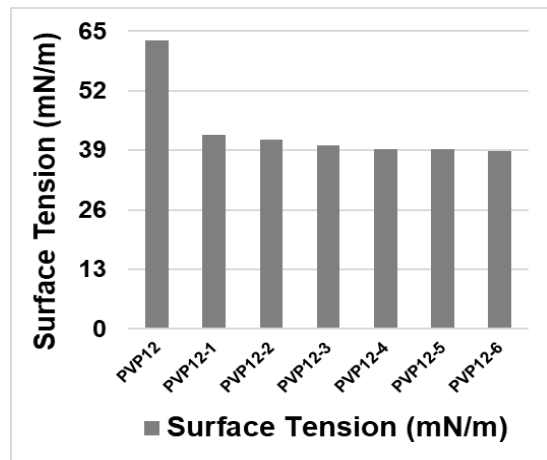


(b)

Figure 1. Conductivity, viscosity, and surface tension results of PVP solutions



(a)



(b)

Figure 2. Conductivity, viscosity and surface tension results of PVP solutions with various surfactant concentrations.

In the literature, it is clearly seen in the studies of PVP nanofibers that the average fiber diameter increases as the polymer concentration increase [22-24].

SEM images and fiber diameter histogram curves of PVP nanofibers with various concentrations of surfactants are given in Figure A.2 (in Appendix). The relationship between average fiber diameter and fiber diameter uniformity coefficient is also given in Figure 4.

According to Figure A.2. and Figure 4; it is possible to say, fiber morphology has improved, the beaded structure has been removed and the average fiber diameter has increased slightly with surfactant concentration increase. Generally, ultra-fine (approx. 200-250 nm) and uniform nanofibers were produced. It is well known from the literature; beads can be minimized with lower surface tension of the polymer solution. Elimination of beads can be realized in two different ways. One of them is of using surfactant and the other one is the selection of solvent which has low surface tension [25]. In this study, using of a surfactant was preferred to minimize the number of beads into the nanofiber structure. There are similar studies in the literature on non-ionic surfactants, both beads decreased and average fiber diameter increased [16, 26-27].

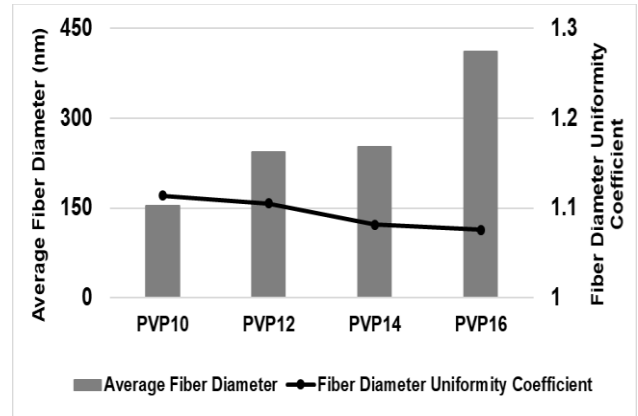


Figure 3. Average fiber diameter and fiber diameter uniformity coefficient of PVP nanofibers

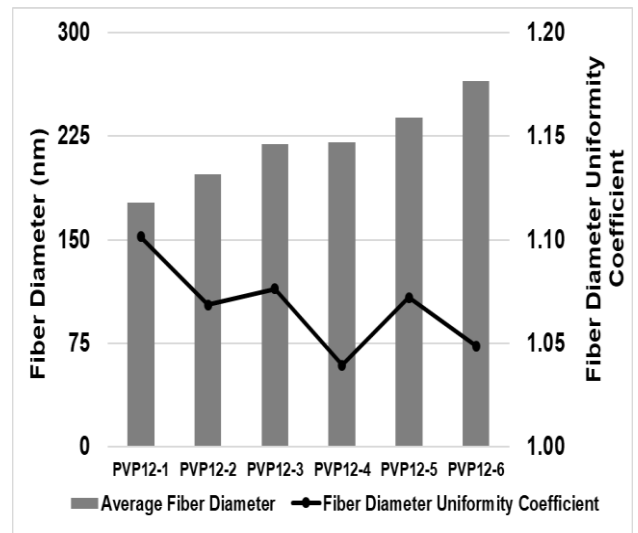


Figure 6. Average fiber diameter and fiber diameter uniformity coefficient of PVP nanofibers with various concentrations of surfactant

4. Conclusion

Within the scope of the study, biocompatible PVP based nanofibers with various polymer and surfactant concentrations were produced by the electrospinning method.

Optimum polymer concentration was determined as 12 wt % PVP in terms of fiber morphology and fiber diameter. Various concentrations of surfactants such as 1, 2, 3, 4, 5, 6 wt % were applied to the PVP solution at 12 wt % polymer concentration. Generally; viscosity, conductivity and average fiber diameter increase with polymer and surfactant concentration increase and beaded structure was eliminated. Surfactant addition has been affected solution surface tension while polymer concentration has not. Moreover, density was increased both polymer and surfactant concentrations. According to the results; ultra-fine, smooth and uniform fibers have been produced, and these biocompatible nanofiber materials are thought to have potential in the medical and cosmetic industry.

Declaration

The author(s) declared no potential conflicts of interest with respect to the research, authorship, and/or publication of this article. The author(s) also declared that this article is original, was prepared in accordance with international publication and research ethics, and ethical committee permission or any special permission is not required.

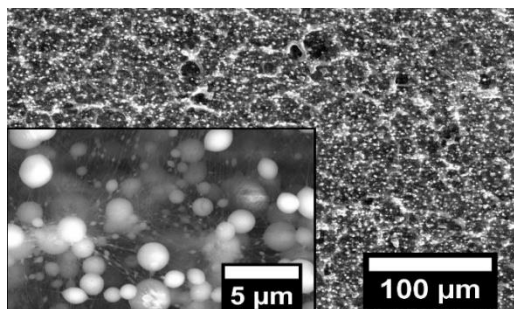
Acknowledgment

This work was supported by Suleyman Demirel University Scientific Researches Project Unit under Research Project (project no: FDK-2019-6761). Part of this study was presented at International Conference on Technology and Science organized on 14-16 November, 2019 in Burdur Mehmet Akif Ersoy University.

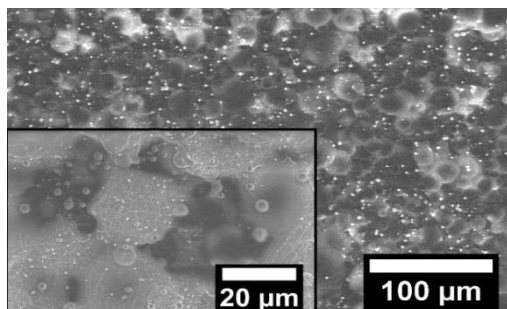
References

- Subbiah, T., et al., *Electrospinning of nanofibers*. Journal of applied polymer science, 2005. **96**(2): p. 557-569.
- Tucker, N., et al., *The history of the science and technology of electrospinning from 1600 to 1995*. Journal of engineered fibers and fabrics, 2012. **7**(2_suppl): p. 155892501200702S10.
- Bhardwaj, N., and S.C. Kundu, *Electrospinning: a fascinating fiber fabrication technique*. Biotechnology advances, 2010. **28**(3): p. 325-347.
- Dhandayuthapani, B., U.M. Krishnan, and S. Sethuraman, *Fabrication and characterization of chitosan-gelatin blend nanofibers for skin tissue engineering*. Journal of Biomedical Materials Research Part B: Applied Biomaterials, 2010. **94**(1): p. 264-272.
- Salles, T.H.C., C.B. Lombello, and M.A. d'Ávila, *Electrospinning of gelatin/poly (vinyl pyrrolidone) blends from water/acetic acid solutions*. Materials Research, 2015. **18**(3): p. 509-518.
- Deitzel, J.M., et al., *The effect of processing variables on the morphology of electrospun nanofibers and textiles*. Polymer, 2001. **42**(1): p. 261-272.
- Lubasova, D. and L. Martinova, *Controlled morphology of porous polyvinyl butyral nanofibers*. Journal of Nanomaterials, 2011. **2011**.
- Shao, H., et al., *Effect of electrospinning parameters and polymer concentrations on mechanical-to-electrical energy conversion of randomly-oriented electrospun poly (vinylidene fluoride) nanofiber mats*. RSC advances, 2015. **5**(19): p. 14345-14350.
- Tarus, B., et al., *Effect of polymer concentration on the morphology and mechanical characteristics of electrospun cellulose acetate and poly (vinyl chloride) nanofiber mats*. Alexandria Engineering Journal, 2016. **55**(3): p. 2975-2984.
- Thompson, C., et al., *Effects of parameters on nanofiber diameter determined from electrospinning model*. Polymer, 2007. **48**(23): p. 6913-6922.
- Veleirinho, B., M.F. Rei, and J. Lopes-DA-Silva, *Solvent and concentration effects on the properties of electrospun poly (ethylene terephthalate) nanofiber mats*. Journal of Polymer Science Part B: Polymer Physics, 2008. **46**(5): p. 460-471.
- He, J.-H., et al., *Electrospun nanofibres and their applications*. 2008: ISmithers Shawbury, UK.
- Ramakrishna, S., et al., *An introduction to electrospinning and nanofibers*. 2005. Singapura: World Scientific Publishing Company.
- Rachmawati, H., et al., *The in vitro-in vivo safety confirmation of peg-40 hydrogenated castor oil as a surfactant for oral nanoemulsion formulation*. Scientia Pharmaceutica, 2017. **85**(2): p. 18.
- Fallahi, D., M. Rafizadeh, N. Mohammadi, and B.Vahidi, *Effect of LiCl and non-ionic surfactant on morphology of polystyrene electrospun nanofibers*. e-Polymers, 2008. **8**(1). p. 1-9.
- Deng, L., et al., *Effects of surfactants on the formation of gelatin nanofibres for controlled release of curcumin*. Food chemistry, 2017, 231, p. 70-77.
- Abutaleb, Ahmed, et al. *Effects of surfactants on the morphology and properties of electrospun polyetherimide fibers*. Fibers, 2017. **5**(3) 33.
- Cengiz, F. and O. Jirsak, *The effect of salt on the roller electrospinning of polyurethane nanofibers*. Fibers and Polymers, 2009. **10**(2): p. 177-184.
- Sarac, A.S., *Nanofibers of conjugated polymers*. 2017: Jenny Stanford Publishing.
- Sarhan, W.A., H.M. Azzazy, and I.M. El-Sherbiny, *The effect of increasing honey concentration on the properties of the honey/polyvinyl alcohol/chitosan nanofibers*. Materials Science and Engineering: C, 2016. **67**: p. 276-284.
- Ogino, K., N. Tsubaki, and M. Abe, *Solution properties of mixed surfactant system (II): Electric properties of anionic-nonionic surfactants in aqueous solutions*. Journal of colloid and interface science, 1984. **98**(1): p. 78-83.
- Santibenchakul, S., S. Chaiyasith, and W. Pecharapa, *Effect of PVP concentration on microstructure and physical properties of electrospun SnO₂ nanofibers*. Integrated Ferroelectrics, 2016, **175**(1), p. 130-137.
- Lee, H., et al., *Control of the morphology of cellulose acetate nanofibers via electrospinning*. Cellulose, 2018, **25**(5), p. 2829-2837.
- Kuchi, C., and P. S. Reddy, *Effect of polymer concentration and annealing temperature on TiO₂-PVP composite nanofiber mats prepared with homemade electrospinning*. In AIP Conference Proceedings AIP Publishing LLC, 2018, **1953**(1): p. 030241.
- Chang, W., *Nanofibers: Fabrication, Performance, and Applications*. 2009: Nova Science Publishers, Incorporated.
- Hu, J., M. P. Prabhakaran, X. Ding, and S. Ramakrishna, *Emulsion electrospinning of polycaprolactone: influence of surfactant type towards the scaffold properties*. Journal of Biomaterials Science, polymer edition, 2015, **26**(1), p. 57-75.
- Zheng, J. Y., et al., *The effect of surfactants on the diameter and morphology of electrospun ultrafine nanofiber*. Journal of Nanomaterials, 2014, p. 1-9.

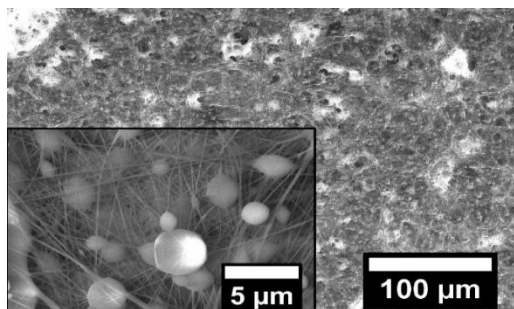
Appendix



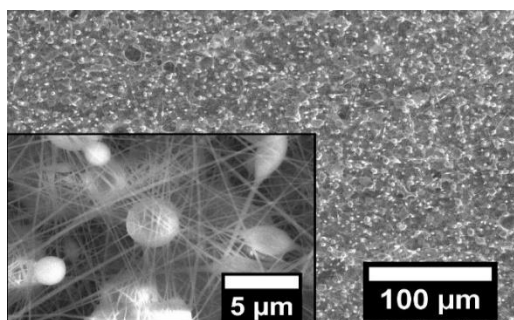
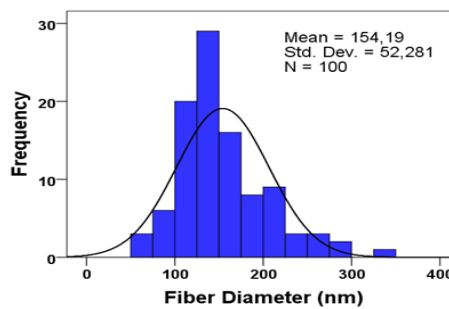
PVP6



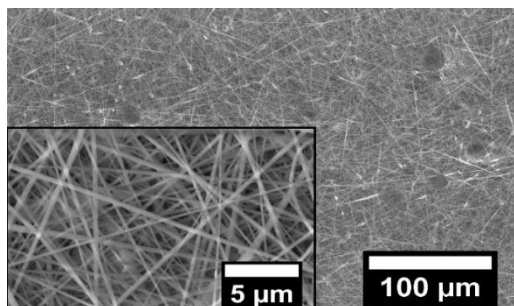
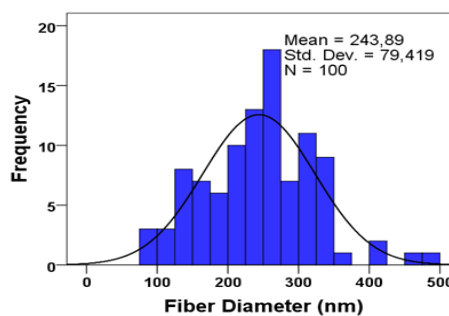
PVP8



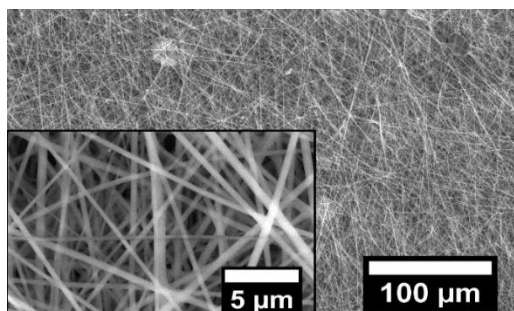
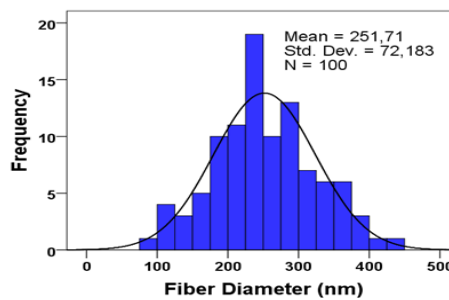
PVP10



PVP12



PVP14



PVP16

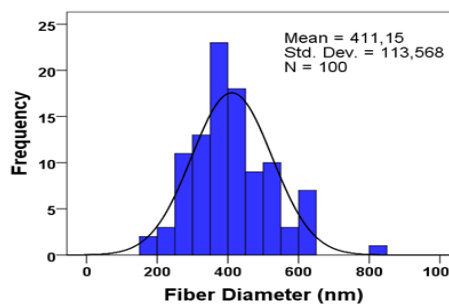
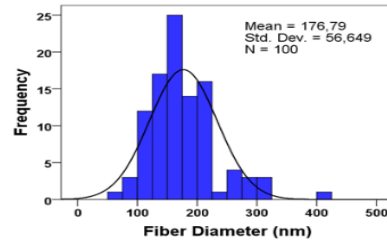
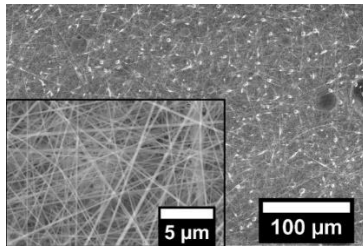
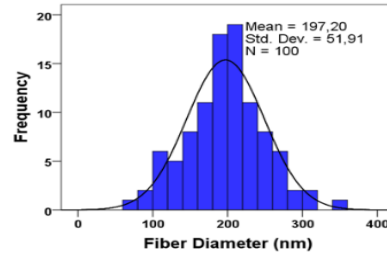
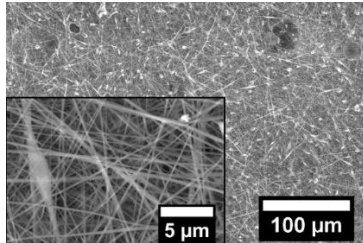


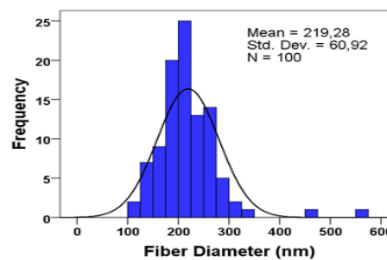
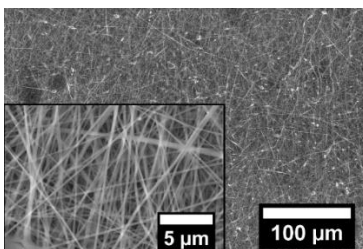
Figure A.1. SEM images (1.000x and 20.000x) and histograms of PVP nanofibers



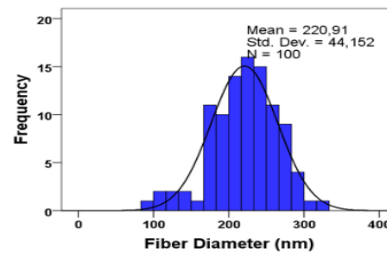
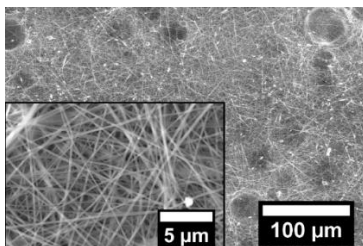
PVP12-1



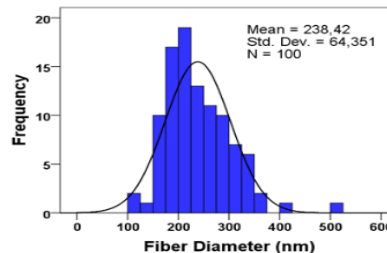
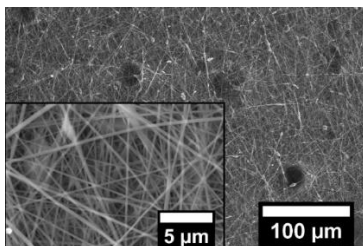
PVP12-2



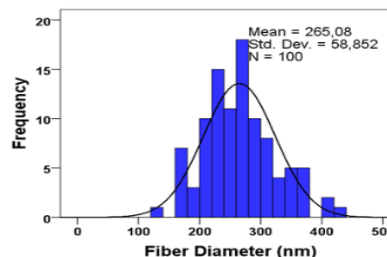
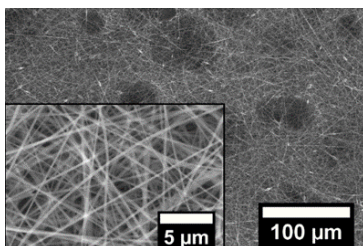
PVP12-3



PVP12-4



PVP12-5



PVP12-6

Figure A.2. SEM images (1.000x and 20.000x) and histograms of various surfactant concentrations of PVP nanofibers

**Research Article**

Investigation of plastic zone dimension in front of an external semi-elliptic crack on pipe of molecular bushing

İlyas Kacar ^{a,*} 

^aNiğde Ömer Halisdemir University Engineering Faculty, Department of Mechatronics Engineering, Niğde, 51240, Turkey

ARTICLE INFO

Article history:

Received 10 April 2020

Revised 01 May 2020

Accepted 05 May 2020

Keywords:

Fracture mechanics

Molecular bushing

Plastic zone

Semi-elliptical crack

Stress intensity factor

Yield criteria

ABSTRACT

In automotive industry, molecular bushings transfer loads from steering gearbox to wheels on a vehicle. The pipe is one of the most vital member of these routing systems and manufactured using 41Cr4 sheet metal. For a pipe of molecular bushing, analytical solutions of crack tip plastic zone size is derived by using four yield criteria: Von Mises, Tresca, Hill48, and Hu2003. Hill48 and Hu2003 are useful criteria for materials with higher anisotropy such as sheet metals. Material's hardening behaviour is modelled using bilinear isotropic hardening rule by coupling with associated flow rule under isotropic and large scale plasticity condition. The solutions are developed for mode-I loading case due to service conditions of the pipe. A finite element simulation is performed to collect stress intensity factors. Results are verified by comparing to those of Irwin and Dugdale. The plastic zone's shape and size are analysed for different anisotropy cases. The results show that plastic zone have "kidney" or "butterfly" shapes depending on the yield criteria used. Increasing anisotropy has significant effect on plastic zone.

© 2020, Advanced Researches and Engineering Journal (IAREJ) and the Author(s).

1. Introduction

The suspension system is used to stabilize the vehicle during driving, allowing the wheels to continually follow the road surface to improve steering stability. The molecular bushing is a part of suspension system. It damps the vibration caused by road condition [1]. They are manufactured using 41Cr4 steels in automotive industry. This structural part is subjected to corrosion leading to crack propagation and fracture [2, 3]. Any damage to this part can lead to loss of driving stability and impaired driving comfort.

All of stresses at the crack tip goes to infinity due to singularity because crack tip radius goes to zero. However, the structural materials have a yield strength and therefore the material exhibits plastic deformation when the stress value reaches to its yield strength. So there will be a plastic zone surrounding the crack front. This plastically deformed zone is called the crack front plastic zone. Although it is assumed that the boundary of this zone is just as a simple circle at the beginning of fracture mechanics, actually, it is seen that it has different shapes

according to the basis of the yield criterion and the stress distribution (plane strain or plain stress) on the crack tip line.

The plastic zone (PZ) size in the region near the tip of a propagating crack is considered as a measure of the material resistance against crack surfaces opening [4]. The larger plastic zone size results in the higher plastic energy absorption and the higher toughness [5, 6]. Inelastic deformation occurs when the yield strength is exceeded. The crack tip singularity in the linear elastic fracture mechanics (LEFM) cannot be sufficient to give plastic flow based on stress distribution [7, 8]. Because during plastic deformation, the boundary of the plastic region will be different in the proximity of the crack tip. Many studies are being done for the singular terms for the correct estimation of the plastic flow that actually occurs [9].

In this study, a semi-elliptical crack is inserted on the external surface of the pipe of a molecular bushing. PZ equations are derived by using the Von Mises, Tresca, Hill48, and Hu2003 yield criteria using the stress field near crack tip. Subsequently, the stress distribution and stress intensity factors (SIF) are determined in front of the crack

* Corresponding author. Tel.: +90 (388) 225 4648; Fax: +90 (388) 221 0112.
E-mail addresses: ikacar@gmail.com (I. Kacar)
ORCID: 0000-0002-5887-8807 (I. Kacar)
DOI: 10.35860/iarej.717634

by elasto-plastic finite element analysis (FEA). Also crack tip blunting, stress, and strain results from finite element simulation is presented in the paper.

2. Problem Description

A pipe contains a semi-elliptical external surface crack under uniaxial tension. Figure 1 shows the details of a V-arm and the pipe of molecular bushing. So the problem has a mode-I loading case. First elastic stress fields at the crack tip is obtained analytically. Further, PZs are determined by using various anisotropic yield criteria.

The pipe material is 41Cr4 and its chemical composition is given in Table 1.

Anisotropy values and mechanical properties for 41Cr4 are given in Table 2. These parameters are necessary to use in yield criteria. In the table r_{θ} values are called anisotropy coefficients or Lankford coefficients and determined from tensile test by using samples preparing at 0° , 45° , and 90° directions with respect to main axis.

The material is assumed as linear elastic and perfect plastic where no hardening is seen during plastic deformation. So, the bilinear isotropic hardening (BISO) rule $\sigma(h) = YS + TM(\epsilon^p)$ is used by taking $YS=560$ MPa and setting TM to zero to ensure perfect plasticity. YS is yield strength and TM is the tangent modulus, and ϵ^p is the actual amount of plastic deformation. Both YS and TM are enough to set the rule. Anisotropic hardening is a potential for further work.

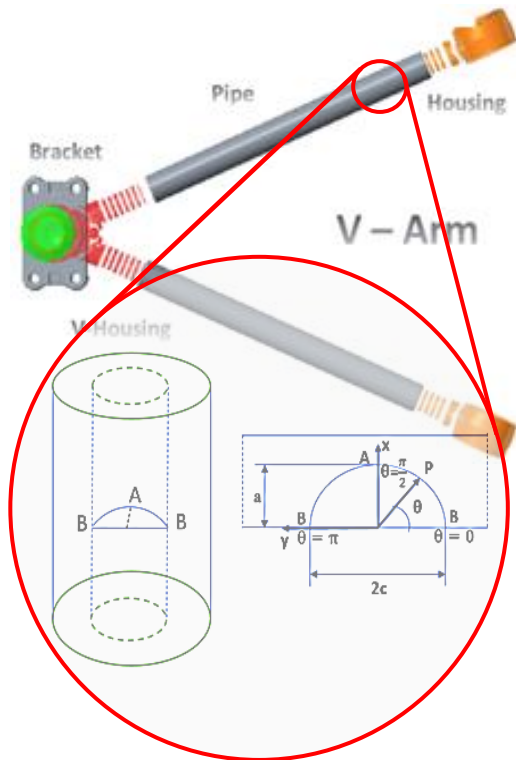


Figure 1. Schematic representation of a semi-elliptical surface crack on the pipe of a molecular bushing

Table 1. Chemical composition of 41Cr4 (EN 1.7035).

C	Si	Mn	Cr	Ni	Al	Cu
0.404	0.349	0.67	0.93	0.061	0.026	0.016

Table 2. Anisotropy values and mechanical properties for 41Cr4 [10, 11].

Material properties	41Cr4 (EN 1.7035)	
Anisotropy coefficients	r_0	0.9
	r_{45}	1.1
	r_{90}	0.9
Poisson ratio	ν	0.29
Yield strength	σ_y	560 MPa
Elasticity modules	E	215 GPa

3. Analysis

Knowing PZ's size and shape is necessary to analyze the crack initiation angle and its propagation. A crack follows the "easiest" path through the plastic zone based on minimum stress or plastic work depending on criterion used. Due to large scale plastic flow in front of a crack and remaining elastic region of geometry, elasto-plastic fracture mechanics analysis is necessary to determine PZ's border. It will be determined by applying some yield criteria on the stress field in front of a crack.

3.1 Crack Tip Stress Field

The stress singularity is inherently present near the crack tip and SIF depends on this singularity. But a failure criterion in classical solid mechanics is not enough to be able to take care of the stress singularity. Because it is based on stress components and these components are not able to exhibit the stress singularity. But equations (1) can exhibit stress singularity due to the term $\sigma \sim K_I r^{-1/2}$. So the stress can go to infinity by getting closer near the crack tip. Although many stress intensity factor calculation methods have been published in handbooks [12], they are limited to primitive shapes only.

For complex shaped geometries, it is a way to find the stress intensity factor by means of FEA [13, 14]. The singular elastic stress field is shown in Figure 2 where radius $R(\theta)$ and angle θ are the polar coordinate axes at the crack tip for a body including a crack under Mode-I loading [3].

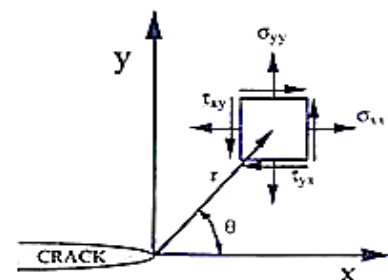


Figure 2. Stress state at crack tip loaded Mode I

$$\begin{aligned} \sigma_{xx} &= \frac{K_I}{\sqrt{2\pi R(\theta)}} \cos\left(\frac{\theta}{2}\right) \left[1 - \sin\left(\frac{\theta}{2}\right) \sin\left(\frac{3\theta}{2}\right)\right] \\ \sigma_{yy} &= \frac{K_I}{\sqrt{2\pi R(\theta)}} \cos\left(\frac{\theta}{2}\right) \left[1 + \sin\left(\frac{\theta}{2}\right) \sin\left(\frac{3\theta}{2}\right)\right] \\ \sigma_{xy} &= \frac{K_I}{\sqrt{2\pi R(\theta)}} \cos\left(\frac{\theta}{2}\right) \sin\left(\frac{\theta}{2}\right) \sin\left(\frac{3\theta}{2}\right) \\ \sigma_{zz} &= 0, \text{ for plane stress} \\ \sigma_{zz} &= \nu(\sigma_{xx} + \sigma_{yy}), \text{ for plane strain} \end{aligned} \quad (1)$$

where ν is Poisson ratio and $R(\theta)$ is radial distance from origin. K_I is called stress intensity factor (SIF). The principal stresses $\sigma_{1,2}$ can be obtained by transformations.

$$\sigma_{1,2} = \frac{\sigma_{xx} + \sigma_{yy}}{2} \pm \sqrt{\left(\frac{\sigma_{xx} - \sigma_{yy}}{2}\right)^2 + (\sigma_{xy})^2} \quad (2)$$

Substituting equations (1) into (2), the principal stresses can be determined.

$$\begin{aligned} \sigma_1 &= \frac{K_I}{\sqrt{2\pi R(\theta)}} \cos\left(\frac{\theta}{2}\right) \left[1 + \sin\left(\frac{\theta}{2}\right)\right] \\ \sigma_2 &= \frac{K_I}{\sqrt{2\pi R(\theta)}} \cos\left(\frac{\theta}{2}\right) \left[1 - \sin\left(\frac{\theta}{2}\right)\right] \\ \sigma_3 &= 0, \text{ for plane stress} \\ \sigma_3 &= \frac{K_I}{\sqrt{2\pi R(\theta)}} \cos\left(\frac{\theta}{2}\right), \text{ for plane strain} \end{aligned} \quad (3)$$

$R(\theta)$, the boundary of PZ, will be obtained by substitution Equation (3) into a yield criterion and solved for $R(\theta)$ for plane stress or strain states separately. For calculation, an m file is written using Matlab® [15].

3.2 Yield Criteria

A stress state can be transformed to an equivalent stress value by means of yield criterion's equation. So a yield criterion is a convenient tool to compare it to the material's yield strength to determine whether plastic deformation is started or not. In this study, equivalent stress is determined by using isotropic yield criteria such as Von Mises [16], Tresca [17], and anisotropic yield criteria such as Hill48 [18] and Hu2003 [19]. General equation of the Von Mises yield function is given in Equation (4).

$$\begin{aligned} f(\sigma_{ij}) &= \phi(\sigma_{1,2,3}) - (\bar{\sigma})^2 = 0 \\ \phi(\sigma_{1,2,3}) &= \frac{|\sigma_1 - \sigma_2|^2 + |\sigma_2 - \sigma_3|^2 + |\sigma_3 - \sigma_1|^2}{2} \end{aligned} \quad (4)$$

where $\bar{\sigma}$ is the equivalent stress, $\phi(\sigma_{1,2,3})$ is its yield function and $\sigma_{1,2,3}$ are principal stresses. Similarly, the Tresca yield function is given in Equation (5).

$$f(\sigma_{ij}) = \phi(\sigma_{1,2,3}) = (\bar{\sigma}) \quad (5a)$$

$$\phi(\sigma_{1,2,3}) = \max(|\sigma_1 - \sigma_2|, |\sigma_2 - \sigma_3|, |\sigma_3 - \sigma_1|) \quad (5b)$$

The quadratic Hill48 yield function is given in Equation (6a). Equation (6b) can be written when anisotropy axes are orthogonal. Its simultaneous solution with Equation (6b) gives Equation (6c).

$$2f(\sigma_{ij}) = F(\sigma_2 - \sigma_3)^2 + G(\sigma_3 - \sigma_1)^2 + H(\sigma_1 - \sigma_2)^2 = 1 \quad (6a)$$

$$(H + G) \cdot (\sigma_1)_y^2 = 1$$

$$(F + H) \cdot (\sigma_2)_y^2 = 1$$

$$(F + G) \cdot (\sigma_3)_y^2 = 1$$

$$\begin{aligned} F &= \frac{(\sigma_0)^2}{2} \left[-\frac{1}{(\sigma_1)_y^2} + \frac{1}{(\sigma_2)_y^2} + \frac{1}{(\sigma_3)_y^2} \right] \\ G &= \frac{(\sigma_0)^2}{2} \left[\frac{1}{(\sigma_1)_y^2} - \frac{1}{(\sigma_2)_y^2} + \frac{1}{(\sigma_3)_y^2} \right] \\ H &= \frac{(\sigma_0)^2}{2} \left[\frac{1}{(\sigma_1)_y^2} + \frac{1}{(\sigma_2)_y^2} - \frac{1}{(\sigma_3)_y^2} \right] \end{aligned} \quad (6b)$$

$$L = \frac{1}{2(\tau_{23})_y^2} = \frac{3(\tau_0)^2}{2(\tau_{23})_y^2}$$

$$M = \frac{1}{2(\tau_{31})_y^2} = \frac{3(\tau_0)^2}{2(\tau_{31})_y^2}$$

$$N = \frac{1}{2(\tau_{12})_y^2} = \frac{3(\tau_0)^2}{2(\tau_{12})_y^2} \text{ where } \tau_0 = \frac{\sigma_0}{\sqrt{3}}$$

$$F(\sigma_2 - \sigma_3)^2 + G(\sigma_3 - \sigma_1)^2 + H(\sigma_1 - \sigma_2)^2 = (\sigma_0)^2 = \bar{\sigma}^2 \quad (6c)$$

where $(\sigma_1)_y$, $(\sigma_2)_y$, and $(\sigma_3)_y$ are the normal yield stresses with respect to the principal anisotropy axes and $(\tau_{23})_y$, $(\tau_{31})_y$, and $(\tau_{12})_y$ are the yield stresses in shear with respect to the axes of anisotropy and τ_0, σ_0 are reference yield stress. It is assumed that the reference axes are on the principle anisotropy axes, which are orthogonal. As a special case, Hill48 criterion becomes Von Mises criterion when $F = 1/2, G = 1/2, H = 1/2$. This case will be used for comparison/verification of the Hill48 equations. Also the coefficients G, H, F are calculated by using anisotropy values as in Equation (7) [20].

$$F = \frac{r_0}{r_{90}(r_0+1)}, \quad G = \frac{1}{r_0+1}, \quad H = \frac{r_0}{r_0+1} \quad (7)$$

These coefficients are calculated as $F=0.5263158, G=0.5263158, H=0.4736842$ while $r_0 = 0.9, r_{45} = 1.1, r_{90} = 0.9$. The quadratic Hill48 yield function is reduced as in Equation (8) for plane stress condition as a special case. To make comparison, both equations are evaluated.

$$(\sigma_1)^2 + \frac{r_0(1+r_{90})}{r_{90}(1+r_0)} (\sigma_2)^2 - \frac{2r_0}{1+r_0} \sigma_1 \sigma_2 = \bar{\sigma}^2 \quad (8)$$

Lastly, a generalized equation of Hu2003 yield criterion is given in Equation (9).

$$f(\sigma_{ij}) = \frac{1}{\sigma_0^4} \sigma_1^4 - \frac{4r_0}{(1+r_0)\sigma_0^4} \sigma_1^3 \sigma_2 + \left(\frac{1}{\sigma_b^4} - \frac{1}{\sigma_0^4} - \frac{1}{\sigma_{90}^4} + \frac{4r_0}{(1+r_0)\sigma_0^4} + \frac{4r_{90}}{(1+r_{90})\sigma_0^4} \right) \sigma_1^2 \sigma_2^2 - \frac{4r_{90}}{(1+r_{90})\sigma_0^4} \sigma_1 \sigma_2^3 + \frac{1}{\sigma_{90}^4} \sigma_2^4 = 1 \quad (9)$$

where $\sigma_0, \sigma_{45}, \sigma_{90}$ are yield stresses at the direction $0^\circ, 45^\circ, 90^\circ$ with respect to rolling direction and σ_b is yield stress from equi-biaxial test. Equivalent stress formula can be obtained from this equation by solving it for σ_0 which it is also called equivalent stress.

3.3 Plastic Zone Equations

It was assumed that the boundary of this zone was just as a simple circle at the beginning of fracture mechanics. In Equation (10), the first approximation for PZ size for plane stress case is given. It defines just a constant circle whose left quadrant is located at the crack tip [21].

$$R(\theta)_{dg} = \frac{1}{2 \cdot \pi} \left(\frac{K_1}{\sigma_y} \right)^2 \quad (10)$$

where $R(\theta)_{dg}$ stands for the plain stress state case, $R(\theta)_{dsd}$ shows the plain strain state case. Later, Irwin [22] assumed that the radius of PZ would be greater twice. It is seen in Equation (11). It estimates PZ for isotropic materials under mode-I loading.

$$R(\theta)_{dg} = \frac{1}{\pi} \left(\frac{K_1}{\sigma_y} \right)^2 \quad (11)$$

In Equation (12), Dugdale's formula [23] presented another circle with greater diameter than Irwin's circle.

$$R(\theta)_{dg} = \frac{\pi}{8} \left(\frac{K_1}{\sigma_y} \right)^2 \quad (12)$$

These formulas do not take care of θ -dependence of PZ size and just calculate $R(\theta)$ at $\theta=0$. Actually, the PZ size depends on yield criterion; materials strain hardening and thickness. In any loading case, while the outmost surface of the bodies is subjected to plane stress state, it is getting become plain strain state towards inner surface. As a yield criterion gives the elasto-plastic boundary, a PZ boundary becomes a yield boundary when it is solved by using a yield criterion. PZ is obtained by substitution stress field into the yield criterion and then solved for radius $R(\theta)$. Because crack initiation starts at the outer surface first, plane stress equations are used in the scope of this study. When the yield criterion is Von Mises, PZ equations will become as in Equation (13).

$$R(\theta)_{dg} = -\frac{1}{2\pi} \left(\frac{K_1}{\bar{\sigma}} \right)^2 \left(\frac{1 + \cos \theta}{2} \right) \left(\frac{3 \cos \theta}{2} - \frac{5}{2} \right) \quad (13a)$$

$$R(\theta)_{dsd} = -\frac{1}{2\pi} \left(\frac{K_1}{\bar{\sigma}} \right)^2 \left(\frac{1 + \cos \theta}{2} \right) \left(-4\nu^2 + 4\nu + \left(\frac{3 \cdot \cos \theta}{2} - \frac{5}{2} \right) \right) \quad (13b)$$

It is seen that when $\theta=0$ then Equation (13a) becomes Equation (10). Both equations are validated by comparing to Equation (14) derived for mode-I case using Von Mises criterion [24, 25]. Its graphics are given in subsequent sections.

$$R(\theta)_{dg} = \frac{1}{4 \cdot \pi} \left(\frac{K_1}{\bar{\sigma}} \right)^2 \left(1 + \cos \theta + \frac{3}{2} \sin^2 \theta \right) \quad (14a)$$

$$R(\theta)_{dsd} = \frac{1}{4 \cdot \pi} \left(\frac{K_1}{\bar{\sigma}} \right)^2 \left((1 + \cos \theta) (1 - 2\nu^2) + \frac{3}{2} \sin^2 \theta \right) \quad (14b)$$

Similarly, results from Tresca criterion [25] are obtained as in Equation (15)

$$R(\theta)_{dg} = \frac{1}{2\pi} \left(\frac{K_1}{\bar{\sigma}} \right)^2 \left(\frac{\cos \theta}{2} + \frac{1}{2} \right) \left(\sin \frac{\theta}{2} + 1 \right)^2 \quad (15a)$$

$$R(\theta)_{dsd} = \frac{1}{8\pi} \left(\frac{K_1}{\bar{\sigma}} \right)^2 \left(2 * \cos \frac{\theta}{2} + \sin \theta - 4\nu \cos \frac{\theta}{2} \right)^2 \quad (15b)$$

Both equations are validated by comparing to Equation (16) derived for mode-I case using Tresca criterion [25].

$$R(\theta)_{dg} = \frac{1}{2 \cdot \pi} \left(\frac{K_1}{\bar{\sigma}} \right)^2 \left(\cos \frac{\theta}{2} + abs(\cos \frac{\theta}{2} \sin \frac{\theta}{2}) \right)^2 \quad (16a)$$

$$R(\theta)_{dsd} = \frac{1}{2 \cdot \pi} \left(\frac{K_1}{\bar{\sigma}} \right)^2 \left((1 - 2\nu) \cos \frac{\theta}{2} + abs(\cos \frac{\theta}{2} \sin \frac{\theta}{2}) \right)^2 \quad (16b)$$

Similarly, results from Hill48 are seen in Equation (17).

$$R(\theta)_{dg} = \frac{1}{2 \cdot \pi} \left(\frac{K_1}{\bar{\sigma}} \right)^2 \left(\frac{1 + \cos \theta}{2} \right) \left(F + G + (F + G + 4H) \sin^2 \left(\frac{\theta}{2} \right) + (2G - 2F) \sin \left(\frac{\theta}{2} \right) \right) \quad (17a)$$

$$R(\theta)_{dsd} = \frac{1}{2 \cdot \pi} \left(\frac{K_1}{\bar{\sigma}} \right)^2 \left(\frac{1 + \cos \theta}{2} \right) \left(F + G - 4F\nu - 4G\nu + 4F\nu^2 + 4G\nu^2 + (F + G + 4H) \sin^2 \left(\frac{\theta}{2} \right) + (-2F + 2G + 4F\nu - 4G\nu) \sin \left(\frac{\theta}{2} \right) \right) \quad (17b)$$

Result from quadratic Hill48 is seen in Equation (18). It is just for the plain stress state case.

$$R(\theta)_{dg} = \frac{1}{2 \cdot \pi} \left(\frac{K_1}{\bar{\sigma}} \right)^2 \left(\frac{1 + \cos \theta}{2} \right) \left(\left(\sin \left(\frac{\theta}{2} \right) + 1 \right)^2 - H(\cos(\theta) + 1) + \left(F \left(\sin \left(\frac{\theta}{2} \right) - 1 \right)^2 * (r_{90} + 1) \right) \right) \quad (18)$$

Result for plastic zone size calculations by using Hu2003 criterion is as follow.

$$\begin{aligned}
 R(\theta)_{dg} = & \frac{1}{2\pi} \left(\frac{K_1}{\sigma \sigma_{90} \sigma_b} \right)^2 \left(\frac{1+\cos\theta}{2} \right) \left| \sigma_{90}^4 \bar{\sigma}^4 + (4\sigma_b^4 \sigma_{90}^4 - \right. \\
 & 4\sigma_b^4 \bar{\sigma}^4 - 8H\sigma_{90}^4 \sigma_b^4 + 8HU\bar{\sigma}^4 \sigma_b^4) \sin\left(\frac{\theta}{2}\right) + \\
 & (8\sigma_{90}^4 \sigma_b^4 - 2\sigma_{90}^4 + 8\bar{\sigma}^4 \sigma_b^4 - 8H\sigma_{90}^4 \sigma_b^4 - \\
 & 8HU\bar{\sigma}^4 \sigma_b^4) \left(\sin\left(\frac{\theta}{2}\right) \right)^2 + (4\sigma_{90}^4 \sigma_b^4 - 4\bar{\sigma}^4 \sigma_b^4 + \\
 & 8H\sigma_{90}^4 \sigma_b^4 - 8HU\bar{\sigma}^4 \sigma_b^4) \left(\sin\left(\frac{\theta}{2}\right) \right)^3 + (\sigma_{90}^4 \bar{\sigma}^4 + \\
 & 8H\sigma_{90}^4 \sigma_b^4 + 8HU\bar{\sigma}^4 \sigma_b^4) \left(\sin\left(\frac{\theta}{2}\right) \right)^4 \left. \right|^{1/2}
 \end{aligned} \tag{19}$$

where $HU=r_{90}/(r_{90}+1)$.

3.4 Finite Element Analysis of Elasto-Plastic Pipe Containing A Semi Elliptical Surface Crack

Analysis is performed on the pipe’s three-dimensional finite element model by using Ansys© [26], as shown in Figure 3. Its fracture module is used for crack insertion. It first calculates the energy at the crack tip (this energy is called the *J*-integral). Then the SIF (K_I), is calculated using the *J*-integral [13].

The dimensions of the model is taken the same with the pipe. No symmetry conditions are applied. A semi-elliptical crack is inserted on the surface of the pipe. The crack is parallel to pipe’s cross-section. Tetragonal elements are used in order to obtain good match between crack’s and pipe body’s elements. While one end of the pipe is fixed, a uniform 560 MPa remote tensile stress is applied to the surface normal of the other end. It causes to yield the material in PZ. So mode-I condition is guaranteed. Analysis is performed using BISO rule to ensure elasto-plastic behavior. Analysis has both material nonlinearity and large deformation. So a nonlinear structural analysis is performed in 20 load steps. Geometry is updated in each iteration. No contact is used.

The parameters necessary to define the semi-elliptical crack are shown on Figure 4. The crack tip curve is divided into 100 front elements. FEA uses domain integral over counters in the crack tip, so 6 counters which surround the crack curve are set. The largest counter radius is taken as 0.01mm.

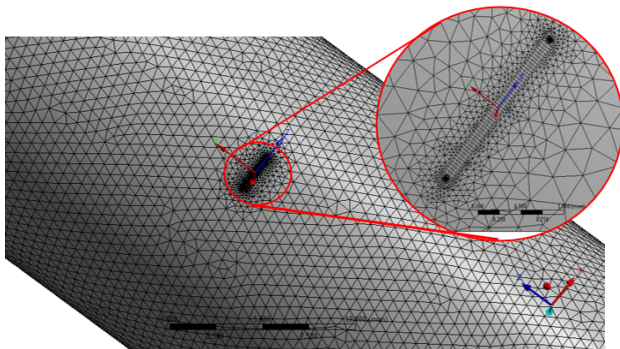


Figure 3. The location of the crack on the meshed model.

Element grow rate is 1.2 through crack tip ligament. The model includes 145987 elements in total after finite element meshing.

It is reported that when compared with the rigorous solution which is a type of analytical solution, the error on SIF values is less than 1% in the interval $0.0001\text{mm} < r < 0.01\text{mm}$ where r is radial distance from the crack tip [27]. Thus, it is clear that the stress intensity factor fund in this range can be trustable. So the SIF obtained from FEA can meet the requirements of engineering applications. Taking that the length of the element in the crack tip is 0.002 mm, we ensure that it stays in the range and is enough to be able to catch SIF with error less than 1%.

4. Results and Discussion

4.1 SIF Solutions

The stress intensity factors (SIF, K_I) obtained from FEA are seen in Figure 5. Results are based on contours which surround the crack curve. The innermost is counter 1. The most critical SIF value may be seen either at the surface (B) or at the deepest point (A) generally. The figure includes 6 curves for 6 counters surrounding the crack tip.

The higher SIF means the more resistance to crack initiation. So, the minimum $K_I = 0.73582 \text{ MPa}\sqrt{\text{mm}}$ will be considered.

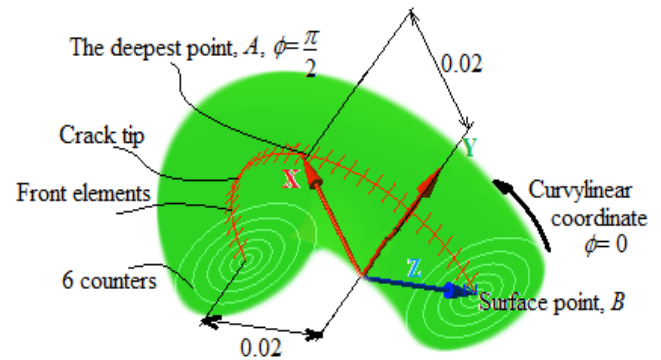


Figure 4. Parameters of the semi-elliptical surface crack

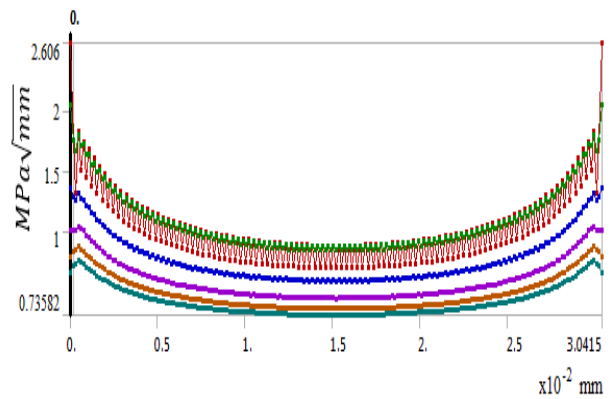


Figure 5. SIF results in the crack front

4.2 Plastic Zone Sizes

PZ equations are drawn using those numerical values. SIF is taken as $K_1 = 0.73582 \text{ MPa}\sqrt{\text{mm}}$. A polar coordinate axis is located at the crack tip and θ is taken between 0-360°. The yield strength is substituted for $\bar{\sigma}$. For verification, the Von Mises based PZ equations (13) are compared to Equation (14) [24, 25]. The Tresca based PZ equations (15) are compared to Equation (16) [24, 25] as seen in Figure 6. It is seen that curves have the same sizes [8, 28]. A self-comparison between the quadratic Hill48 and specific Hill48 for plane stress based PZ equations is done on Figure 7. It is verified that both of Equation (16, 18) draw the same zone size. Figure 7 also includes PZs from Irwin, Dugdale and first approximation equations for comparison.

As seen in Figure 8, the darker blue line is obtained when $F=1/2, G=1/2, H=1/2$ where Hill48 equation turns to Von Mises equation. So, these equations are completely consistent with the ones shown by [29, 30].

4.3 Anisotropy Dependencies

For Hill48 and Hu2003 criteria, $F, G, H, N, M,$ and HU coefficients depend on anisotropy coefficients r_0, r_{45}, r_{90} . By changing the anisotropy coefficients from $r_{45} = 1.1, r_{90} = 0.9$ to zero gradually, PZs are drawn. Figure 8, 9 show anisotropy dependencies of PZs based on Hill48 and Hu2003 criteria. Results are verified using the fact that Hill48 criterion becomes Von Mises criterion when $F = 1/2, G = 1/2, H = 1/2$. In literature, any study including Hu2003 is not seen. So the obtained results from Hu2003 equations are just given. At first sight, it is seen that the Hu's PZ size is much smaller than that of Tresca but bigger than that of Hill48.

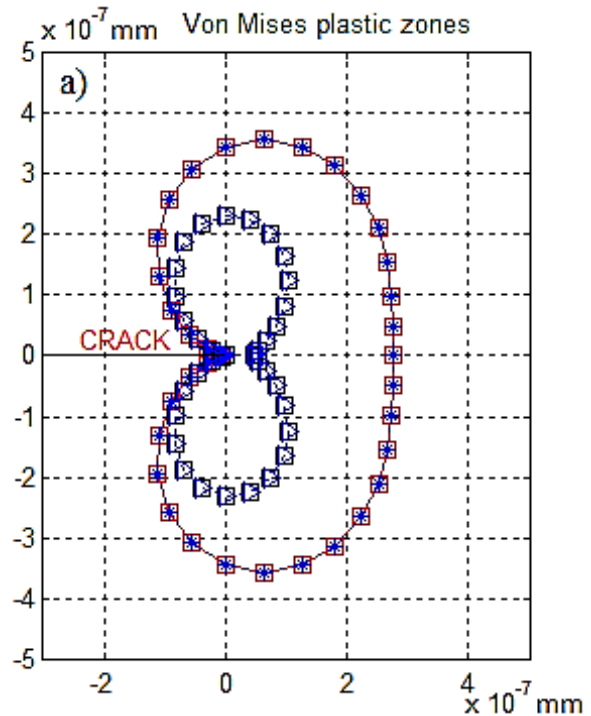
It is noted that when anisotropy increases, the zone shape transits kidney to butterfly-like shape. While, PZ at the cracked-plane direction is getting shorten, its size is increasing at $\pm 30^\circ-60^\circ$. It will affect the crack initiation angle because the larger PZ produces the higher SIF due to the more energy requirement for plastic deformation. R -criterion [31] is one of the criteria used to predict crack propagation path based on PZ's size.

4.4 FEA Results

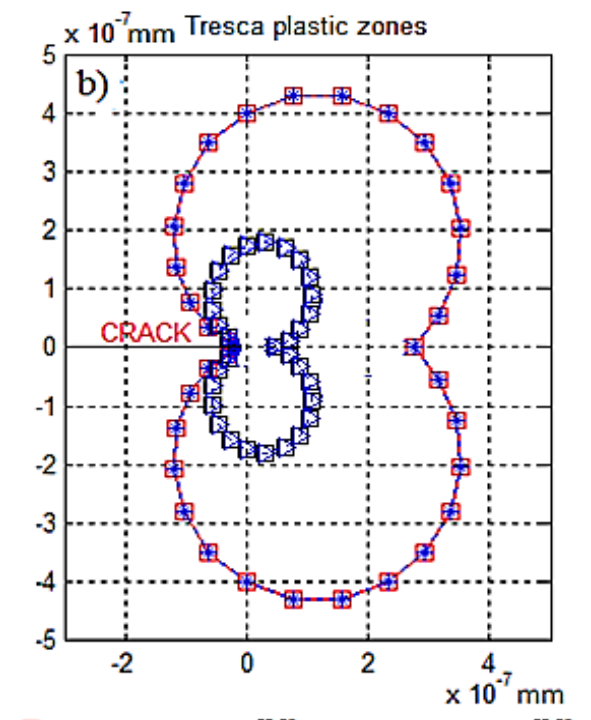
The nonlinear structural analysis takes 7 hours 56 minutes on the computer with 4 GB RAM and 2.4 GHz CPU. Equivalent total strain and stress developed on the crack tip are seen in Figure 10 and 11. As expected, stress becomes constant after yield starts because perfect plastic material model has no hardening behavior. Diddering on the straight section of the curve is due to residuals on each increment in the load steps. Stress counters and strain iso-lines show that PZ takes butterfly-like shape at the crack tip through the crack curve.

4.5 Blunting of the Crack Tip

Figures 12 shows blunting of the crack tip. It is drawn by exaggerating 100 times. Bluntness cause to shape change at the crack tip. After deformation, no skewness on the crack tip elements are seen. This comparison implies no complication during blunting.



—□— Pl.stress-A.Uguz [24] □ Pl.strain-A.Uguz [24]
 - - * - - Pl.stress-Present - - > - - Pl.strain-Present



—□— Pl.stress-P.Schreurs [25] □ Pl.strain-P.Schreurs [25]
 - - * - - Pl.stress-Present - - > - - Pl.strain-Present

Figure 6. Comparisons of plastic zone sizes based on (a) Von Mises and (b) Tresca

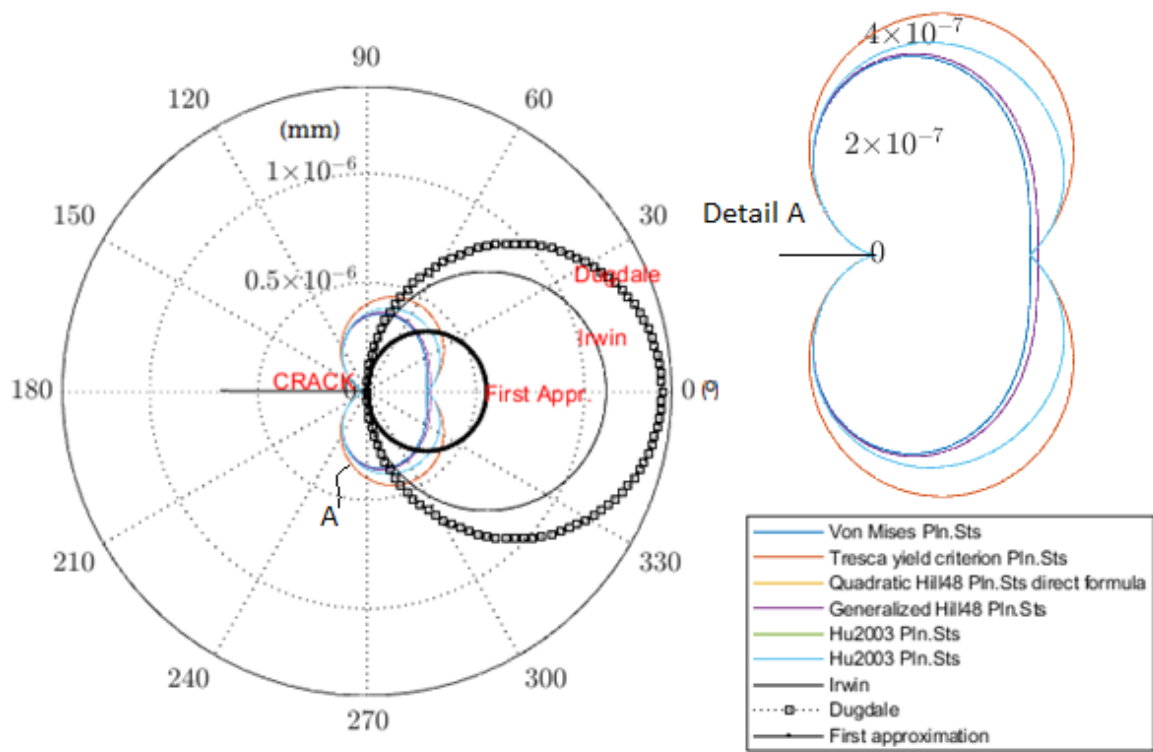


Figure 7. Plastic zones sizes based on various criteria

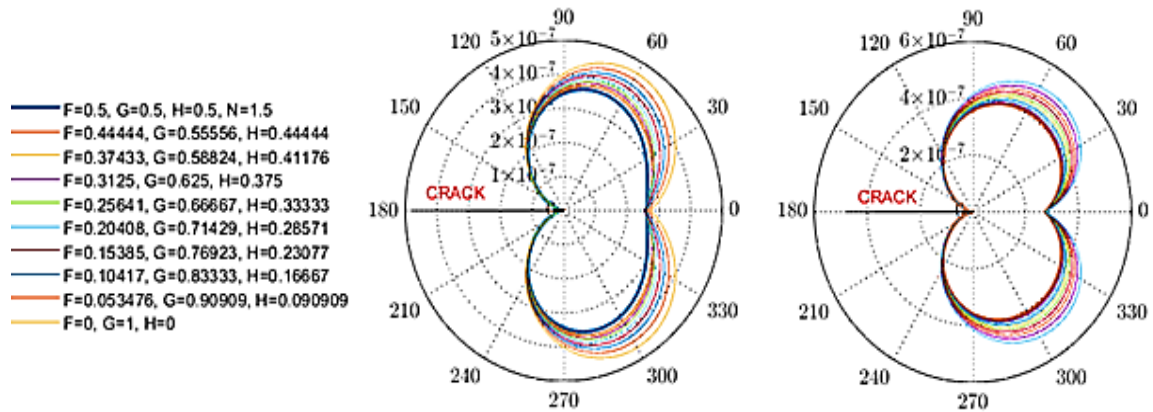


Figure 8. While r_0 and r_{90} change, PZ based on (a) Hill48 and (b) Hu2003

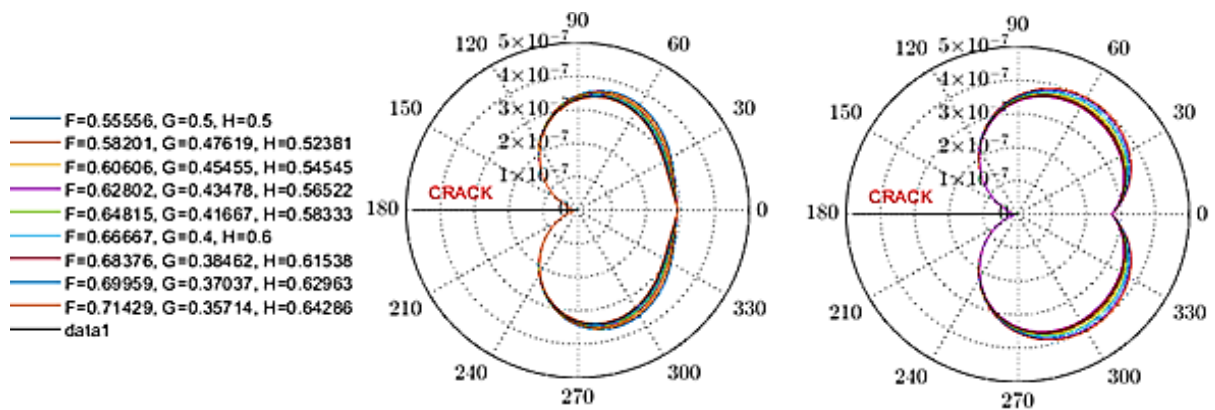


Figure 9. While r_0 and r_{45} change, PZ based on (a) Hill48 and (b) Hu2003

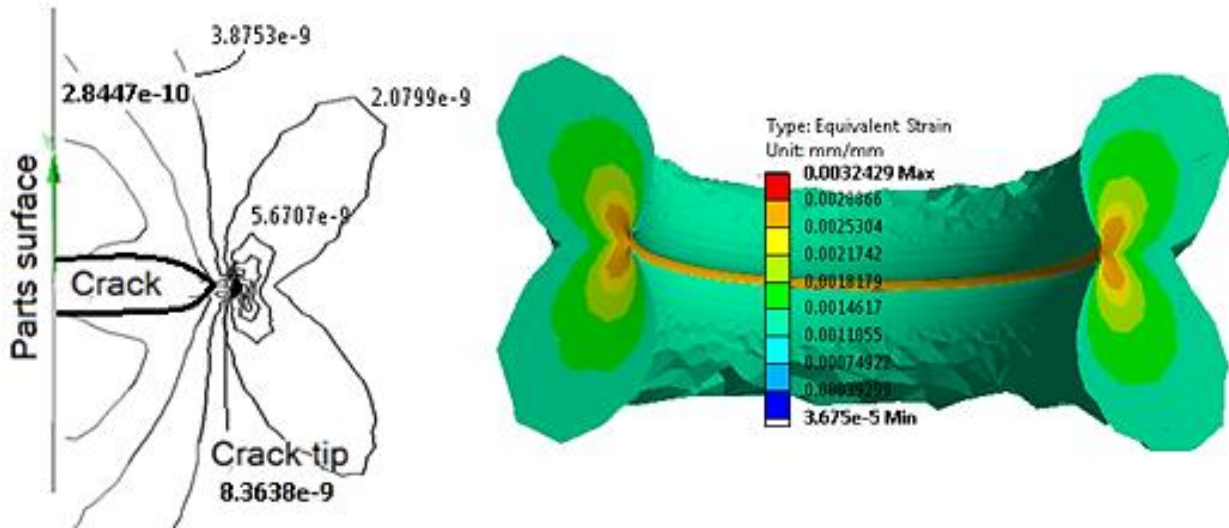


Figure 10. Equivalent strain iso-lines and 3D model from FEA (Unit: mm/mm)

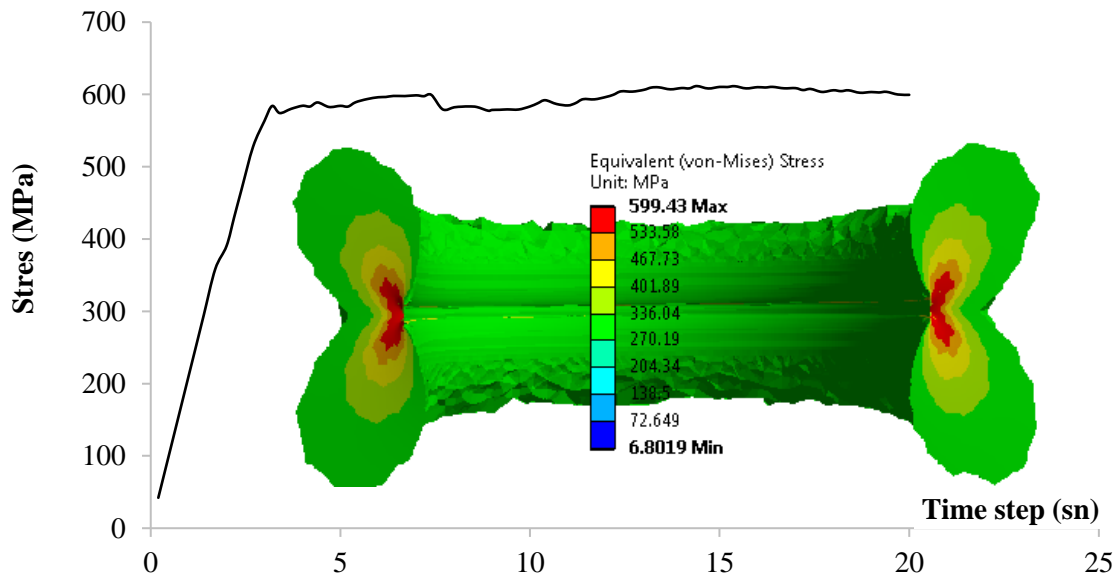


Figure 11. Equivalent stress distribution along the crack tip curve

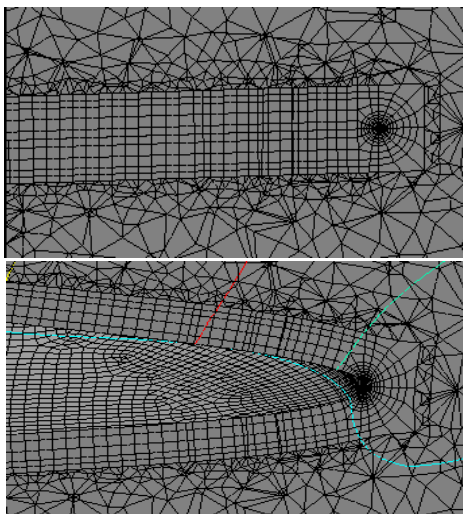


Figure 12. Crack tip profile a) before loading b) blunting after loading

5. Conclusions

PZs are necessary for calculation of crack propagation path. PZ's shape and size are analyzed for different anisotropy conditions. SIFs are obtained by performing a finite element simulation under isotropic and large-scale plasticity conditions. Also stress, strain distribution and blunting of the crack tip is given. So the following inferences are concluded.

- PZ sizes are obtained for the pipe made from 41Cr4 sheet metal by using four yield criteria: the Von Mises, Tresca, Hill48, and Hu2003.
- Results obtained from the Von Mises and Tresca verify that the derived equations provide the same shapes with literature. The area of PZ based on Tresca is larger than that of the Von Mises. The larger PZ leads to the higher SIF.

- Hill48-based PZ equation is verified using the fact that the equation must turn to Von Mises equation when $F=1/2, G=1/2, H=1/2$.
- With respect to rolling direction, especially transverse anisotropy has higher effect on the PZ in the equation based on Hill48 and Hu2003. While PZ size increases for increasing anisotropy in transverse direction, PZ size decreases for increasing anisotropy at 45° . Increasing anisotropy affects the PZ's size.
- For increasing transverse anisotropy, Hill48-based PZ's shape transits from kidney to butterfly shape. Similarly, it transits from kidney to hearth shape for increasing anisotropy at 45° , it is a characteristic shape generally seen for increasing shear stresses or inclined angle in some cases.
- It is seen that stress becomes constant when material starts to yield due to no hardening in perfect plastic nature of selected hardening model.

Within the scope of this study, PZs are obtained. Crack propagation analyses will be performed as a future work.

Declaration

The author declared no potential conflicts of interest with respect to the research, authorship, and/or publication of this article. The author(s) also declared that this article is original and prepared in accordance with international publication and research ethics. Neither ethical committee permission nor special permission is required.

References

1. Alizadeh Kaklar, J. and H. Saeidi Googarchin, *Approximate stress intensity factors for a semi-circular crack in an arbitrary structure under arbitrary mode I loading*. Theoretical and Applied Fracture Mechanics, 2018. **94**: p. 71-83.
2. Burcham, M.N., et al., *Characterization and Failure Analysis of an Automotive Ball Joint*. Journal of Failure Analysis and Prevention, 2017. **17**(2/2017): p. 13.
3. Uguz, A. and S.H. Oka, *Modeling the effects of mechanical loads - Finite element modeling of ball joints under dynamic loading*. Materialpruefung/Materials Testing, 2004. **46**: p. 506-512.
4. Verim Ö. and M. Yumurtacı, *Application of reverse engineering approach on a damaged mechanical part*. International Advanced Researches and Engineering Journal, 2020. **4**(1): p. 21-28.
5. Do, T.D., et al., *Determination of Plastic Zone Sizes at the Crack Tip*. Materials Characterization: Modern Methods and Applications, 2016: p. 175-197.
6. Yi, Z.H. and S. Sun, *Thickness Effect on Fracture Toughness and Plastic Zone Size*. Proceedings of the 2010 International Conference on Mechanical, Industrial, and Manufacturing Technologies (Mimt 2010), 2010: p. 1-5.
7. Armentani, E., et al., *Plastic zone size as EPFM parameter*. Advances in Fracture and Damage Mechanics, 2003. **251-2**: p. 173-178.
8. Gao, X., et al., *Analytic solutions to crack tip plastic zone under various loading conditions*. European Journal of Mechanics a-Solids, 2010. **29**(4): p. 738-745.
9. Adetifa, O.A., *Estimating Plastic Zone Sizes for Edge Cracks*. International Journal of Fracture, 1984. **24**(4): p. R115-R120.
10. MakeltFrom. *Hardened (+H) 1.7035 Steel*. 2020 February 25, 2019 []; Available from: <https://www.makeitfrom.com/material-properties/Hardened-H-1.7035-Steel>.
11. Creese, R.C., *Introduction to Manufacturing Processes and Materials*. 1999: CRC Press, Taylor and Francis Group.
12. Tada, H., P.C. Paris, and G.R. Irwin, *The Stress Analysis of Cracks Handbook*. 1973, Hellertown, Pennsylvania: Del. Research Corporation.
13. Kacar, İ., *Fracture mechanics: weight function method*, in *Academic Studies in Engineering Sciences-2019/2*, T.Y. Ali Kılıçer, Editor. 2019, Ivpe press: Cetinje-Montenegro, Cetinje, Montenegro. p. 149-173.
14. Kacar, İ., *An example application for calculating the stress intensity factor by using the weight function method*, in *Academic Studies in Engineering Sciences-2019/2*, T.Y. Ali Kılıçer, Editor. 2019, Ivpe press: Cetinje-Montenegro, Cetinje, Montenegro. p. 174-188.
15. MathWorks Inc, *MATLAB : the language of technical computing : computation, visualization, programming : installation guide for UNIX version 5*. 1996: Natwick : Math Works Inc., 1996.
16. Mises, R.V., *Mechanics of solid bodies in the plastically-deformable state*. Mathematisch-physikalische Klasse, 1913. **1**: p. 582-592.
17. Nadai, A., *Theory of flow and fracture of solids*. 2nd ed. ed. Engineering societies monographs. 1950: New York, NY : McGraw-Hill.
18. Hill, R., *A theory of the yielding and plastic flow of anisotropic metals*. Mathematical, Physical and Engineering Sciences, 1948. **193**(1033): p. 281-297.
19. Kılıç S., Toros S., Kacar İ and Fahrettin Ö., *Sonlu Elemanlar Analizlerinde Sac Metal Şekillendirme Parametrelerinin İncelenmesi*, in *Geleceğin Dünyasında Bilimsel ve Mesleki Çalışmalar-Mühendislik ve Teknoloji*, Ö.T. M. Lüy, E. Çam, N. Barışçı, M. D. Demirbaş & M. Güçyetmez, Editor. 2018, Ekin Basım Yayın Dağıtım: Bursa.
20. Colby, R.B., *Equivalent Plastic Strain for the Hill's Yield Criterion under General Three-Dimensional Loading*, in *Department of Mechanical Engineering at the Massachusetts Institute of Technology*. 2013, Massachusetts Institute of Technology: Massachusetts Institute of Technology. p. 45.
21. Sun, C.T. and Z.H. Jin, *Chapter 6 - Crack Tip Plasticity*, in *Fracture Mechanics*, C.T. Sun and Z.H. Jin, Editors. 2012, Academic Press: Boston. p. 123-169.
22. Irwin, G.R., *Plastic Zone Near a Crack Tip and Fracture Toughness*, in *Sagamore Ordnance Material Conference*. 1960. p. IV63-IV78.
23. Dugdale, D.S., *Yielding of steel sheets containing slits*. Journal of the Mechanics and Physics of Solids, 1960. **8**(2): p. 100-104.
24. Uğuz, A., *Kırılma Mekaniğine Giriş*. 1.Baskı ed. 1996, Bursa: Vipaş Yayınları.
25. Schreurs, P. *Fracture Mechanics (4A780)*. 2020 [cited 2020 January, 2020]; Available from:

<http://www.mate.tue.nl/~piet/edu/frm/htm/frmnum1112.html>.

26. DeSalvo, G.J. and J.A. Swanson, *ANSYS engineering analysis system user's manual*. 1985, Houston, Pa: Swanson Analysis Systems.
27. Ji, X., F. Zhu, and P.F. He, *Determination of stress intensity factor with direct stress approach using finite element analysis*. *Acta Mechanica Sinica*, 2017. **33**(5): p. 879-885.
28. Ivey, J., *Analytic Solutions for the Crack-Tip Plastic Zone under Mixed Mode Loading Conditions*, in *Mechanical Engineering*. 2017, University of New Mexico: Albuquerque, New Mexico.
29. Khan, S.M.A. and M.K. Khraisheh, *The anisotropic R-criterion for crack initiation*. *Engineering Fracture Mechanics*, 2008. **75**(14): p. 4257-4278.
30. Cao, J., et al., *Study of anisotropic crack growth behavior for aluminum alloy 7050-T7451*. *Engineering Fracture Mechanics*, 2018. **196**: p. 98-112.
31. Khan, S.M.A. and M.K. Khraisheh, *A new criterion for mixed mode fracture initiation based on the crack tip plastic core region*. *International Journal of Plasticity*, 2004. **20**(1): p. 55-84.



e-ISSN: 2618-575X

INTERNATIONAL ADVANCED RESEARCHES
and
ENGINEERING JOURNAL

Journal homepage: www.dergipark.org.tr/en/pub/iarejInternational
Open Access Volume 04
Issue 02

August, 2020

Research Article

Investigation of nonlinear behavior of high ductility reinforced concrete shear walls

Saeid Foroughi ^{a,*}  and S. Bahadır Yüksel ^a 

^a Konya Technical University, Faculty of Engineering and Natural Sciences, Department of Civil Engineering, 42130, Konya / Turkey

ARTICLE INFO**Article history:**

Received 24 February 2020

Revised 04 May 2020

Accepted 24 May 2020

Keywords:

Curvature ductility
Displacement ductility
Lateral force
Moment-curvature
Nonlinear behavior
Peak displacement
Shear wall

ABSTRACT

In this study, the nonlinear behavior of ductile reinforced concrete (RC) shear walls having different parameters was analytically investigated. The purpose of this study is to determine the effect of axial load, longitudinal reinforcement ratio and transverse reinforcement ratios on the moment-curvature and lateral force-lateral peak displacement relationships of RC shear walls. RC shear walls that have various parameters were designed by taking into account the regulation of the Turkish Building Earthquake Code (TBEC, 2018). By considering the nonlinear behavior of the materials, behaviors of the RC shear walls were examined within the framework of the moment-curvature relation. The moment-curvature relations of RC shear walls with different parameters were obtained with the Mander model which takes into consideration the lateral confined concrete strength for different parameters. The effects of the analyzed parameters on the nonlinear behavior of the RC shear walls were evaluated in terms of curvature ductility, moment capacity, peak displacement, the angular displacement and displacement ductility values. It was seen that changes in the transverse reinforcement, longitudinal reinforcement, and axial load levels had important influence on the moment-curvature and lateral force-lateral peak displacement behavior of the RC shear walls.

© 2020, Advanced Researches and Engineering Journal (IAREJ) and the Author(s).

1. Introduction

Predicting the deformation capacity of RC shear walls is very important for a comprehensive performance-based seismic evaluation of existing or new buildings [1]. In order to achieve a more accurate simulation of the real structural behavior, designers need the accurate moment-curvature relationship for RC members and stress-strain relationships for unconfined and confined concrete [2]. To be able to understand if a structural design, realized regarding a specific seismic code or not, achieves the main aim of the seismic design, displacement ductility can be utilized [3].

RC shear walls are used effectively in earthquake-resistant building design or strengthening of existing structures in terms of the earthquake. In the seismic design performed displacement-based and for the performance assessment of structural members, sectional deformation quantities, such as ductility and curvature, have great importance. Nonlinear analysis are tools where the deformation response of structural elements is predicted

according to the displacement-based procedures [4-5]. In this study, a parametric study was conducted in order to determine the effects of axial load levels (N/N_{max}), longitudinal reinforcement ratio, transverse reinforcement diameter and transverse reinforcement spacing on RC shear wall behavior. Many modeling approaches and analysis programs represent the nonlinear behavior of RC shear walls with different approaches. The behaviors of RC shear walls were examined over moment-curvature and lateral load-lateral peak displacement relations considering the nonlinear behavior of the materials. For this analytical study, a rectangular cross-sectional RC shear walls were designed. The rules are given in TS500 [6] and TBEC [7] are taken into consideration in the design of RC shear walls (Figure 2 and Table 1). The effects of different longitudinal reinforcement ratios, different axial load levels, transverse reinforcement diameters, and spacing on the nonlinear behavior of RC shear walls were investigated.

Inelastic behavior of the sections were obtained with the

* Corresponding author. Tel.: +90 332 205 17 71.

E-mail addresses: saeid.foroughi@yahoo.com (S. Foroughi), sbyuksel@ktun.edu.tr (S.B. Yüksel)

ORCID: 0000-0002-7556-2118 (S. Foroughi), 0000-0002-4175-1156 (S.B. Yüksel)

DOI: 10.35860/iarej.693724

aid of the moment-curvature relationship based on the actual material behavior. The effects of axial load level, transverse reinforcement, longitudinal reinforcement, and special seismic cross-ties on the moment-curvature behaviors for the RC shear wall models were investigated and interpreted in detail. Lateral force-lateral peak displacement relationships were obtained and interpreted with the aid of the moment-curvature relationships of the RC shear walls.

2. Nonlinear Displacement in Reinforced Concrete Shear Walls

A significant part of the seismic design of concrete wall buildings is to ensure that the flexural displacement capacity of the shear walls is bigger than the flexural displacement demand [8]. The flexural displacement characteristic of a cantilever shear wall is normally the sum of the yield and the plastic displacement [9]. To determine the seismic response of RC structural walls, the plastic hinge method is still utilized broadly in seismic designs performed displacement-based and in the performance evaluation processes [10].

In the moment-curvature relationship, the RC shear wall peak displacement value up to the yield curvature can be calculated by Equation (1). The lumped plastic rotation (θ_p), along the plastic hinge length (L_p) is then computed using Equation (2). Where φ_u refers to the maximum curvature and φ_y refers to the yield curvature, as shown in Figure 1.

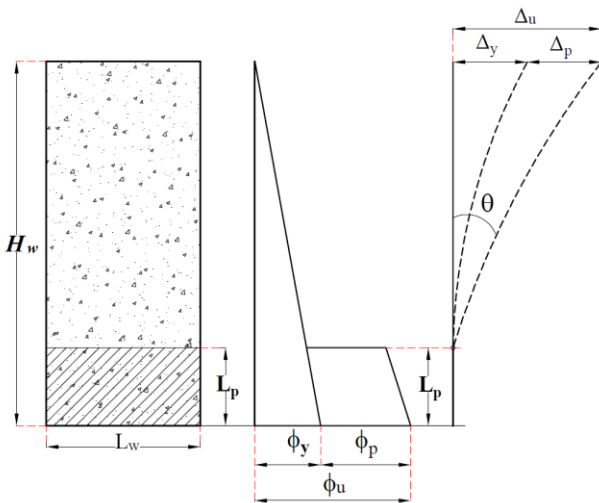


Figure 1. Theoretical model of elastic and plastic displacements in cantilever RC shear wall

In the plastic hinge analysis, the total peak displacement of the RC shear wall before the collapse (Δ_u) is obtained by summing its yield displacement (Δ_y) and plastic displacement (Δ_p) components (Equation (4)). H_w is the total height in the RC shear walls. After the calculation of both displacements, displacement ductility is determined

as $\mu_\Delta = \Delta_u/\Delta_y$. The angular displacement of the RC shear wall before the collapse (θ_u) can be calculated by Equation (5).

$$\Delta_y = \frac{\varphi_y \times H_w^2}{3} \quad (1)$$

$$\theta_p = \varphi_p L_p = (\varphi_u - \varphi_y) L_p \quad (2)$$

$$\Delta_p = (\varphi_u - \varphi_y) \times L_p \times (H_w - 0.50L_p) \quad (3)$$

$$\Delta_u = \Delta_y + \Delta_p \quad (4)$$

$$\theta_u = \frac{\varphi_y \times H_w}{2} + (\varphi_u - \varphi_y) \times L_p \quad (5)$$

To be able to determine the plastic hinge length (L_p), different equations have been suggested. For obtaining a safe displacement capacity from the curvature capacity, plastic hinge length may be considered as half of the shear wall length [8]. According to [7-8, 10-12], the length of the plastic deformation region called as plastic hinge length (L_p) is taken as the half of the section length in the active direction ($L_p = 0.50h$). The most significant parameter that affects the plastic hinge length is the dimensions of the reinforced concrete shear walls. The increases in plastic hinge length significantly affect the displacement and displacement ductility values of reinforced concrete shear walls [13].

3. Materials and Method

In this study, the nonlinear behavior of the rectangular cross-sectional high ductile RC shear walls were analytically investigated by changing the axial load levels, transverse reinforcement diameter, longitudinal reinforcement ratios, and transverse reinforcement spacing. For this analytical study, a rectangular cross-sectional concrete shear wall with 300mm×3000mm dimensions were designed. In TBEC [7] the ratio of the length of the long edge ($l_w = 3000\text{mm}$) of the RC shear walls to the thickness ($b_w = 300\text{mm}$) in the plan has been determined to be greater than six ($l_w > 6b_w$). As the ratio of the total height ($H_w = 10000\text{mm}$) in the RC shear walls to the plan length ($l_w = 3000\text{mm}$) is chosen to be greater than two ($H_w/l_w > 2$), the shear walls confined boundary elements are formed at both ends of the walls. Confined boundary region dimensions (l_u) of RC shear walls are chosen as 300mm×600mm.

The reinforcement diameters and reinforcement ratio used in the shear wall cross-sections were determined by considering the limitations given by TBEC [7]. According to TBEC [7], total cross-section area of each of the longitudinal and transverse web reinforcement on both faces of the structural wall shall not be less than 0.0025 of the cross-section area of the shear wall web remaining in between the shear wall boundary regions. The ratio of the

total longitudinal reinforcement area at each wall boundary region to the gross wall cross-section area shall not be less than 0.0025 along with the critical shear wall height. The longitudinal and transverse web reinforcement spacing of the RC shear walls were designed according to TBEC [7]. Longitudinal web reinforcement and longitudinal reinforcements in boundary regions limitations were checked for the designed RC shear wall according to the TBEC [7]. Checked of the longitudinal reinforcement limitations in web and boundary regions for the designed RC shear wall are given Table 2. For all

models, as concrete grade, C30 was selected, and as reinforcement, B420C was used. The stress-strain curves presented in TBEC [7] were utilized for the reinforcement behavior model. In the analytical study for RC shear walls, the material parameters given in Table 3 for reinforcement and concrete are used. For concrete classes, concrete elasticity modulus (E_c) are calculated according to the concrete compressive strengths (f_{ck}) given in TS500 [6], ($E_c = 3250\sqrt{f_{ck}} + 14000 \text{ MPa}$).

$$\frac{A_s}{(l_w - 2l_u) \times b_w} \geq 0.0025 \leftrightarrow \frac{A_s}{(3000 - 2 \times 600) \times 300} \geq 0.0025 \leftrightarrow A_s \geq 1350 \text{ mm}^2 \tag{6}$$

$$\frac{A_s}{l_w \times b_w} \geq 0.002 \leftrightarrow \frac{A_s}{3000 \times 300} \geq 0.002 \leftrightarrow A_s \geq 1800 \text{ mm}^2 \tag{7}$$

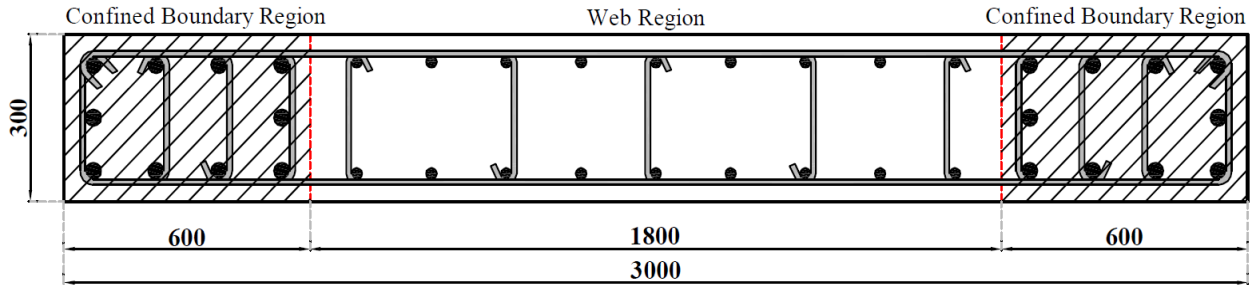


Figure 2. The sectional geometry and reinforcement appearance of RC shear walls

Table 1. Details for the designed RC shear wall cross-sections

No	Longitudinal reinforcement on confined boundary region	Transverse reinforcement on confined boundary region	Longitudinal reinforcement on shear wall web region	Transverse reinforcement on shear walls
P1	10Φ16mm	Φ8/150mm	18Φ12mm	Φ8/150mm
P2	10Φ16mm	Φ8/100mm	18Φ12mm	Φ8/100mm
P3	10Φ16mm	Φ8/50mm	18Φ12mm	Φ8/50mm
P4	10Φ16mm	Φ10/100mm	18Φ12mm	Φ10/100mm
P5	10Φ16mm	Φ12/100mm	18Φ12mm	Φ12/100mm
P6	10Φ16mm	Φ14/100mm	18Φ12mm	Φ14/100mm
P7	10Φ18mm	Φ12/100mm	18Φ12mm	Φ12/100mm
P8	10Φ20mm	Φ12/100mm	18Φ12mm	Φ12/100mm
P9	10Φ20mm	Φ12/100mm	18Φ14mm	Φ12/100mm
P10	10Φ20mm	Φ12/100mm	18Φ16mm	Φ12/100mm

Table 2. Longitudinal reinforcement limitations in web and boundary regions for the designed shear wall [7]

Longitudinal web reinforcement limitation			
Selected Reinforcement	18Φ12mm	18Φ14mm	18Φ16mm
$\frac{A_s}{(L_w - 2l_u) \times b_w} \geq 0.0025$	0.0038 \geq 0.0025	0.0051 \geq 0.0025	0.0067 \geq 0.0025
Longitudinal reinforcements in boundary region limitation			
Selected Reinforcement	10Φ16mm	10Φ18mm	10Φ20mm
$\frac{A_s}{L_w \times b_w} \geq 0.002$	0.0022 \geq 0.002	0.0028 \geq 0.002	0.0035 \geq 0.002

Table 3. Material parameters for concrete and reinforcement [7]

Standard Strength	Parameters	Values
Concrete: C30	Strain at maximum stress of unconfined concrete (ϵ_{co})	0.002
	Ultimate compression strain of concrete (ϵ_{cu})	0.0035
	Characteristic standard value of concrete compressive strength (f_{ck})	30MPa
Reinforcement: B420C	Yield strain of reinforcement (ϵ_{sy})	0.0021
	Strain hardening value of reinforcing steel (ϵ_{sp})	0.008
	Strain in reinforcing steel at ultimate strength (ϵ_{su})	0.080
	Characteristic yield strength of reinforcement (f_{yk})	420MPa
	Ultimate strength of reinforcement (f_{su})	550MPa

The relationships of moment-curvature were determined and shown as graphically by applying SAP2000 Software that takes into account nonlinear behaviors of materials [14]. The designed cross-section models of the reinforced shear wall were thought as consisting of three components. These components were confined concrete, cover concrete, and reinforcement steel. The material models of SAP2000 [14] are determined by taking into account the Mander unconfined concrete model for cover concrete, and the Mander confined concrete model [15] for core concrete. To be able to identify the moment-curvature relations of RC members, a concrete model suggested by the Mander model [15] that was broadly utilized, commonly accepted, and mandatory in TBEC [7] was utilized. In terms of reinforcement modeling, material parameters for reinforcement presented in TBEC [7] was utilized.

The influences of the analyzed parameters on the nonlinear behaviors of the RC shear walls were evaluated in terms of curvature ductility (μ_ϕ) and the moment capacity, yield displacement, plastic displacement, total peak displacement, the angular displacement of the shear wall (θ_u) and displacement ductility (μ_Δ) values. The moment-curvature and lateral force-lateral peak displacement curves were drawn for RC shear walls with different parameters and were interpreted by comparing the curves. The curvature ductility factor (μ_ϕ) is obtained by the ratio of curvature determined at the ultimate limit state and the curvature determined at the first yield ($\mu_\phi = \phi_u / \phi_y$).

The combined effect of seismic and vertical loads (N_{dm}) and cross-section area of the shear wall should meet the condition of $A_c \geq N_{dm} / 0.35 f_{ck}$ [7]. The moment-curvature, displacement and displacement ductility values were obtained for 0.15, 0.25, and 0.35 of axial load ratio for the RC shear wall sections. To be able to examine the influence of the axial load on the cross-section behaviors, the shear wall models were examined for three different axial forces: $N_1 = 4050kN$, $N_2 = 6750kN$ and $N_3 = 9450kN$.

It has been observed in previous studies that the moment-curvature behaviors of the reinforced concrete columns are affected significantly by changes occurring in

axial load, transverse reinforcement diameter, longitudinal reinforcement diameter, and transverse reinforcement spacing [16].

Yield displacement, plastic displacement and total displacement values of the elements were calculated for different axial load levels according to the calculated by plastic hinge length in RC shear wall sections. Elastic and plastic displacements are taken into consideration in the total displacement relations of RC shear walls. In calculating the total displacement of the RC shear walls, the yield and maximum curvature values were obtained from the moment-curvature relations which take into account the section height, plastic hinge length and nonlinear behavior are taken into consideration.

4. Research Findings and Discussion

The limits of the damage regions were calculated based on the moment-curvature relations of RC shear walls according to various parameters. Curvature and moment values were obtained for the yield curvature and curvature values before the collapse condition in RC shear wall sections. The curvature ductility of the RC shear wall sections were calculated according to the yield curvature and ultimate curvature values. Depending on the curvature values which were obtained from the curvature-moment relations, the peak displacement in the case of yield and pre-collapse, angular displacement of the shear walls and the peak displacement ductility values were obtained. The effects of the analyzed parameters on the nonlinear behaviors of the RC shear walls were evaluated in terms of curvature ductility and the moment capacity, yield displacement, plastic displacement, total peak displacement, the angular displacement of the shear wall, and displacement ductility values. The results of the investigations carried out on the moment-curvature relations are presented in tables and the failure types and behaviors of the RC shear wall sections are analyzed.

Yield curvature and maximum curvature values of the curvature-moment relations of the sections were obtained for the calculation of the total displacement values of the RC shear walls. According to different axial load levels, the displacement ductility of the shear walls was calculated

by obtaining yield, plastic and total displacement values of RC shear walls.

Comparison of the moment-curvature and lateral force-lateral peak displacement relationships of P1, P2 and P3 shear walls for different axial load levels are given in Figure 3. For constant axial load levels of P1, P2 and P3, moment-curvature relationships for different transverse reinforcement spacing are given in Figure 4. Moment-curvature and lateral force-lateral peak displacement relationships of P4, P5 and P6 for different axial load levels are given in Figure 5. For constant axial load levels of P4, P5 and P6, moment-curvature relationships for different transverse reinforcement diameters are given in Figure 6. Comparison of the moment -curvature and lateral force-lateral peak displacement relationships of P7 and P8 for various axial load levels are given in Figure 7. For constant axial load levels, moment-curvature relationships

for different longitudinal reinforcement diameters at the confined boundary region of P7 and P8 are given in Figure 8. Moment-curvature and lateral force-lateral peak displacement relationships of P9 and P10 for various axial load levels are given in Figure 9 comparatively. For constant axial load levels, comparison of the curvature-moment relations for various longitudinal reinforcement diameters at the web region of P9 and P10 are shown in Figure 10.

Values of curvature and moment were obtained for the yield curvature and curvature values before the collapse condition for various axial load levels in RC shear wall sections with different transverse reinforcement spacing. The μ_ϕ , Δ_y , Δ_u , θ_u and μ_Δ values of the P1, P2 and P3 shear wall sections for different transverse reinforcement spacing are presented in Table 4.

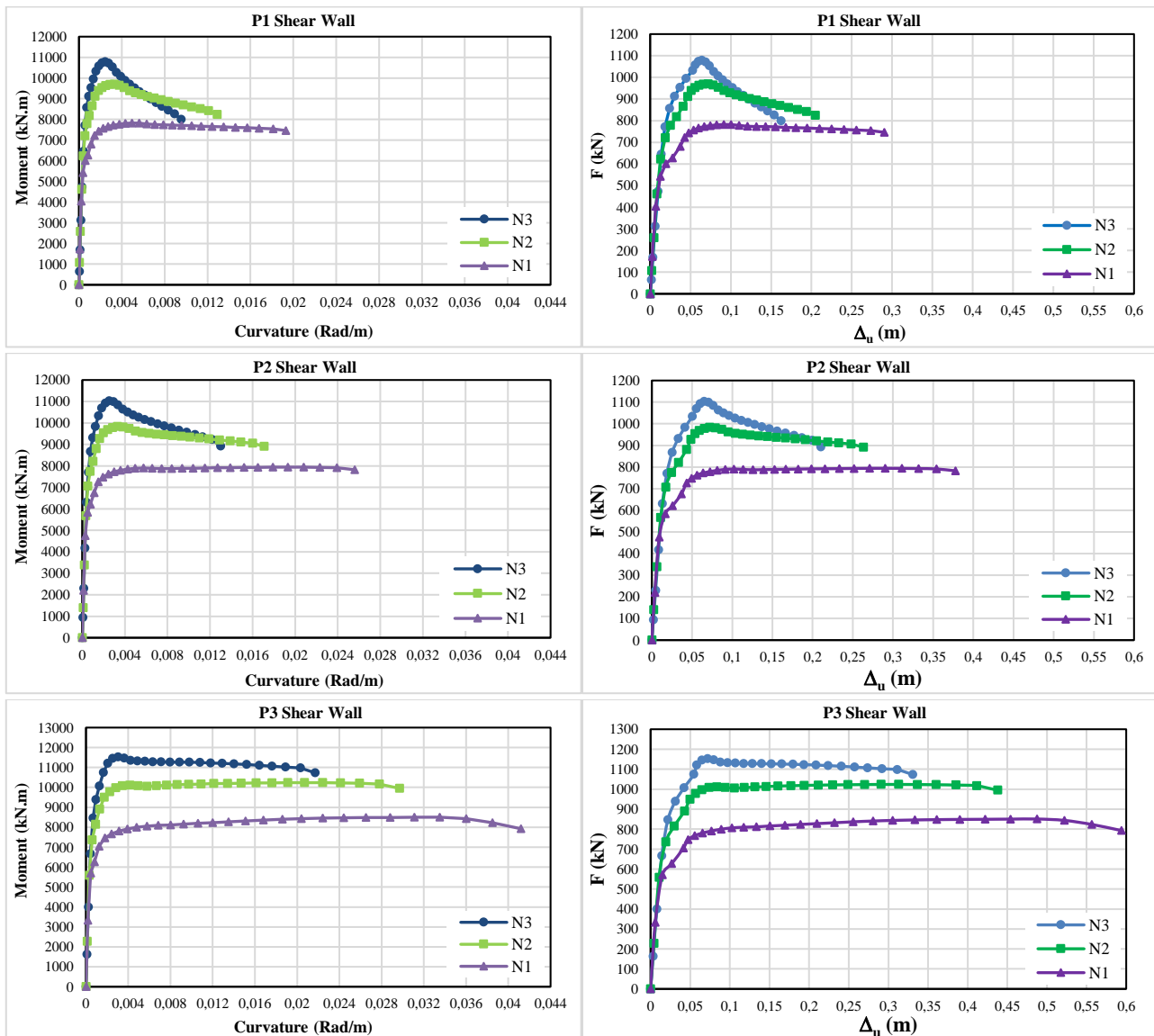


Figure 3. Moment-curvature and lateral force-lateral peak displacement relationships for different axial load levels

In RC shear walls (P4, P5 and P6) with different transverse reinforcement diameters, moment and curvature values were obtained for the yield curvature and curvature values before the collapse condition for different

axial load levels. According to the yield curvature and curvature values before the collapse, μ_ϕ , Δ_y , Δ_u , θ_u and μ_Δ values of P4, P5 and P6 shear wall sections are presented in Table (5).

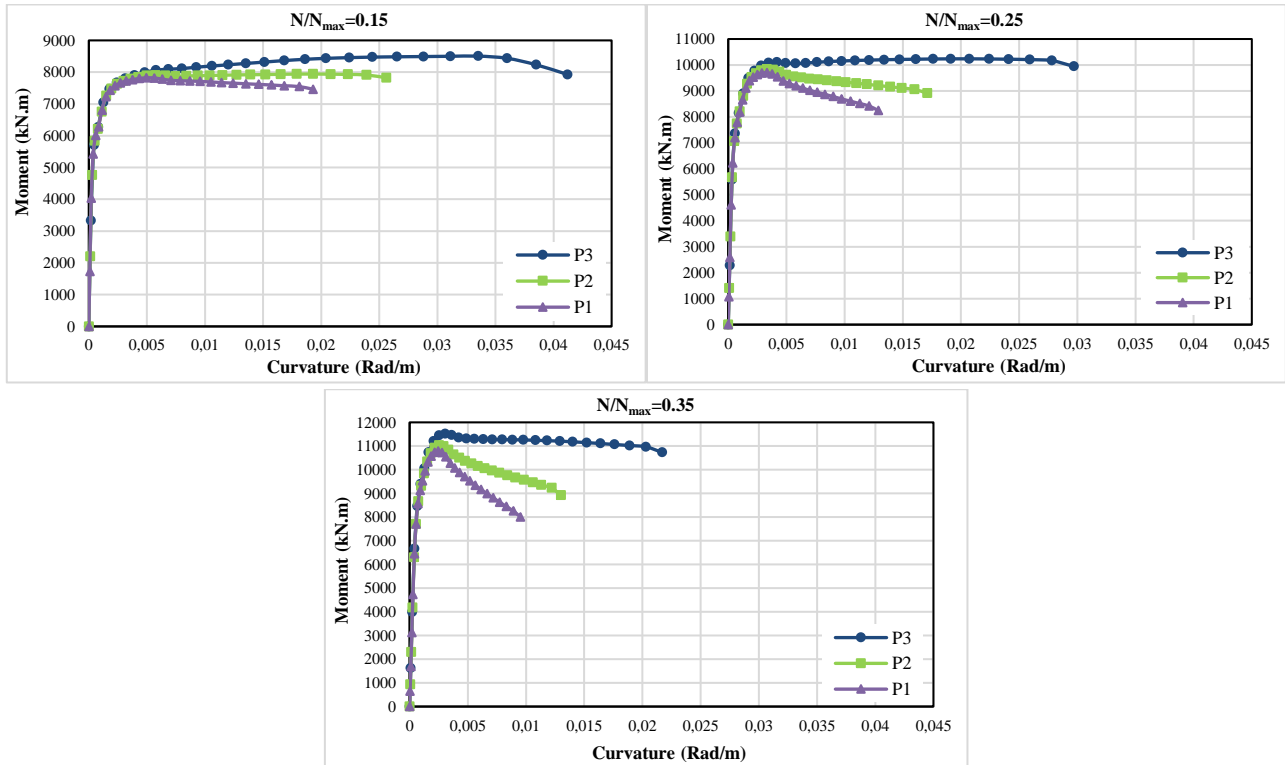


Figure 4. For different transverse reinforcement spacing, moment-curvature relations

Table 4. Analysis results of P1, P2 and P3 for different transverse reinforcement spacing

No	N/N_{max}	M_y (kN.m)	ϕ_y (Rad/m)	M_u (kN.m)	ϕ_u (Rad/m)	μ_ϕ	Δ_y (m)	Δ_u (m)	θ_u (Rad)	μ_Δ
P1	0.15	6847	0.0012	7523	0.0193	16.78	0.038	0.290	0.033	7.57
	0.25	8841	0.0013	9404	0.0129	9.70	0.044	0.205	0.024	4.62
	0.35	10290	0.0016	10490	0.0095	6.14	0.052	0.162	0.020	3.14
P2	0.15	6867	0.0012	7941	0.0256	22.26	0.038	0.378	0.042	9.85
	0.25	8871	0.0013	9837	0.0171	12.86	0.044	0.263	0.030	5.94
	0.35	10379	0.0015	11028	0.0130	8.44	0.051	0.210	0.025	4.10
P3	0.15	6895	0.0012	8506	0.0412	35.83	0.038	0.594	0.066	15.50
	0.25	8964	0.0013	10236	0.0297	22.50	0.044	0.438	0.049	9.95
	0.35	10546	0.0015	11519	0.0217	14.28	0.051	0.331	0.038	6.53

Table 5. Analysis results of P4, P5 and P6 shear wall sections for different transverse reinforcement diameters

No	N/N_{max}	M_y (kN.m)	ϕ_y (Rad/m)	M_u (kN.m)	ϕ_u (Rad/m)	μ_ϕ	Δ_y (m)	Δ_u (m)	θ_u (Rad)	μ_Δ
P4	0.15	6835	0.0012	8187	0.0360	31.30	0.038	0.522	0.058	13.61
	0.25	8896	0.0013	9946	0.0242	18.20	0.044	0.362	0.041	8.16
	0.35	10449	0.0015	11223	0.0173	11.23	0.051	0.270	0.031	5.26
P5	0.15	6897	0.0012	8471	0.0403	33.00	0.038	0.597	0.066	15.57
	0.25	8971	0.0013	10169	0.0327	24.59	0.044	0.480	0.054	10.82
	0.35	10531	0.0015	11487	0.0243	15.88	0.051	0.367	0.042	7.19
P6	0.15	6926	0.0012	8672	0.0406	35.30	0.038	0.657	0.072	17.64
	0.25	9043	0.0013	10610	0.0426	29.27	0.044	0.550	0.061	14.02
	0.35	10671	0.0015	11756	0.0299	19.80	0.050	0.444	0.050	8.83

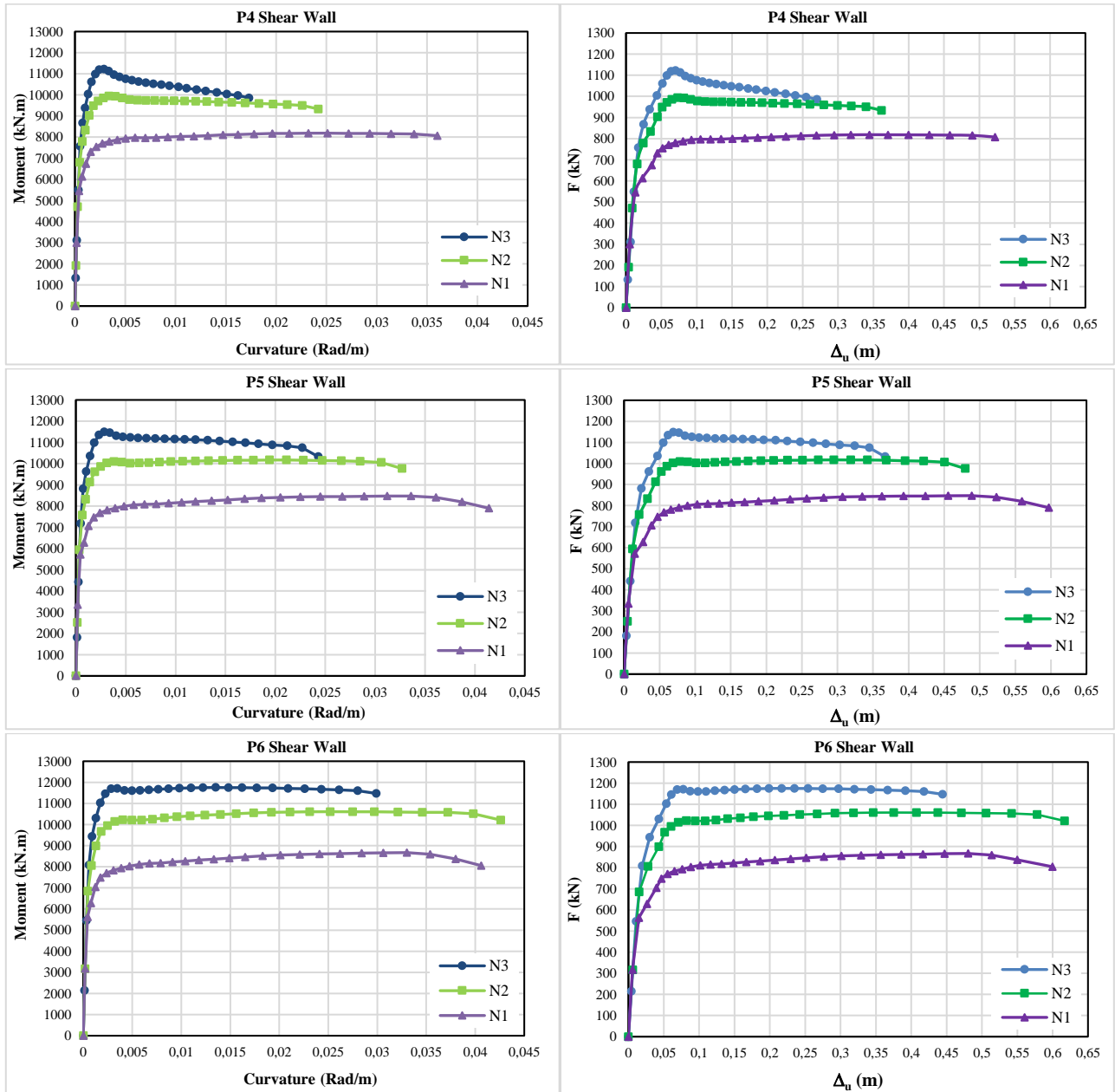


Figure 5. Moment-curvature and lateral force-lateral peak displacement relationships for different axial load levels

Moment and curvature values were obtained for the yield curvature and curvature values before the collapse condition of P7 and P8 with different longitudinal reinforcement diameters at the confined boundary region

for different axial load levels. According to the yield curvature and curvature values before the collapse condition, μ_ϕ , Δ_y , Δ_u , θ_u and μ_Δ values of the P7 and P8 shear wall sections are presented in Table 6.

Table 6. Analysis results of P7 and P8 shear walls for different longitudinal reinforcement diameters at the confined boundary region

No	N/N_{max}	M_y (kN.m)	ϕ_y (Rad/m)	M_u (kN.m)	ϕ_u (Rad/m)	μ_ϕ	Δ_y (m)	Δ_u (m)	θ_u (Rad)	μ_Δ
P7	0.15	7328	0.0012	9144	0.0414	35.69	0.039	0.597	0.066	15.44
	0.25	9403	0.0013	10798	0.0327	24.59	0.044	0.480	0.054	10.82
	0.35	10972	0.0015	12011	0.0243	15.88	0.051	0.367	0.042	7.19
P8	0.15	7811	0.0012	9891	0.0413	35.3	0.039	0.596	0.066	15.28
	0.25	9896	0.0013	11503	0.0323	24.29	0.044	0.474	0.053	10.69
	0.35	11464	0.0015	12595	0.0243	15.88	0.051	0.367	0.042	7.19

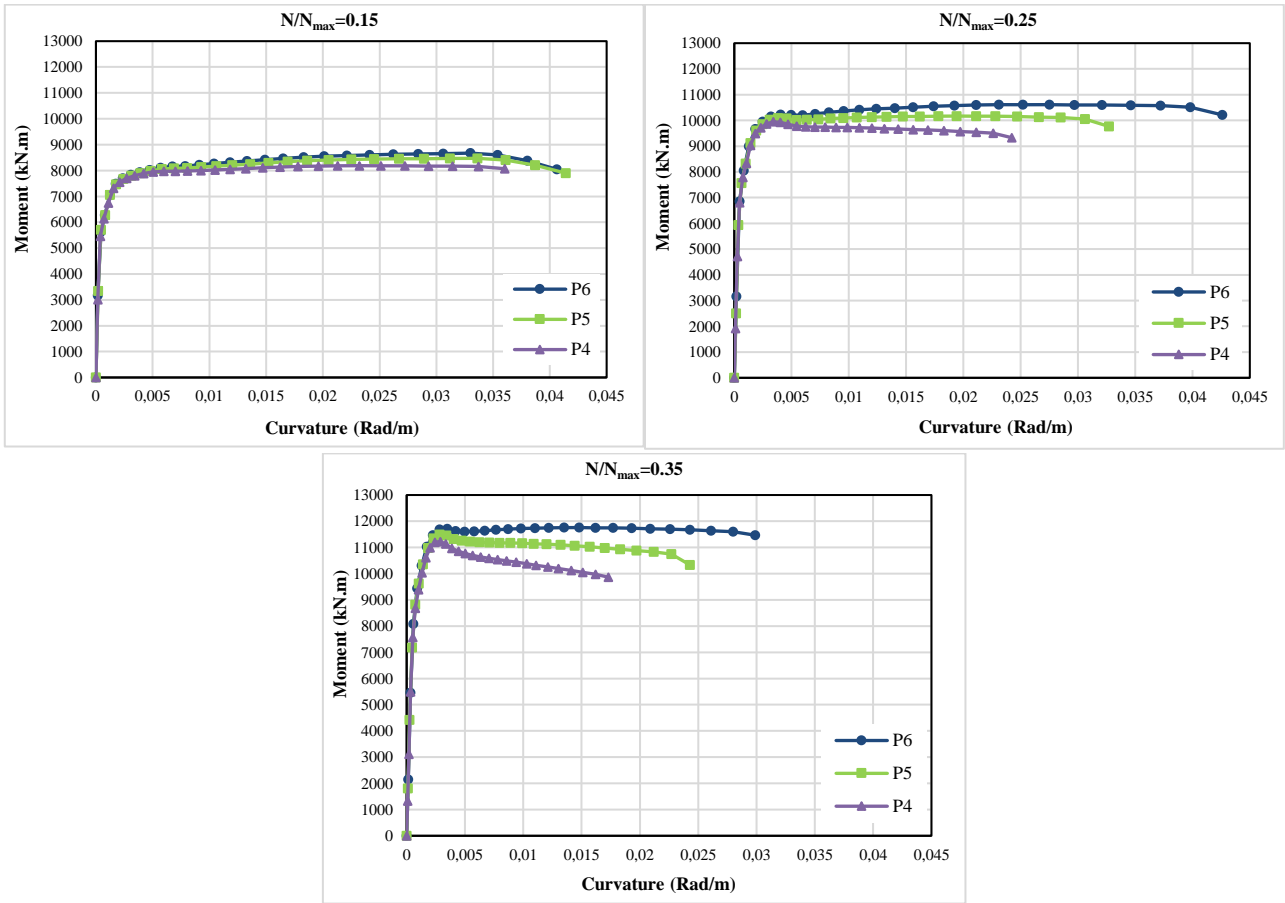


Figure 6. Moment-curvature relationships of P4, P5 and P6 for different transverse reinforcement diameters

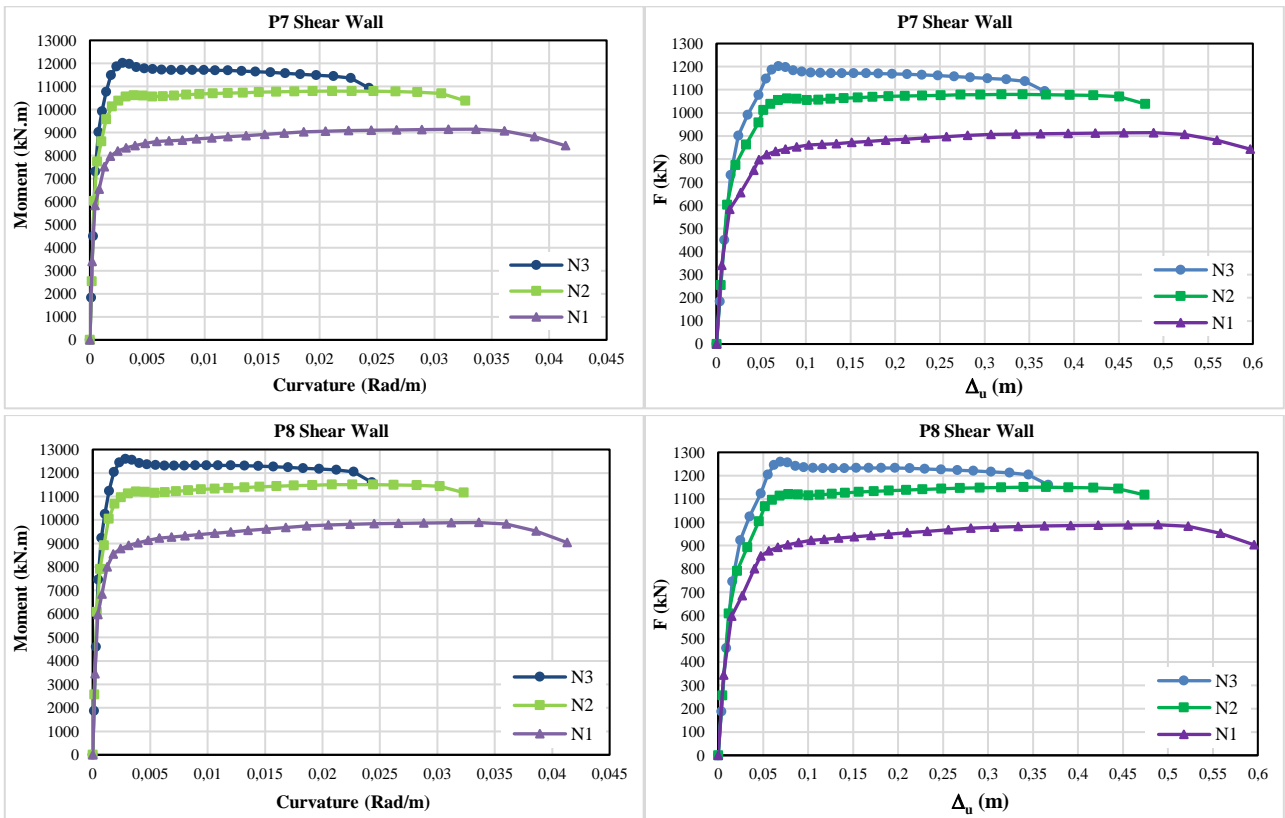


Figure 7. Moment-curvature and lateral force-lateral peak displacement relationships for different axial load levels

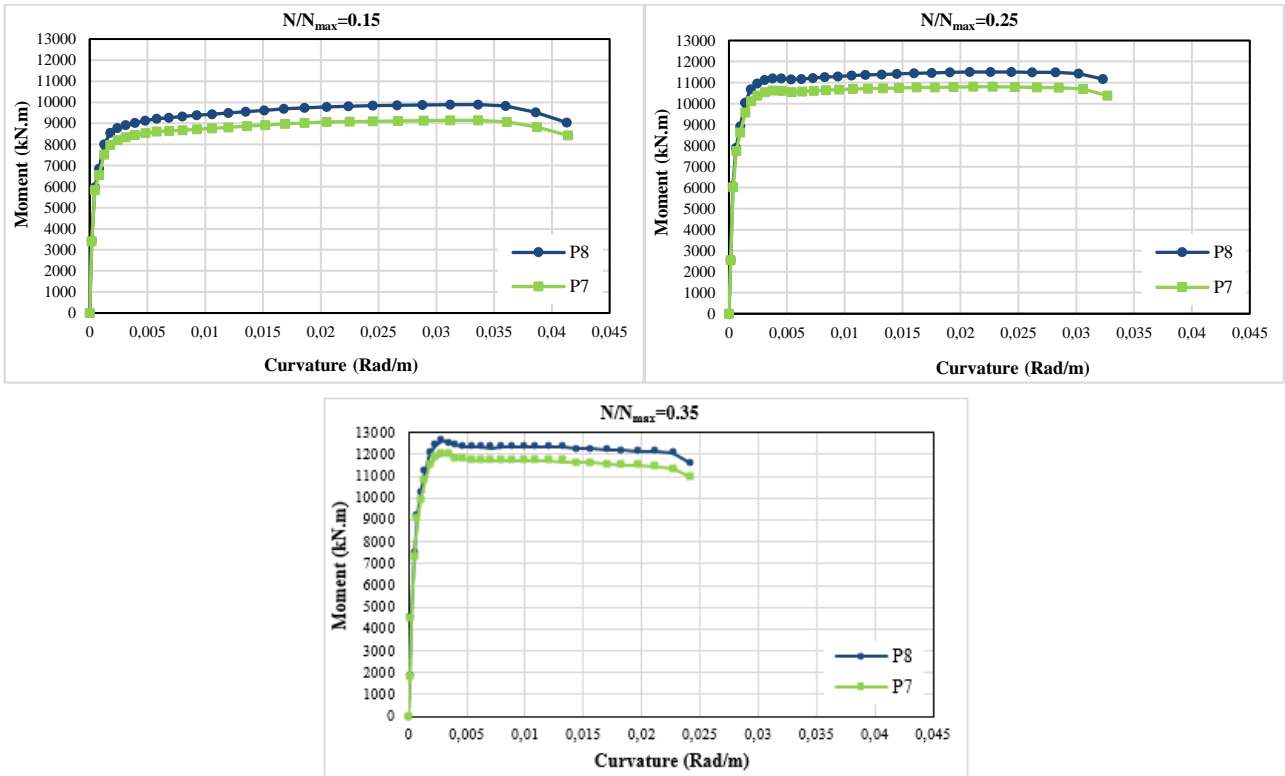


Figure 8. Moment-curvature relations with various longitudinal reinforcement diameters at the confined boundary region for P7 and P8 shear wall sections

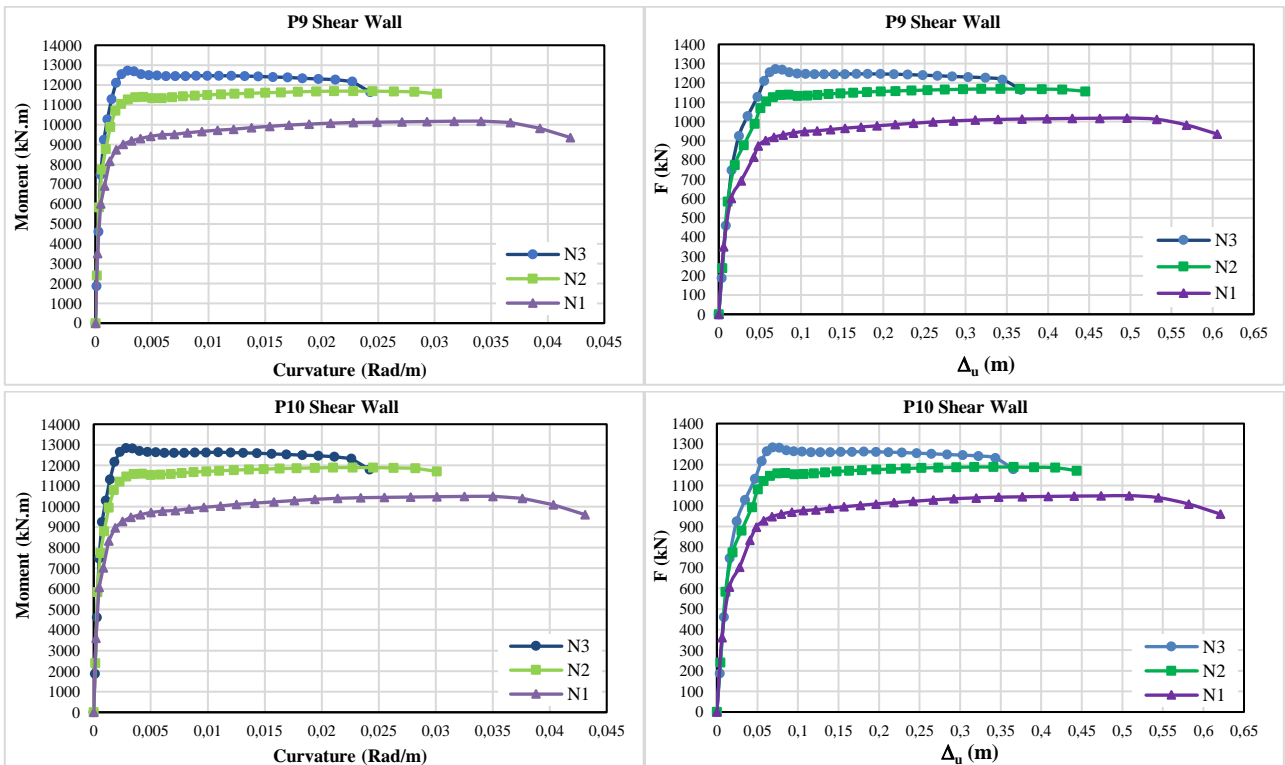


Figure 9. Moment-curvature and lateral force-lateral peak displacement relationships for different axial load levels

Moment and curvature values were obtained for the yield curvature and curvature values before the collapse condition of P9 and P10 shear wall sections with different longitudinal reinforcement diameters at the web region for

different axial load levels. According to the yield curvature and curvature values before the collapse condition, μ_ϕ , Δ_y , Δ_u , θ_u and μ_Δ values of the P9 and P10 shear wall sections are presented in Table (7). Effects of various parameters

on the ultimate moment, total displacement, curvature ductility, displacement ductility and angular displacement before the collapse for different axial load levels of the

shear walls are given in Figures (11, 12, 13,14 and 15) respectively.

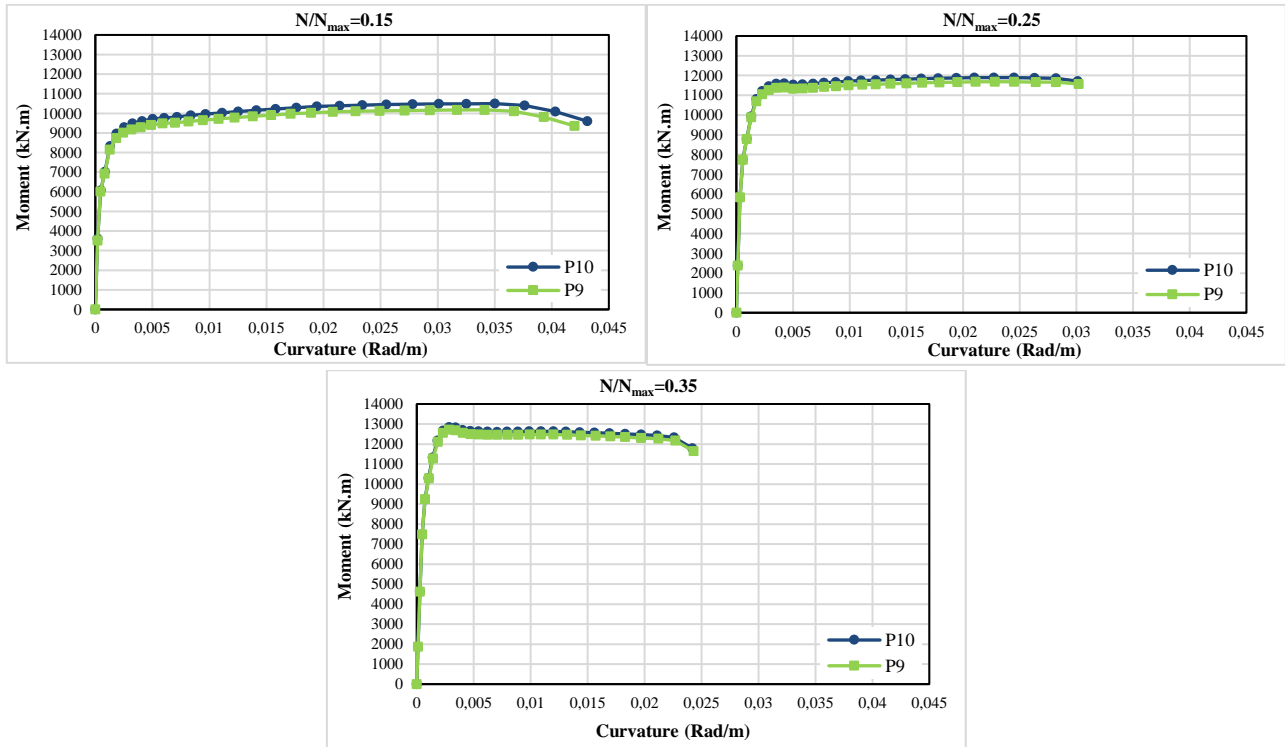


Figure 10. Moment-curvature relations for different longitudinal reinforcement diameters at the web region of P9 and P10 shear wall sections

Table 7. Analysis results of P9 and P10 shear wall for different longitudinal reinforcement diameters at the web region

No	N/N_{max}	M_y (kN.m)	φ_y (Rad/m)	M_u (kN.m)	φ_u (Rad/m)	μ_φ	Δ_y (m)	Δ_u (m)	θ_u (Rad)	μ_Δ
P9	0.15	7899	0.0012	10180	0.042	35.9	0.039	0.606	0.067	15.53
	0.25	9955	0.0013	11688	0.0302	22.55	0.045	0.445	0.050	9.97
	0.35	11514	0.0015	12715	0.0243	15.88	0.051	0.367	0.042	7.19
P10	0.15	7986	0.0012	10500	0.0431	36.84	0.039	0.621	0.069	15.92
	0.25	10026	0.0013	11892	0.0301	22.46	0.045	0.444	0.050	9.93
	0.35	11570	0.0015	12848	0.0242	15.82	0.051	0.366	0.042	7.17

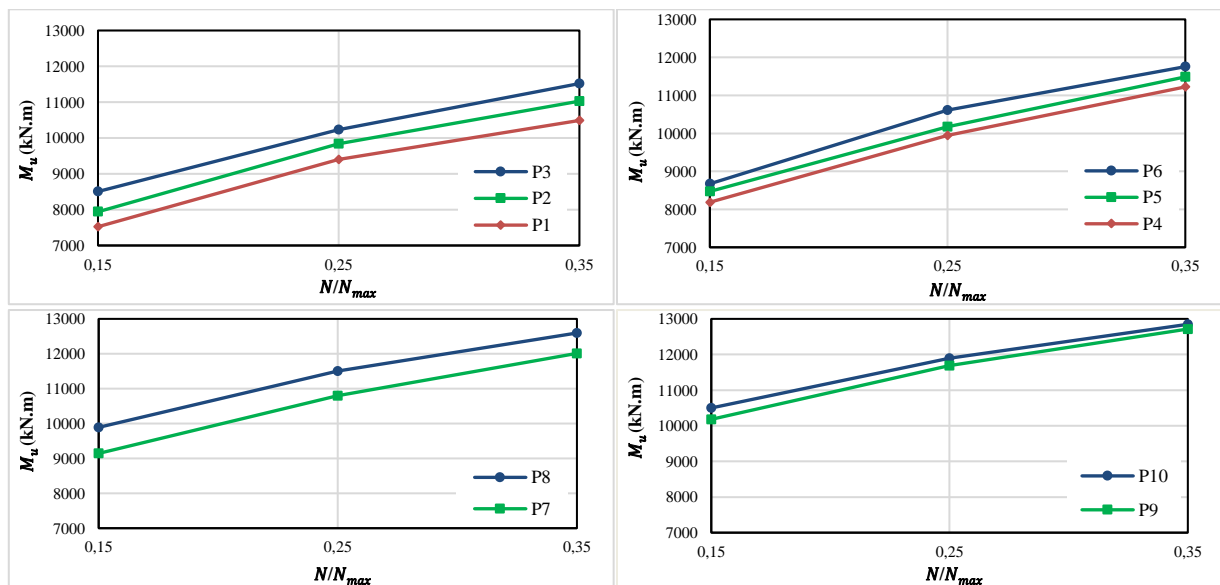


Figure 11. Effects of different parameters on the ultimate moment for various axial load levels

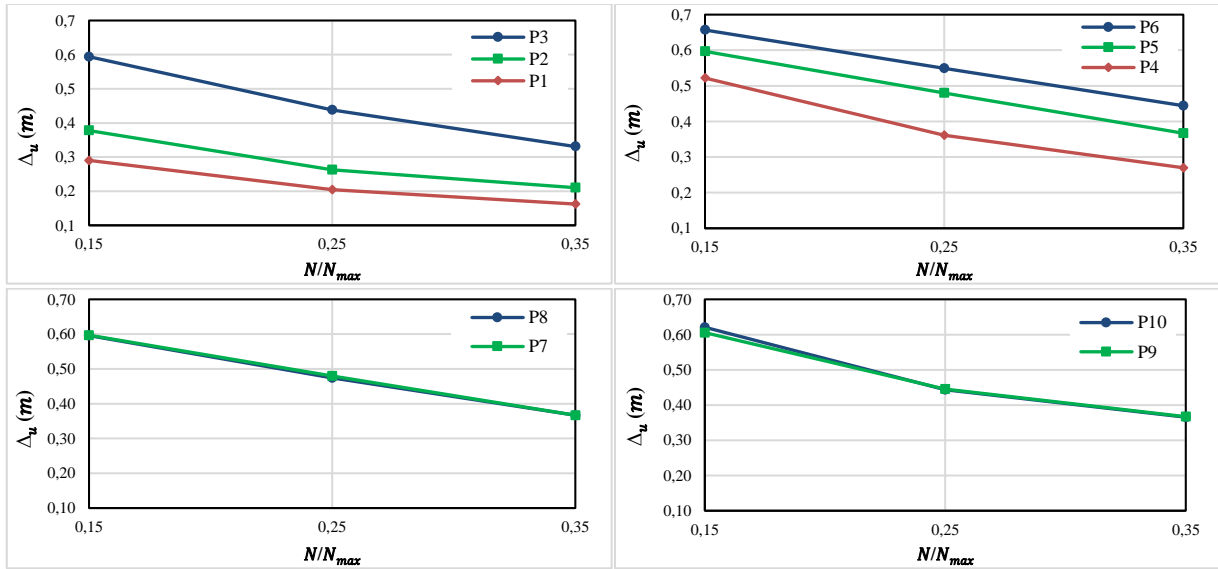


Figure 12. Effects of different parameters on the total displacement for various axial load levels

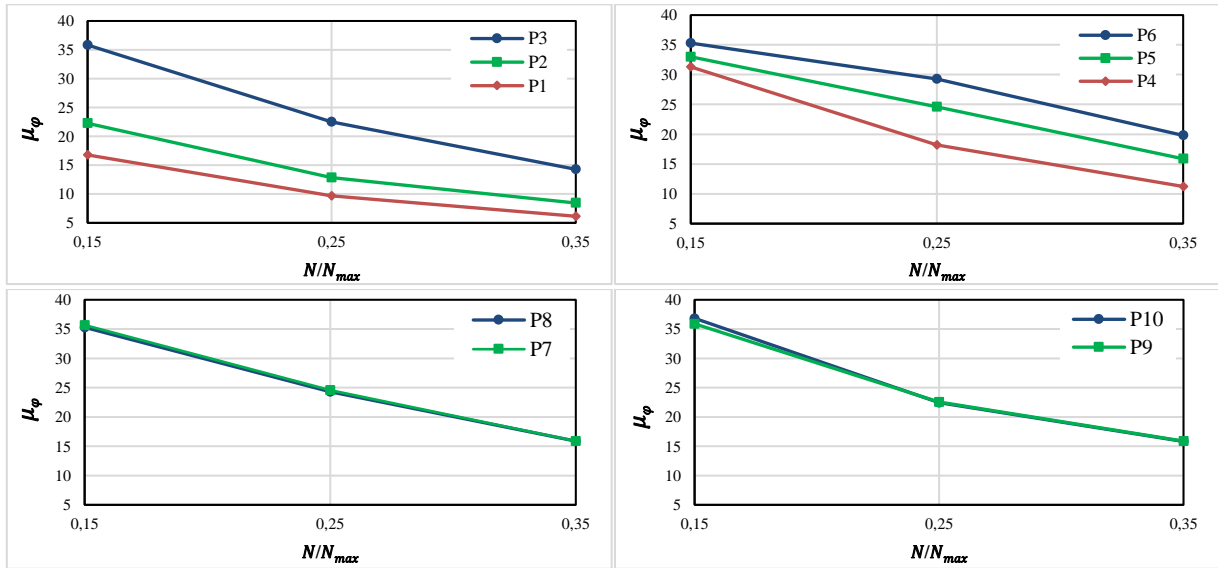


Figure 13. Influence of various parameters on the curvature ductility for different axial load levels

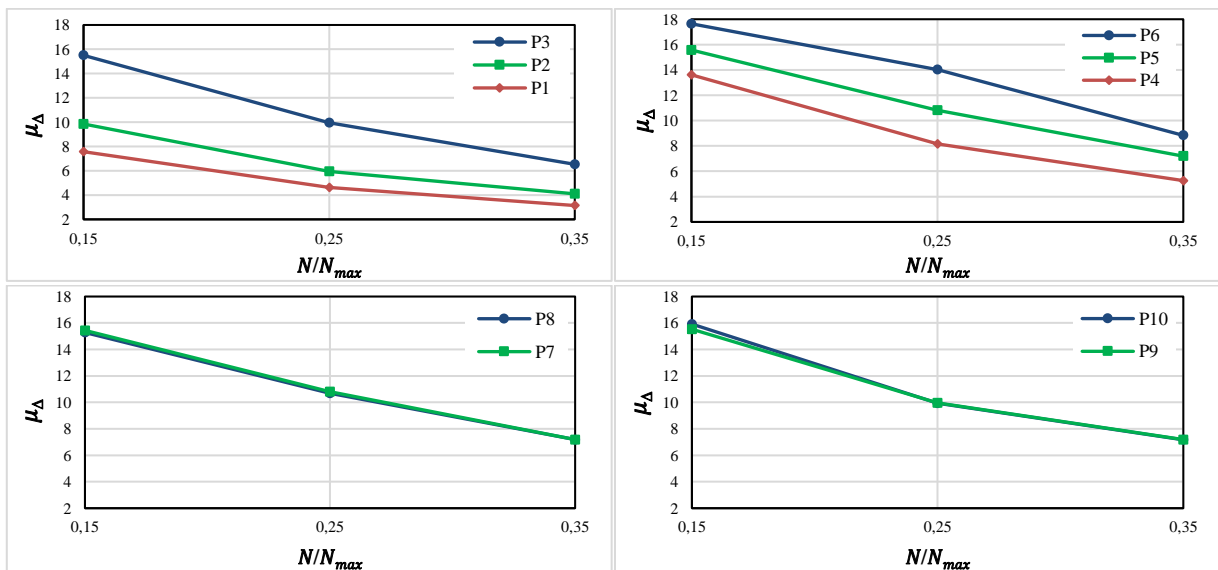


Figure 14. Influence of different parameters on the displacement ductility for different axial load levels

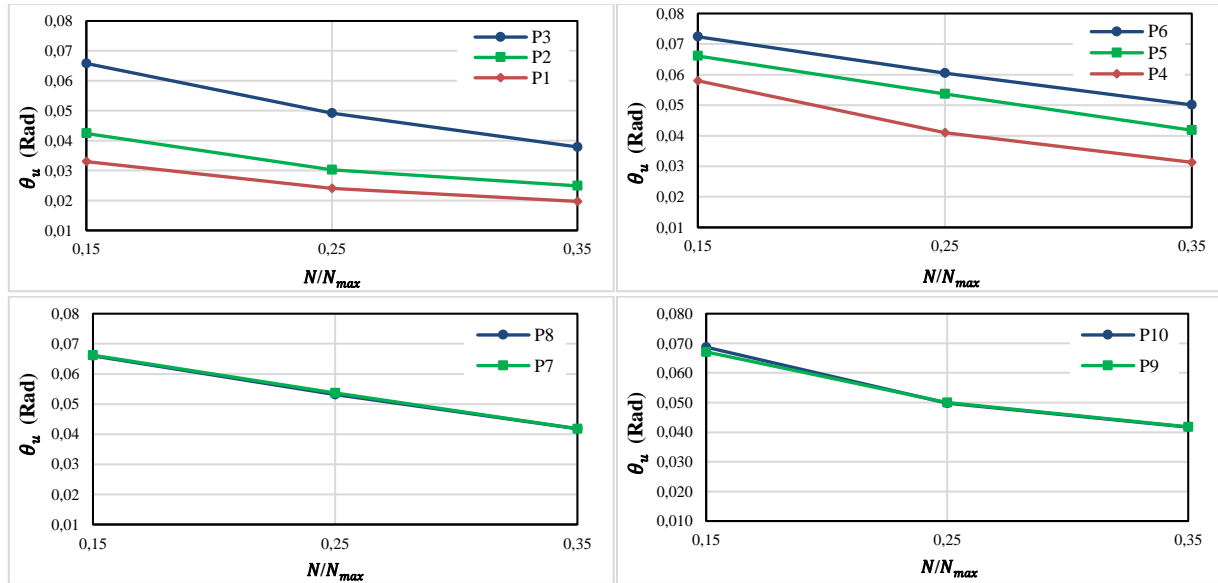


Figure 15. Effects of different parameters on the angular displacement before the collapse for different axial load levels

The results of the investigations conducted on the moment-curvature and lateral load-lateral peak displacement analysis of RC shear walls are given above. Based on the results of the analyses, it can be said that as the axial load values increase, yield, curvature, and ultimate moment values also increase. On the other hand, values of the curvature ductility and ultimate curvature decrease as the axial load values increase for the constant transverse reinforcement ratios. Curvature ductility values of the RC shear walls for constant transverse reinforcement and longitudinal reinforcement ratios decrease with increasing axial load ratio. It is observed that there are important decreases in ductility capacities of the shear walls as a result of increase in axial force. Looking at the moment-curvature graphs, it is seen that for fixed axial loads, the curvature ductility decreases as the transverse reinforcement spacing increases. It is observed that the curvature ductility increases significantly as the transverse reinforcement spacing decreases. There is a positive relationship between the transverse reinforcement diameters and the ductility of the cross-section and the maximum moment bearing capacity. In other words, as the former increases, the later ones also increase. Similarly, as the transverse reinforcement diameters increase, values of the ultimate curvature, moment, and curvature ductility values also increase; however, values of yield curvature and moment keep to be almost constant. While keeping the other parameters constant, an increase in the longitudinal reinforcement diameter leads to increase in values of yield moment, ultimate moment, yield curvature, and ultimate curvature; but, values of the curvature ductility decrease. Yield and ultimate moment capacities increase with the increment of longitudinal reinforcing ratio at the confined boundary and web region of the RC shear walls. There are differences in the yield curvature, ultimate curvature, yield displacement, plastic displacement, total peak displacement

and displacement ductility values calculated according to different axial load levels. Yield displacement value increases however, plastic displacement, total peak displacement and displacement ductility values decrease with increasing axial load levels. Total peak displacement and displacement ductility values increase as the transverse reinforcement diameter of the shear wall increases. Total peak displacement and displacement ductility values decrease with the increase of the transverse reinforcement spacing of the shear wall. Total peak displacement and displacement ductility values almost constant with the increase of the longitudinal reinforcement ratio at the confined boundary and web region of the shear wall. Since the yield curvature value of the sections does not change, the peak-displacement value of the sections remains constant in the case of yield and however, the peak-displacement and angular displacement values are decreases before the collapse.

5. Conclusions

The results of this study show that changes in the longitudinal, and transverse reinforcements and axial load levels significantly affect the moment-curvature and lateral force-lateral peak displacement behaviors of the RC shear walls. In terms of affecting section ductility, axial load can be shown as one of the important parameters. According to the results, the ratio of transverse reinforcement affects the cross-section behaviors of RC shear walls. As the transverse reinforcement diameter increases, the optimum moment bearing capacity and the ductility of the cross-section also increase. As the transverse reinforcement ratio increases, the ductile behavior is ensured more because of the increment of curvature ductility on RC shear walls. The value of displacement ductility decreases with increasing yield

displacement values and decreasing of total peak displacement values. Since the curvature values of the sections are constant in the yield state, the total peak-displacement values remain constant in the yield state and the angular displacement values of the peak displacement and sections before the collapse increase. As the axial load level increases, the total peak-displacement and angular displacement values of the sections decrease. There is not much change in the angular displacement values of the sections with the increase in the longitudinal reinforcement diameters at the confined boundary and web region of shear walls.

Declaration

The author(s) declared no potential conflicts of interest with respect to the research, authorship, and/or publication of this article. The author(s) also declared that this article is original, was prepared in accordance with international publication and research ethics, and ethical committee permission or any special permission is not required.

References

- Özdemir, M. A., Kazaz, İ., and Özkaya, S. G., *Evaluation and comparison of ultimate deformation limits for RC columns*, Engineering Structures, 2017. **153**: p. 569–581.
- Foroughi, S., and S. B. Yuksel, *Investigation of the Moment-Curvature Relationship for Reinforced Concrete Square Columns*, Turkish Journal of Engineering (TUJE), 2020. **4**(1): p. 36-46.
- Perez, J. C. V., and M. M. Mulder, *Improved Procedure for Determining the Ductility of Buildings under Seismic Loads*, Revista Internacional de Metodos Numericos para Calculo y Diseno en Ingenieria, 2018. **34**(1): p. 27.
- Kazaz, İ., Gülkan, P., and Yakut, A., *Deformation Limits for Structural Walls with Confined Boundaries*, Earthquake Spectra, 2012. **28**(3): p. 1019-1046.
- Kazaz, İ., Gülkan, P., and Yakut, A., *Examination of code performance limits for shear walls*, 15 WCEE, LISBOA, 2012.
- TS500, *Requirements for Design and Construction of Reinforced Concrete Structures*, Turkish Standards Institute, 2000. Ankara, Turkey.
- TBEC, *Turkish Building Earthquake Code: Specifications for Building Design under Earthquake Effects*, T.C. Bayındırlık ve İskan Bakanlığı, 2018. Ankara.
- Bohl, A., and P. Adebar, *Plastic hinge lengths in high-rise concrete shear walls*, ACI Structure Journal, 2011. **108**(2): p. 148-157.
- Hoult, R. H., Goldsworthy, and E. Lumantarna, *Plastic Hinge Length for Lightly Reinforced Rectangular Concrete Walls*. Journal of Earthquake Engineering, 2018. **22**(8): p. 1447-1478.
- Kazaz, İ., *Analytical Study on Plastic Hinge Length of Structural Walls*. Journal of Structural Engineering, 2013. **139**(11): p. 1938-1950.
- Uniform Building Code, International Council of Building Officials, Whittier, California, 1997.
- Park, R., and T. Paulay, *Reinforced concrete structures*, Wiley, New York, 1975.
- Foroughi, S., and S. B. Yuksel, *Investigation of Displacement Behavior of Reinforced Concrete Shear Walls with Different Plastic Hinge Relationships*, International Journal of Eastern Anatolia Science Engineering and Design, 2019. **1**(2): p. 196-211.
- SAP2000, Structural Software for Analysis and Design, Computers and Structures, Inc, USA.
- Mander, J. B., M. J. N. Priestley, and R. Park, *Theoretical stress-strain model for confined concrete*, Journal of Structural Engineering, 1988. **114**(8): p. 1804-1826.
- Foroughi, S., and S. B. Yuksel, *Analytical Investigation of Curvature Ductility of Reinforced Concrete Columns*, Uludağ University Journal of the Faculty of Engineering, 2020. **25**(1): p. 27-38.

**Research Article**

A novel design of a compact wideband patch antenna for sub-6 GHz fifth-generation mobile systems

Mehmet Yerlikaya ^{a,*} , Seyfettin Sinan Gültekin ^b and Dilek Uzer ^b

^aKaramanoğlu Mehmetbey University, Department of Electrical and Electronics Engineering, Karaman, Turkey

^bKonya Technical University, Department of Electrical and Electronics Engineering, Konya, Turkey

ARTICLE INFO

Article history:

Received 13 February 2020

Revised 20 May 2020

Accepted 02 June 2020

Keywords:

Log-periodic array

Patch antenna

Sub-6 GHz

5G antenna

ABSTRACT

In this paper, a new broadband patch antenna design for fifth-generation (5G) sub-6 GHz mobile systems is presented. The proposed 5G antenna has a very compact size with an overall dimension of 10.7×22.5 mm². The 5G antenna consists of a log-periodic patch in the form of an equilateral triangle with a 50 Ω microstrip line feed and a ground plane of rectangular shape. The prototype of the proposed 5G antenna was made by etching on an FR4 substrate with a 1.6mm thickness, 4.3 dielectric constant and 0.02 tangent loss. The 5G antenna is designed and simulated for the frequency band range of 3.4-4.2 GHz. According to the measurement results, the 5G antenna impedance band range is determined as 3.1-3.9 GHz. Besides, the proposed 5G antenna has also near-omnidirectional radiation patterns both simulation and measurement at the resonance frequencies of 3.8 GHz and 3.5 GHz, respectively. According to these results, the proposed antenna is showed similar radiation characteristics in both measured and simulated results. With all these radiation and physical properties, the proposed log-periodic patch antenna is very suitable for sub-6 GHz 5G mobile applications.

© 2020, Advanced Researches and Engineering Journal (IAREJ) and the Author(s).

1. Introduction

Fifth-generation (5G) is a new mobile broadband technology that is in its early stages and is planned to be widely used after 2020. Mobile communication systems, which became widespread after the 2000s, are evolved quite rapidly with different technologies over the last three decades from the analog transmission-based first generation (1G) to Internet Protocol (IP) based fourth-generation (4G) technologies. LTE-A (Long Term Evolution - Advanced) is an insufficient technology against the increasing demand for data, owing to smart devices are also defined as mobile users on the Internet of Things (IoT). Increasing demands for high data rates, low connection latency, low cost, low energy usage, and support for more users paved the way for the emergence of the fifth-generation (5G) technology. After the 5G, which is called next-generation technology, it is planned to overcome shortcomings of 4.5G and replace it in the near future. [1].

5G technology aims to meet the requirements of high data rates, faster connections and much more versatility than existing wireless networks. The most important expectation for the commercialization of 5G technology is the determination of all required standards, especially frequency spectrum sharing. Today, cellular communication is widely used in the sub-6 GHz band, especially at frequencies below the 3 GHz spectrum. The frequency spectrum of 5G systems is defined in two ranges as sub-6 GHz and above-6 GHz in terms of physical properties [2]. The International Telecommunication Union (ITU) adopted the IMT-2020 (International Mobile Telecommunication-2020) standards at the meeting held in Geneva in 2015. These standards contain the requirements for 5G networks, devices and services and are published as a report. According to this report; the frequency bands of 3.4 GHz to 3.6 GHz, 5 GHz to 6 GHz, 24.25 GHz to 27.5 GHz, 37 GHz to 40.5 GHz and 66-76 GHz are allocated for 5G communication [3]. After this development, the

* Corresponding author. Tel.: +90-338-226-2000 (5155) Fax: +90-338-226-2214

E-mail addresses: myerlikaya@kmu.edu.tr (M. Yerlikaya), ssgultekin@ktun.edu.tr (S. S. Gültekin), duzer@ktun.edu.tr (D. Uzer)

ORCID: 0000-0001-8018-840X (M. Yerlikaya), 0000-0002-6287-9124 (S.S. Gültekin), 0000-0003-3850-3810 (D. Uzer)

DOI: 10.35860/iarej.688973

frequency band between 3.4 GHz to 3.6 GHz is shared with mobile services in almost all countries and the availability of this spectrum for IMT is increasing worldwide. 3.4-3.8 GHz frequencies, which is the combination of LTE 42 and LTE 43 bands, is a band that is common to almost all countries, and this frequency band has significant potential for 5G researchers. International regulatory associations defined the different parts of 3.3-4.2 GHz spectrum for 5G sub-6 GHz as given in Figure 1.

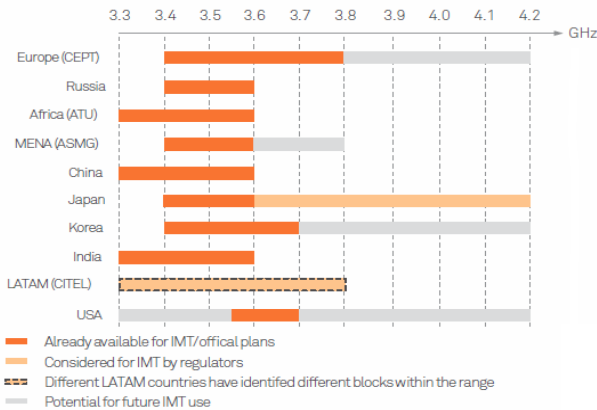


Figure 1. Worldwide availability and planning of the 3.3-4.2 GHz frequency ranges [4]

As in all wireless communication systems, one of the most important elements of 5G mobile technologies is the antenna design appropriate to the system. Lots of antenna researchers focus on this topic and several sub-6 GHz 5G antennas are also proposed [5-7].

A hybrid MIMO antenna system with multiple antennas is presented by Ban et al. [5]. The proposed hybrid MIMO antenna system consists of two separate antenna modules for LTE and 5G. The LTE module has a two-element MIMO antenna system that can cover GSM, UMTS and LTE operations. In the 5G module, there is an eight-element MIMO array working with 3.5 GHz band that can cover 3400-3600 MHz frequencies. The proposed hybrid MIMO antenna has a 140 mm × 70 mm overall size and prototyped on an FR4 substrate with 0.8 mm thickness while each MIMO element has a 16 mm × 3 mm dimensions.

Parchin et al. [6] also proposed a MIMO antenna consisting of four elements for 5G mobile terminals. Each antenna element consists of a double-fed square ring slot resonator and its dimensions are 30 mm × 30 mm × 1.6 mm. The proposed MIMO antenna system has an overall dimension of 75 × 150 mm² and is etched on an FR4 substrate with 4.4 relative permittivity. The proposed 5G MIMO antenna system has a dual-polarized 3.4-3.8 GHz frequency bandwidth.

Chattha [7] reported a two-element Planar Inverted-F Antenna (PIFA) antenna system that each element is fed by dual-port. Both PIFA elements are the same and each identical element consists of a radiating plate with 16 mm × 33 mm; while the PIFA antenna has a ground plane with

50 mm × 100 mm overall size. Also, an FR4 substrate with 4.4 relative permittivity and the thickness of 1.5 mm was used in the prototype of the proposed PIFA antenna.

Patch antennas, also called planar or microstrip antennas, are the most common types of antennas used in mobile systems because of their small size and ease of manufacture. Today's mobile communication systems, low profile broadband antennas are needed for high mobility and high-speed data transmission. However, a narrow bandwidth is one of the main shortcomings of traditional patch antennas. In the literature, different methods such as slots [8], defective ground structures (DGS) [9] and log-periodic arrays [10-12] have been tried to solve the narrow bandwidth problem of patch antennas.

In this paper, a compact wideband patch antenna for 5G mobile communication systems is presented. The 5G antenna geometry consists of a rectangular shaped ground plane and an equilateral triangle-shaped log-periodic patch array fed by a microstrip line. The dielectric constant of the FR4 substrate, 4.3, is used as the relative permittivity in the design of the proposed antenna, and its total size is 10.7×22.5×1.6 mm³. In this study, the antenna design and simulations has been carried out by using the Method of Moments (MoM) based IE3D package program [13]. The log-periodic array patch antenna has also been prototyped by printed circuit board (PCB) technology.

2. Antenna Geometry

The detailed two-dimensional (2D) geometry of the proposed 5G patch antenna is given in Figure 2 and the dimensions of the antenna are given in Table 1. The proposed 5G antenna composed of a microstrip-fed log-periodic patch on the top and a dielectric substrate with a rectangular ground plane on the bottom. FR4 material with 1.6 mm thickness, 4.3 relative permeability and 0.02 loss tangency was used as the dielectric substrate of the antenna.

The proposed antenna has an overall size of 10.7×22.5 mm² while the antenna patch consists of a log-periodic array with a small in size of 9.3×10.7 mm². The log-periodic patch of the proposed 5G antenna is fed by a microstrip line of 3.1 mm width and 10.5 mm length. In addition, a strip line with a dimension of 1.55×2.7 mm² is added between the microstrip line and the log-periodic patch to increase the impedance matching. The antenna ground plane consists of a rectangular-shaped structure with a size of 10.7 × 8 mm².

2.1 Log-Periodic Patch Designing Process

The antenna patch proposed in this study is based on an equilateral triangle-sized log-periodic array using log-periodic array design methods [14-15]. To calculate the length of the longest element (L_{max}) of the log-periodic array, Equation (1) is used:

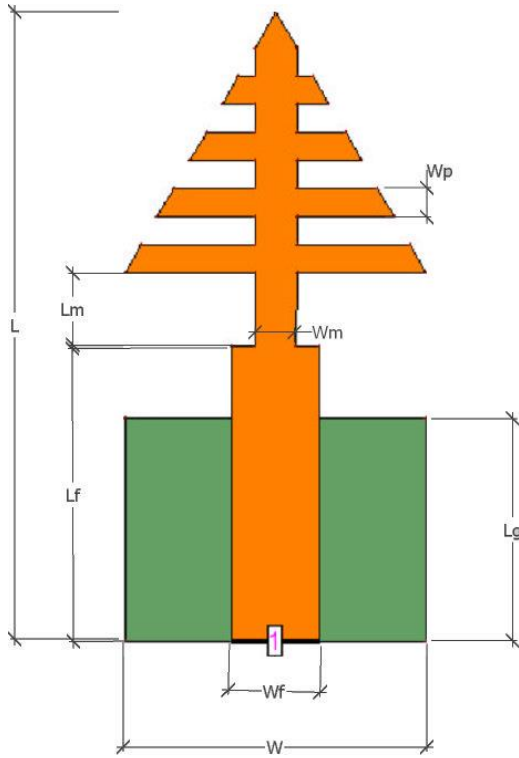


Figure 2. The detailed 2D geometry of the log-periodic patch 5G antenna

Table 1. Dimensions of the the log-periodic patch 5G antenna

Dimensions	Explanation	Size (mm)
W	Total width of the antenna	10.7
L	Total length of the antenna	22.5
W_f	Width of microstrip line	3.1
L_f	Length of microstrip line	10.5
L_g	Length of ground plane	8.0
W_m	Width of matching stripline	1.55
L_m	Length of matching stripline	2.7
W_p	Length of each log elements	1.0

$$L_{\max} = \frac{c}{4f_{\min}\sqrt{\epsilon_r}} \quad (1)$$

where c is the speed of light in vacuum, ϵ_r is the relative permittivity of a dielectric substrate and f_{\min} is the minimum frequency of the antenna operating band. In this study, the operating band is determined as a 3.4-4.2 GHz range to cover whole frequencies for sub-6 GHz 5G applications [4]. Thus, f_{\min} is given as 3.4 GHz. Also, since FR4 material is used as the dielectric substrate, the value of 4.3 is determined as the relative permeability.

Another parameter that needs to be determined in the log-periodic array design is the number of array elements. The total number of elements (N) for the log-periodic array can be calculated by Equation (2):

$$N = 1 + \frac{\log(B \times B_{ar})}{\log(1/\tau)} \quad (2)$$

where B is the bandwidth ratio, B_{ar} is the active region bandwidth and τ is scaling factor. The scaling factor (τ) is given as 0.87 and the bandwidth ratio and active region

bandwidth parameters are determined from Equations (3-4), respectively:

$$B = \frac{f_{\max}}{f_{\min}} \quad (3)$$

$$B_{ar} = 1.1 + 7.7(1-\tau)^2 \cot \alpha \quad (4)$$

where α is the half-angle of the antenna. Since the proposed antenna has an equilateral triangle sized patch, 30° is used as the half-angle of the antenna.

By using Equations (3) and (4), B and B_{ar} are calculated as 1.235 and 1.325, respectively. According to Equations 3 and 4, N is calculated as 5 from Equation (2). By using Equation (1), the length of the longest element is determined as 10.7 mm.

Finally, the antenna microstrip feed line length of L_f and microstrip feed line width of W_f are given as 10.5 mm and 3.1 mm using the calculation tool of the IE3D package program.

3. Results and Discussions

The proposed log-periodic patch antenna for sub-6 GHz 5G mobile applications is also printed on a double-sided FR4 dielectric substrate with a thickness of 1.6 mm and 4.3 relative permittivity. The photograph of the prototyped antenna is shown in Figure 3.

Firstly, the impedance bandwidth was determined for the analysis of the proposed log-periodic antenna. To determining the bandwidth, return loss graph was examined from the IE3D package program. Then, the antenna return loss measurement was made between the frequency range of 2 GHz to 5 GHz and verified with the simulated results. In this study, Keysight PNA 5224A vector network analyzer was used in all measurements. The simulated and measured S_{11} results are given comparatively in Figure 4. From the Figure 4, the -10 dB bandwidth is obtained as 3.4-4.2 GHz from the simulations, while the range for measurement results is determined as 3.1-3.9 GHz. Although there are some differences between the graphs, both measurement and simulation results are suitable for the frequency bands of sub-6 GHz 5G mobile systems [4].

After determining the antenna bandwidth, radiation pattern measurement and simulation studies were carried out. The 2D radiation pattern of the proposed 5G antenna for the E -plane ($\phi = 0^\circ$ or xz -plane) and H -plane ($\phi = 90^\circ$ or yz -plane) at 3.5 GHz frequency is shown in Figure 5a. In addition, the simulated three-dimensional (3D) radiation pattern of the log-periodic patch antenna at 3.5 GHz is also given in Figure 5b. From Figure 5a, maximum gains are 1.92 dBi and 1.9 dBi for E -plane and H plane, respectively. As can be seen from the 3D radiation pattern, it is understood that the maximum gains are in the E and H planes. As seen in Figure 5, the proposed 5G antenna has a near-omnidirectional radiation pattern at resonant frequency of 3.5 GHz.

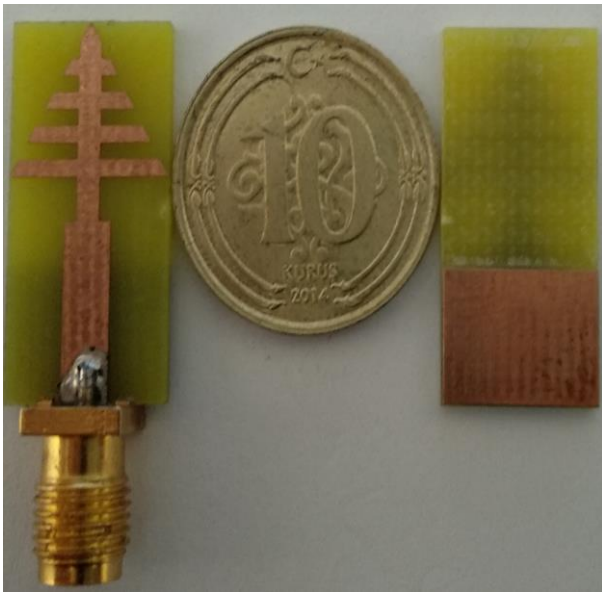


Figure 3. Photograph of the prototyped the log-periodic patch 5G antenna

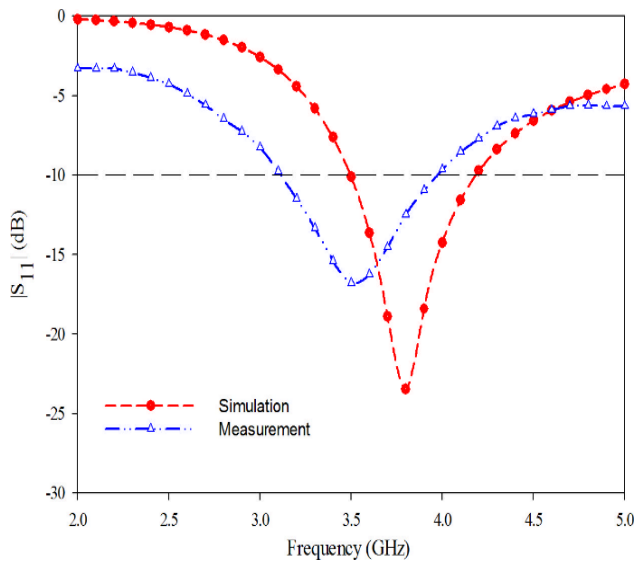


Figure 4. Measured and simulated S_{11} graph of the log-periodic patch 5G antenna

Thirdly, simulated maximum gain and total efficiency values of the proposed 5G patch antenna are obtained. The compared maximum gain and total efficiency graphs of the 5G antenna are presented in Figure 6. As can be seen from the figure, the gain and efficiency curves are similar as it is expected. The maximum gain value for the antenna is 2.3 dBi at 3.8 GHz. Likewise, the total efficiency of the proposed antenna is 73% at 3.8 GHz.

Finally, the proposed 5G antenna simulated surface current distributions at 3.5 GHz is given in Figure 7. According to current distributions in Figure 7, the majority of the radiation concentrated on the antenna patch and matching line.

According to these results, the proposed antenna stands out especially in terms of its small size and wide bandwidth compared to the antennas in the literature [5-7].

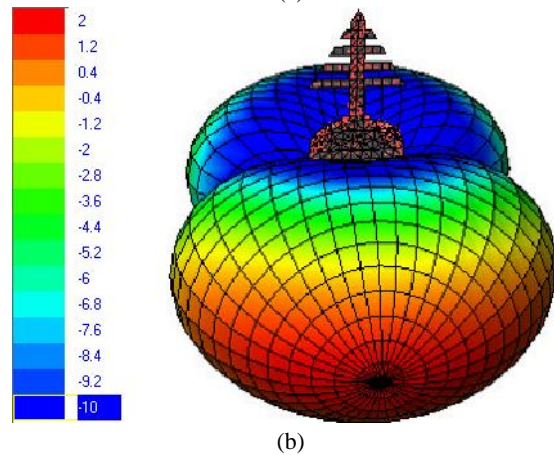
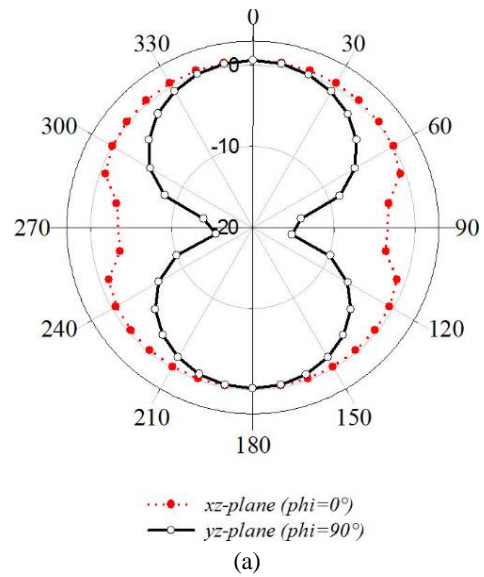


Figure 5. Radiation patterns of the log-periodic patch 5G antenna at 3.5 GHz: (a) 2D radiation pattern on E and H planes, (b) 3D radiation pattern

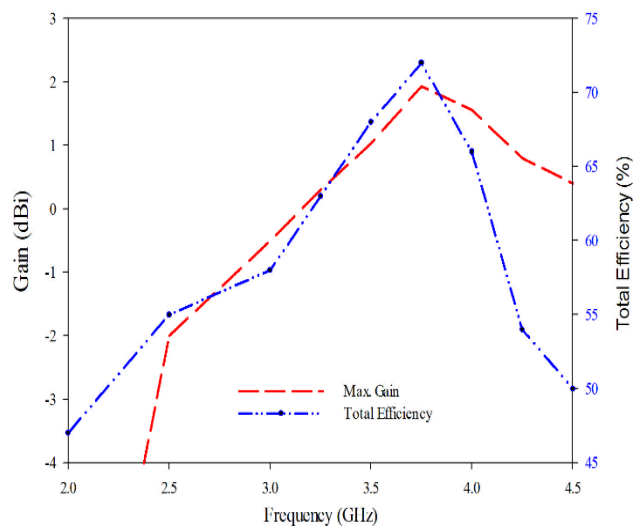


Figure 6. The maximum gain and total efficiency graph of the log-periodic patch 5G antenna

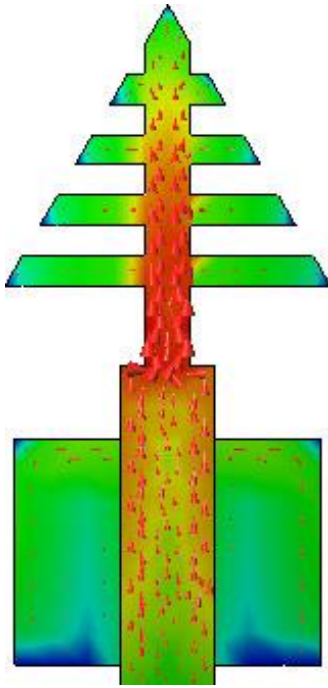


Figure 7. The simulated surface current distributions of the log-periodic patch 5G antenna at 3.5 GHz

4. Conclusion

In this study, a novel wideband patch antenna with the log-periodic array is presented for sub-6 GHz 5G mobile systems. The proposed patch antenna has a very compact structure with total size of $10.7 \times 22.5 \text{ mm}^2$. The proposed 5G patch antenna is designed and manufactured on a double-sided FR4 substrate which has a relative permittivity of 4.3, a tangent loss of 0.02 and a thickness of 1.6 mm. The proposed antenna has a frequency bandwidth of 3.4-4.2 GHz by simulations, while this operating band is measured in the range 3.1-3.9 GHz. Besides, the antenna has a near-omnidirectional radiation pattern and a maximum gain value of 2.3 dBi.

Declaration

The author(s) declared no potential conflicts of interest with respect to the research, authorship, and/or publication of this article. The author(s) also declared that this article is original, was prepared in accordance with international publication and research ethics, and ethical committee permission or any special permission is not required.

References

1. Rappaport, T.S., Sun, S., Mayzus, R., Zhao, H., Azar, Y., Wang, K., Wong, G.N., Schulz, J.K., Samimi, M., and Gutierrez Jr, F.; *Millimeter wave mobile communications for 5G cellular: it will work!*. IEEE Access, 2013. 1 (1): p. 335-349.
2. Lee, J., Tejedor, E., Ranta-aho, K., Wang, H., Lee, K.-T., Semaan, E., Mohyeldin, E., Song, J., Bergljung, C., and Jung, S.; *Spectrum for 5G: global status, challenges, and enabling technologies*. IEEE Communications Magazine, 2018. 56 (3): p. 12-18.

3. Marcus, M. J.; *5G and IMT for 2020 and beyond [spectrum policy and regulatory issues]*. IEEE Wireless Communications, 2015. 22(4): pp. 2-3.
4. Huawei Technologies Co. Ltd.; *5G Spectrum Public Policy Position*, 2017.
5. Ban, Y. L., Li, C., Wu, G. and Wong, K. L.; *4G/5G multiple antennas for future multi-mode smartphone applications*. IEEE Access, 2016. 4: p. 2981–2988.
6. Parchin, N. O., Al-Yasir, Y. I. A., Ali, A. H., Elfergani, I., Noras, J. M., Rodriguez, J., and Abd-Alhameed, R.A.; *Eight-element dual-polarized MIMO slot antenna system for 5G smartphone applications*. IEEE Access, 2019. 7: p. 15612-15622.
7. Chattha, H.T.; *4-Port 2-Element MIMO antenna for 5G portable applications*. IEEE Access, 2019. 7: p.96516-96520.
8. Ambresh, P.A., Hadalgi, P.M. and Hunagund, P.V.; *Planar microstrip slot antenna for S & C band wireless applications*. Journal of Physics: Conference Series, 2013. 435(1): p. 12-22.
9. Ansari, J.A., Verma, S., Verma, M.K. and Agrawal, N.; *A novel wide band microstrip-line-fed antenna with defected ground for CP operation*. Progress In Electromagnetics Research, 2015. 58: p.169-181.
10. Nasir, S.A., Arif, S., Mustaqim, M. and Khawaja, B.A.; *A log-periodic microstrip patch antenna design for dual band operation in next generation wireless LAN applications*, in IEEE 9th International Conference on Emerging technologies (ICET2013): Islamabad. p. 1-5.
11. Amini, A. and Oraizi, H.; *Miniaturized UWB log-periodic square fractal antenna*. IEEE Antennas and Wireless Propagation Letters, 2015. 14: p.1322-1325.
12. Yerlikaya, M., Gültekin, S.S. and Uzer, D., *A Low Profile Wideband Log Periodic Microstrip Antenna Design for C-Band Applications*. Advanced Electromagnetics, 2019. 8(2): p.48-52.
13. Mentor Graphics, *IE3D™ Version 15*. HyperLynx®3D EM, 2015, Wilsonville.
14. Carrel, R., *The design of log-periodic dipole antennas*. IRE International Convention Record, 1958. 9: p. 61-75.
15. Campbell, C., Traboulay, I., Suthers, M. and Kneve, H., *Design of a stripline log-periodic dipole antenna*. IEEE Transactions on Antennas and Propagation, 1977. 25(5): p.718-721.



Research Article

Numerical analysis of the harvester having toroidal structure and examination of the application results

Mahmut Kabakulak ^{a,*}  and **Serdal Arslan** ^a 

^aDepartment of Electricity, Vocational School, Harran University, Turkey

ARTICLE INFO

Article history:

Received 26 February 2020

Revised 22 April 2020

Accepted 26 April 2020

Keywords:

Ansys Maxwell

Energy harvesting

Electromagnetic field

Toroidal core

ABSTRACT

In most places with energy transmission, data of the line can be obtained with sensors. However, in recent years, the energy requirement of sensors has been met through harvesters. The electrical power required for sensor systems can be provided through electromagnetic fields around the line, especially through the electrical power transmission line or energy-carrying cable systems. In this study, numerical analysis of the harvester with toroidal coil, which was intended to be used for sensor feeds, was performed using Ansys Maxwell. In addition, experimental studies of the harvesters with toroidal core were carried out. The results were compared with some studies in the literature. Considering line current and saturation effects, it was seen that the studied toroid models were appropriate for home sensor applications.

© 2020, Advanced Researches and Engineering Journal (IAREJ) and the Author(s).

1. Introduction

Today, in addition to fossil fuel energy systems, alternative energy sources have become widespread due to both increasing energy demand and environmental pollution [1, 2]. This has increased the number of power transmission and distribution lines. Due to the widespread use of overhead power lines in energy transmission and distribution, it is important to follow the lines and reduce the failures in order to increase the energy continuity and reliability on the lines as the system infrastructure ages. In order to maintain the safe transmission of energy, power lines need to be checked regularly. This is usually done directly (visual inspection), indirectly (wireless status monitoring systems) and by helicopter video inspection. In terms of other applications, a free transmission line control system, where an unmanned air vehicle conducts all activities and when doing this, it is charged from the line through the energy harvester, has been proposed [3]. For example, in China, the weight of a vibration device and the weight of a universal device is limited to 1 kg and 2.5 kg, respectively [4]. The problem can be solved by increasing the power density of the energy harvester. Wired monitoring systems are not widely used today since they

require expensive communication especially over long distances [5]. Existing systems are based on the weather-data collection method used to estimate icing conditions. On the other hand, optical measurement allows the detection of the icing process by the direct measurement system depending on energy harvesting based on other methods such as microwaves and ultrasound measurement [5]. In a study, various methods such as lightning current measurement systems using current detectors, cathode-ray oscillography, cathode-ray oscillography, and Rogowski coils were examined and a new lightning current measurement system based on energy harvesters was proposed [6]. Partial discharge sensors can be utilized to monitor partial discharges of transformers using the harvester [7]. Reducing air pollution hazards and keeping particulate matter data at specific limits are of vital importance. For air-based data, a cheap wirelessly connected sensor system, which is positioned individually on the conductors of overhead power lines, has been proposed [8]. White et al. [8] conducted tests by using a printed circuit board containing ozone, carbon monoxide, temperature and humidity sensors, as well as a Bluetooth, power management circuit, and a harvesting coil. In order to obtain a higher power density in electromagnetic

* Corresponding author. Tel.: +90 414 318 30 00.

E-mail addresses: m.kabakulak@harran.edu.tr (M. Kabakulak), serdalarслан@harran.edu.tr (S. Arslan)

ORCID: 0000-0002-0016-6735 (M. Kabakulak), 0000-0002-1187-5633 (S. Arslan)

DOI: 10.35860/iarej.694834

harvesting applications, a material with high saturation flux density is preferred [4]. Test results for various core applications are given in Table 1. If the toroidal core volume and outer diameter are constant, the smaller the inner diameter, the greater the maximum output power [9]. The output power increases as the difference between the outer diameter and the inner diameter of the toroidal coil used for harvesting increases. In addition, the output power increases as the toroidal height increases [9]. The diameter change affects the power change more than the change in height. The presence and increase of the air gap in the toroid decrease the output power. In order to obtain maximum output power in toroidal core applications, inner resistance of the coil should not be larger than the load resistance [9]. In addition, the number of smaller turns is preferable when the line current is large [9]. The structure of the energy harvesting device shown in Figure 1 consists of toroidal core with winding placed on the harvesting line. Power line generates a magnetic field around the core. The magnetic field density, generated in the coil, produces indirect proportion to the magnetic permeability of the core and the harvester produces a voltage induced in the coil [10]. In fact, based on the basic principle of the induction voltage with variable magnetic field over time, the induced voltage is directly proportional to the magnetic permeability of the core material [10]. The higher the core permeability, the larger the magnetic permeability of the core; it is important to note that the induced electric voltage is so high. By using a material with high magnetic permeability, a smaller magnetic core can provide high power density. Due to the high permeability of the ferrite and iron powder alloy, the nanocrystalline core is recommended for compact, autonomous magnetic induction-based energy harvesting devices because of its high power density [10]. However, when current is high, the flux density in the core no longer changes or it changes very slowly due to the vacuum permeability. When it is saturated, the inductance of the inductor approaches zero and very little energy is harvested [11]. Therefore, to be able to study the behavior of the core, an accurate model should be established [11].

Table 1. Test results for various core applications

Ref.	Core Material	Line Current (A)	Harvested Power (mW)	Shape
[4]	Si-steel	10	350	Toroid
[10]	Ferrite	5	16.8	Toroid
[10]	Nano-crystalline	5	9	Toroid
[10]	Iron powder	5	-	Toroid
[8]	Si-steel	100	0.0015	U Core
[9]	Si-steel	102.5	0.01764	Toroid

In the literature, multiple circuits have been proposed for wireless charging systems. Usually, the AC/DC rectifier has been proposed for energy harvesting from power-module transmission lines, including power matching, digital logical unit, and supercapacitors used to store harvested energy [12]. Batteries are used as the primary sources to ensure the full functionality of the high-voltage wireless sensor node in power lines. In addition, batteries are used to support the functionality of the test and debugging unit during the field-testing phase [12]. However, while increasing the life and safety of the sensor system, harvesters can also serve as a unique source without a battery [13].

As a continuation of our previous studies [14-17], the electromagnetic harvester with a toroidal structure was examined in this study. Harvesters with different toroidal structures were compared with similar studies in the literature. Section two provides information about the features of the model and methodology of the study. In section three, numerical analysis of toroidal type models and the data of the experiment are examined and the results are discussed in the final section.

2. Materials and Method

In Figure 1, drawings of the toroidal model are given. Here, “ D_0 ” refers to outer diameter, “ D_i ” refers to inner diameter and “ L ” refers to thickness. The harvesters with toroidal amorphous materials, whose technical specifications are given in Table 2, were studied. For these models whose numerical analysis was done with the Ansys Maxwell software, experiments were conducted by installing the experiment set shown in Figure 2. Then, the experimental data and numerical analyses were compared.

The mean magnetic flux pathway (L_{mT}) for Toroidal nudes is calculated using Equation 1 [18]:

$$L_{mT} = \frac{\pi(D_0 - D_i)}{\ln\left(\frac{D_0}{D_i}\right)} \quad (1)$$

If the winding length for the toroidal cores is written as L_{TB} , Equation 2 is obtained.

$$L_{TB} = (D_0 - D_i) + 4r + 2L \quad (2)$$

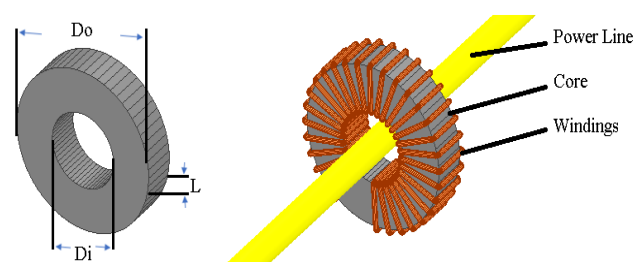


Figure 1. General structure of the toroidal-core model harvester

Table 2. Technical characteristics of the toroidal type harvester models

Models	Do (mm)	Di (mm)	L (mm)	N (number of turns)	Wire Diameter (mm)	Calculation Rdc (Ω)	Measured (LCR meter) Rdc (Ω)	Measured (LCR meter) L (H)
Model 1	55	37	30	91	0.95	0.19	0.23	0.745
Model 2	52	32	20	91	0.50	0.51	0.60	0.505
Model 3	42	24	16	91	0.50	0.43	0.49	1.232

where r is the conductor diameter, ρ is resistivity, S is cross-sectional area of the copper wire, N is the number of turns in the coil and L is the core thickness. Equation 3, which is the calculation of winding resistance, is obtained approximately for these toroidal cores.

$$R = \rho \frac{(D_o - D_i) + 4r + 2L}{S} N \quad (3)$$

Core losses at various frequency and induction levels are measured using various excitation waveforms. Based on measurements [18], the coefficients of the Steinmetz Equation (4) are estimated:

$$P_w = k_w (f / f_0)^\alpha (B / B_0)^\beta \quad (4)$$

where P_w is the core loss per unit weight, f_0 is the basic frequency (1 Hz), and B_0 is the basic flux density (1 T). Also, k_w , α , and β are Steinmetz coefficients derived from experimental data. When the waveform was sinusoidal, the coefficients were taken as $k_w=0.003369$, $\alpha=1.301033$, and $\beta=2.135959$ [18]. The images of the toroidal model harvesters in the experiment set are given in Figure 2.

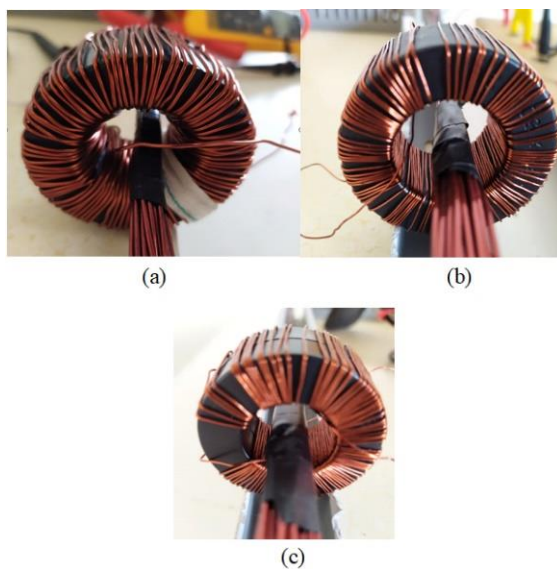


Figure 2. Images of toroidal models in the experiment set; (a) Model 1, (b) Model 2, (c) Model 3

The experimental setup created for the energy harvesting system is given in Figure 3. The materials in this experiment set are listed as load group, power line, and harvester cores. In order to pass current through the line, the load group consisting of incandescent lamps was connected in different ways (series and parallel) between itself, and the line current was generated; then, this current was measured with a clamp multimeter and recorded. To increase the line current and magnetic field density around the line, the number of conductors on the line was increased.

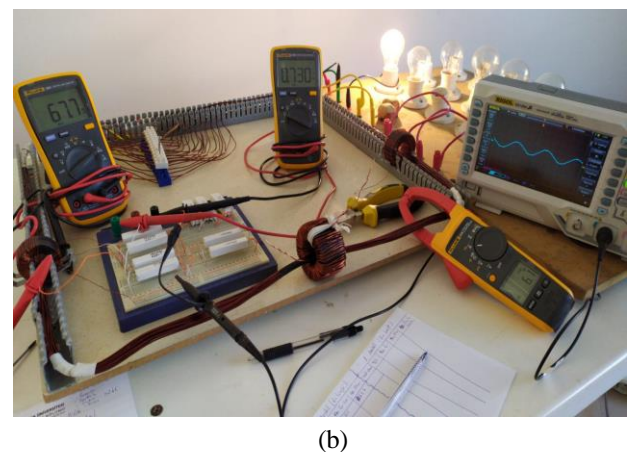
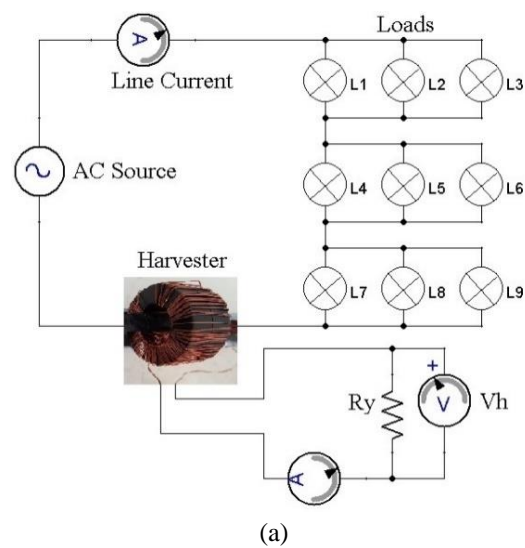


Figure 3. (a) Electrical circuit diagram of the experimental setup, (b) Harvester experimental setup

The line conductor was wrapped with more than one winding on a rectangular wooden floor by using cable channel. The cores in the toroidal geometry used for energy harvesting (Figure 2) were placed on the line. In this experiment set (Figure 3), the voltages and currents harvested at different loads from the harvesters were measured with multimeters and recorded.

Experiments of toroidal type models having amorphous structure were carried out in the experimental setup (Figure 3) where the electrical line was modeled. 3 A, 6.2 A and 9.2 A were passed on the line respectively, the harvester load (R_y) was also changed between 11 Ω and 330 Ω , and the current and voltage harvested at different line currents and at different loads were measured and recorded. The harvested power is calculated by multiplying the harvested current and voltage. Harvested current, voltage and power graphs of the data recorded in the excel file were obtained according to the load.

3. Numerical Analysis of the Toroidal Models and Data of the Experiment

Solving complex structures with finite element method (FEM) provides both high accuracy and time savings. Therefore, in the study, ANSYS Maxwell commercial software, which is using FEM, is used because it has wide drawing and solver (Transient, Magnetostatic, Eddy current, etc.) infrastructure. This program creates subregions in the structure by dividing the structure into multiple tetrahedron pieces to determine the magnetic field in nonhomogeneous structures. It determines the area of each region with separate polynomials for each subregion. In case the core material is not linear, analysis is done by using the B-H curve with a linear approach by Newton-Raphson method. After the analysis is completed, error analysis is carried out, and the solver continues to analyze the faulty finite element repeatedly until the determined criteria are fulfilled. As a result, magnetic field intensity, magnetic flux density, inductance values and forces can be obtained for materials determined with this software [19, 20]. The software uses the Ampere's law and Maxwell's equations in the static field solution of electromagnetic problems [22, 23]. Gauss' law is considered in magnetostatic analysis. Equation 5 between magnetic field intensity (B) and magnetic field intensity (H) is given in:

$$H = \frac{B}{\mu_0 \mu_r} \quad (5)$$

Here μ_0 and μ_r are the permeability of the vacuum and relative permeability of material, respectively. The curl of the vector potential (A), is defined as Equation 6, gives us the magnetic field:

$$\vec{B} = \nabla \times \vec{A} \quad (6)$$

J is the conduction current density. Equation 7 is defined as the Ampere's law.

$$\nabla \times \vec{H} = \vec{J} \quad (7)$$

Equation 8 is derived using Equation 5 and Equation 6. Thus, the software solves Equation 8 using the finite element method.

$$\nabla \times \left(\frac{1}{\mu_0 \mu_r} \nabla \times \vec{A} \right) = \vec{J} \quad (8)$$

Line current (6.2 A) of the Model 1, whose technical specifications are given in Table 2, was determined and static magnetic analysis of it was performed with Ansys Maxwell. In Figure 4, the magnetic flux density change of the core and results of the flux lines analysis are shown.

Determinations were made such that 6.2 A-line current would pass through the middle of the Toroidal model. The magnetic flux density value for this model is the value of 1.35 T at most. This flux density decreases towards the outside of the toroidal. In addition, because the toroidal model consists of a single piece, magnetic flux lines do not deteriorate and leakage fluxes do not occur. The iron loss was calculated using the Steinmetz formula given in Equation 4. This loss was 0.89 Watts on average.

The graph of the harvested-power (Ph) change by the change of line current (I_{line}) and load resistance (R_y) in the experiments conducted for Model 1 is given in Figure 5. The maximum harvested power at 3 A line current was measured as 96.77 mW at 235 Ω load-resistance. The maximum power at 6.2 A line current was measured as 277.98 mW at 88 Ω load-resistance. The maximum power at 9.2 A line current was measured as 443.78 mW at 55 Ω load-resistance. As seen in the experimental data, as the line current increases, the load-resistance at which the maximum harvested power occurs decreases.

The graph of the harvested-voltage (Vh) change by the change of line current (I_{line}) and load resistance (R_y) in the experiments conducted for Model 1 is given in Figure 6. In cases where line current was 3 A and 6.2 A, as the harvester load increased, the harvested voltage increased too. At 9.2 A line current, the harvested voltage increased up to 235 Ω load-resistance, then as the load increased, the harvested voltage began to drop.

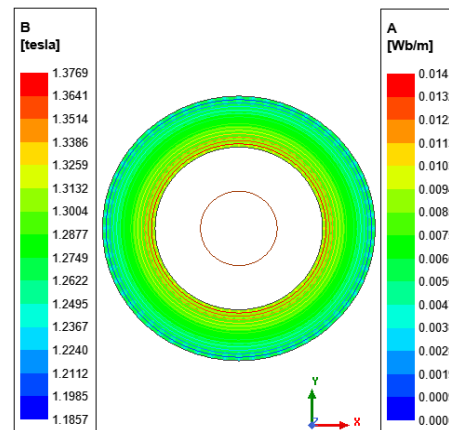


Figure 4. Model 1; magnetic flux density change and flux lines

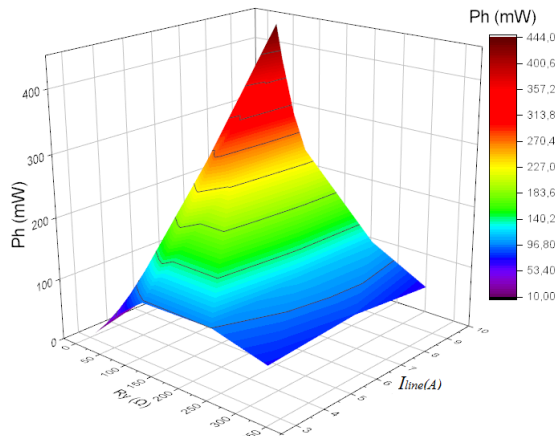


Figure 5. Harvested power change graph for Model 1

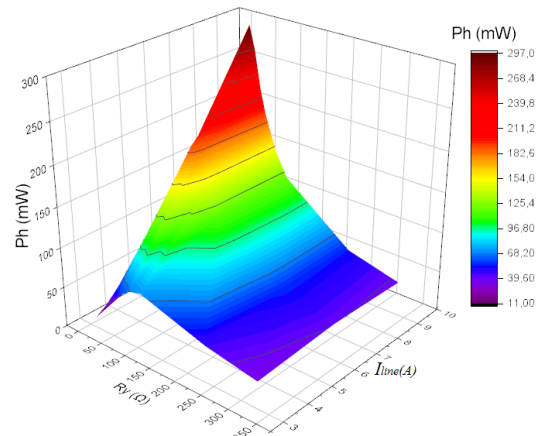


Figure 7. The harvested power change graph for Model 2

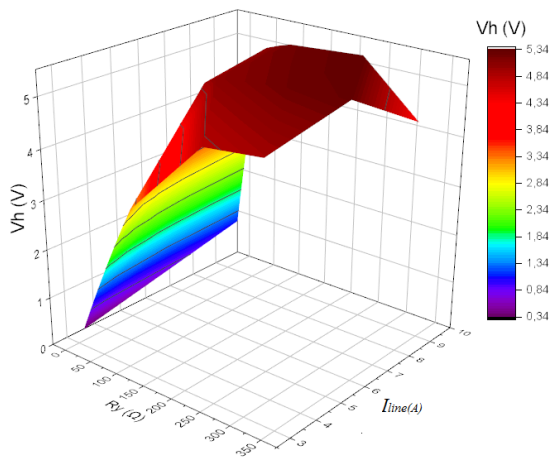


Figure 6. Harvested voltage change graph for Model 1

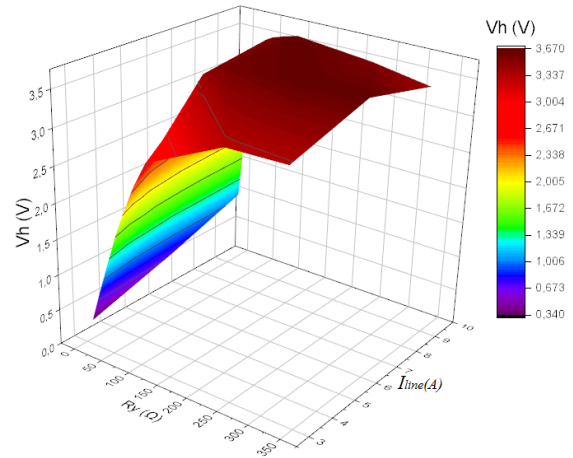


Figure 8. The harvested voltage change graph for Model 2

The graph of the harvested-power (Ph) change by the change of line current (I_{line}) and load resistance (R_y) in the experiments conducted for Model 2 is given in Figure 7. The maximum harvested power at 3 A line current was measured as 71.69 mW at 110 Ω load-resistance. The maximum power at 6.2 A line current was measured as 188.80 mW at 55 Ω load-resistance. The maximum power at 9.2 A line current was measured as 296.36 mW at 33 Ω load-resistance. As seen in the experimental data, as the line current increases, the load-resistance at which the maximum harvested power occurs decreases.

The graph of the harvested-voltage (V_h) change by the change of line current (I_{line}) and load resistance (R_y) in the experiments conducted for Model 2 is given in Figure 8. In cases where line current was 3 A and 6.2 A, as the harvester load increased, the harvested voltage increased too. At 9.2 A line current, the harvested voltage increased up to 150 Ω load-resistance, then as the load increased, the harvested voltage began to drop.

The graph of the harvested-power (Ph) change by the change of line current (I_{line}) and load resistance (R_y) in the experiments conducted for Model 3 is given in Figure 9. The maximum harvested power at 3 A line current was measured as 52.56 mW at 55 Ω load-resistance.

The maximum power at 6.2 A line current was measured as 99.26 mW at 22 Ω load-resistance. The maximum power at 9.2 A line current was measured as 132.04 mW at 15 Ω load-resistance. As seen in the experimental data, as the line current increases, the load-resistance at which the maximum harvested power occurs decreases.

The graph of the harvested-voltage (V_h) change by the change of line current (I_{line}) and load resistance (R_y) in the experiments conducted for Model 3 is given in Figure 10. In cases where line current was 3 A, as the harvester load increased, the harvested voltage increased too. At 6.2 A line current, the harvested voltage increased up to 235 Ω load resistance and then load values began to decrease. At 9.2 A line current, the harvested voltage increased up to 110 Ω load-resistance, then as the load increased, the harvested voltage began to decrease.

As seen in the experimental data, as the line current increases, the load-resistance at which the maximum harvested power occurs decreases. The reason for this condition can be based on equal in load impedance value to the equivalent source resistance. In the total impedance calculation of the harvester, since the magnitude of the coil-winding resistance is very small compared to the resistance generated by the core losses, those creating the actual impedance are core losses. Therefore, as the line current

increases, the load at which the maximum power occurs in the harvester decreases [4].

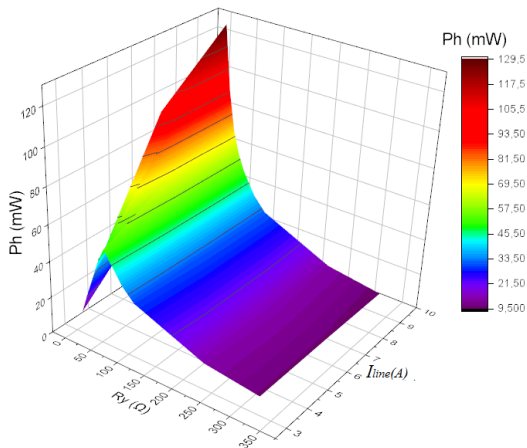


Figure 9. The harvested power change graph for Model 3

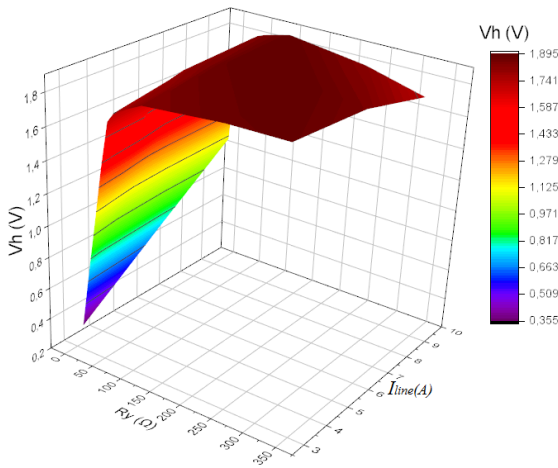


Figure 10. The harvested voltage change graph for Model 3

The harvested power change graph, which was combined according to load change in experiments conducted on 9.2 A line current of toroidal models, is given in Figure 11. When the graphs of the toroidal type models were examined, it was observed that as the harvester load increased, the harvested current decreased, and the harvested voltage increased up to a certain load value. However, the harvested power reached its maximum at a certain load value. Since there is no air gap in the structures of the toroidal cores, more magnetic flux passes over them.

As seen in the graphs, as the line current increased, more power was harvested, but the core reached saturation at smaller loads. The power and output voltage changes with the reduced permeability in the saturated magnetic core [21].

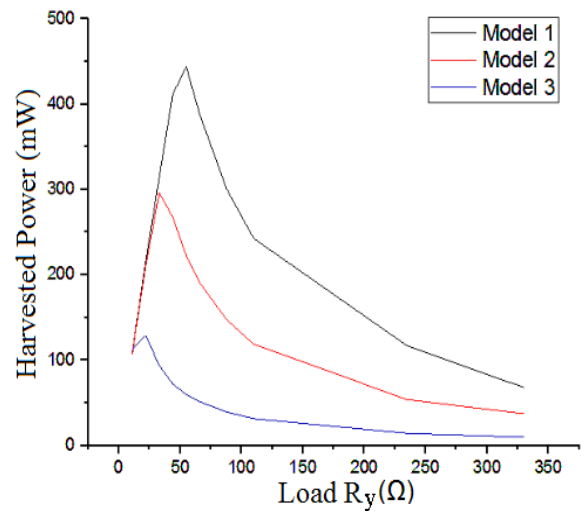


Figure 11. The harvested power change graph in toroidal models

Table 3. Comparison of power densities

Study	Core Material	Line Current (A)	Ry (Ω)	Number of Winding	D ₀	D _i	$\frac{D_0 - D_i}{2}$	L	Power Density (mW/cm ³)
[10]	Ferrite	5	-	156	36	23	6.5	15	7.83
[10]	Nanocrystalline	5	-	96	33.5	27.5	3	4	1.98
[10]	Iron powder	5	-	111	38.4	21.5	8.45	11.1	0
[4]	Silicon steel	5	900	200	75	55	10	30	2.38
This study Model 1	Amorphous	6.2	88	92	54	37	8.5	30	7.63
This study Model 2	Amorphous	6.2	55	92	50	32	9	20	8.14
This study Model 3	Amorphous	6.2	22	92	40	25	7.5	15	8.64
[4]	Silicon steel	10	770	200	75	55	10	30	9.54
This study Model 1	Amorphous	9.2	55	92	54	37	8.5	30	12.18

In a way supporting previous studies [4, 10], it was seen that Model 1 harvested more power due to the greatness of its volume and its smaller internal diameter than the Model 2. The fact that the volume of Model 3 was very small caused it to reach saturation at smaller loads and led less power to be harvested. In Table 3, the comparison of the power density of the models examined in this study with the previous studies on toroidal geometric harvesters is given.

When Table 3 was examined, it was seen that compared to the ferrite-core harvester, 10.34% more power density was obtained from the amorphous-core model 3 harvester with approximately the same line current and approximately the same internal diameters. Again, when the power densities of the Model 3 harvester and the nanocrystalline harvester with approximately the same line current and approximately the same internal diameters were compared, it was observed that approximately 4.3 times more power density was obtained from the Model 3 harvester with the amorphous core. When the power density of the harvester, which had 10 A line current and silicon steel material, was compared with the Model 1 9.2 A line-current harvester with amorphous material, it was figured out that 27.67% more power density was obtained from the Model 1 harvester. Again, when Table 3 is examined, it is understood that although the power density is independent of the number of winding, the magnitude of the line current affects it. Considering the same line current and winding number, although the power value of the Model 1 is the highest in Figure 11, it is the smallest in terms of power density.

4. Conclusions

When the toroidal models in this study were compared, it was seen that from the harvesters with the same core material and the same line current, more power density was obtained in the Model with a lower internal diameter. In this context, more power density was obtained from the Model 3 harvester, where the internal diameter, hence the air gap between the line and the harvester, was the lowest. When the same line current and winding numbers are taken into account, the values, at which the output power of the discussed models are maximum, change. Especially for core designs with a toroidal structure or closed flux path, the operating current can create saturation in the core material. Therefore, it is essential to perform the numerical analysis of the system to be studied by taking the line current into account. In addition, in the literature, due to its very low magnetic permeability, the iron-powder core material is not considered appropriate for use in harvesters. However, the harvester with amorphous material has been found to be appropriate for sensor systems. However, the system should be designed taking into account the saturation effects. In terms of future studies, experiments will be carried out on the operation of the toroid-structured model in the home sensor application. In addition, studies on special and different types

of harvester models will also be performed.

Declaration

The author(s) declared no potential conflicts of interest with respect to the research, authorship, and/or publication of this article. The author(s) also declared that this article is original, was prepared in accordance with international publication and research ethics, and ethical committee permission or any special permission is not required.

Acknowledgment

This study was produced from the master's thesis prepared by the first author under the supervision of the second author.

This work supported by the Scientific Research Project Unit of the Harran University under Research Project (project no: 18060), Turkey.

References

1. Yilmaz, C., and M. Kanoglu, *Investigation of hydrogen production cost by geothermal energy*. International Advanced Researches and Engineering Journal, 2017. **1**(1): p. 5-10.
2. Sen, O., and C. Yilmaz, *Thermodynamic performance analysis of geothermal and solar energy assisted power generation and residential cooling system*. International Advanced Researches and Engineering Journal, 2020. **4**(1): p. 41-47.
3. Boles, J.D., et al. *Inductive power harvesting for a touchless transmission line inspection system*. in *IEEE Power and Energy Society General Meeting (PESGM) 2016*: Boston, USA. p.1-5.
4. Liu, Y., et al., *A novel high-density power energy harvesting methodology for transmission line online monitoring devices*. Review of Scientific Instruments, 2016. **87**(7): p. 075119.
5. Moser, M.J., et al., *Strong and weak electric field interfering: Capacitive icing detection and capacitive energy harvesting on a 220-kV high-voltage overhead power line*. IEEE transactions on industrial electronics, 2010. **58**(7): p. 2597-2604.
6. Yang, F., et al., *A novel self-powered lightning current measurement system*. IEEE Transactions on Industrial Electronics, 2017. **65**(3): p. 2745-2754.
7. Yuan, S., et al., *A high-efficiency helical core for magnetic field energy harvesting*. IEEE Transactions on Power Electronics, 2016. **32**(7): p. 5365-5376.
8. White, R.M., et al., *Atmospheric sensors and energy harvesters on overhead power lines*. Sensors, 2018. **18**(1): p. 114.
9. Wang, W., et al., *Optimization design of an inductive energy harvesting device for wireless power supply system overhead high-voltage power lines*. Energies, 2016. **9**(4): p. 242.
10. Dos Santos, M.P., et al. *Energy harvesting using magnetic induction considering different core materials*. in *2014 IEEE International Instrumentation and Measurement Technology Conference (I2MTC)2014*:Montevideo, Uruguay. p.1-3.

11. Zhuang, Y., et al. *An improved energy harvesting system on power transmission lines*. in *IEEE Wireless Power Transfer Conference (WPTC)2017*: Taipei, Taiwan. p.1-3.
12. Zhao, X., et al. *Energy harvesting for overhead power line monitoring*. in *International Multi-Conference on Systems, Signals & Devices 2012*: Chemnitz, Germany. p.1-5.
13. Çelik, K., E. Kurt, and Y. Uzun, *Experimental and theoretical explorations on the buckling piezoelectric layer under magnetic excitation*. *Journal of Electronic Materials*, 2017. **46**(7): p. 4003-4016.
14. Kabakulak, M., M.T. Güllüoğlu, and S. Arslan. *A wireless energy harvesting system design and numerical analysis*. in *3rd International Congress of Professional and Technical Sciences 2018*: Gaziantep, Turkey. p.418-425.
15. Kabakulak, M., M.T. Güllüoğlu, and S. Arslan. *Energy harvester analysis in common simulation platform*. in *1st International GAP Mathematics - Engineering - Science and Health Sciences Congress2018*: Sanliurfa, Turkey. p. 26-32.
16. Kabakulak, M., M.T. Güllüoğlu, and S. Arslan. *Comparison of energy harvesters according to change of conductor form*. in *1st International Mersin Symposium 2018*: Mersin, Turkey. p.16-26.
17. Kabakulak, M., M.T. Güllüoğlu, and S. Arslan. *Energy Harvesting from Busbar*. in *1st International Mersin Symposium2018*: Mersin, Turkey. p.27-36
18. *METGLAS® 2605-SA1 core datasheet*. 2018 [01 January 2020]; Available from: https://www.netl.doe.gov/sites/default/files/netl-file/METGLAS-2605-SA1-Core-Datasheet_approved%5B1%5D.pdf.
19. Fenercioğlu, A., and Tarimer, I., *Solution Processes of a Magnetic System's Magnetostatic Analysis with Maxwell 3D Field Simulator*. *Selçuk Teknik Dergisi*, 2007. **6**(3): p. 221-240.
20. Arslan S., *Medium frequency spot welding transformer and machine design*. MSc Thesis, 2011, Turkey: Gazi University, Graduate School of Natural and Applied Sciences.
21. Park, B., Kim, et al. *Optimization design of toroidal core for magnetic energy harvesting near power line by considering saturation effect*. *AIP Advances*, 2018. **8**(5): p. 1-7.
22. Kabakulak M., *Energy harvesting from electromagnetic fields around overhead power lines*. MSc Thesis, 2020, Turkey: Harran University, Graduate School of Natural and Applied Sciences.
23. ANSYS, *Ansys Maxwell 2019 version Help File*, p.1-2955.



Research Article

Determination of optimal PID control parameters by response surface methodology

Adnan Aldemir ^{a,*}  and Mohammed Sadralddin Anwer ^a 

^aVan Yüzüncü Yıl University, Faculty of Engineering, Department of Chemical Engineering, 65080, Van, Turkey

ARTICLE INFO

Article history:

Received 30 March 2020

Revised 15 May 2020

Accepted 22 May 2020

Keywords:

Dynamic analysis

Liquid level control

Optimum control parameters

PID control

Response surface
methodology

ABSTRACT

Proportional–Integral–Derivative (PID) controllers are the most widely used systems in industrial applications and in academic research regarding control engineering. In this study, the optimal PID control parameters of a liquid level control system were determined with Response Surface Methodology. Dynamic analysis was carried out on the liquid level control system to prepare the reaction curve. Accordingly, dead time, time constant and process gain values were determined as 16s, 261s and 0.842, respectively. Based on the dynamic analysis, PID parameters were calculated in accordance with the Cohen-Coon, Ziegler-Nichols, Yuwana-Seborg methods, which are the commonly used tuning methods. The K_p , τ_i , τ_D parameters were calculated as 30.77, 29.15 and 5.4 with the Cohen-Coon method, as 0.453, 30.0 and 7.5 with the Ziegler-Nichols method and as 1.63, 686.3 and 117.7 with the Yuwana-Seborg method, respectively. The PID control parameters applied for the 40cm, 50cm and 60cm set points and ISE and IAE control performance values after experiments were calculated. The K_p , τ_i and τ_D values were selected as the independent parameters, while the ISE and IAE values were chosen as the dependent variables. The numerical values of the responses for the runs in the design matrices were determined with a closed-loop PID controller with the liquid level system block diagram that was designed in MATLAB/Simulink. The simulations proposed by the trial version of Design Expert 7.0 program were performed in order and the IAE and ISE values were calculated after the simulations were processed. In this study, minimum ISE and IAE values were selected to determine the best PID parameters of a liquid level control system. The optimal PID control parameters of the liquid level system required to obtain the lowest ISE and IAE values were determined as 23.14, 28.31 and 11.50 for K_p , τ_i and τ_D , respectively.

© 2020, Advanced Researches and Engineering Journal (IAREJ) and the Author(s).

1. Introduction

PID controllers are the most commonly used systems in the industrial field including motor drives, magnetic and optical memories, automotive and flight control, instruments and meters, robotics, and find the most research and application area in control engineering [1]. PID controller is successful design in industrial automatic control for its simple structure, stability, reliability and convenient adjustment [2-3]. PID controllers are used as pneumatic, hydraulic or mechanical controllers or had a simple interface for manual tuning of the controller. PID control output is generated by the addition of three terms called proportional, which depends on the current error, integral, which depends on the sum of past errors and derivative, which depends on future errors based on

current rate of change of errors (Figure 1). Traditional methods for tuning PID controllers are divided into three categories as formula based, rule based and optimization based tuning methods [4]. Various experimental methods such as the Ziegler-Nichols and Cohen-Coon methods, have been developed to tune PID control parameters and most have been applied to real systems [5-6]. Researchers have projected experimental PID tuning approach grounded upon trial and error approach and procedure response curve approaches. These methods are time-consuming, costly and optimizing by establishing mathematical model considering the specific control mechanism, is convenient and efficient [7]. However, the parameters determined by these methods may not be effective in nonlinear, variable parameter and unstable

* Corresponding author. Tel.: +90-432-225-1725; Fax: +90-432-225-1730.

E-mail addresses: adnanaldemir@yyu.edu.tr (A. Aldemir), mohammedsadralddin@gmail.com (M. S. Anwer),

ORCID: 0000-0001-9884-0961 (A. Aldemir), 0000-0002-0562-5144 (M. S. Anwer)

DOI: 10.35860/iarej.711314

systems. In such cases, it is necessary to determine the optimal control parameters. The advantages of optimal control parameters are independent problems, universal search, high robustness and multi objective orientation. In general, it is difficult to define the “optimality” of a controller, due to the fact that there are several important aspects to consider, such as set-point response, minimum error, disturbance rejection, robustness, input usage and noise sensitivity [8]. Therefore, different optimization techniques have been applied for PID tuning parameters [9].

$$C(s) = \frac{U(s)}{E(s)} = K_p + \frac{\tau_I}{s} + \tau_D s \quad (1)$$

Central Composite Design (CCD) is one of the most useful experimental planning methodologies when there are two or more factors. Thus, CCD can be used to evaluate the optimal values for a set of PID controller parameters (K_c , τ_i , τ_D) that provide the best result to performance criterion, such as the integral of square of error (ISE), integral of the absolute of the error (IAE).

There are several response surface methodology (RSM) applications that are used to determine optimal control parameters. RSM has been applied to optimize PID controller parameters for the pH and electrical conductivity values of a batch electrocoagulation process in which pulp and paper mill wastewater was treated, and to investigate the effects of control action on pollutant removal and energy consumption. ISE, IAE, ITAE and ITSE values are selected as responses which indicators of controller performance [10]. Control of the absorption column was carried out using a PID controller with the affluent water flow to the column corresponding to the manipulated variable and the component (CO_2) concentration in the gas stream effluent to the column corresponding to the controlled variable. The numerical values for proportionality constants K_p , τ_i and τ_D were defined using the experimental design of CCD, the study range of which was defined from an initial estimate. The response variable was selected the ITAE performance criteria. The experimental design runs were performed using simulations in a program developed with MATLAB software.

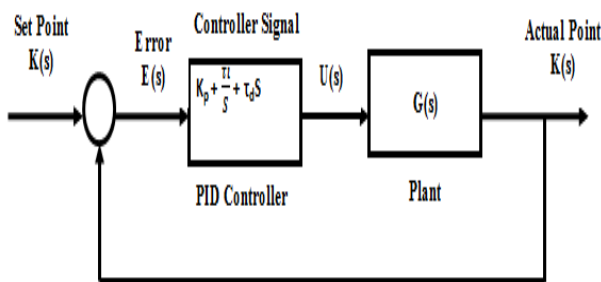


Figure 1. Diagram of feedback control with a PID controller

The responses ranged from 0.1979 to 1.1632, and the lowest value represented approximately 55% improvement in ITAE in comparison to the simulation using the initial estimated values. It was observed that the p-value for the significant terms was much lower than 0.05, which confirmed its significance [11]. The Proportional Integral (PI) control coefficients for a permanent magnet brushless direct current motor drive were determined with RSM. PI control parameters, K_p and τ_i selected input parameters and maximum overshoot with settling time selected responses. A total of 13 experiments were carried out and the optimal values of the K_p and τ_i parameters were obtained as 638.65 and 56.814, respectively. The experimental results were given to show the validity of this method [12].

Liquid level control in tanks and vessels is one of the most common controls in the process industries [13]. Level control is crucial for the successful operation of most chemical plants as the desired production rates and inventories are achieved through the proper control of flows and levels [14]. However, liquid level control is difficult due to problems such as, maximum overshoot, steady-state error and oscillating transient response [15].

The most commonly used performance indexes for PID control are ISE and IAE, which are given Equation (2) and Equation (3), respectively.

$$ISE = \int_0^{\infty} e(t)^2 dt \quad (2)$$

$$IAE = \int_0^{\infty} |e(t)| dt \quad (3)$$

In the present study, three different tuning methods applied to the liquid level experimental system under the same conditions and the on-line liquid level results of these tuning methods were compared for different set points. After the experiments, the ISE and IAE values were calculated to determine the optimal PID controller parameters of this experimental system.

2. Materials and Method

2.1 Experimental System

The liquid level control system used in this study consisted of three liquid tanks which built on mechanic assembly, a pneumatic valve connected to a regulator to adjust air pressure, an electronic panel showing liquid level and valve openings and hand valves acting at different points. The water in the storage tank was carried in pvc pipes with a submersible pump, passed through the pneumatic valve and filled into the level measuring tank. To prevent overflow, the level measuring tank was connected to a discharge tank underneath with a pvc discharge pipe located in the middle of the level measuring tank. A manually adjustable valve was located at the bottom of the level measuring tank to affect the disturbance on the system.

Discharge and storage tanks were connected to each other with a pvc pipe to balance the liquid level in them. A discharge valve was connected to the bottom of these tanks to discharge the water in them. The compressed air required for the operation of the pneumatic valve was supplied by a compressor in a laboratory and the air was sent to the valve by adjusting the desired pressure value with a regulator. The experimental liquid level control system is given in Figure 2.

The liquid level control experiments were performed with on-line computer software developed by the manufacturer of this control system. During the on-line experiments on the liquid level control system conducted with this computer software, the valve opening value which was determined as the input variable and the liquid level data which was determined as the output variable were automatically recorded on a Microsoft Excel file. The graphics of the liquid level and valve opening value changes were displayed on screen. In addition, the data acquisition time was adjusted in seconds. The IAE and ISE values were calculated with three different set level values and measured level values after the on-line experiments. The equations of the PID control parameters for the Cohen-Coon, Ziegler-Nichols and Yuwana-Seborg tuning methods are given in Table 1.

2.2 Experimental Design and Optimization Procedure

Experiments were performed to determine the best PID control parameters for liquid level control. The PID tuning parameters (K_p , τ_i , τ_D) which values were proposed by the program recorded on the liquid level control system and on-line experiments were carried out.



Figure 2. Experimental system: on-line computer connected to the liquid level control system

Table 1. Equations of the PID controller parameters for the three tuning methods

Method	Cohen-Coon	Ziegler-Nichols	Yuwana-Seborg
K_p	$\frac{1}{K_c} \frac{\tau}{t_d} \left(\frac{4}{3} + \frac{t_d}{4\tau} \right)$	$K_u/1.7$	$\frac{a}{K_m} \left(\frac{d_m}{\tau_m} \right)^{-b}$
τ_i	$t_d \frac{32 + 6(t_d/\tau)}{13 + 8(t_d/\tau)}$	$P_u/2.0$	$\tau_m c + \left(\frac{d_m}{\tau_m} \right)^d$
τ_D	$t_d \frac{4}{11 + 2(t_d/\tau)}$	$P_u/8.0$	$\tau_m e \left(\frac{d_m}{\tau_m} \right)^f$

All other operating conditions were kept constant while the values of K_p , τ_i and τ_D were changed during the liquid level control experiments. It was expected that the liquid levels would be at a steady state by initially operating the valve opening at 10% for 300 s. At the end of 300s, the previously recorded K_p , τ_i and τ_D parameters were changed with the keys on the control panel of the experimental system and the effects of these PID parameters were observed on the liquid level control. During the experiments, liquid level and valve opening changes were continuously monitored and the values of these input and output variables were continuously recorded in seconds. The ISE and IAE values were calculated for different set level values and measured level values after the on-line experiments.

3. Results and Discussion

3.1 Dynamic Analyses for Determining the Process Parameters

Two different dynamic analyses were carried out on the liquid level control system to determine the PID control parameters.

In the first dynamic analysis, an experiment, in which a step change was applied to the valve value to prepare the reaction curve and determine the dead time, time constant and process gain values, was performed. The system was initially operated at 13% valve value and liquid level was expected to become steady state. A positive effect was given to the valve value and 70% valve opening value is provided. The liquid level that was fixed at 10 cm at the first valve value was observed to increase to 58 cm after the step change was applied to the valve value (Figure 3). The PID control parameters were calculated in accordance with the equations of the Cohen-Coon and Ziegler-Nichols methods using control coefficients that were determined from the first dynamic experiment given in Table 2.

Table 2. Coefficients of the experimental liquid level system

Parameter	τ_d	τ	K_c
Value	16s	261s	0.842

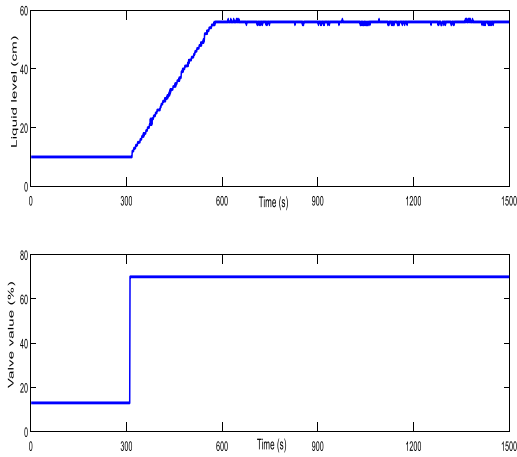


Figure 3. Liquid level changes in accordance with the step effect of valve position

In the second dynamic analysis, a proportional control value was determined by taking the integral and derivative terms as zero and a step effect was given to the set point when the system was under this proportional control action. The output variable was oscillated by changing the proportional control value. The process parameters were calculated by the oscillation of the output variable. The system was initially operated at a 13% valve value and the liquid level was fixed at 10 cm. The output variable was oscillated by changing the proportional control action after the integral and derivative terms as zero. The liquid level changed between 27 cm and 72 cm in the measuring (upper) tank (Figure 4). The PID control parameters were calculated in accordance with the equations of the Yuwana-Seborg method using control coefficients that were determined from the second dynamic experiment given in Table 3.

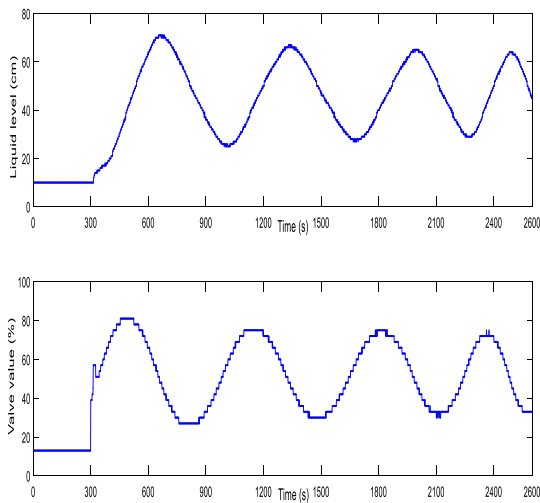


Figure 4. Liquid level changes with valve value for calculate Yuwana-Seborg constants

Table 3. Control coefficients calculated in accordance with the Yuwana-Seborg method

Parameter	Value	Parameter	Value
R ₀	13 %	α ₁	-0.177
R	70 %	σ	0.605
C ₀	10 cm	K _m	58.74
C	60 cm	K	14.68
C _{p1}	72 cm	β ₁	2.44
C _{p2}	67 cm	β ₂	3.53
C _{m1}	26 cm	τ _m	925.8
C _∞	47.678	d _m	311.1

3.2 PID Control Results of The Coefficients Determined with The Cohen-Coon Method

Table 4 presents the PID control coefficients calculated using the equations of the Cohen-Coon method, which are given in Table 2. The liquid level control experiments were carried out by selecting different set points by using the PID coefficients determined in accordance with the Cohen-Coon method. In these control experiments, the changes in the valve values and liquid level profiles over time were observed and the experimental results obtained are shown in Figures 5-7. The experimental results for the different set points were investigated and it was observed that the pneumatic valve was worked on-off form irregularly. It was determined that the valve was successful for level control despite the incessant and irregular on-off operation. The same behaviour of manipulated variable was shown other studies, such as temperature control [16]. According to the experimental results, it was determined that the liquid level control using PID parameters obtained in accordance with Cohen-Coon method showed good performance and that these coefficients were suitable enough for liquid level control. Cohen-Coon parameters were achieved fast and stable regulation result. Cohen-Coon parameters work well in processes where the dead time is less than two times the length of the time constant and can even be stretched further if the process demands. One main issue with the Cohen-Coon parameters is that they tend to not be extremely robust, in other words, a small change in the process parameters can result in the closed loop system to become unstable and lead to oscillatory closed loop behaviour [17].

Table 4. PID control coefficients calculated in accordance with the Cohen-Coon method

Parameter	K _P	PB	τ _I	τ _D
Value	30.77	3.25	29.15	5.41

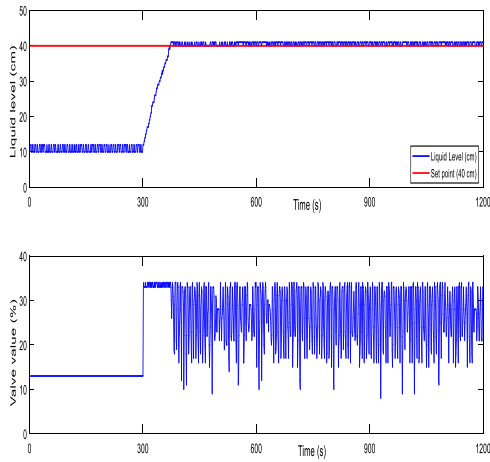


Figure 5. Liquid level changes with valve value for set point 40 cm using C-C method

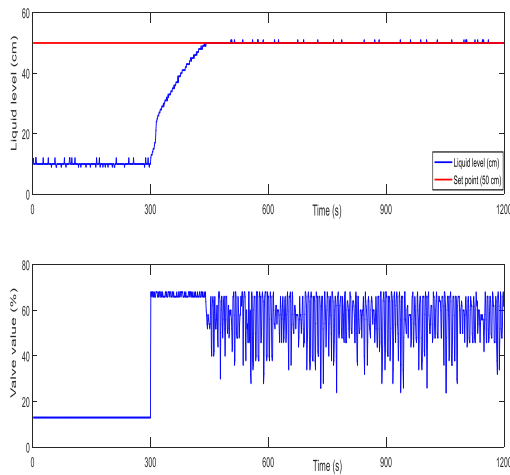


Figure 6. Liquid level changes with valve value for set point 50 cm using C-C method

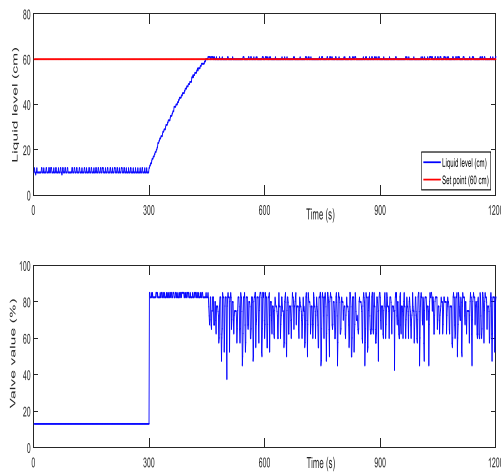


Figure 7. Liquid level changes with valve value for set point 60 cm using C-C method

3.3 PID control results of the coefficients determined with the Ziegler-Nichols method

The PID control coefficients calculated by using the values of the dead time and time constant parameters that were determined from the reaction curve are presented in Table 5. The PID control experiments were performed by selecting three different set points using the PID coefficients determined in accordance with the Ziegler-Nichols method. In these control experiments, the change in valve value and liquid level profiles over time was observed, and the experimental results are shown in Figures 8-10. According to the valve value, the liquid level was observed to be fixed at 1 cm, 2 cm and 5 cm offset for 40, 50, 60 cm set points respectively after oscillation. The experimental results for the different set points were investigated and it was observed that the valve opening value was fixed at %32, %70 and %99 for 40, 50, 60 cm set points respectively. The PID coefficients determined in accordance with the Ziegler-Nichols method were not sufficient for high level control and were not suitable for liquid level control. The parameters determined in accordance with the Ziegler-Nichols method were found to be satisfactory for first order processes with small dead times but under set point change and long dead time they failed to keep the process within an acceptable limit [18].

3.4 PID Control Results of Coefficients Determined with The Yuwana-Seborg Method

The process constants which were determined using the Figure 4 and determined PID control parameters were given in Table 6.

Table 5. PID control coefficients calculated in accordance with the Ziegler-Nichols method

Parameter	K_P	PB	τ_I	τ_D
Value	0.453	220.75	30.00	7.51

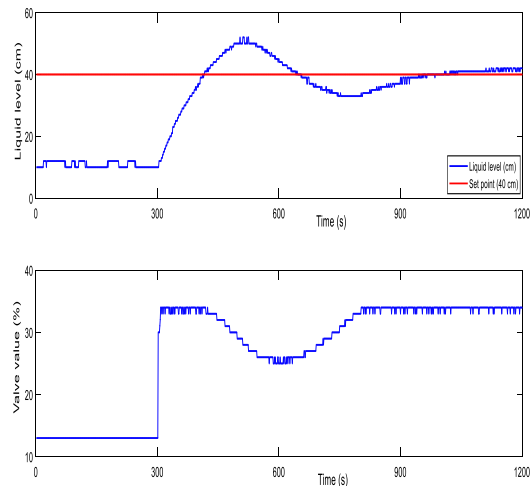


Figure 8. Liquid level changes with valve value for set point 40 cm using Z-N method

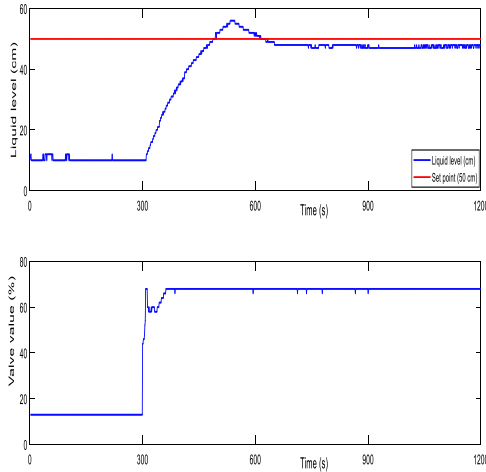


Figure 9. Liquid level changes with valve value for set point 50 cm using Z-N method

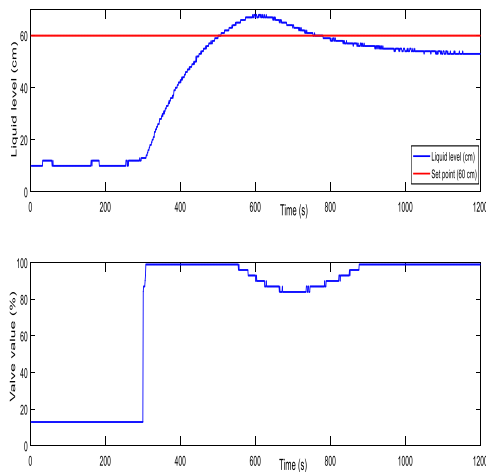


Figure 10. Liquid level changes with valve value for set point 60 cm using Z-N method

The PID control experiments were performed by selecting different set points using the PID coefficients determined in accordance with the Yuwana-Seborg method. In these control experiments, the change in the valve value and liquid level profiles over time was observed, and the experimental results are shown in Figures 11-13. According to the valve value, the liquid level was observed to be fixed at 7 cm, 15 cm and 3 cm offset for 40, 50, 60 cm set points, respectively, after oscillation. The experimental results for the different set points were investigated and it was observed that the valve opening value was fixed at 34%, 34% and 99% for 40, 50, 60 cm set points, respectively. The PID coefficients that were determined in accordance with the Yuwana-Seborg method were not sufficient for liquid level control as can be seen from Figures 11-12. The fact that it requires only a single closed-loop test and that the algorithm is simple are the practical advantages of the Yuwana-Seborg method. Its main disadvantage, on the other hand, is that the test is carried out under proportional

control which introduces steady state offset during testing, which in turn creates off-specification products [19]. In addition, this method cannot be used for mildly underdamped or overdamped closed-loop responses. Furthermore, it is inaccurate, particularly when a large dead-time exists due to the use of the first order with the dead time [20].

The experimental results were investigated for the performance comparison of PID controllers using three classical tuning methods. Comparison to these methods with Cohen-Coon method were shown good performance on this experimental system for liquid level control. It was observed that the manipulated variable showed the same behavior with the Cohen-Coon and Ziegler-Nichols parameters on the liquid level control and wireless temperature control. However, the Ziegler-Nichols parameters showed better performance than the Cohen-Coon parameters on the wireless temperature control [21]. In general, it is difficult to define the “optimality” of a controller, due to the fact that there are several important aspects to consider, such as set-point response, disturbance rejection, robustness, input usage and noise sensitivity. Often, a control loop is evaluated exclusively on the basis of its response to a set point change, and in process control most important way to comparison of the PID controller performance is calculated the error values [22]. Therefore, the IAE and ISE values are the most common determinants used to determine controller performance in control engineering. The IAE and ISE values calculated using the data obtained after applying three different tuning methods with three different set points are given in Table 7 and Table 8, respectively.

Table 6. PID control coefficients determined in accordance with the Yuwana-Seborg method

Parameter	K_p	PB	τ_I	τ_D
Value	1.63	61.35	686.30	117.7

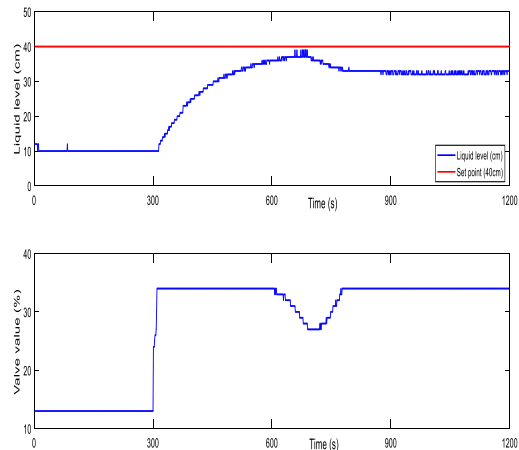


Figure 11. Liquid level changes with valve value for set point 40 cm using Y-S method

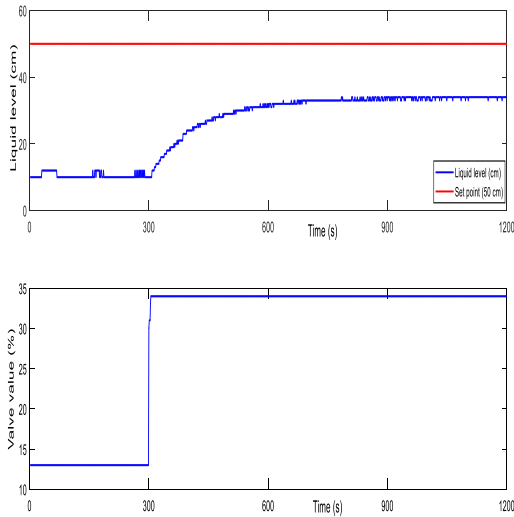


Figure 12. Liquid level changes with valve value for set point 50 cm using Y-S method

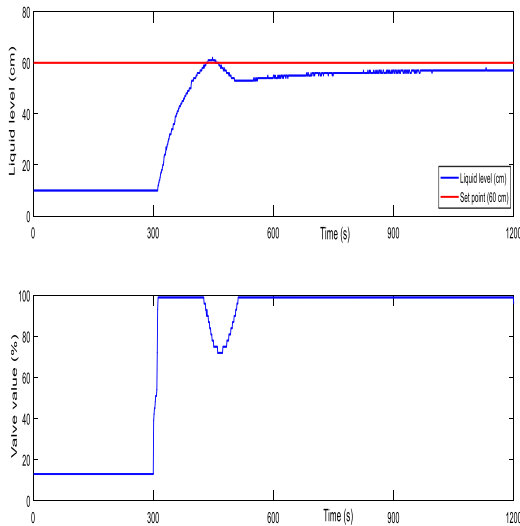


Figure 13. Liquid level changes with valve value for set point 60 cm using Y-S method

Table 7. IAE values calculated for the three PID tuning methods

Set Point	Cohen-Coon	Ziegler-Nichols	Yuwana-Seborg
40 cm	1455	4495	7714
50 cm	1983	5008	17536
60 cm	3216	7233	5796

Table 8. ISE values calculated for the three PID tuning methods

Set Point	Cohen-Coon	Ziegler-Nichols	Yuwana-Seborg
40 cm	17915	48155	93950
50 cm	41593	87640	366660
60 cm	92168	137865	104558

3.5 Preparing a Simulation Diagram and Code to Calculation of Responses

The PID parameters of K_p , τ_i and τ_D , the values of which were proposed by the program recorded on the MATLAB code, are given in Figure 14. All other simulation conditions were kept constant while the values of K_p , τ_i and τ_D were changed for the liquid level control simulations. The simulations proposed by the Design Expert 7.0 program were performed using the MATLAB/Simulink program to determining the optimum PID tuning parameters (Figure 15). The level was expected to be at a steady state by initially operating the valve opening at 10% for 300 s. At the end of 300s, the previously recorded K_p , τ_i and τ_D parameters were changed with the keys on the MATLAB program and the effect of these PID parameters were observed on the liquid level control. During the simulations, the changes in the liquid level were continuously monitored and the values of these input and output variables were continuously recorded in minutes. The ISE and IAE values were determined by using a constant set level and measured level after the simulations and these values were processed in the Design Expert 7.0 program to be analyzed.

3.6 Simulation Results and the Statistical Analysis of CCD

The K_p , τ_i and τ_D parameters of PID were selected as the independent operating variables, while the ISE and IAE values were determined as the responses. Experimental design was prepared with the Design-Expert 7.0.0 trial program and the subsequent statistical analysis was conducted by RSM. A statistical approach with CCD was applied to determine the interaction between these variables. The simulation ranges of the K_p , τ_i and τ_D parameters for CCD were determined with the parameters which determined according to the Cohen-Coon and Ziegler-Nichols parameters. The region of exploration to locate the optimum operating conditions was determined as 11.0 – 40.0, 15.0 – 45.0 and 6.0 – 20.0 for K_p , τ_i and τ_D , respectively.

```

%proportional constant Kp
Kp=0.5;
%integral constant TII
TII=1;
%derivative constant TDD
TDD=0.001;
[t,x,y]=sim('AAAyeniSim',20);
plot(t,y(:,1))
grid
title('liquid level versus time');
IAE=sum(abs(y(:,2)-y(:,1)));
ISE=sum((y(:,2)-y(:,1)).^2);
SONUC=[Kp, TII, TDD, ISE, IAE];
save PIDveriKriter.matSONUC
    
```

Figure 14. MATLAB code for the PID parameters to calculate the IAE and ISE values

A total of 20 experiments were conducted within the scope of the CCD and the tuning parameters at the center point were 25.50, 30.00 and 13.00 for K_p , τ_i and τ_D , respectively which were used for the optimization of PID. Simulation runs were used different PID coefficients and calculated IAE, ISE responses after simulations are given in the Table 9. The data presented in Table 9 were processed by the program to create an empirical model for the representation of the ISE and IAE values in terms of the K_p , τ_i and τ_D variables. According to the regression analysis, which was performed with a 95% confidence interval, it was determined that the lack of fit error and the p-values were significant. Quadratic models were used to fit the obtained data by least squares analysis and the empirical models obtained for ISE and IAE are given in Equation (4) and Equation (5), respectively.

$$ISE = +54058.10816 - 1977.96024 * [K_p] - 708.58871 * [T_i] - 367.21030 * [T_D] + 6.07529 * [K_p * T_i] - 2.37562 * [K_p * T_D] + 3.03929 * [T_i * T_D] + 38.40208 * [K_p^2] + 8.51565 * [T_i^2] + 12.39114 * [T_D^2] \quad (4)$$

$$IAE = +5704.62464 - 207.56067 * [K_p] - 65.26341 * [T_i] - 81.63389 * [T_D] - 0.055172 * [K_p * T_i] + 7.38916E-003 * [K_p * T_D] - 0.040476 * [T_i * T_D] + 4.51624 * [K_p^2] + 1.18198 * [T_i^2] + 3.59113 * [T_D^2] \quad (5)$$

The statistical significance of the quadratic model, which was applied to explain the experimental data, was

tested by analysis of variance (ANOVA) results. Evaluation of models for ISE and IAE responses are given in the Table 10 and Table 11, respectively. The ANOVA results of the quadratic model for ISE and IAE responses are given in the Table 12 and Table 13, respectively. It can be seen from the tables that the regression was statistically significant at an F-value of 12.94 and 4.06 for the ISE and IAE values, respectively. Very low probability values (0.0002 for ISE and 0.0197 for IAE) were determined for the two responses. Therefore, an adequate precision of 12.426 for ISE and 7.095 for IAE was obtained with the quadratic model that described the control system used in this study, indicating a satisfactory signal for the liquid level control. The regression results are statistically significant which show that P model 0.0002 and 0.0197 for ISE and IAE, respectively. In this case K_p , K_p^2 and T_i^2 were determines as significant model terms for ISE, while only K_p^2 was a significant term for IAE.

The statistical results of the ISE and IAE responses on the liquid level control are given in Table 14 and Table 15, respectively. According to the ANOVA results, the model R^2 values were determined as 92.09% and 78.52% for ISE and IAE, respectively. The adjusted R^2 values were found to be 84.98% and 59.18% for ISE and IAE, respectively. The R^2 values showed that there was a high correlation between the observed values and the predicted values. These results indicated that the regression model provided a good explanation for the relationship between the variables and the responses

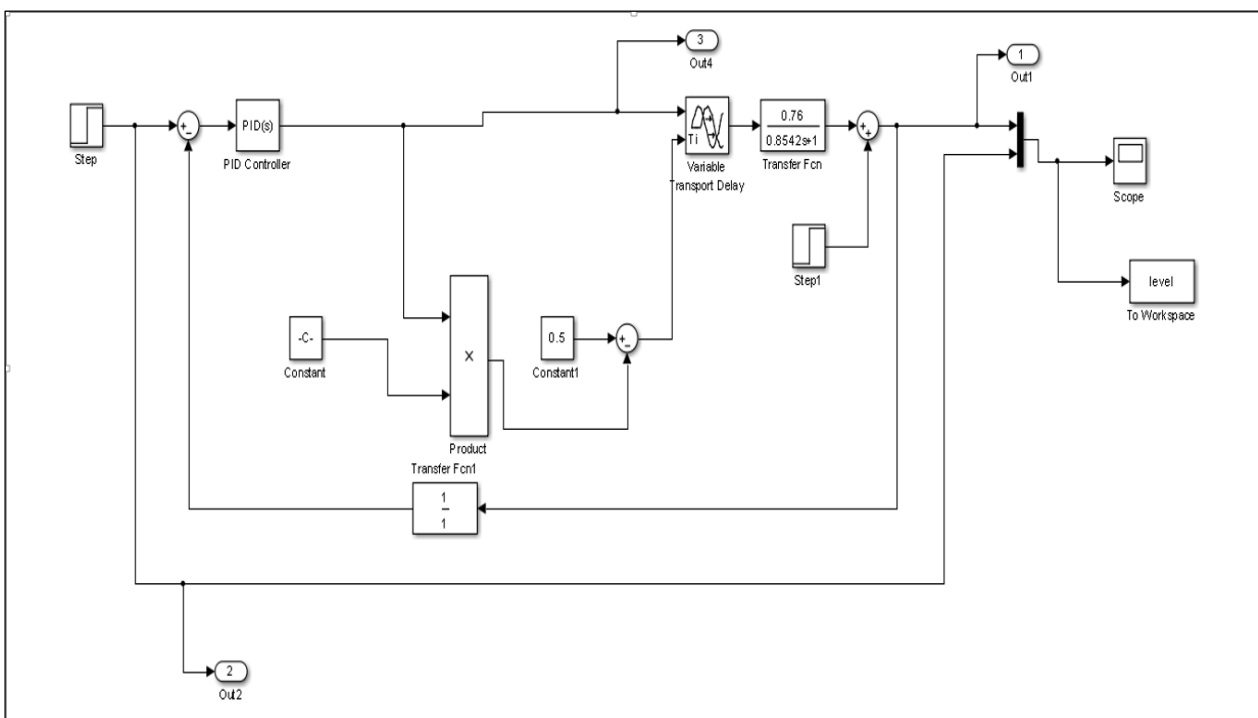


Figure 15. MATLAB/Simulink diagram of the liquid level control system

Table 9. Results of the simulation runs with the calculated two responses

Run Number	Kp (X ₁)	τ_1 (X ₂)	τ_D (X ₃)	ISE (R ₁)	IAE (R ₂)
1	25.50 (0)	30.00 (0)	13.00 (0)	17452	1971
2	25.50 (0)	30.00 (0)	13.00 (0)	17452	1971
3	25.50 (0)	30.00 (0)	1.23 (- α)	17489	1943
4	11.00 (-1)	45.00 (+1)	6.00 (-1)	23654	2793
5	25.50 (0)	30.00 (0)	24.77 (+ α)	17569	1995
6	40.00 (+1)	45.00 (+1)	6.00 (-1)	33476	4153
7	49.89 (+ α)	30.00 (0)	13.00 (0)	37645	4029
8	11.00 (-1)	15.00 (-1)	20.00 (+1)	27126	3157
9	25.50 (0)	55.23 (+ α)	13.00 (0)	21898	2635
10	11.00 (-1)	45.00 (+1)	20.00 (+1)	23718	3245
11	11.00 (-1)	15.00 (-1)	6.00 (-1)	26983	3127
12	40.00 (+1)	15.00 (-1)	6.00 (-1)	32875	4096
13	25.50 (0)	4.77 (- α)	13.00 (0)	20564	1832
14	40.00 (+1)	45.00 (+1)	20.00 (+1)	33931	4169
15	1.11 (- α)	30.00 (0)	13.00 (0)	39652	4305
16	25.50 (0)	30.00 (0)	13.00 (0)	17452	1971
17	25.50 (0)	30.00 (0)	13.00 (0)	17452	1971
18	25.50 (0)	30.00 (0)	13.00 (0)	17452	1971
19	25.50 (0)	30.00 (0)	13.00 (0)	17452	1971
20	40.00 (+1)	15.00 (-1)	20.00 (+1)	30698	4568

Table 10. Evaluation of the models in terms of best fit with the results of the ISE response

Source	Sum of Squares	Degree of Freedom	Mean Square	F-value	p-value	
Mean vs Total	1.21E+010	1	1.21E+010			
Linear vs Mean	5.014E+07	3	1.671E+07	0.250	0.8589	
2FI vs Linear	1.525E+07	3	5.083E+06	0.063	0.9784	
Quadratic vs 2FI	9.588E+08	3	3.196E+08	36.35	<0.0001	Suggested
Cubic vs Quadratic	6.380E+07	4	1.595E+07	3.97	0.0656	
Residual	2.412E+07	6	4.020E+06			
Total	1.321E+10	20	6.607E+08			

Table 11. Evaluation of the models in terms of best fit with the results of the IAE response

Source	Sum of Squares	Degree of Freedom	Mean Square	F-value	p-value	
Mean vs Total	1.676E+08	1	1.676E+08			
Linear vs Mean	1.411E+06	3	4.703E+05	0.430	0.7354	
2FI vs Linear	1301.00	3	433.67	3.21E-4	1.0000	
Quadratic vs 2FI	1.349E+07	3	4.496E+06	11.03	0.0016	Suggested
Cubic vs Quadratic	1.926E+06	4	4.816E+05	1.34	0.3547	
Residual	2.15E+06	6	3.583E+05			
Total	1.866E+08	20	9.328E+06			

Table 12. ANOVA results of the ISE for liquid level control

Source	Sum of Squares	Degree of Freedom	F-value	p-value	
Model (Quadratic)	1.024E+09	9	12.94	0.0002	significant
X ₁ :K _p	4.997E+07	1	5.68	0.0383	
X ₂ :T ₁	31846.64	1	3.62E-03	0.9532	
X ₃ :T _D	1.395E+05	1	0.016	0.9022	
X ₁ X ₂	1.397E+07	1	1.59	0.2361	
X ₁ X ₃	4.651E+05	1	0.053	0.8227	
X ₂ X ₃	8.147E+05	1	0.093	0.7671	
X ₁ ²	9.395E+08	1	106.86	<0.0001	
X ₂ ²	5.291E+07	1	6.02	0.0341	
X ₃ ²	5.313E+06	1	0.60	0.4549	
Residual	8.792E+07	10			
Lack of Fit	8.792E+07	5			
Pure Error	0.000	5			
Cor Total	1.112E+09	19			

Table 13. ANOVA results of the IAE for liquid level control

Source	Sum of Squares	Degree of Freedom	F-value	p-value	
Model (Quadratic)	1.490E+07	9	4.06	0.0197	significant
X ₁ :K _p	1.292E+06	1	3.17	0.1054	
X ₂ :T ₁	42570.21	1	0.17	0.7532	
X ₃ :T _D	76752.82	1	0.19	0.6736	
X ₁ X ₂	1152.00	1	2.826E-03	0.9587	
X ₁ X ₃	4.50	1	1.104E-05	0.9974	
X ₂ X ₃	144.50	1	3.545E-04	0.9853	
X ₁ ²	1.299E+07	1	31.88	0.0002	
X ₂ ²	1.019E+06	1	2.50	0.1449	
X ₃ ²	4.462E+05	1	1.09	0.3201	
Residual	4.076E+06	10			
Lack of Fit	4.076E+06	5			
Pure Error	0.000	5			
Cor Total	1.898E+07	19			

Table 14. Statistical values of the ISE for liquid level control

Std. Dev.	2965.12	R-Squared	0.9209
Mean	24599.50	Adj R-Squared	0.8498
C.V. %	12.05	Pred R-Squared	0.3992
PRESS	6.681E+08	Adeq Precision	12.426

Table 15. Statistical values of the IAE for liquid level control

Std. Dev.	638.46	R-Squared	0.7852
Mean	2894.65	Adj R-Squared	0.5918
C.V. %	22.06	Pred R-Squared	0.6343
PRESS	3.101E+07	Adeq Precision	7.095

Table 16. Optimization criteria of the program for studied range

Parameters	Goal	Lower limit	Upper limit
$K_p (X_1)$	is in range	11	40
$\tau_i (X_2)$	is in range	15	45
$\tau_D (X_3)$	is in range	6	20
ISE (R_1)	minimize	17452	39652
IAE (R_2)	minimize	1832	4568

Table 17. Optimum PID parameters and responses recommended by the program

PID control parameters	Numerical values	ISE (R_1)	IAE (R_2)	Desirability
$K_p (X_1)$	23.14			
$\tau_i (X_2)$	28.31	17368	1908	1.00
$\tau_D (X_3)$	11.50			

3.7 Determination the Optimum PID Parameters for Liquid Level Control

Numerical optimization was applied to determine the optimum PID parameters for liquid level control. The optimization criteria specified in the Materials and Methods section were entered into the Design Expert 7.0.0 trial program, which proposed optimization solutions. The optimization criteria of the Design Expert program for liquid level control with the PID tuning parameters are given in Table 16 and the optimization solutions proposed by the program are given in Table 17.

The optimization procedure was carried out with a desirability function. According to this function, the ISE and IAE values of every determined response were transformed into a dimensionless desirability value (d). The value of the functions ranged between 0 and 1. The value of d increased as the desirability of the corresponding response increased. In this study, the minimum ISE and IAE values are selected for the better PID parameters of liquid level control system. In order to obtain the lowest ISE and IAE values, the optimum values of the PID tuning parameters for liquid level control were determined as 23.14, 28.31 and 11.50 for K_p , τ_i and τ_D .

4. Conclusion

In this study, RSM was used for the determination of optimum PID controller parameters to minimize the ISE and IAE performance criteria after three most widely used tuning methods applied to the experimental liquid level system. Dynamic analysis carried out on the liquid level control system for prepare the reaction curve and the dead time, time constant and process gain values were determined. PID control parameters were calculated with Cohen-Coon, Ziegler-Nichols, Yuwana-Seborg which commonly used tuning methods. These parameters applied for the 40cm, 50cm and 60cm set points and after experiments ISE and IAE control performance values were calculated. K_p , τ_i , τ_D selected as independent parameters and ISE and IAE values are chosen as dependent variables (responses). Numerical values of the responses for the runs were determined using closed-loop PID controller with liquid level system block diagram which designed in MATLAB/Simulink. Simulations in the proposed list by the trial version of Design Expert 7.0

program were performed in order and the IAE and ISE values calculated after the simulations were processed by processing the results. Optimal PID control parameters of liquid level control system determined in order to obtain the lowest ISE and IAE values were K_p 23.14, τ_i 28.31 and τ_D 11.50. Although the results of this research have demonstrated the effectiveness of the proposed optimal PID parameter tuning method and its potential future, other control applications need to be implemented to test the robustness under different disturbances. As discussed in this research, for liquid level control system the PID controller with fixed PID parameters is not suitable for all conditions and it has the limitation of not dealing well with an external disturbance such as high frequency noise, and small plant parameter changes. For these systems, the proposed method is a better choice. For complex systems without an exact mathematical model, the identification scheme can be integrated into the PID control parameter tuner design to fulfill the online optimization if needed. This provides more flexibility for control system designers.

Declaration

The author(s) declared no potential conflicts of interest with respect to the research, authorship, and/or publication of this article. The author(s) also declared that this article is original, was prepared in accordance with international publication and research ethics, and ethical committee permission or any special permission is not required.

Acknowledgement

The authors would like to thanks the Van Yüzüncü Yıl University, Department of Chemical Engineering for using the real-time experimental liquid-level control set-up.

Nomenclature

$e(t), \varepsilon$: error
G_s	: transfer function
IAE	: Integral of Absolute of the Error
ISE	: Integral of Square of the Error
K_p	: proportional constant
PB	: proportional band
RSM	: Response Surface Methodology
τ	: time constant
τ_d	: dead time
τ_i	: integral constant
τ_D	: derivative constant
U_s	: process gain
min	: minute
t	: time (second)
cm	: centimeter

References

1. Srivastava, S. Pandit, V. S., A PI/PID controller for time delay systems with desired closed loop time responses and guaranteed gain and phase margins. Journal of Process Control, 2016. 37: p.70–77.

2. Guangyue, L., Shangqi, L., Pingping, S., Yang, L., Yanyan, L., *A new optimization method for steam-liquid level intelligent control model in oil sands steam-assisted gravity drainage (SAGD) process*, Petroleum Exploration And Development, 2016. **43**(2): p.301–307.
3. Ravikishore, C., Praveen Kumar D.T.V. and Padma Sree, R., *Enhanced performance of PID controllers for unstable time delay systems using direct synthesis method*, Indian Chemical Engineer, 2020. **56**(3): p.1-17.
4. Huang, C. N., Chung, A., *An intelligent design for a PID controller for nonlinear systems*. Asian Journal of Control, 2016. **18**(2): p.447-455.
5. Ziegler J. G. Nichols N. B., *Optimum settings for automatic controllers*, Transactions of the Asme, 1993. **115**(2): p. 220–222.
6. Cohen, C., *Theoretical consideration of retarded control*. Transaction of the Asme, 1953. **75**: p.827-834.
7. Bequette, B. W., 2003, *Process Control: Modeling, Design and Simulation*, Prentice Hall Upper Saddle River, NJ.
8. Grimholt, C. Skogestad, S., *Optimal PI and PID control of first-order plus delay processes and evaluation of the original and improved SIMC rules*, *Journal of Process Control*, 2018. **70**: p.36-46.
9. Anil, C., Sree, R. P., *Design of Optimal PID Controllers for Integrating Systems*, Indian Chemical Engineer, 2014. **56**(3): p.215-228.
10. Camcioglu, S., Ozyurt, B., Doğan, İ. C., Hapoglu H., *Application of response surface methodology as a new PID tuning method in an electrocoagulation process control case*, Water Science and Technology, 2017. **76**(12): p. 3410-3427.
11. Gasparovic, C. L. M., Eyng, E., Frare, L. M., Arioli R., Orssatto F., *PID tuning by central composite rotational design methodology: a case study of absorption column for biogas purification*, International Journal of Innovative Computing, Information and Control, 2018. **14**(1): p.15-32.
12. Demirtaş, M., Karaođlan, A. D., *Optimization of PI parameters for DSP-based permanent magnet brushless motor drive using response surface methodology*, Energy Conversion and Management, 2012. **56**: p.104-111.
13. Gouta, H., Said, S. H., Barhoumi, N., M'Sahli, F., *Observer-Based backstepping controller for a state-coupled two-tank system*. IETE Journal of Research, 2015. **61**(3): p.259-268.
14. Başı, A., Derdiyok, A., *Implementation of an adaptive fuzzy compensator for coupled tank liquid level control system*, Measurement, 2016. **91**: p.12-18.
15. Boiko, I., *Variable-structure PID controller for level process*, Control Engineering Practice, 2013. **21**(5): p.700-707.
16. Jain, T., Nigam, M. J., *Optimization of PD-PI controller using swarm intelligence*. International Journal of Computational Cognition, 2008. **6**(4): p.55-59.
17. Mehta, A. K., Swarnalatha, R., *Performance evaluation of conventional PID control tuning techniques for a first order plus dead time blending process*. Journal of Engineering Science and Technology. 2018. **13**: p.3593-3609.
18. Selvaraj, S. P., Nirmalkumar, A., *Constrained GA based online PI Controller parameter tuning for stabilization of water level in spherical tank system*. International Journal of Mechanical & Mechatronics Engineering, 2015. **15**(1): p.19-31.
19. Mamat, R., Fleming, P., *Method for on-line identification of a first order plus dead-time process model*. Electronics Letters. 1995. **31**: p.1297 - 1298.
20. Wang, D-J., *Synthesis of PID controllers for high-order plants with time-delay*, Journal of Process Control, 2009. **19**(10): p.1763-1768.
21. Aldemir, A., Hapođlu, H., *Comparison of PID tuning methods for wireless temperature*. Journal of Polytechnic, 2016. **19**(1): p.9–19
22. Grimholt, C., Skogestad, S., *Optimal PI and PID control of first-order plus delay processes and evaluation of the original and improved SIMC rules*. Journal of Process Control. 2018. **70**: p.36-46.



Research Article

Removal of Maxilon Red GRL dye in continuous system adsorption column using waste pine sawdust**İlknur Şentürk^{a,*} and Muhammed Reha Yıldız^b** ^aDepartment of Environmental Engineering, Engineering Faculty, Sivas Cumhuriyet University, Sivas, 58140, Turkey^bDepartment of Environmental Engineering, Graduate School of Sciences, Sivas Cumhuriyet University, Sivas, 58140, Turkey

ARTICLE INFO

Article history:

Received 17 February 2020

Revised 13 April 2020

Accepted 24 April 2020

Keywords:

Activation

Adsorption

Breakthrough curves

Column study

Maxilon Red GRL

ABSTRACT

In this study, the effect of various design parameters on the removal of the Maxilon Red GRL dye, used in textile dyeing, in continuous system adsorption column was investigated using pine sawdust that were pre-treated with sulfuric acid. In each selected study parameter, the values read at certain times for the ratio of the output water concentration to the input concentration (C_t/C_i) were recorded into the graph and the breakthrough curves were drawn. The adsorption capacity (q_m) obtained under the best conditions (10 cm bed height, 6 mL/min flow rate and 100 mg/L initial concentration) selected according to breakthrough curve data is 483.32 mg/g. In the latest stage, with a 0.4 M NaOH solution, the applicability of regeneration to the adsorbent bed was examined. The results of the study showed that the adsorbing capacity of the used adsorbent continued for another even after regeneration. Furthermore, the data obtained from the breakthrough curve was adapted to the Adams-Bohart, Thomas, and Yoon-Nelson models. It was understood that compared to other models, the Thomas model was more appropriate for the identification of breakthrough curves.

© 2020, Advanced Researches and Engineering Journal (IAREJ) and the Author(s).

1. Introduction

In many industries such as leather, textiles, plastics, food, cosmetics, dyes in different structures are often used to color products. However, if the dyes that are mixed into wastewater after the dyeing process are discharged into the receiving waters without removal, they cause both color formation, which is not acceptable from an aesthetic point of view, and carcinogenic and mutagenic effects on aquatic life. Therefore, such colored wastewater must be treated with appropriate treatment methods before discharge to the receiving environment.

Basic dyes, acid dyes, azo dyes and disperse dyes are commonly used in the textile industry. Most of these dyes, such as Maxilon Red GRL (MR GRL), are an azo dye and used for dyeing wool, fibers, silk, and carpet [1]. Azo group dyes are one of the most problematic dyes found in industrial wastewater. Their presence in the waters may be a potential threat to the life of the living organisms [2]. Moreover, many of the reaction products of azo dyes, such as aromatic amines, are also highly carcinogenic. Therefore, removal of these

dyes from the aquatic system is of primary importance for the environment.

Although there are many methods used for the removal of dyes, most of the traditional wastewater treatment methods are insufficient for the removal of such dyes and by-products [3]. Therefore, researchers are investigating alternative treatment methods that are more environmental and effective. Among alternative treatment methods, adsorption is gaining more and more attention, especially because of the advantages it presents related to the removal of color and dissolved molecule [4]. The choice of efficient, cheap, easily obtainable adsorbent materials makes the method even more advantageous. Therefore, many researchers study on the use of low-cost or no-cost agricultural and industrial wastes as adsorbents for the removal of dyes from wastewater [5].

Sawdust produced in abundance from furniture production, industrial activities, and forestry activities are preferred as adsorbents in adsorption studies. Sawdust have several important advantages such as cost, quantity, renewability, and biodegradability. Because they mostly

* Corresponding author. Tel.: +90 0346 2191010.

E-mail addresses: ilknursenturk@cumhuriyet.edu.tr (İ. Şentürk), muhammedrehay@gmail.com (M.R. Yıldız)

ORCID: 0000-0002-8217-2281 (İ. Şentürk), 0000-0001-5534-0510 (M.R. Yıldız)

DOI: 10.35860/iarej.689639

consist of cellulose, hemicellulose, and lignin, these properties convert the sawdust into a suitable adsorbent for adsorption [6,7]. Researches has shown that sawdust can be used as an efficient adsorbent to remove various types of dyes and other undesirable pollutants from wastewater mixtures.

Recent searches have headed on the application of different modification agents to improve the adsorption capacity of the adsorbent. Several chemical activating agents are used by researchers, such as zinc chloride ($ZnCl_2$), phosphoric acid (H_3PO_4), potassium hydroxide (KOH), calcium chloride ($CaCl_2$), sulfuric acid (H_2SO_4), sodium hydroxide (NaOH), hydrochloric acid (HCl), nitric acid, etc. [8]. These activating agents are used to modify the adsorbent inorganic acid (stronger acid) (HCl, H_2SO_4 , and HNO_3); the treatment has shown that the addition of H_2SO_4 increases adsorbent efficiency, surface area, and porosity [9]. The same results were obtained in our previous study [10].

In the performed literature review, any study on the effect of pre-treated sawdust as waste material for MR GRL on the batch and continuous system adsorption potential was not encountered. In terms of industrial, for the fixed bed adsorption system, the evaluation of adsorbent efficiency is more useful than batch system studies. The reason for this is that the data obtained from batch system studies may show inconsistencies with the data obtained from column studies. Therefore, it is very important to investigate the adsorption system by using fixed-bed systems [11]. Large amounts of colored wastewater are treated in the adsorption column to ensure the adsorption of the dye onto the adsorbent surface. The dye-loaded solid adsorbent mass obtained at the end of this process will yield a less dense dye when regenerated. This dye can be re-evaluated within an 'Industrial Ecology' framework. If such a system is not available, it will be sent back to the adsorption column to be treated. If regeneration of the adsorbent is not possible, the dye-loaded adsorbent will be disposed of as a hazardous waste.

The most important advantage of the adsorption process is to ensure that toxic and dangerous dyes in large wastewater masses are removed by holding onto the solid surface. Thus, both the volume of waste to be treated is reduced and the solid mass obtained can be disposed of more easily or can be used as a fuel in boilers.

In this study, removal from the aquatic environment of MR GRL was performed in the continuous system adsorption column by using pre-acid-treated pine sawdust. By investigating the effect of different operating parameters such as adsorbent bed height, input dye concentration, flow rate, and regeneration efficiency, the MR GRL removal efficiency of pre-treated pine sawdust in the continuous system adsorption column was investigated.

2. Materials and Methods

2.1 Adsorbent

Primarily, natural pine sawdust, obtained from an industry engaged in woodworking, were washed with pure water 5-6 times to be free from dirt, dust, and impurities contained within it. Then, they were dried in a drying-oven at $80^\circ C$ for 24 hours. The sawdust in a large grain fraction ranging from +0.38 -2 mm (USA standard) were made suitable for pre-treatment. 20 g was taken from the sawdust prepared for pre-treatment and transferred to 500 mL Erlenmeyer flask; then, 200 mL 1 N H_2SO_4 solution was added on it. While the mouth of the Erlenmeyer flask closed, the mixture was kept in the oven at $150^\circ C$ for 24 hours. After the material, brought to room temperature, was washed several times with pure water, it was kept overnight in a 1% $NaHCO_3$ solution to remove the remaining acid. The material was then washed again with pure water and dried in the drying-oven at $80^\circ C$ for 24 hours. The resulting adsorbent material was named as pre-acid-treated sawdust and stored in a brown glass bottle for use in studies [12,13].

2.2 Dye (Adsorbate)

In Table 1, the properties of the dye used in the study are given. The stock dye solution was prepared by weighing the dye and dissolving it in distilled water in a way that it would be at a concentration of 1 g/L. Images of the adsorbent before and after adsorption are given in Figure 1.



Figure 1. Unloaded adsorbent and the adsorbent loaded with MR GRL

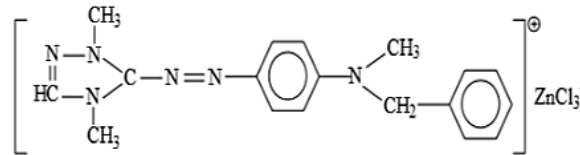
2.3 Continuous System Adsorption Experiments

Continuous system adsorption studies were conducted in a 37 cm long transparent plexiglass column with an inner diameter of 1.4 cm. The experiment assembly is equipped with a peristaltic pump (Shenchen Pump, YZ1515x) for continuous flow rate. After the lower base of the column was supported with glass wool, the desired amount of adsorbent material was placed in the column in a way that there was no space between them, and the top of the adsorbent was again supported by glass wool. After the adsorbent bed was prepared in this way, the bed was washed with distilled water for a certain period of time to get rid of air bubbles and to ensure proper distribution of fluid in the column [15].

Table 1. Properties of the Maxilon Red GRL dye

Chemical formula	λ_{\max} (nm)	Molecular weight (g/mol)	Type	Group	Reference
$C_6H_{12}N_6 \cdot ZnCl_3$	531	429.9	Cationic	Azo Group 1	[14]

Chemical Structure



The MR GRL dye solution, prepared in different concentrations, was pumped to down from the adsorbent bed at the specified flow rate. The output concentration of the dye solution taken from the column output at specific times was analyzed spectrophotometrically. The system was operated until the output dye concentration matches the input dye concentration. The different operating parameters such as bed height, flow rate, and initial dye concentration on the column treatment efficiency was studied. It was studied at three different flow rates (4, 6, and 8 mL/min), at 5, 10 and 15 cm bed height (1.2, 2.4 and 3.6 g of adsorbents were used, respectively), and at three different dye concentrations (50, 100 and 150 mg/L). Studies were continued on the determined optimum condition for each parameter and the effect of the next parameter was examined. With desorption studies, the reusability of adsorbent substance has also been investigated. Time-breakthrough curves of C_t/C_i were drawn for different column operating parameters (where C_t is the dye concentration at the column output at the end of the t (min) period and C_i is the input concentration).

The breakthrough time (t_b) in this study is the time elapsed when the output dye concentration reaches 5-10% of the feed concentration. The exhaustion time (t_e) is the time elapsed when the output dye concentration reaches 90% of the input dye concentration [16].

The maximum adsorption capacity q_m (mg/g) is defined as the ratio (m) of the adsorbed dye mass (q_a) to the adsorbent mass in the column [Eq 1] [15,17].

$$q_m = q_a/m \quad (1)$$

2.4. Continuous System Desorption Studies

By being passed 100 mg/L concentration of dye solution from the column, which had 10 cm bed height, at a flow rate of 6 mL/min, adsorption of dye by the column bed was ensured. Subsequently, the exhausted material after adsorption was regenerated with a 0.4 M NaOH solution at a flow rate of 6 mL/min. After the regeneration process, the adsorbent substance was washed with pure water until the pH was neutral. After the original cycle, three more cycles of adsorption-desorption studies were conducted, and the

reusability of the adsorbent substance was examined.

3. Results and Discussion

3.1. Effect of Flow Rate (Q)

With pre-treated pine sawdust, the effect of flow rate on MR GRL adsorption was studied at three different flow rates (4, 6, 8 mL/min). Figure 2 shows the effect of the flow rate on the breakthrough curve under the determined operating conditions. It is seen that adsorption is faster at a low flow rate. When the flow rate is low, the adsorption efficiency is better because enough time is provided for the dye ions to reach and pass through numerous reaction sites on the adsorbent surface. The contact time between the adsorbent and the adsorbent decreases as the increased flow rate will allow the dye molecules to move faster in the column. Thus, the removal rate and mass transfer rate of the dye decreases [18].

As the flow rate rises, the breakthrough point was reached in a shorter time and a smoother and steeper curve was obtained. For an effective adsorption, the length of time the dye molecules stay in the column is very important. Because, there is always a threshold value for each sorption process [19]. As seen in Figure 2, the column adsorption capacity (q_m) decreased from 674.15 mg/g to 431.79 mg/g as the flow rate increased from 4 mL/min to 8 mL/min. As can be seen, the highest removal rate was obtained at a flow rate of 4 mL/min and a larger volume of dye solution was treated.

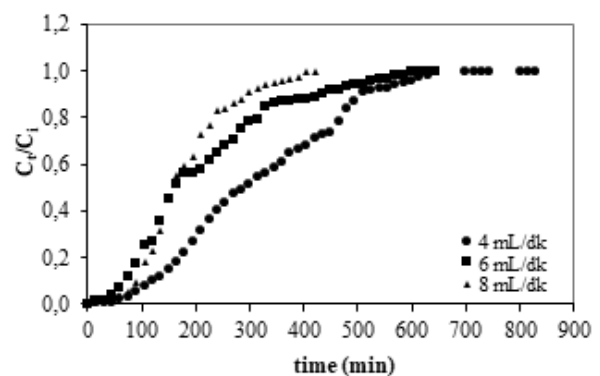


Figure 2. Effect of the Flow Rate ($C_i = 50$ mg/L, $H = 5$ cm, $pH = 5.7-6.0$, $T = 25^\circ C$)

3.2 Effect of the Adsorbent Height (H)

Depending on the amount of adsorbent used in the column, the removal efficiency varies. Therefore, the adsorbents of 1.2, 2.4 and 3.6 g, corresponding to the bed height of 5, 10 and 15 cm, were placed in the column in a way that there is no space between them. The breaking curves obtained for different bed heights are given in Figure 3. Since dye molecules are more in contact with the adsorbent surface as bed height (i.e. adsorbent mass) increases, the dye removal efficiency has increased. Because a larger mass transfer region is formed along with the increased adsorbent mass, the increase in dye removal is probably due to the obtainability of additional active binding sites for the sorption of MR GRL dye [20,21]. Similar results were also obtained in the column study conducted by Li et al. [21]. Also the same results were also observed by Cruz et al. [22] for removal of crystal violet with bone char. In fact, Gupta and Babu [23] obtained similar breakthrough curves for Cr (VI) removal. Such results are frequently encountered in liquid phase adsorption systems where mass transfer is limited by diffusion.

The MR GRL dye in the input wastewater was adsorbed by the adsorbent in the early minutes, and this trend continued with the increase in bed height. However, after a certain period of time, the MR GRL dye concentration in the water coming out of the column increased and eventually adsorption reached equilibrium. It was seen that dye adsorption was proportional to the amount of adsorbent in the column. When the adsorbent height in the column was increased from 5.0 cm to 15.0 cm, the MR GRL adsorption capacity increased from 434.48 mg/g to 554.02 mg/g. The adsorbing capacity of the adsorbent bed and the spreading rate of the pollutant increased with increasing bed height. The same results were reported by Alardhi et al. [24].

3.3. Effect of Dye Concentration (C_i)

The breakthrough curves obtained at different initial concentrations (50, 100 and 150 mg/L) by keeping the other operating parameters such as pH, bed height and flow rate constant are given in Figure 4. As seen in the Figure 4, when the input dye concentration was reduced, the break time was significantly increased and a better column performance was achieved. The reason could be that at lower concentrations, there will be lower competition between dye molecules that will be adsorbed to the surface of the adsorbent due to a decrease in mass transfer or diffusion coefficient. Based on this, it can be said that the diffusion process depends on the input dye concentration [20,21,25].

When the dye concentration at the column entrance increased from 50 mg/L to 150 mg/L, the adsorption capacity increased from 479.64 mg/g to 497.93 mg/g. This result also means that the MR GRL dye removal efficiency decreased. Based on this, it can be based on the following conclusion that the designed adsorption process is applicable for the

removal of more dilute dye concentrations. The same results were also achieved for anionic dye adsorption by waste tea residue [26].

When Table 2 is examined, it seems that when the initial dye concentration increases, the adsorbent's saturation time decreases and adsorption capacity increases. Since the initial dye concentration increases, the adsorption bed will reach saturation more quickly, so the breakthrough curve is achieved in a shorter time (Table 2). When the dye concentration to be treated is increased from 50 mg/L to 150 mg/L, the adsorbent exhaustion time (t_c) decreased from 525 min to 132 min. This situation can be explained in the following way; as the input dye concentration increases, the adsorbent substance needs much more time to achieve adsorption equilibrium. The reason could be that when the input concentration is high, the adsorbent bed reaches the saturation much earlier and the breakthrough moment is reached before all active regions of the adsorbent are not filled by the dye molecules [27].

3.4. Reusability of the Adsorbent Bed

In order for the adsorption study to be economical and efficient, the regenerability of the adsorbent substance used in the continuous system adsorption column is quite important. The regeneration process can be explained as getting back or releasing the substance clinging to the surface of the adsorbent [28].

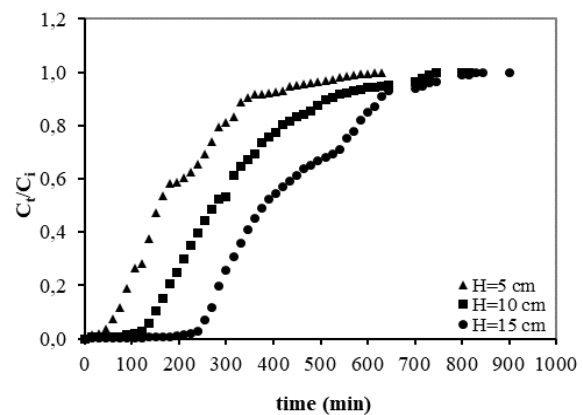


Figure 3. Effect of bed height on breakthrough curve ($C_i = 50$ mg/L, $Q = 6$ mL/min, $pH = 5,7-6,0$, $T = 25^\circ C$)

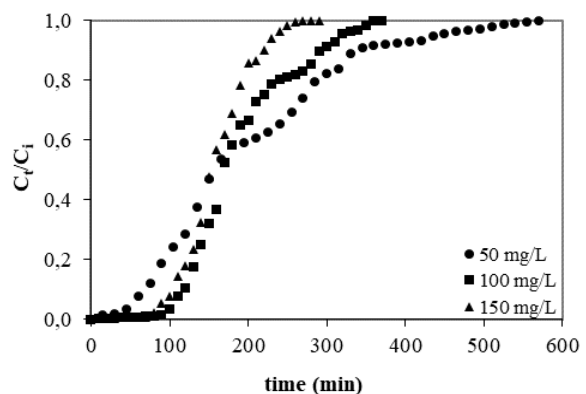


Figure 4. Effect of initial concentrations ($Q = 6$ mL/min, $H = 10$ cm, $pH = 5.7-6.0$, $T = 25^\circ C$)

For this reason, regeneration efficiency was tried to be determined by adsorption-desorption cycles performed consecutively. Washing with desorption fluid was proceed until there was no MR GRL dye stay in the filtrate at the exit of the colon. Then to remove the remaining NaOH solution in the adsorbent bed, the column bed was washed with pure water until the pH was neutral. Adsorption-desorption process was repeated in 3 cycles. The breakthrough curves obtained after each cycle are given in Figure 5.

The adsorption capacities of the raw adsorbent and the adsorbent undergoing the regeneration process are given in Figure 6. While the maximum adsorption capacity (q_m) in the continuous system was 588.79 mg/g for the original cycle, it was found to be 446.74 mg/g at the 3rd cycle. While the q_m value showed a significant decrease in the first cycle after the original cycle, a very small decrease was observed in the 2nd and 3rd cycles. The fact that good efficiency and high adsorption capacity were achieved even after the 3rd cycle suggests that the pine sawdust adsorbent, which has undergone acidic treatment, can be used efficiently as several-repetitions in the continuous system for the removal of the Maxilon Red GRL.

3.5. Dynamic Mathematical Models Used in Continuous Systems

In order to describe the dynamic behavior of the removal of pollutants in the fixed bed column and to characterize bed performance, mathematical models such as Adams-Bohart, Thomas and Yoon-Nelson were used. Detailed information about the mathematical models used in the study and the equations used in the modeling were given in detail in the study published by Şentürk and Alzein [15]. The results obtained from the breakthrough curves through the specified models are given in Table 3.

As seen in Table 3, the data obtained from the breakthrough curve did not show conformity with the Adams-Bohart model (see R^2 values). It was understood that the Thomas and Yoon-Nelson models could be used to interpret the colon system (the mean R^2 value was 0.9557). The Thomas model is one of the most popular models used in colon adsorption studies, where the second-order reaction kinetic model and the Langmuir isotherm are used together. When the R^2 values gotten under separate working conditions for the Thomas model are examined, it is observed that the R^2 value obtained at 10 cm bed height, 6 mL/min flow rate and 100 mg/L initial dye concentration is 0.9607.

In addition, according to the data obtained from Table 3, since the input dye concentration increased, the q_{Th} value of the Thomas model decreased, but the k_{Th} value increased. However, because the contact time between the dye and the adsorbent increased with the increase in bed height, the k_{Th} value decreased this time.

Table 2. Parameters of the column breakthrough curve for MR GRL.

H (cm)	Q (mL/dk)	C_i (mg/L)	t_b (dk)	t_e (dk)	q_m (mg/g)
5	4	50	120	500	474.17
5	6	50	95	435	434.48
5	8	50	70	295	431.79
10	6	50	150	525	479.64
15	6	50	265	630	554.02
10	6	100	100	190	483.32
10	6	150	72	132	497.93

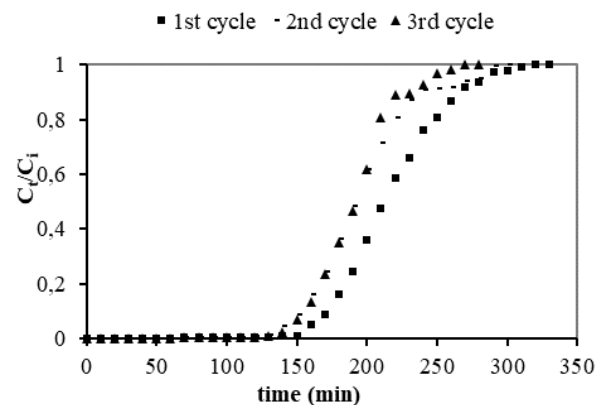


Figure 5. Column breakthrough curves after regeneration

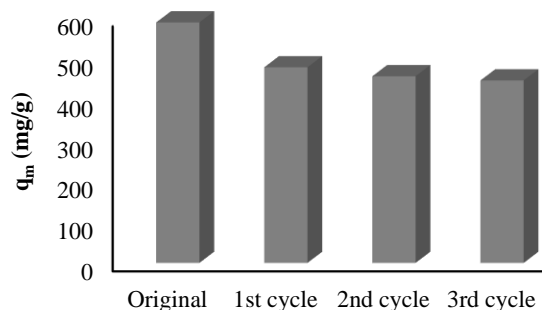


Figure 6. Column adsorption capacities (q_m) of MR GRL dye on raw and regenerated adsorbents after adsorption-desorption cycle

Similarly, at 10 cm bed height and 6 mL/min flow rate, while the q_m (mg/g) value increased from 41.22 mg/g to 47.12 mg/g when dye concentration increased from 50 to 100 mg/L, it decreased again to value of 38.35 mg/g when the concentration reached to 150 mg/L. Here, it is seen that the column has reached its maximum adsorption capacity at 10 cm bed height, 6 mL/min flow rate and 100 mg/L dye concentration.

When the τ values obtained from the Yoon-Nelson model were examined, it is observed that the $t_{0.5}$ value obtained at 10 cm bed height, 6 mL/min flow rate and 100 mg/L dye concentration showed proximity to the τ value.

Table 3. Model parameters for the Maxilon Red GRL dye

Column System Operation Parameters	H (cm)	5	10	15	5	5	10	10
	Q (mL/min)	6	6	6	4	8	6	6
	C ₀ (mg/L)	50	50	50	50	50	100	150
Parameters of the Adams-Bohart Model	k _{AB} 10 ⁵ (L/mg min)	8.87	13.90	29.12	9.59	19.02	16.82	15.42
	N ₀ 10 ⁻³ (mg/L)	17.69	10.99	7.68	15.16	16.50	10.64	12.86
	R ²	0.5836	0.6990	0.8344	0.6717	0.7329	0.8102	0.8586
Parameters of the Thomas Model	k _{Th} (mL/min mg)	2.72	2.66	2.58	2.74	3.31	2.99	3.13
	q _{Th} (mg/g)	48.48	46.23	35.75	50.20	59.37	40.09	37.47
	q _m (mg/g)	49.23	41.22	36.32	51.33	60.11	47.12	38.35
	R ²	0.9518	0.9360	0.9605	0.9663	0.9535	0.9607	0.9608
Parameters of the Yoon-Nelson Model	k _{YN} (min ⁻¹)	1.35	1.32	1.49	1.37	2.22	2.92	4.67
	τ (min)	432.31	323.19	195.41	301.11	174.41	189.62	143.33
	t _{0.5} (min)	375	270	165	285	150	180	140
	R ²	0.9518	0.9360	0.9605	0.9663	0.9535	0.9607	0.9608

A similar condition was also observed at a dye concentration of 150 mg/L. However, no proximity between these two values was observed for other parameters. Therefore, contrary to the interpretation made above based on the value of R², the model results given in Table 3 clearly show that the Yoon-Nelson model is not compatible with the breakthrough curve data.

4. Conclusion

During this study, in which the continuous adsorption of the Maxilon Red GRL dye in the system was examined using sulfuric acid-activated pine sawdust, no changes were made in parameters such as pH and temperature, and the effects of column height, flow rate and dye concentration on the column breakthrough curve were investigated. Flow rate is an important parameter that should be examined in the design of column systems. It was seen that the MR GRL dye removal and the q_m value in the column decreased with the increase in flow rate. Furthermore, the rise of the flow rate led to low breakthrough capacity, a decrease in retention time, and thus a decrease in the amount of dye adsorbed by the adsorbent bed. The second parameter examined is the column bed height. It was observed that as bed height increased, there was an increase in breakthrough time (t_b), exhaustion time (t_e) and maximum adsorption capacity (q_m) values. Another parameter examined in this study is the dye concentration at the entrance to the column. It was found that efficiency and adsorbing capacity decreased as dye concentration increased. The maximum adsorption capacity (q_m) obtained under the selected best conditions (10 cm bed height, 6 mL/min flow rate, and 100 mg/L initial concentration) is 483.32 mg/g.

Changes in the removal efficiency of the adsorbent after the regeneration applied to the exhausted adsorbent were also investigated. While the maximum MR GRL adsorption capacity (q_m) of the adsorbent was 588.79 mg/g when studying with the raw adsorbent, which had never been

regenerated, q_m of the adsorbent decreased to 446.74 mg/g after the 3rd regeneration.

The Adams-Bohart model, Thomas model, and Yoon-Nelson model were adapted to experimental results obtained from the continuous system. The results showed that the Thomas model was more appropriate for defining breakthrough curves.

Designing of adsorption column with acid activated pine sawdust suggests that activated pine sawdust can be used as low-cost industrial adsorbent in the larger scale. Continuous system adsorption column ensures efficient use of the driving force in the column and more efficient wastewater treatment. Continuous system working columns are a small form of adsorption columns used in the industry and provide very important information for understanding the treatment process. The results obtained from the study showed that MR GRL dye removal with acid-pretreated pine sawdust can be treated in a continuous system adsorption column. However, for industrial application, it should also be worked with real textile wastewater containing MR GRL dye.

Declaration

The author(s) declared no potential conflicts of interest with respect to the research, authorship, and/or publication of this article. The author(s) also declared that this article is original, was prepared in accordance with international publication and research ethics, and ethical committee permission or any special permission is not required.

References

1. Canbaz, G. T., Çakmak, N. K., Eroğlu, A., and Açık, Ü., Removal of Acid Orange 74 from wastewater with TiO₂ nanoparticle. *International Advanced Researches and Engineering Journal*, 2019. **03**(01): p. 75-80.
2. Deniz, F., *Effective removal of Maxilon red GRL from aqueous solutions by walnut shell: Nonlinear kinetic and equilibrium models*. *Environmental Progress & Sustainable Energy*, 2014. **33**: p. 396-401.

3. Sumanjit, Walia T. P. S., and Kaur R., *Removal of health hazards causing acidic dyes from aqueous solutions by the process of adsorption*. The Online Journal of Health and Allied Sciences: OJHAS, 2007. **6**(3:3): p. 1-10.
4. El-Sayed, G., *Electrochemical Decolorization of Maxilon Red GRL Textile Dye*. International Research Journal of Pure and Applied Chemistry, 2014. **4**: p. 402-416.
5. Doğan, M., Karaoğlu, M. H., and Alkan, M., *Adsorption kinetics of maxilon yellow 4GL and maxilon red GRL dyes on kaolinite*. Journal of Hazardous Materials, 2009. **165**: p. 1142-1151.
6. Deniz, F., and Kepekci, R. A., *Bioremoval of Malachite green from water sample by forestry waste mixture as potential biosorbent*. Microchemical Journal, 2017. **132**: p. 172-178.
7. Özacar, M., and Şengil, İ. A., *Adsorption of metal complex dyes from aqueous solutions by pine sawdust*. Bioresource Technology, 2005. **96**: p. 791-795.
8. Akl, M. A., Mostafa, M. M., and Bashanaini, M. S. A., *Enhanced Removal of Some Cationic Dyes from Environmental Samples Using Sulphuric Acid Modified Pistachio Shells Derived Activated Carbon*. Journal of Chromatography & Separation Techniques, 2016. **7**:329. doi:10.4172/2157-7064.1000329.
9. Thenmozhi, R., and Santhi, T., *Characterization of activated Acacia nilotica seed pods for adsorption of Nickel from aqueous solution*. International Journal of Environmental Science and Technology (IJEST), 2015. **12**: p. 1677-1686.
10. Şentürk, İ., and Alzein, M., *Adsorption of Acid Violet 17 onto Acid-Activated Pistachio Shell: Isotherm, Kinetic and Thermodynamic Studies*. Acta Chimica Slovenica, 2020. **67**: p. 55-69.
11. Banerjee, S., Sharma, G. C., Gautam, R. K., Chattopadhyaya, M. C., Upadhyay, S. N., and Sharma, Y. C., *Removal of Malachite Green, a hazardous dye from aqueous solutions using Avena sativa (oat) hull as a potential adsorbent*. Journal of Molecular Liquids, 2016. **213**: p. 162-172.
12. Garg, V. K., Gupta, R., Bala Yadav, A., and Kumar, R., *Dye removal from aqueous solution by adsorption on treated sawdust*. Bioresource Technology, 2003. **89**: p. 121-124.
13. Şentürk, İ., Yıldız, M. R., *Highly efficient removal from aqueous solution by adsorption of Maxilon Red GRL dye using activated pine sawdust*. Korean J. Chem. Eng., 2020. **37**: p. 985-999.
14. Irinislimane, H., and Belhaneche-Bensemra, N., *Extraction and Characterization of Starch from Oak Acorn, Sorghum, and Potato and Adsorption Application for Removal of Maxilon Red GRL from Wastewater*. Chemical Engineering Communications, 2017. **204**: p. 897-906.
15. Şentürk, I., and Alzein, M., *Acidic dye removal from aqueous solution in continuous system column using pistachio shells activated with H₂SO₄*. AKU J. Sci. Eng., 2019. **19**: p. 697-708.
16. Wu, X., Wu, D., Fu, R., and Zeng, W., *Preparation of carbon aerogels with different pore structures and their fixed bed adsorption properties for dye removal*. Dyes Pigments, 2012. **95**: p. 689-694.
17. Yusuf, M., Khan, M. A., Otero, M., Abdullah, E. C., Hosomi, M., Terada, A., and Riya, S., *Synthesis of CTAB intercalated graphene and its application for the adsorption of AR265 and AO7 dyes from water*. Journal of Colloid and Interface Science, 2017. **493**: p. 51-61.
18. Muthukumaran, C., Sivakumar, V. M., Sumathi, S., and Thirumarimurugan, M., *Adsorptive Removal of Recalcitrant Auramine-O Dye by Sodium Dodecyl Sulfate Functionalized Magnetite Nanoparticles: Isotherm, Kinetics, and Fixed-Bed Column Studies*. International Journal of Nanoscience, 2020. **19**: 1950004.
19. Şentürk, İ., Alzein, M., *Adsorptive removal of basic blue 41 using pistachio shell adsorbent - Performance in batch and column system*. Sustain. Chem. Pharm., 2020. **16**: 100254.
20. Al-Degs, Y. S., Khraisheh, M. A. M., Allen, S. J., and Ahmad, M. N., *Adsorption characteristics of reactive dyes in columns of activated carbon*. Journal of Hazardous Materials, 2009. **165**: p. 944-949.
21. Tamez Uddin, Md., Rukanuzzaman, Md., Maksudur Rahman Khan, Md., and Akhtarul Islam, Md., *Adsorption of methylene blue from aqueous solution by jackfruit (Artocarpus heteropyllus) leaf powder: A fixed-bed column study*. Journal of Environmental Management, 2009. **90**: p. 3443-3450.
22. Cruz, M. A. P., Guimarães, L. C. M., da Costa Júnior, E. F., Rocha, S. D. F., and Mesquita, P. da L., *Adsorption of crystal violet from aqueous solution in continuous flow system using bone char*. Chemical Engineering Communications, 2020. **207**: p. 372-381.
23. Gupta, S., and Babu, B. V., *Modeling, simulation, and experimental validation for continuous Cr(VI) removal from aqueous solutions using sawdust as an adsorbent*. Bioresource Technology, 2009. **100**: p. 5633-5640.
24. Alardhi, S. M., Albayati, T. M., and Alrubaye, J. M., *Adsorption of the methyl green dye pollutant from aqueous solution using mesoporous materials MCM-41 in a fixed-bed column*. Heliyon, 2020. **6**: e03253.
25. Li, W., Yue, Q., Tu, P., Ma, Z., Gao, B., Li, J., and Xu, X., *Adsorption characteristics of dyes in columns of activated carbon prepared from paper mill sewage sludge*. Chemical Engineering Journal, 2011. **178**: p. 197-203.
26. Jain, S. N., Tamboli, S. R., Sutar, D. S., Jadhav, S. R., Marathe, J. V., Shaikh, A. A., and Prajapati, A. A., *Batch and continuous studies for adsorption of anionic dye onto waste tea residue: Kinetic, equilibrium, breakthrough and reusability studies*. Journal of Cleaner Production, 2020. **252**: 119778.
27. Ramavandi, B., Farjadfard, S., and Ardjmand, M., *Mitigation of orange II dye from simulated and actual wastewater using bimetallic chitosan particles: Continuous flow fixed-bed reactor*. Journal of Environmental Chemical Engineering, 2014. **2**: p. 1776-1784.
28. El Boujaady, H., Mourabet, M., El Rhilassi, A., Bennani-Ziatni, M., El Hamri, R., and Taitai, A., *Interaction of adsorption of reactive yellow 4 from aqueous solutions onto synthesized calcium phosphate*. Journal of Saudi Chemical Society, 2017. **21**: p. 94-100.